

Electromagnetic Design and Beam Dynamics Studies in Elliptic Superconducting Radiofrequency (SRF) Cavities

By
Arup Ratan Jana
PHYS03201304004

Raja Ramanna Centre for Advanced Technology, Indore

A thesis submitted to the
Board of Studies in Physical Sciences
In partial fulfilment of requirements
For the Degree of
DOCTOR OF PHILOSOPHY
of
HOMI BHABHA NATIONAL INSTITUTE

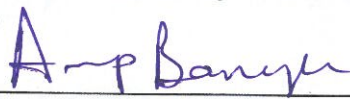
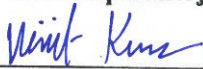

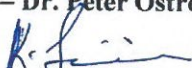

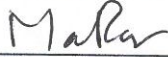

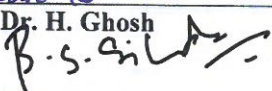


August, 2019

Homi Bhabha National Institute¹

Recommendations of the Viva Voce Committee

As members of the Viva Voce Committee, we certify that we have read the dissertation prepared by Arup Ratan Jana entitled "Electromagnetic Design and Beam Dynamics Studies in Elliptic Superconducting Radiofrequency (SRF) Cavities" and recommend that it may be accepted as fulfilling the thesis requirement for the award of Degree of Doctor of Philosophy.

	07/01/2021
Chairman – Dr. Arup Banerjee	Date:
	7.1.2021
Guide – Dr. Vinit Kumar	Date:
	January 2, 2021
External Examiner – Dr. Peter Ostroumov	Date:
	6/1/2021
External Member – Dr. Srinivas Krishnagopal	Date:
	07.01.2021
Member1 - Dr. Aparna Chakrabarti	Date:
	07.01.2021
Member2 - Dr. M. P. Singh	Date:
	07/01/2021
Member3 - Dr. H. Ghosh	Date:
	7/1/21
Member4 - Dr. Satya Bulusu	Date:

Final approval and acceptance of this thesis is contingent upon the candidate's submission of the final copies of the thesis to HBNI.

I/We hereby certify that I/we have read this thesis prepared under my/our direction and recommend that it may be accepted as fulfilling the thesis requirement.

Date: 14/1/21

Place: INDORE

Guide: 

Dr. Vinit Kumar

¹ This page is to be included only for final submission after successful completion of viva voce.

STATEMENT BY AUTHOR

This dissertation has been submitted in partial fulfilment of requirements for an advanced degree at Homi Bhabha National Institute (HBNI) and is deposited in the Library to be made available to borrowers under rules of the HBNI.

Brief quotations from this dissertation are allowable without special permission, provided that accurate acknowledgement of source is made. Requests for permission for extended quotation from or reproduction of this manuscript in whole or in part may be granted by the Competent Authority of HBNI when in his or her judgement the proposed use of the material is in the interests of scholarship. In all other instances, however, permission must be obtained from the author.



Arup Ratan Jana

DECLARATION

I, hereby declare that the investigation presented in the thesis has been carried out by me.
The work is original and has not been submitted earlier as a whole or in part for a degree
/ diploma at this or any other Institution / University.

Arup Ratan Jana

Arup Ratan Jana

LIST OF PUBLICATIONS ARISING FROM THE THESIS

- **List of Journal publications**

1. “Electromagnetic Design of a $\beta_g = 0.9$, 650-MHz Superconducting Radio Frequency Cavity”

Arup Ratan Jana, Vinit Kumar, Abhay Kumar, and Rahul Gaur

IEEE Trans. Appl. Supercond., **23**, Issue 4, pp. 3500816-3500816, (2013)

<https://doi.org/10.1109/TASC.2013.2256356>

2. “A study of dynamic Lorentz force detuning of 650 MHz $\beta_g = 0.9$ superconducting radio frequency cavity”

Abhay Kumar, **Arup Ratan Jana** and Vinit Kumar

Nucl. Instrum. Methods Phys. Res., Sect. A, **750**, pp. 69-77 (2014)

<https://doi.org/10.1016/j.nima.2014.03.005>

3. “On the Electromagnetic Design of a $\beta_g = 0.61$, 650 MHz Superconducting Radiofrequency Cavity”

Arup Ratan Jana and Vinit Kumar

IEEE Trans. Appl. Supercond., **24**, Issue 6, pp. 1-16, (2014)

<https://doi.org/10.1109/TASC.2014.2332435>

4. “Influence of material parameters on the performance of niobium based superconducting RF cavities”

Arup Ratan Jana, Abhay Kumar, Vinit Kumar and Sindhunil Barman Roy

Pramana - Journal of Physics, **93** 3, pp.51 (1-11), (2019)

<https://doi.org/10.1007/s12043-019-1813-4>

5. “Beam optics studies and lattice design of the 1 GeV H^- injector linac for ISNS”

Arup Ratan Jana and Vinit Kumar

Nucl. Instrum. Methods Phys. Res., Sect. A, **942**, pp. 162299, (2019)

<https://doi.org/10.1016/j.nima.2019.06.040>

Contd..

- **List of Conference publications**

1. “Lattice design and beam dynamics simulations for the 1 GeV ISNS SRF LINAC”
Arup Ratan Jana, Mukesh Kumar Pal, Ram Prakash, Rahul Gaur *et. al.*
Proc. Indian Particle Accelerator Conference-2018, Indore, India, (2018)
2. “On the requirement of high purity level of material for niobium based SRF cavity”
Arup Ratan Jana, Abhay Kumar, Vinit Kumar and Sindhunil Barman Roy
Proc. Indian Particle Accelerator Conference-2018, Indore, India, (2018)
3. “Design Studies for Medium and High beta SCRF Cavities for Indian Spallation Neutron Source”
Arup Ratan Jana and Vinit Kumar
LINAC2014, Geneva, Switzerland, (2014)
4. “Akruti-Wrapper for Poisson SUPERFISH”
Devendra Sinnarkar, Rajiv Jain, **Arup Ratan Jana**, Abhay Kumar *et. al.*
National Symposium on Nuclear Instrumentation, NSNI-2013, Mumbai, (2013)
5. “Electromagnetic design issues in elliptic superconducting radio frequency cavity for H⁻ LINAC”,
Vinit Kumar, **Arup Ratan Jana** and Rahul Gaur
Proc. Indian Particle Accelerator Conference-2013, Kolkata, India, (2013)
6. “Analysis of regenerative beam break up instability in linear accelerators”
Vinit Kumar, **Arup Ratan Jana**, Nita S Kulkarni and Rinky Dhingra
Proc. Indian Particle Accelerator Conference-2013, Kolkata, India, (2013)
7. “Electromagnetic design optimization studies for $\beta_g = 0.61$, 650 MHz elliptic superconducting radio frequency cavity”,
Arup Ratan Jana, Vinit Kumar and Rahul Gaur,
Proc. Indian Particle Accelerator Conference-2013, Kolkata, India, (2013)

DEDICATED

To the loving memories of my parents

To Mahuwa

&

To the indomitable flow of eternity that hums

“At the feel in my pulse of the rhythm of creation

Cadenced by the swing of the endless time.”

“অসীম কালের যে হিল্লোলে জোয়ার-ভাঁটায় ভুবন দোলে
নাড়ীতে মোর রক্তধারায় লেগেছে তার টান,
বিস্ময়ে তাই জাগে আমার গান॥”

Quoted from Kabiguru **Rabindranath Tagore’s** song (**Gitan / Nature / 8**).
উদ্ধৃতিটি কবিগুরু রবীন্দ্রনাথ ঠাকুর বিরচিত গীতবিতান নামক গ্রন্থের প্রকৃতি পর্যায়ের অষ্টম সঙ্গীতের অংশবিশেষ।

ACKNOWLEDGEMENTS

I would like to convey my sincere thanks to

- *My HBNI guide Dr. Vinit Kumar for his excellent guidance, for helping me with his in-depth knowledge in the subject and also for his patience with the language corrections during documentation of the work.*
- *Dr. Sindhunil Barman Roy for his guidance in improving the quality of work towards a conclusion as well for introducing me to the importance of material aspects in the design.*
- *Mr. Abhay Kumar, for his concern, encouragement, the valuable ideas and expertise in ANSYS simulations that he extended to me.*
- *Dr. Kamal Kumar Pant for his extended concern, support and constant encouragement.*
- *All members of the Accelerator and Beam Physics Section and FEL & Utilization Section group for their concern and help.*
- *The chairman, of my Doctoral committee, Dr. Arup Banerjee, for his critical review and useful suggestions on my work.*
- *All members of my Doctoral committee, especially Dr. M. P. Singh for his concern and constant encouragement.*
- *Both of the Reviewers of my thesis for their critical reviews and excellent suggestions.*
- *All unknown reviewers of my journal publications for their critical reviews and*
- *Andrei Lunin from FNL, USA for the valuable help he offered, explaining his indigenous simulation methodology.*
- *All of my teachers whose constant effort has shown the way of life from the day one of my school, especially Shri Brindaban Das and Shri Kritibas Maity for their selfless guidance and concern.*
- *Dr. Sailee Chowdhury for her concern and support in correcting the thesis.*
- *Smt. Bharati Gupta and Anwita Gupta for their effort in correcting the thesis.*
- *All my family members for their unconditional, selfless concern and deepest sincerity.*
- *Mahuwa for her endless effort to arrange my haphazard life with all her ability, and*
- *the little one named Senjuti (Jhinuk), whose giggles gave me the strength to continue through the thick and thin of this journey.*

Contents

List of Figures	vii
------------------------	------------

List of Tables	xix
-----------------------	------------

1 Introduction	1
-----------------------	----------

1.1 A brief review on the Spallation Neutron Sources	2
--	---

1.2 Introduction to the Indian Spallation Neutron Source	4
--	---

1.2.1 Layout of the accelerator for Indian Spallation Neutron Source . .	5
--	---

1.3 Specification of the ISNS accelerator	7
---	---

1.4 An optimized SRF linac design for the proposed ISNS	8
---	---

1.5 A brief discussion on the negative hydrogen ion	11
---	----

1.6 A note on the spallation process	13
--	----

1.7 Beam loss in an H^- linac	13
---	----

2 Electromagnetic design of medium and high β elliptic Superconducting Radio- Frequency (SRF) cavity	19
--	-----------

2.1 Energy gain and other considerations in SRF cavities	20
--	----

2.1.1	Energy gain in an RF cavity	20
2.1.2	Figures of merit to characterize an RF cavity	22
2.1.3	Design constraints and the other generalities	24
2.2	Parametrization of a TESLA type geometry and its geometry optimization	25
2.2.1	TESLA shape in terms of seven independent parameters	25
2.2.2	Approach followed for the geometry optimization of TESLA type elliptic cavity	28
2.3	Geometry optimization of an elliptic cavity midcell	30
2.4	Some aspects of multicell elliptic SRF cavities	38
2.5	Optimization of the end cell-geometry	41
2.6	Optimization of the iris radius	44
2.7	RF parameters obtained for the optimized multicell cavity geometry. . . .	46
2.8	Geometry optimization for a low loss SRF cavity	47
2.9	Summary and conclusion	51
3	Study on Higher Order Modes (HOMs) and wake-fields in elliptic SRF cavi- ties	57
3.1	Studies on HOMs in a multicell elliptic SRF cavity	58
3.1.1	Classification of HOMs and other general considerations	58
3.1.2	Energy exchange between beam particles and HOMs	59
3.2	HOMs in the medium and high β elliptic cavities	67
3.2.1	Higher order monopole modess in the multicell elliptic cavities . .	68

3.3	Dipole HOMs in the multicell elliptic SRF cavities	71
3.4	Wakefield analysis of multicell elliptic SRF cavities	76
3.4.1	Calculation of the wake Loss factor in these SRF cavities	77
3.4.2	Parasitic heat loss and the calculation of the wake potential	80
3.4.3	Heat load due to resonant excitation of HOMs	82
3.5	Summary and conclusion	88
4	Study on the Lorentz Force Detuning (LFD) in elliptic SRF cavities	91
4.1	General discussion on the Lorentz force detuning	92
4.2	Static and dynamic LFD in an elliptic SRF cavity - a theoretical framework	95
4.2.1	Static Lorentz force detuning in an elliptic SRF cavity.	95
4.2.2	Periodic Lorentz pressure and the Dynamic LFD in an elliptic SRF cavity.	96
4.3	Discussion on the Finite element model	100
4.4	LFD analysis of elliptical cavities designed for ISNS	104
4.4.1	LFD analysis on $\beta_g = 0.9$ 650 MHz 5-cell elliptical SRF cavity . .	104
4.4.2	LFD analysis of a 650 MHz, $\beta_g = \mathbf{0.61}$, 5-cell elliptic SRF cavity	116
4.5	Discussion and conclusion	120
5	Influence of material properties on the performance of Nb based SRF cavities	123
5.1	Introduction	124
5.2	Material properties and the performance of the superconducting cavities .	126

5.2.1	A review on the contemporary works	137
5.3	Numerical calculations and analysis of results	139
5.4	Conclusions	147
6	Lattice design and beam dynamics of the 1 GeV H^- linac for ISNS	151
6.1	Layout of the front end linac and some general considerations	152
6.2	Basic beam dynamics considerations and the lattice layout of the 1 GeV 1 MW H^- linac	155
6.2.1	Single particle dynamics and envelope equations in presence of space charge	156
6.2.2	A brief review on the design recipe of a high power hadron linac .	160
6.2.3	Lattice design and layout of the ISNS linac	162
6.3	Beam dynamics calculations for ISNS linac	172
6.3.1	Beam optics calculations for the zero current	173
6.3.2	Multi-particle beam dynamics simulations	180
6.3.3	Studies on the envelope instabilities	185
6.3.4	Analysis on the beam halo, using particle core model	195
6.3.5	Studies on the beam loss estimation of the optimized linac	199
6.4	Discussion and conclusion	200
7	Conclusions and future work	207

List of Figures

1.1	Schematic of the accelerator for the proposed Indian Spallation Neutron Source.	6
1.2	Beam time structure for the proposed ISNS linac - (i) macro-pulse, (ii) midi-pulse and (iii) micro-pulse.	7
1.3	Four kicker injection scheme.	12
1.4	Different stages of nuclear spallation.	14
1.5	Maximum allowable fractional beam loss limit as a function of the beam energy (broken red line) estimated considering a power loss of 0.1 W/m. Here we also show the fractional loss due to intrabeam stripping (solid black line) obtained for the ISNS linac. Fractional loss because of Lorentz stripping , is estimated $< 10^{-12}$ for the ISNS linac. It is therefore not shown here.	15
1.6	Maximum allowable focusing magnetic field strength, which is averaged over a lattice period, as a function the beam energy. Calculation corresponds to the maximum allowable fractional loss shown in Fig. 1.5. .	17
2.1	Two dimensional schematic of the half-cell geometry of a TESLA type elliptic cavity.	28

2.2	For the $\beta_g = 0.61$ cavity, variation of B_{pk}/E_{acc} , as well as E_{pk}/E_{acc} as a function of B , where, $a/b = A/B = 1$ and $\alpha = 88^\circ$	32
2.3	For the $\beta_g = 0.61$ cavity, variation of (a) E_{pk}/E_{acc} and (b) B_{pk}/E_{acc} as a function of A . In these simulations, the parameter B is kept fixed at 55.550 m for the $\beta_g = 0.61$ cavity. Here, $\alpha = 88^\circ$,	35
2.4	Plotting of B_{pk}/E_{acc} (a) as a function of A and (b) as a function of a/b for the $\beta_g = 0.61$ cavity. For each of these points, $E_{pk}/E_{acc} = 2.36$. Data for plotting these curves are taken from Fig. 2.3.	36
2.5	Variation of E_{pk}/E_{acc} as a function of a/b for different values of A for the $\beta_g = 0.61$ cavity. Note that $B=55.550$ mm in this figure.	37
2.6	Plotting of E_s/E_{acc} as a function of z , where, the solid line corresponds to $a/b = 0.53$, for which E_{pk}/E_{acc} shows the minima in a $\beta_g = 0.61$ cavity geometry. Here, the other two curves are for $a/b = 0.55$ and 0.51 respectively, which peak at higher value of E_s/E_{acc} , and $z = 0$ corresponds to the equator plane.	38
2.7	Variation of transit time factor T with the normalized parameter (β/β_g) for the 5 cell, $\beta_g = 0.61$ cavity. The two vertical lines correspond to $\beta/\beta_g = 0.85$ and 1.27 , which is explained in the text on the context of $\beta_g = 0.61$ multicell cavities.	39
2.8	Geometry of the end-cell for the $\beta_g = 0.61$ cavity.	43
2.9	Field flatness and resonant frequency as a function of the $\beta_g = 0.61$ cavity end-half cell length L_e	44
2.10	Variation of k_c (in %) and (and R/Q) with the R_{iris} , where the dotted line shows the value of $\kappa_c \sim 0.775\%$	45

2.11	Variation of the magnitude of the axial electric field along the beam axis for the optimized $\beta_g = 0.61$ cavity.	50
2.12	Field contours for one half of the $\beta_g = 0.61$ cavity.	51
2.13	Dispersion curve for the $TM_{010}-\pi$ mode of the $\beta_g = 0.61$ cavity.	52
2.14	R/Q values of the monopole modes are plotted as a function of β for the 5 normal mode frequencies of the first pass band.	53
2.15	Optimum values of B_{pk}/E_{acc} as a function of α . Here the value of E_{pk}/E_{acc} is kept fixed at 2.0 for each data point.	54
2.16	Optimized value of B_{pk}/E_{acc} as a function of wall angle α using (i) our step-by-step one dimensional optimization procedure, as well as (b) the conventional multi-variable optimization technique, for the TESLA design. Also here, we have shown the data point which correspond the design used for the TESLA project.	54
3.1	Plot of R/Q of the monopole modes as a function of β , for the five modes of the third pass-band.	70
3.2	Plot of the axial electric field amplitude along the length of the cavity, for the HOM at 1653.2 MHz in this unmodified geometry.	70
3.3	Amplitude of the axial electric field of the mode at 1653.2 MHz along the cavity length, for the geometry with modified end cell at one side.	72
3.4	Plot of (a) field contour for the fundamental mode at 650.0 MHz, and (b) field contour for the HOM at 1653.2 MHz, for the modified end-cell.	72
3.5	R_{\perp}/Q values of five dipole modes of first passband plotted as a function of β	73

3.6	Dispersion diagram for the first four dipole passbands is shown here. Mode frequencies are plotted with respect to the corresponding values of phase advance per cell.	74
3.7	Here $g(\psi)$ values plotted as function of β for the dipole mode resonating at 965.85 MHz.	75
3.8	Threshold current values are plotted as a function of β for the dipole mode resonating at 965.85 MHz.	76
3.9	Integrated loss factor $\mathcal{K} = \sum k_n$ is plotted as a function of β . The blue line here is generated by summing over the individual loss factors of ~ 200 modes.	79
3.10	Integrated loss factor $\mathcal{K} = \sum k_n$ as a function of the frequency f , calculated (a) following semi-numerical method for $\beta \rightarrow 1$, and (b) calculated using ABCI, for a beam bunch with Gaussian distribution of rms bunch length $\sigma \sim 5$ mm.	80
3.11	Longitudinal wake potential generated by a Gaussian bunch having 1 pC charge passing through the optimized 5-cell cavity.	81
3.12	Fourier components of ISNS beam pulse and the coefficients at different frequencies.	83
3.13	Normalized HOM power in the steady state, plotted for different values of Q_{ext} at an HOM frequency of $f = 1.625$ GHz, which is the 5^{th} harmonic of the micro-pulse repetition rate, and 1625^{th} harmonic of the midi-pulse repetition rate.	85

3.14	Time averaged HOM power (P_{avg}) plotted as a function of Q_{ext} . (a) Here the HOM frequency is 1.625 GHz, hence micro and midi-pulses both are in resonance, (b) Here HOM frequency is 1.626 GHz, therefore only midi-pulses are in resonance.	86
3.15	The normalized time averaged HOM power plotted as a function of HOM frequency. Here we took $Q_{ext} = 10^7$	87
3.16	Normalized time-averaged HOM power from the beam time structure near $f = 1.625$ GHz which is the fifth harmonic of the micro-pulse repetition rate. Here $Q_{ext} = 10^7$	87
4.1	(a) Typical Lorentz pressure distribution on the inner wall of an SRF cavity half-cell, and (b) the corresponding deformation (Not to scale).	93
4.2	(a) Schematic of a multicell SRF cavity along with helium vessel and stiffener rings. (b) Inset is the 15° sector model of the cavity assembly. . .	94
4.3	Temporal profile of the amplitude of the normalized cavity voltage (in blue), and the amplitude of the normalized Lorentz pressure pulse (in black).	97
4.4	Fourier series representation of the normalized Lorentz Pressure Pulse Shape. Here $\mathcal{F}(\omega) _{\text{Norm}}$ denotes normalized amplitudes corresponding to the participating frequencies.	100
4.5	Figure shows the 5° sector model of the cavity-helium vessel assembly. .	102
4.6	Starting geometry of the cavity and the ‘tori-flat’ helium vessel assembly. Torus radius of the helium vessel is 35 mm in this configuration.	105

4.7	LFD as a function of the stiffness of the helium vessel. Here calculations were performed without including stiffener rings in the design. Also, the values of $-K_{LFD}$ is shown here.	106
4.8	LFD is plotted as a function of the radial location of the stiffener rings. Helium vessel stiffness was kept fixed at 4.9 kN/mm in this calculation. Values of $-K_{LFD}$ is shown here.	107
4.9	LFD as a function of the radial locations of the stiffener rings. Here, the stiffness of the helium vessel is 4.9 kN/mm. In the vessel, an axial elongation of $9.5 \mu\text{m}$ was considered in this simulation. Corresponding values of K_{LFD} is also shown here.	109
4.10	Reduction in the field flatness with increasing radial position of the stiffener rings.	110
4.11	Dynamic LFD with mean radial position of the stiffener rings at 119.5 mm.	113
4.12	Normalized dynamic LFD and change in the cavity length with a mean radial position of the stiffener ring at 119.5 mm during a single pulse. . .	114
4.13	Longitudinal displacement of the cavity w.r.t. its central plane as a function of time, with mean radial position of stiffener at 119.5 mm.	114
4.14	Resonant conditions corresponding to a mean radial position of stiffener at 113.5 mm, where the displacement is calculated w.r.t. central plane of the cavity.	115
4.15	Resonant conditions corresponding to a mean radial position of stiffener at 101.5 mm, where the displacement is calculated w.r.t. central plane of the cavity.	115

4.16	Resonant conditions corresponding to a mean radial position of stiffener at 80.5 mm, where the displacement is calculated w.r.t. central plane of the cavity.	115
4.17	Static LFD as a function of the radial position of the stiffener rings. The compensation due to cavity elongation provided by an axial elongation of $8.3 \mu\text{m}$ of the cavity-helium vessel assembly is taken into account.	118
4.18	Helium vessel displacement required to compensate for LFD, as a function of the radial position of the stiffener rings.	119
4.19	. (a) Structural mode frequencies ($f_{\text{structural}}$) as a function of the stiffness and density of the tuner material (normalized with respect to the density of titanium) for five structural modes, and (b) enlarged view of the plot of the lowest order structural mode frequency. Here, the length of the annular tuner material is taken as 20 mm.	121
5.1	R_{BCS} (calculated using the nonlocal response of electric field) at 2 K plotted as a function of l_e for niobium, where, $\lambda_0 = 39 \text{ nm}$, $\xi_0 = 32 \text{ nm}$ and $\Delta = 1.9k_B T_c$	130
5.2	Enhancement factor $\mathcal{F} = R_s/R_{BCS}$ plotted as a function of β_0	132
5.3	Plot of $R(y)$ as a function of T/T_c	134

5.4	Total thermal conductivity κ of RRR 300 graded niobium plotted as a function of temperature T . Here the blue curve represents the case without the phononic contribution. The enhancement in κ due to phonons at low temperature is observed in a pre-strained, small grain niobium sample [126], which is shown in the continuous black curve. Here the dotted black curve represents the case with reduced phonon peak in $\kappa(T)$, in commensurate with the experimental observation in Ref. [127] for an SRF cavity.	136
5.5	Model of a 2.8 mm thick infinite Nb plate geometry. Applied magnetic field B_a on the surface is denoted by the ‘dot’s. Inner surface of the plate is in vacuum, whereas the outer surface of the plate is immersed in a liquid helium bath at 2K.	142
5.6	For 1.3 GHz TESLA cavity made of RRR 300, Q_0 is plotted as a function of B_a , considering three possible variations of $\kappa(T)$ described in Fig. 5.4.	142
5.7	For 1.3 GHz TESLA cavity, B_{th} values are plotted as a function of σ_{no} . Here, the blue curve represents the case where phononic contribution is not considered. The continuous and the dotted black curves here represent the cases of full and scaled down phononic contribution, respectively.	145
5.8	Plot of Q_0 as a function of B_a , as obtained from the analysis performed on an ISNS cavity [36] for a fixed value of RRR 100 grade Nb, for three possible variations of $\kappa(T)$. For these calculations, we considered 4 mm thick plate geometry. We have taken $R_i = 10 \text{ n}\Omega$ in this analysis.	147
5.9	Surface temperature variation along the length of the cavity, obtained from a three-dimensional analysis. Picture shown in the inset is the ANSYS TM generated surface profile of the temperature.	149

6.1	Schematic and RMS beam envelope calculated in the 1.9 m long LEBT line (not to scale). Two solenoids with strength ~ 0.196 T and ~ 0.235 T, respectively, will be used to shape the beam there.	153
6.2	Schematic of the ~ 4 m long MEBT line (not to scale), along with the RMS beam envelopes. The blue and red curve represent the horizontal and vertical beam envelope, respectively. Inset shows the longitudinal beam envelope.	154
6.3	Required field gradient of the eleven quadrupole magnets, shown along the length of the MEBT line.	154
6.4	Schematic configuration of the lattice structures used in different energy sections of the injector linac: (a) $\beta_g = 0.11$ SR0 section, (b) $\beta_g = 0.22$ SR1 section, (c) $\beta_g = 0.42$ SR2 section, (d) $\beta_g = 0.61$ EC1 section and (e) $\beta_g = 0.81$ EC2 section.	167
6.5	Total number of 5-cell, 650 MHz elliptic cavities required to accelerate the beam from 168 MeV to 1 GeV as a function of β_g plotted for both medium and high beta cavity sections.	168
6.6	Dedicated matching sections used in between (a) SR0 and SR1(1) sections, (b) SR2(1) and SR2(2) sections, and (c) the SR2(2) section and medium energy EC1 section.	169
6.7	Transit time factors (TTF) normalized against their maximum values are plotted as a function of β for the five different lattice sections used in the injector linac. The straight lines show the transition β from one section to the other.	172

6.8	Figure on top shows the calculated acceleration gradient (E_{acc}) in the RF cavities and the required strength of solenoid / quadrupole magnets along the length of the linac. In the bottom, calculated variation in the synchronous phase ϕ_s of all RF cavities is shown.	177
6.9	Longitudinal (black dashed line) and transverse phase advance (horizontal: solid red line and vertical: dotted blue line) per unit length is plotted along the length of the linac without space charge (top) and with space charge (bottom) for the designed value of a beam current of around 14.5 mA.	178
6.10	Beam distribution at the exit of Radio-Frequency Quadrupole (RFQ). . . .	181
6.11	Horizontal (top, black), Vertical (top, blue) and longitudinal (middle, blue) rms beam size in the linac along the length. In the other figure (bottom) color map shows radial distribution of the normalized particle density throughout the linac, along with the available aperture (black). . .	184
6.12	RF bucket boundaries at $+2 \phi_s $ and $- \phi_s $ (black) are shown along with phase distribution in the linac.	185
6.13	Longitudinal (right) as well as transverse (left) rms beam envelope across the transitions from (a) SR0 to SR1(1) section, (b) SR1(1) to SR1(2) section, (c) SR1(2) to SR2(1) section, (d) SR2(1) to SR2(2) section and (e) SR2(2) to EC1 section respectively.	186
6.14	Evolution of the normalized rms beam emittance in the longitudinal (black broken line) direction, vertical (red solid line) direction and horizontal (blue dotted line) direction along the length of linac.	187
6.15	Evolution of the normalized transverse 4 D and the 6 D rms emittance values are plotted along the linac length.	187

6.16	Longitudinal (broken black line), horizontal (dotted blue line) and vertical (solid red line) tune depression along the length of the linac.	188
6.17	Lattice footprint are plotted on the Hofmann chart for ISNS injector linac with $\epsilon_z/\epsilon_x = 1.12$. Here $k_z/k_{xy}=1$ denotes fourth order even resonance, whereas, $k_z/k_{xy}=2$ denotes the third order even resonance. All lattice footprints (shown in coloured dots) are nearly confined in the resonance free zone of the Hofmann diagram, between these two resonances.	188
6.18	Longitudinal (top) and transverse (bottom) full unnormalized acceptance of the linac. Here background colour shows the input beam distribution, on which the acceptances are shown in black.	189
6.19	RF power requirement for the different cavities along the length of the linac.	190
6.20	Along with the unit circle which is shown in black, eigenvalues of the envelope oscillations of a three-dimensional beam bunch in a periodic lattice are shown on the complex plane.	193
6.21	Phase advance per period ϕ_n (top), and modulus of eigenvalue of normal modes of mismatched envelope oscillation, plotted as a function of tune depression for $\sigma_{\zeta_0} = 89^\circ$. Note that in this case, eigen values could not be calculated accurately beyond a value of $\sigma = 87.5^\circ$, because of some numerical accuracy.	194
6.22	Oscillations in the beam envelope along x , y and z direction, as obtained from the simulation for 10% mismatch in the beginning, is shown for $\sigma_{\zeta_0} = 89^\circ$	195
6.23	Phase advance per period ϕ_n (top) and modulus of eigenvalues of normal modes of mismatched envelope oscillation is plotted as a function of the tune depression for $\sigma_{\zeta_0} = 105^\circ$. In the figure we have marked five distinct regions as described in the text.	196

6.24	Maximum extent of the halo particles (x_{max}) in the transvers plane as a function of the beam mismatch (μ) for the proposed injector linac. Here, different curves corresponds to different tune values (η).	198
6.25	Calculated power loss per unit length (solid black line) as well as integrated power loss (broken red line) due to the occurrence of intrabeam stripping along the length of the linac.	201
6.26	Phase advance per period ϕ_n of mismatched envelope oscillation as a function of the tune depression considering $\sigma_{z0} = 95^0$	205
6.27	Phase advance per period ϕ_n of mismatched envelope oscillation as a function of the tune depression considering $\sigma_{x0} = 95^0$, $\sigma_{y0} = 105^0$ and $\sigma_{z0} = 100^0$	205
1	Variation of σ_{H^-} is plotted as a function of the relative velocity β_r	238
2	Evolutions of the transverse and longitudinal rms angular momentum spread obtained from TRACEWIN simulation, along the length of the ISNS injector linac.	242

List of Tables

1.1	Important parameters of the ISNS linac and accumulator ring assembly	8
2.1	Geometrical parameters for the optimized mid-cell geometry of the $\beta_g = 0.61$ cavity.	37
2.2	RF parameters for the optimized mid half cell in the $\text{TM}_{010-\pi}$ mode for the optimized $\beta_g = 0.61$ cavity. These values are calculated considering $R_s = 10 \text{ n } \Omega$	37
2.3	Calculation for the cell-to-cell coupling coefficient κ_c for the $\beta_g = 0.61$ cavity.	41
2.4	RF parameters for a 5-cell $\beta_g = 0.61$ cavity in the $\text{TM}_{010-\pi}$ mode.	48
2.5	Optimized geometry of a $\beta_g = 0.81$, 650-MHz cavity mid cell.	48
2.6	RF parameters for a 5-cell $\beta_g = 0.81$ cavity in the $\text{TM}_{010-\pi}$ mode.	48
2.7	Optimized geometry of a $\beta_g = 0.9$, 650-MHz cavity mid-cell.	49
2.8	RF parameters for a 5-cell $\beta_g = 0.9$ cavity in the $\text{TM}_{010-\pi}$ mode.	49
3.1	Optimized geometric parameters for the modified end half-cell.	71

3.2	Few prominent dipole modes supported in the $\beta_g = 0.61$ cavity geometry. Here, β_m indicate β value at which corresponding m^{th} dipole shows the maximum R_{\perp}/Q value.	75
3.3	Beam time structure for the ISNS injector linac	83
4.1	The detailed geometry of the helium vessel.	108
4.2	Static and dynamic LFD for different radial positioning of the stiffener rings.	116
4.3	Figures of merit of a design with mean radial position of stiffener at 119.5 mm	117
4.4	Participating structural modes of the 5-cell $\beta_g = 0.61$ cavity	118
5.1	Q -values at B_{th} for 1.3 GHz TESLA cavity.	145
5.2	Q -values at B_{th} for 650 MHz ISNS cavity.	146
6.1	Design details of the RF cavities used in the proposed linac lattice.	170
6.2	Magnets used in the linac lattice and their design details.	170
6.3	Detailed lattice parameters of the injector linac.	170
6.4	Design and the detailed parameters of the matching sections.	171
6.5	Emittance values and Twiss parameters of the beam distribution at the exit of RFQ	181

Chapter 1

Introduction

It is the year 1932. British physicist Sir James Chadwick [1] from Cavendish Laboratory discovered an electrically neutral sub-nuclear particle named neutron [2]. At the time of discovery, no one could presume that within two decades, the immense power of this apparently innocent electrically neutral particle would shake the entire world with deadly shock in the form of a devastating nuclear weapon, the ‘*Atomic-Bomb*’ [3], [4]. Apart from this dark episode, the enormous potential of this particle has endowed the scientists with the power to probe and unravel the internal structure of almost all materials, especially those consisting of light elements like hydrogen or boron *etc.* for their good scattering cross section, which makes them complementary to x-rays [5], [6].

In the post-war period (World War - II: 1939 to 1945 [7], [8]), important milestones were achieved by the pioneering research of Ernest Wollan, Clifford Shull and Bertrame N. Brockhouse on the development of neutron diffraction technique and neutron spectroscopy [9], [10], [11]. With these remarkable contributions, neutron science has overwhelmingly established itself as a useful tool to investigate the structure and properties of materials, crossing the closed wall of the Manhattan Project [12]. Today’s neutron science is extremely matured and advanced with the pace of technology. From the conventional crystallography in solid-state physics to the complex tomography of

protein samples in modern-day biology - across the horizon, precise scientific investigations using neutron scattering and diffraction techniques have fetched completely new knowledge previously unknown to mankind [13].

1.1 A brief review on the Spallation Neutron Sources

So far, two principal manmade sources of neutrons are there - nuclear reactors [14], [15] and spallation neutron sources (SNSs) [16], [17]. Typically, nuclear reactors produce a continuous beam of neutrons, having a flux of $\sim 10^{14}$ neutrons $\text{cm}^{-2} \text{s}^{-1}$ [18]. Although there is successful demonstration of a reactor at Dubna (IBR) [19], Russia, which operates in the pulsed mode with higher peak flux, yet, this concept has not become popular, as it is not very effective. Excluding this reactor, spallation sources are the principal way to produce pulsed neutron beam with high peak flux of $\sim 10^{16}$ neutrons $\text{cm}^{-2} \text{s}^{-1}$ [20], which is extremely useful for the time of flight experiments. Another advantage with spallation based neutron sources is that unlike nuclear reactors, these sources have no issues regarding proliferation or inventory of long lived radioactive isotopes.

Interestingly, even before the discovery of fission (1939) [21], [22], Nobelist Glenn T. Seaborg, in 1937 gave the concept of nuclear spallation [23]. However, spallation based neutron sources could be demonstrated only in late 70s'. Perhaps this was because of the associated complexity involved in building a suitable proton or negative hydrogen ion (H^-) accelerator. Among these complexities in developing a state of the art SNS, one challenging task is to design a high power hadron accelerator.

Spallation based neutron sources also have an eventful history. Chronologically, the first successful spallation neutron source **ZING-P**, acronym for Zero Gradient Synchrotron (ZGS) Intense Neutron Generator - Prototype, was built at Argonne in 1974, using a 200 MeV accelerator. In this SNS, the 20 W average power proton beam was capable of producing 5×10^{11} neutrons per pulse [24],[25]. Not only that, after the

demonstration of this accelerator based spallation technology, tradition of success was continued in the same laboratory in another project named Intense Pulsed Neutron Source (**IPNS**) [26] in the early 1980s (1982) [27]. This was a rapid-cycling synchrotron (RCS) based spallation source for the production of slow neutrons. Another milestone was reached in Los Alamos after the commissioning of the proton storage ring in 1985, with the implementation of the SNS concept there [28]. Further developments of the accelerator based spallation technology took place with time in a series of projects in different laboratories like **ISIS** (UK) [29], **ANL** [26], **RAL** [29], **PSI** [30] *etc.* In the last two decades, remarkable advancements in this technology has been realized through the demonstration of **SNS** at **Oak Ridge** [31] and **J-PARC**, Japan [32]. These two machines are indeed milestones, being the world's first megawatt class machines, where the aim of high peak neutron flux of $\sim 10^{16}$ neutrons $\text{cm}^{-2} \text{s}^{-1}$ is finally materialized. More recently, **CSNS** in China has been commissioned [33]. New SNS project like European Spallation Source (**ESS**) at Lund, Sweden is in a very advanced stage [34].

So far, two different types of design schemes have been successfully demonstrated worldwide to build an SNS. Those are described below:

1. For SNS at Oak Ridge, a superconducting linac boosts up the energy of the H^- ion beam to around 1 GeV, and the millisecond long pulse of H^- beam is then compressed to intense microsecond long pulse of protons in an accumulator ring, and finally hits a neutron rich spallation target of high-Z material [35];
2. For J-PARC, Japan, a millisecond long pulsed proton beam gains relatively low energy (~ 400 MeV) in the linac section. Then, through a 3 GeV Rapid Cycling Synchrotron (RCS), this beam attains its desired energy and comes out as a compressed microsecond long pulse before hitting the spallation target.

Both of these schemes have their own challenges and advantages. In a rapid cycling synchrotron, proton beam is non-relativistic at the entrance, and after every cycle of

revolution, energy of the beam increases gradually. As a result, the revolution time period of the beam decreases continually with each cycle. Therefore, RCS necessarily needs an advanced high-gradient magnetic alloy-loaded (generally ferrite loaded) RF cavity, to maintain synchronism between the beam and the RF cycle. In such a cavity, the operating frequency can be tuned in a programmable manner in each turn, to ensure the right RF phase for the beam. The design and operation of such a cavity is technologically challenging. Not only that, controlling space charge force in a dense beam bunch, particularly in the low energy realm, is a real challenge in this scheme. However, such a machine comprising of injector linac with an energy of few hundred MeV and the RCS to boost the energy to \sim GeV, can also be built using normal conducting cavities and normal conducting magnets, which reduces the capital cost. The complexities associated with the cryogenic plant is not there in such normal conducting accelerator. On the other hand, cryogenic plant is an essential part of an SNS, where the full energy is gained from superconducting linac. Therefore, capital cost of the machines based on full energy superconducting injector linac and accumulator ring are considerably high. In this scheme, high energy beam bunch enters an accumulator ring and gets compressed there. Hence, space charge related issues are not that stringent in this scheme of SNS, and one can go for higher current in these machines.

1.2 Introduction to the Indian Spallation Neutron Source

There is a proposal to build an Indian Spallation Neutron Source (ISNS) to participate in the wonderful voyage of neutron based discoveries in various fields of applied sciences. After a thorough feasibility study, we have adopted the scheme similar to SNS at Oak Ridge for the Indian SNS project, in which a megawatt class injector linac will accelerate negative hydrogen ion beam up to the designed energy. Beyond a brief normal conducting front-end section, in this linac, the 3 MeV beam will be energized up to an energy of 1 GeV through a superconducting linear accelerator which will be followed by

an accumulator ring. This linac will comprise of five different families of Superconducting Radio-Frequency (SRF) cavities. Amongst these, two families of elliptical SRF cavity will be used in the medium energy (~ 150 to 450 MeV) and high energy section (around 450 MeV onwards) of this 1 GeV injector linac [36], [37]. In this context, studies on (i) the electromagnetic design optimization of these elliptic cavities and (ii) the beam optics and lattice design of this 1 GeV injector linac are the two objectives of the research presented in this thesis.

We would like to emphasize that ISNS project is also seen as an important step towards Accelerator Driven Sub-critical System (ADS) [38] for the utilization of thorium for energy production, as both ISNS and Indian ADS [39] [40] [41] will require an expertise in building high average power superconducting linac.

The next subsection will describe the normal conducting front-end of the injector section, followed by the 1 GeV superconducting linac and the accumulator ring.

1.2.1 Layout of the accelerator for Indian Spallation Neutron Source

Proposed layout of the accelerator for Indian Spallation Neutron Source is shown in Fig. 1.1 [41].

Normal conducting front-end

As shown in Fig. 1.1, normal conducting front-end of the injector linac consists of an ion source, Low Energy Beam Transport (LEBT) line [42], Radio Frequency Quadrupole (RFQ) [43] and Medium Energy Beam Transport (MEBT) line [44]. A multi-cusp ion source will produce a 2 millisecond long H^- ion [45] beam pulse with an energy of 50 keV, repeating with a pulse repetition rate (PRR) of 50 Hz [46]. The 15 mA pulsed current of H^- ions will be then transported to the normal conducting 325 MHz RFQ through a matching section, called the LEBT line. In order to facilitate the beam injection to the accumulator ring, as well as extraction from there, the beam will be chopped to a pulse

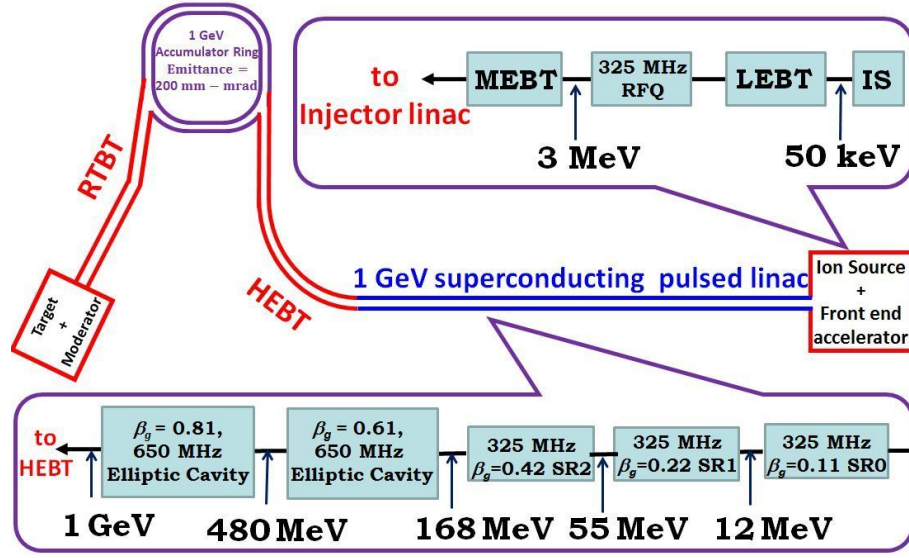


Figure 1.1: Schematic of the accelerator for the proposed Indian Spallation Neutron Source.

width of 650 nanosecond @1MHz in the LEBT line. The beam pulse with a reduced peak current of 10 mA will then be transported to the RFQ, where the millisecond long beam pulse will be adiabatically bunched at 325 MHz, acquiring a longitudinal emittance. Here, it is important to emphasize that due to pre-chopping in LEBT line and bunching in RFQ, the 2 millisecond macro beam pulse will acquire a complex time structure, which is described in Fig. 1.2 [37]. Finally, after gaining an energy of around 3 MeV, the beam will enter another matching section, called the Medium Energy Beam Transport (MEBT) line. This section will match the beam to the required input parameters of the superconducting injector linac and also perform final chopping of the beam.

Superconducting linear accelerator

Through the MEBT line, the 3 MeV H^- beam of 2 ms pulse width and pulse current of 10 mA will be transported to the superconducting injector linac, which will accelerate the beam up to energy 1 GeV. After traversing through three families of spoke resonator (SR) in the low energy section, and two families of elliptical cavity in the medium and high energy section of the injector linac, finally the 1 GeV beam will be transported to the injection point of the accumulator ring through a High Energy Beam Transport

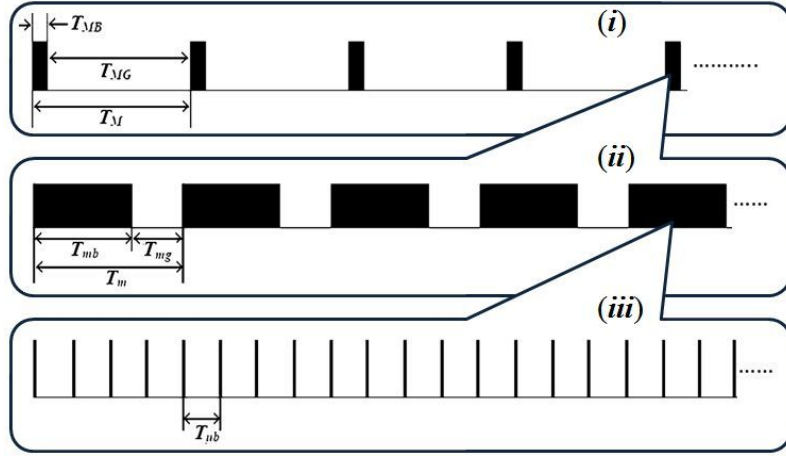


Figure 1.2: Beam time structure for the proposed ISNS linac - (i) macro-pulse, (ii) midi-pulse and (iii) micro-pulse.

(HEBT) [47] line with a suitable bend.

Accumulator ring

The beam follows 2000 turn charge exchange injection scheme, while being injected into an accumulator ring of ~ 262 m circumference. After completing this 2000 turn injection, beam pulse will be then further compressed in another few hundred turns (around 200 to 300 turns) by the programmable RF cavity voltage in the accumulator ring [42], [48]. Such a compression of the μs beam is necessary to create a clean gap between the head and tail of the circulating beam, in order to accommodate for the finite rise time of the extraction kicker magnet. From the accumulator ring, extracted beam will be transported finally towards a suitable spallation target made of neutron-rich high Z material, through Ring to Target Beam Transport (RTBT) line [49].

1.3 Specification of the ISNS accelerator

Lattice design of ISNS accumulator ring specifies better than ~ 0.8 mm-mrad of normalized rms beam emittance requirement in all three planes. However, our target is to confine the normalized rms beam emittance to around 0.45 mm-mrad in all these three

planes. As because the targeted emittance will ensure an emittance growth budget of 75% in the design. Also, this choice of a normalized rms emittance to around 0.45 mm-mrad will favour the design of the charge exchange stripper foil placed in the beam line in terms of foil heating. In our design, obtained value of the normalized rms beam emittance at the exit of RFQ are 0.397 mm-mrad in x , 0.4 mm-mrad in y and 0.447 mm-mrad in the z directions [41]. Table 5.1 summarizes a few important parameters of the ISNS accelerator.

Table 1.1: Important parameters of the ISNS linac and accumulator ring assembly

Parameter	Base Value	Unit
Average power of proton beam on target	1.0	MW
Kinetic energy of proton beam on target	1.0	GeV
Average beam current on target	1.0	mA
Pulse repetition rate	50	Hz
Protons per pulse on target	1.25×10^{14}	protons
Charge per pulse on target	20	μC
Energy per pulse on target	20	kJ
Ion type (Front end, Linac, HEBT)	H^-	
Linac beam macropulse duty factor	10%	
Linac length (excluding the front end)	~ 196	m
Ion type (Ring, RTBT, Target)	proton	
Ring filling time	2.0	ms
Ring revolution frequency	1.0	MHz
Number of injected turns	2000	
Emittance growth (RMS) budget for the linac	$\sim 75\%$	

1.4 An optimized SRF linac design for the proposed ISNS

For the high power superconducting hadron linac, our design optimization goal is typically twofold:

- design should be compact to minimize the number of SRF cavities.
- uncontrolled beam loss should be restricted below 1 W/m throughout the linac.

As mentioned earlier, requirement of a cryo plant is inevitable in a superconducting accelerator, which increases both capital and runtime cost of the design. A compact design reduces the establishment cost of the linac in terms of the required number of SRF cavities. Besides, an SRF linac with less number of cavities and less number of cryomodules will also be expected to produce smaller static heat load. However, in the case of a compact design, the dynamic heat load may appear as a point of concern, if one sets large operating gradient in the RF cavities. Here, we want to mention that, in our design, compactness is achieved mainly through efficient lattice design, and simultaneously restricting the acceleration gradient to a nominal value used / reported by the contemporary projects. Therefore, in this linac, it is expected that the dynamic heat load will also be nominal, and the total heat load will be manageable with a typical cryo plant used or planned to be used in the contemporary SRF accelerator laboratories / projects. Our calculation shows that the total estimated heat load for this linac will be less than 500 W, which is nominal. However, if required, this issue will be revisited when we will complete the studies on the cryoplant requirement for our ISNS linac. In the remaining of this section, we elaborate further on the motivation behind various studies that have been targeted in this thesis, in order to achieve the two goals described in the beginning of this sub-section:

- To realize a compact design, cavity geometry is optimized to enhance their accelerating capabilities. However, the properties of the cavity material, such as surface resistance, thermal conductivity and critical fields can also limit the optimum electromagnetic performance of the cavity.

Therefore the first target was to perform the geometry optimization of the elliptic cavities for improved electromagnetic performance.

- The cavity geometry was optimized for its fundamental mode, *i.e.*, the mode that has the lowest resonant frequency. However, in the cavity, some parasitic modes can also be excited by the beam. These modes can act back on the beam and can

add more heat load to the cryogenics.

Therefore, the next target of this research was to study the effects of these high frequency parasitic modes.

- Apart from this, electromagnetic field developed in the cavity will also deform the cavity shape. Due to this deformation, resonant frequency of the cavity is detuned from the design frequency, and as a result, the RF cavity starts reflecting input power.

Therefore, the third target of the research was to perform the analysis on the field induced detuning, where the stiffness and tuning of the cavity assembly has been optimized to take care of these issues.

- Breakdown of the superconducting properties of an SRF cavity material restricts the electromagnetic performance of the cavity by limiting the peak magnetic field value developed on inner surface of the cavity. Such breakdown is highly influenced by the purity level of the superconducting cavity material.

Hence, the fourth target of the research work was to perform a rigorous magneto-thermal analysis to study the effect of material purity on the limiting values of the peak surface magnetic field.

- In a high power hadron linac, lost beam particle may induce long-lived radioactivity in the machine, which may restrict the required hands on maintenance activities. Therefore, the design should ensure that while operating the machine, beam loss should be stringently limited below the allowable limit in the linac. A low beam loss design requires a fine control on the dynamics of the beam.
- In order to meet these stringent beam dynamics criteria in the linac, rigorous analyses should be performed on the single beam particle dynamics, as well as on their collective motions, under the influence of the electromagnetic field of the RF cavity and Coulombic repulsions acting between them.

Hence, the fifth target of the research work was to perform rigorous beam dynamics studies to evolve a low loss accelerator design of the proposed injector linac.

It is interesting to point out that in the linac, we will have H^- ions, but in the accumulator ring, there will be protons. It may be in order to briefly discuss the H^- ions and its utility in the SNS scheme.

1.5 A brief discussion on the negative hydrogen ion

Negative hydrogen ion or H^- is a hydrogen anion, *i.e.*, hydrogen atom with an extra loosely bound electron in addition to its orbital electron. First theoretical proof of its existence was provided by Hans A. Bethe [45]. Later the remarkable work of Subrahmanyan Chandrasekhar on the description of stellar atmosphere based on H^- ion created an early interest on these ion species [50]. The ground state energy of a negative hydrogen ion is around -14.36 eV, whereas, the loosely bound electron of an H^- ion has a small binding energy of around 0.75 eV. As such this electron is prone to leave the anion under the effect of any electromagnetic field or even thermal radiation present in an accelerator environment. Stripping of this loosely bound electron converts H^- ion to a neutral hydrogen atom, and hence, this process could be seemingly a major source of beam loss in an H^- accelerator.

Beam loss is extremely detrimental in a high power hadron machine because of the probable hazards of the induced radioactivity. The use of H^- ion beam has however an advantage in the scheme of SNS, where the full energy beam from linac is injected to an accumulator ring through multi-turn injection scheme.

In this injection scheme, four kicker magnets are used to shape the design beam orbit. Kicker magnets are basically short pulsed dipole magnets with sharp rise and fall times. As it is shown in Fig. 1.3, in the four kicker multi-turn injection scheme, both the

injected and the stored beam pass through one of the kicker magnets (K2 here) simultaneously. There, inside the dipole magnet K2, the H^- and proton beams entering at different inclinations are aligned by ensuring that the injected and stored beam receives a kick in the opposite directions. This is possible, only when the injected and stored beam are with opposite polarity. This precisely explains the reason for the compulsion to accelerate H^- ion beam in the linac. Once aligned, both H^- and proton beam travel together. Proton beam passes undisturbed. However, both electrons from the negative hydrogen ion are detached by the stripper foil, converting it to a proton beam.

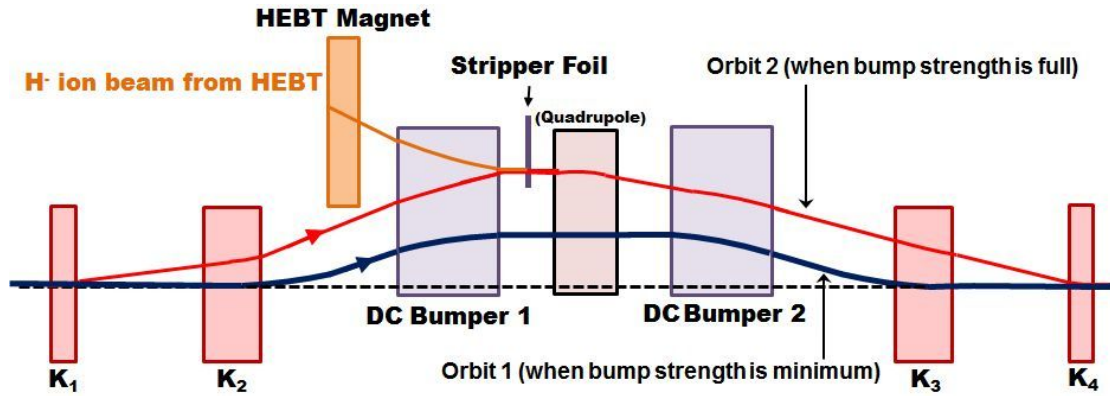


Figure 1.3: Four kicker injection scheme.

In this injection scheme, it is possible to control the phase space area of the beam in a precise manner. This is because the charge exchange process is not a Hamiltonian process. Therefore, Liouville's theorem is not applicable here, and with the help of this charge exchange process, we can perform multi-turn injection of beam slices in the proton synchrotron, while keeping the phase space area of the beam under control. This scheme was invented at the Institute of Nuclear Physics at Novosibirsk in Russia in 1960s [51].

As mentioned earlier, the dense microsecond long pulses of 1 GeV protons finally hit the spallation target. In this process, called the high energy spallation, participants are the 1 GeV protons and the nuclei of the high Z spallation material. In the following section briefly we will briefly discuss the spallation process.

1.6 A note on the spallation process

The millisecond long beam pulse from the linac gets compressed about thousand (in our case, 2000) times in the accumulator ring, and converted in to 1 GeV microsecond long proton pulse. After extraction, such extremely dense proton pulse hits a spallation target. The high velocity protons have very small de Broglie wavelength ($\lambda_{\text{de Broglie}}$). To give an example, for the 1 GeV proton beam, speed v of an individual particle turns out to be $\sim 0.875 c$, where c is the speed of light. This corresponds to $\lambda_{\text{de Broglie}} \sim 0.1$ fm. Due to its small value of $\lambda_{\text{de Broglie}}$, an impinging proton interacts only with nearby nucleons. In this way, the high speed proton starts transferring kinetic energy to few nucleons. These nucleons immediately get ejected from their corresponding nuclei: amongst them there are neutrons, which decide the yield of the spallation process. Typically, a 1 GeV proton particle can yield about 23 neutrons [52]. However, as it is shown in Fig. 1.4, spallation core goes through different stages like intra-nuclear cascade, pre-equilibrium stage, and evaporation or fission [53] with time. Along with neutrons, in a nuclear spallation process, the other products like Gamma-ray, π or μ -mesons are also produced.

Interestingly, yield produced by a proton in terms of the number of spallation neutrons per unit energy, saturates nearly at 1 GeV energy. Although the number of spallation neutron per proton increases proportionally with energy beyond 1 GeV, optimizing the cost and operation complexities of the linac, conventionally, the output energy of the SNS linac is kept around 1 GeV.

1.7 Beam loss in an H⁻ linac

In a megawatt class hadron machine like ISNS, long-lived radio-activation of the accelerator components [54] may be induced by the lost beam particles. To allow the ‘hands-on’ maintenance of accelerator after four hours of shut-down, residual

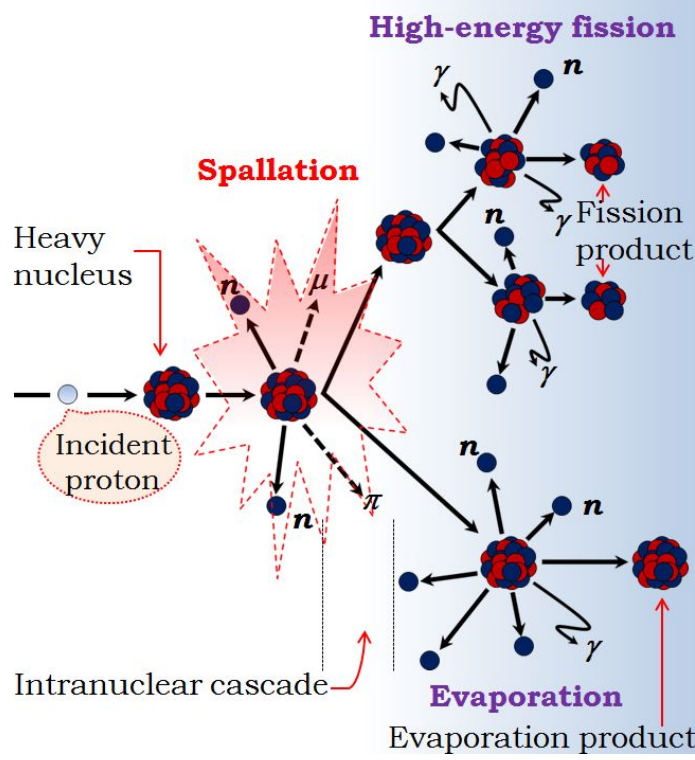


Figure 1.4: Different stages of nuclear spallation.

radioactivity must be kept below the worldwide acceptable limit of 100 mrem/hr [54]. This corresponds to a strict allowable limit of 1 W/m average beam loss throughout the machine for beam energies above 100 MeV [54], [55]. Not just that, for an accelerator with long straight section (*e.g.*, linac or the arm of the accumulator ring), even a more stringent limit of 0.1 W/m is targeted in some circumstances. Figure 1.5 shows fractional beam loss limit acceptable for our 1 GeV ISNS linac, which has been calculated following Ref. [56].

Among different dominant loss mechanisms, stripping of loosely bound electron from a negative hydrogen ion is the major part-taker in an H^- linac. From literature review, we have identified four dominant mechanisms, which are responsible for the stripping of H^- ions :

- One mechanism is ‘Lorentz stripping’, which is caused by the interaction of H^- ions with electric field in their rest frame [57].

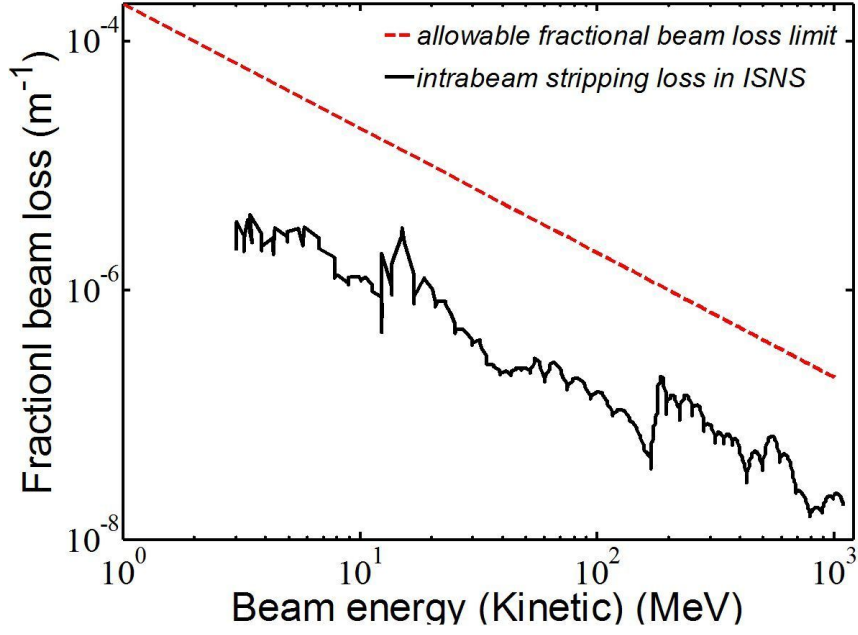


Figure 1.5: Maximum allowable fractional beam loss limit as a function of the beam energy (broken red line) estimated considering a power loss of 0.1 W/m. Here we also show the fractional loss due to intrabeam stripping (solid black line) obtained for the ISNS linac. Fractional loss because of Lorentz stripping, is estimated $< 10^{-12}$ for the ISNS linac. It is therefore not shown here.

- Another one is binary collisions of H^- ions in the beam bunch which is known as the ‘intra-beam stripping’ [56] [58]. (Also see the APPENDIX A)
- Interaction between H^- ion and background photons in the beam frame, may cause ‘black-body radiation stripping’ [56], and
- also, especially in the poor vacuum condition, interaction of the residual gas with H^- may produce beam loss known as the ‘Residual gas stripping’ [56].

Analysis of beam stripping suggests some constraints, which need to be satisfied during the beam optics design. For example, upper limit of the external focusing magnets strength is chosen to ensure that there is no beam loss due to Lorentz stripping, whereas beam loss due to intrabeam stripping restricts the lower limit of the beam size (or beam emittance) [58].

As mentioned earlier, in the case of ‘Lorentz stripping’, electron in H^- ions strip-off

because of electric field in the beam frame, which is a rest frame for the ion. The transverse magnetic field B_{LF} of the external focusing magnet in the ‘lab frame’ transforms to transverse electric field $E = \beta\gamma c B_{LF}$ in the ‘rest frame’ of the H^- ion beam, where β denotes the speed v of the ion in unit of the speed of light c , and $\gamma = 1/\sqrt{1-\beta^2}$ is the relativistic factor. In the presence of this field, life time τ_0 of the H^- ions is given by the following equation [57] [59]:

$$\tau_0 = \frac{A}{E} \exp \frac{B}{E}, \quad (1.1)$$

Here $A = 3.073 \times 10^{-6}$ V.s/m, and $B = 44.14 \times 10^8$ V/m. Using this equation, one can obtain the fractional loss rate of H^- ion beam as $1/(\beta c \tau_{LF})$. Here, $\tau_{LF} = \gamma \tau_0$ is the lifetime H^- ions in the lab frame. Accordingly, considering an allowable loss rate of 0.1 W/m, we have calculated the upper limit of the focusing magnetic field strength for our 1 MW injector linac, as a function of the beam energy which is shown in Fig. 1.6. Here, it is noteworthy that Eq. (1.1) is applicable when the magnetic field is transverse to the beam as in a quadrupole. Therefore, this formula is not directly applicable in the case of solenoid magnets where the transverse magnetic field is dominant only near the edges.

As it appears in Fig. 1.6, in the medium and high energy (>100 MeV to 1 GeV) range of the linac, tolerable values of the applied focusing field strength will vary from 0.5 T to 2 T. In this calculation we have estimated the field limit as averaged over the lattice length [57]. However, in a typical lattice, magnets occupy only 10 to 20 % of the lattice length. Therefore, for the quadrupoles in the medium and high energy section, suitably scaled up values of the limiting magnetic field will be 5 to 10 times the value shown in Fig. 1.6.

In a more precise calculation of Lorentz stripping, one should also incorporate electromagnetic field of the RF cavity along with field strengths of the external focusing magnets. However, compared to the effect of focusing magnetic field, influence of this

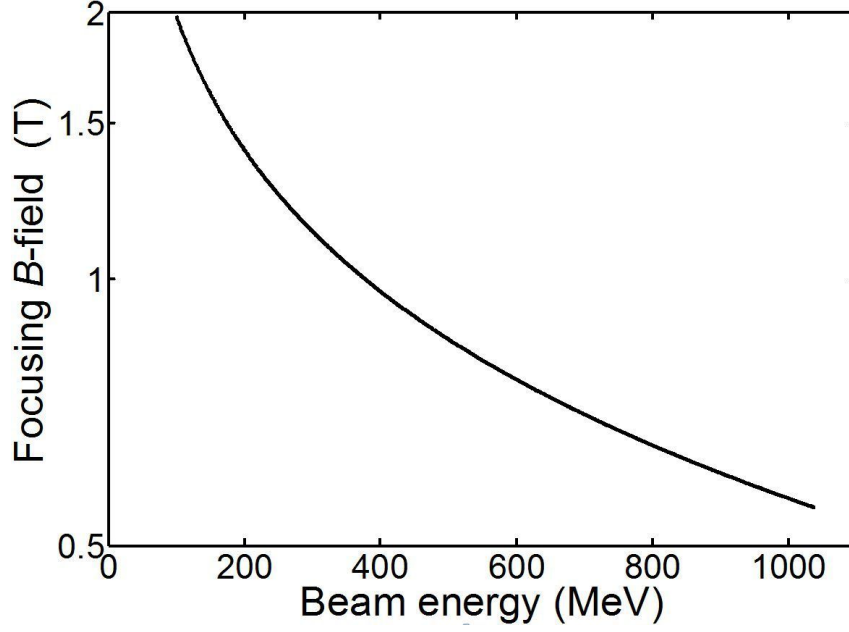


Figure 1.6: Maximum allowable focusing magnetic field strength, which is averaged over a lattice period, as a function the beam energy. Calculation corresponds to the maximum allowable fractional loss shown in Fig. 1.5.

RF field is insignificant [56]. It has been validated for the ISNS linac also¹. The loss rate due to residual gas stripping and blackbody radiation will be negligible for the ISNS which is in line with the observation reported Ref. [56]. Issues related to the beam loss will be revisited in the Chapter 6 after discussing the details of the lattice designed for the injector linac.

Apart from beam stripping, space charge effect and beam instabilities are the other two important issues in the design of a megawatt class accelerator, which can influence the loss of beam particles. However, one can minimize the beam loss due to unwanted resonances and non-linearities by an appropriate beam dynamics design [60].

¹For ISNS linac, calculated beam loss corresponds to the Lorentz stripping influenced by the RF field, is ($\sim 10^{-18}$ W/m).

Chapter 2

Electromagnetic design of medium and high β elliptic Superconducting Radio-Frequency (SRF) cavity

In the contemporary times, Superconducting Radio Frequency (SRF) cavities have become an essential choice for high-energy, high-power particle accelerators [31], [34], [61], owing to their several advantages over normal conducting cavities - such as less Ohmic dissipation on the inner surface of the cavity wall, and the possibility of operating at larger beam aperture radius, which allows higher beam current to be accelerated [62]. Here, we will discuss an optimization recipe that we have developed for the design and optimization of a multicell elliptic SRF cavity [61]. Following this methodology, we have designed three families of elliptic SRF cavities for medium and high energy section of the ISNS linac [41]. In this step-by-step one-dimensional (1D) optimization recipe, maximum achievable value of the acceleration gradient E_{acc} is ensured in the cavity by varying its geometric parameters.

In this chapter, first, we will discuss the procedure followed for the design optimization of the mid-cells in a multicell cavity, where the principal aim is to maximize E_{acc} . Then

the end-cell geometry will be optimized. There, the issue like maximization of field flatness η_F in the multi-cell geometry becomes important.

The geometry will be optimized under the constraint imposed on the peak value of the electric and magnetic field on the cavity surface. Peak value of the surface electric field E_{pk} should be restricted to 40 MV m^{-1} [63] for a 650 MHz niobium cavity, whereas the peak value of the surface magnetic field B_{pk} should be kept below 70 mT [64]¹. Before we start detailed discussion on the electromagnetic design optimization of the cavity, we will describe some general considerations like energy gain of a particle and some important figures of merit, which are commonly used to characterize an RF cavity, in the next section [65], [66].

2.1 Energy gain and other considerations in SRF cavities

2.1.1 Energy gain in an RF cavity

We can categorize the resonating electromagnetic modes into two classes [65] for a cylindrically symmetric cavity structure:

- Transverse electric (TE) like mode: typically these modes have no parallel electric field components along the axis of the cavity and
- Transverse magnetic (TM) like mode: field configuration of these modes typically demonstrates no parallel magnetic field components along the cavity axis.

However, at the iris location or near both the ends of the cavity, where the beam pipe is attached, both TE and TM like modes show finite non-zero parallel component of electric and magnetic field respectively.

Generally these cavities are operated in their fundamental mode to provide acceleration to the beam particles. In the fundamental mode configuration, electric field develops mostly along the axial direction of the cavity and magnetic field lines encircle the cavity

¹This is a conservative limit, and we will show in Chapter 5, it can go even up to 90 mT.

axis, maintaining an azimuthal symmetry. Electromagnetic mode in this particular field configuration is known as TM_{010} mode. The on-axis particles gain energy from the axial electric field component $\mathcal{E}_z(r = 0, z, t)$ of the mode. Energy gain of an on-axis beam particle from the electromagnetic field of a cavity can be calculated as follows [65]:

$$\begin{aligned}\Delta W &= q \int_{s_1}^{s_2} \mathcal{E}_z(0, z, t) dz = q \int_{s_1}^{s_2} E_z(0, z) \cos(\omega t + \phi_1) dz \\ &= q \int_{s_1}^{s_2} E_z(0, z) [\cos \omega t \cos \phi_1 - \sin \omega t \sin \phi_1] dz,\end{aligned}\tag{2.1}$$

where, s_1 is the initial position of the particle at a time $t = 0$ and s_2 is the final position, ϕ_1 denotes the phase of the oscillating electromagnetic field in the cavity at $t = 0$. In the above equation, $\omega = 2\pi f_c$ denotes angular frequency of an electromagnetic mode resonating with a frequency f_c . We can derive the following parameter called transit time factor T [65] from the above equation as:

$$T = \frac{\int_{s_1}^{s_2} E_z(0, z) \cos \omega t(z) dz}{\int_{s_1}^{s_2} E_z(0, z) dz} - \tan \phi_1 \frac{\int_{s_1}^{s_2} E_z(0, z) \sin \omega t(z) dz}{\int_{s_1}^{s_2} E_z(0, z) dz}.\tag{2.2}$$

In fact, the transit time factor T can be considered as a scale factor denoting the ratio between the reduced energy gain from the oscillating (RF) field and the constant energy gain from an equivalent DC field.

In Eq. 2.1, if we choose s_1 and s_2 as the starting and end position of a cavity, we can express it in a compact form as $\Delta W = qE_0TL \cos \phi_1$. This is the *Panofsky equation*, where $E_0 = \frac{1}{L} \int_{s_1}^{s_2} |E_z(0, z)| dz$ denotes average axial electric field and $L = (s_2 - s_1)$ is the length of the cavity. Equation 2.1 can be simplified imposing an additional condition that the corresponding particle arrives at the middle of the cavity at the time $t = 0$. In that special circumstance, that particular value of ϕ_1 in the equation, is denoted as ϕ_s , *i.e.*, the synchronous phase. In an RF cavity, ϕ_s indicates the phase of the electromagnetic mode,

when the synchronous particle arrives at the cavity centre.

According to the *Panofsky equation*, the maximum energy gain of a particle of unit charge depends on the average axial electric field of an RF cavity and the transit-time factor. Here, the product $E_0 T$ gives an estimation of the energy gain of a particle traversing unit length in an RF cavity. This product is denoted as the accelerating gradient E_{acc} . If we want to set a particular E_{acc} , it leads to a certain amount of Ohmic heat dissipation on the inner surface of the cavity. The amount of heat dissipated is proportional to the surface resistance R_s of the cavity material. Although unwanted, such dissipation is unavoidable while setting up an electromagnetic mode in the cavity.

Now, the average power dissipation P_c to set up an electromagnetic mode in the cavity can be calculated as $P_c = \frac{R_s}{2} \int_S H_{\parallel}^2 da$, where H_{\parallel} is the amplitude of the tangential magnetic field on a small elementary area da on the cavity wall and the integration is carried over the entire inner wall of the cavity. In fact heat dissipation is a limiter in the case of a high-gradient, high-duty factor operation of normal conducting cavity and in the case of an SRF cavity, it leads to a cryogenic load. From that point of view, the amount of P_c generates the primary specification for the cryo-plant, which is essential for the operation of a superconducting accelerator.

2.1.2 Figures of merit to characterize an RF cavity

Here, we discuss some important figures of merit, which we commonly use to characterize the electromagnetic performance of an RF cavity [65].

1. **Quality factor Q_0 :** This parameter decides the amount of Ohmic loss P_c of an unloaded cavity, and is expressed as

$$Q_0 = \frac{\omega U}{P_c}. \quad (2.3)$$

For a particular electromagnetic mode, energy stored in the cavity volume is

denoted by $U = \frac{\mu_0}{2} \int_V H^2(\mathbf{r}, t) dV$ where, H is the amplitude of magnetic field at the location \mathbf{r} in the cavity.

2. **(Effective) shunt impedance R :** It is a measure of the effective voltage $V_0 = E_0 L T$ developed on the axis of an RF cavity for a given value of Ohmic dissipation on the cavity wall and is defined as

$$R = \frac{V_0^2}{P_c}. \quad (2.4)$$

3. **R/Q factor:** The shunt impedance and the quality factor together give another important figure of merit for the cavity which is

$$\frac{R}{Q_0} = \frac{(E_0 L T)^2}{\omega U}. \quad (2.5)$$

It is a measure of the efficiency of acceleration per unit stored energy U of an electromagnetic mode resonating at an angular frequency ω . Interestingly, this ratio depends only on the cavity geometry. Material property of the cavity wall has no influence on R/Q_0 of a cavity.

4. **Geometry factor G :** Geometry factor of a cavity is defined as $G = R_s Q_0$. This figure of merit also depends solely on the cavity geometry. In order to produce a cavity voltage V_0 , the amount of heat dissipated on the cavity surface, is proportional to $G \times (R/Q_0)$.

In a multicell cavity, depending on the number of cells, several other normal modes with nearby frequencies are possible, that follow the same field pattern in each cell along with the mode resonating with desired operating frequency. Normal modes decide the overall field pattern along the length of a multicell cavity. For an electromagnetic resonant mode in the multicell geometry, the parameter called pass band depends on the frequency span of these normal modes. Interestingly, the shunt impedance R of a fundamental normal mode in the case of a multicell cavity is maximum for the π mode, where the adjacent cells of a multicell geometry show a phase shift of π in their

electromagnetic oscillation. Therefore, the cell length along beam axis is kept equal to $\beta\lambda/2$ to maintain proper synchronization between the beam and the RF electromagnetic field in the cavity operating in the π mode configuration. Here, $\beta = v/c$ is the speed v of the beam particle scaled by the speed of light c , and λ is the free space wavelength of RF.

Ideally, cell length of a multicell cavity should vary continuously to maintain perfect synchronism between RF field and the beam particle as the beam traverses through and gets accelerated². However, in practice, often a limited sets of these multicell cavities are planned to reduce the complexities associated with the fabrication of a large number of dissimilar set of cavities. In a linac section designed for a range of energy, several cavities with identical geometry are used. The cell-length of the cavities for each set and the required number of sets are optimized to minimize the total number of cavities in the linac. For a particular set of cavity, the optimized cell length is defined as $\beta_g\lambda/2$ in the TM_{010} - π mode of operation where β_g is called the geometric beta of the cavity. Such cavity will offer maximum synchronization, only when the beam particle attains a velocity $\beta = \beta_g$, and the particle in that case will gain nearly the maximum energy. In a more precise sense, energy gain of a particle in the cavity will be maximum at a beta value called β_{opt} which is slightly greater than this β_g . This deviation reduces with an increasing number of cells in the cavity N as [67]

$$\beta_{opt} = \beta_g + \beta_g \frac{6}{\pi^2 \times N^2}. \quad (2.6)$$

Accordingly, for a 5 cell cavity, $\beta_{opt} \approx 1.024 \times \beta_g$, and because of this small deviation, we have considered $\beta_{opt} \approx \beta_g$ in this thesis.

2.1.3 Design constraints and the other generalities

Based on several considerations like availability of the RF power source, past

²This indeed happens in RFQ as well as in Drift Tube Linac (DTL).

experiences and continuing collaborations with contemporary projects *etc.*, operating frequency of these medium and high β SRF elliptic cavities is chosen as 650 MHz for the ISNS injector linac. We have adopted the typical **TESLA** type cavity [61] shape as the base geometry for the further design optimization work. As mentioned in the last chapter, in this design optimization work, we must follow the two design constraints - the first one on the peak value of the surface electric field imposed by the field emission consideration, and the second one on the peak value of the surface magnetic field imposed by the consideration of the breakdown of superconductivity of the material.

In the next section, we will describe our methodology developed for the electromagnetic design optimization of a multicell elliptic SRF cavity.

2.2 Parametrization of a TESLA type geometry and its geometry optimization

2.2.1 TESLA shape in terms of seven independent parameters

For a cavity with multicell geometry, end cells have slightly different geometry compared to the inner cells. Inner cells are identical to each other and they are called mid-cells. As mentioned earlier, **TESLA** type cavity shape is adopted as the base geometry for this optimization work. Figure 2.1 shows the 2D schematic of a typical **TESLA** half-cell, which is evolved by joining two elliptic arcs with their common tangent. The three-dimensional cavity shape is a figure of revolution around the beam axis, obtained using the contour shown in Fig. 2.1. Following the conventional nomenclature associated with the **TESLA** shape, the geometry of a **TESLA** half-cell is described by the following seven independent parameters- iris radius R_{iris} , iris ellipse radii a and b , equator ellipse radii A and B , equator radius R_{eq} , and half-cell length L . There, the wall angle α can be derived from these seven parameters.

In the following six points, we summarize the correlation between the electromagnetic performance and the geometry of the cavity [61]:

1. As mentioned, these multicell elliptic SRF cavities will be operated in a $TM_{010}-\pi$ like standing-wave mode. There the cell length of the cavity should be equal to $\beta_g \lambda/2$ to satisfy synchronism between field of the electromagnetic mode and the traversing beam particles. Hence, for these cavities the half-cell length $L = \beta_g \lambda/2$ is a fixed quantity. Here, we want to mention the following important point. In a hypothetical case, where one can consider a cavity comprising an array of infinite number of identical cells, axial electric field developed in the $TM_{010}-\pi$ mode will be perfectly confined within the cell itself. Then only, the axial electric field E_0 can be obtained from the equation $E_0 = \int_{s_1}^{s_2} |E_z(0, z)| dz / L$, as mentioned earlier. However, cell numbers are finite in a real cavity, and there, the electromagnetic field of a mode penetrates up to some depth in to the beam pipe from the cavity. Hence, there, the accurate value of E_0 can be calculated only integrating over the total length of the field map, and that includes beam pipe lengths up to which the field is non-zero, along with the cavity length L .
2. Beam dynamics considerations and the requirement of a descent cell-to-cell coupling κ_c are the two major factors, which should be considered, while deciding the dimension of R_{iris} . In fact, higher value of R_{iris} lessens the effect of HOMs and wake-field, and gives a higher value of κ_c . On the other hand, such choice results a reduction in the shunt impedance of the fundamental accelerating mode, and as a consequence, maximum achievable accelerating gradient gets reduced.
3. As it is shown in Fig. 2.1, the slope α and the location of the common tangential wall influence the ratio of the volumes of different cavity regions - one of them is the equatorial dome, and the other is the iris region. Amongst, in the $TM_{010}-\pi$ mode configuration, equatorial region of an elliptic cavity prominently stores magnetic energy, whereas the iris region prominently stores electric energy. The

wall slope α has a minor influence on the cell-to-cell coupling, but such influence can significantly control the electric and magnetic peak fields on the cavity surface.

4. The ratio a/b has a strong influence in deciding the parameter E_{pk}/E_{acc} . Therefore, aiming at a maximum achievable acceleration gradient in the cavity, a/b is optimized to minimize the parameter B_{pk}/E_{acc} for a targeted value of E_{pk}/E_{acc} .
5. The equatorial contour of the cavity is defined by the parameter A and B , and is optimized in order to reduce the peak magnetic field value. As it is observed [61], the ratio A/B has nearly no effect on the electromagnetic performance of the cavity. However, the same A/B ratio has strong influence on the mechanical requirements of the cavity like stiffness, rigidity etc.
6. In our optimization work, we use the parameter R_{eq} to tune the cavity frequency. We observe that the adjustment in the length of R_{eq} dose not effect either the electromagnetic characteristics of the cavity or its mechanical properties. Perhaps, it is because the effect of this adjustment is concurrently compensated by the corresponding change in the value of A and B .

Figure 2.1 explicitly shows these seven independent parameters that describe a TESLA type cavirt geometry. As it is discussed above, out of these seven independent parameters, L is fixed. For a multicell cavity, R_{iris} plays an important role in deciding κ_c . However, the optimization of R_{iris} will be presented in the later part of this chapter. We will describe the preliminary part of this design recipe, considering a constant value of R_{iris} . In our simulation, R_{eq} was tuned to achieve the resonant frequency. Therefore, primarily we are left with four independent geometric parameters to consider, while optimizing the cavity geometry.

Based on a thorough review of the existing literature, we find that there are two types approaches for cavity optimizations:

1. One can go for an optimization, targeting for maximum achievable E_{acc} in the cavity geometry, which will optimize capital cost of an accelerator, or

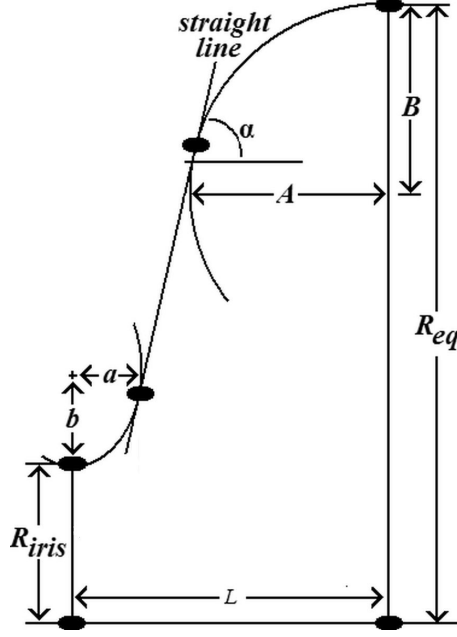


Figure 2.1: Two dimensional schematic of the half-cell geometry of a TESLA type elliptic cavity.

2. The cavity geometry can be optimized by minimizing the power loss on the cavity wall. This approach will optimize the run-time or operational cost as these cavities will produce less heat load to the cryo-plant.

Issues involved in each of these approaches are discussed in the following subsection.

2.2.2 Approach followed for the geometry optimization of TESLA type elliptic cavity

First, we discuss the issues involved in optimizing the acceleration gradient. For an SRF cavity, optimization for the maximum achievable acceleration gradient is performed, considering the constraints imposed on the peak value of the electric field and magnetic field at the cavity surface. Therefore, here E_{acc} is limited by the maximum value of B_{pk} developed on the inner surface of the cavity wall. As discussed earlier, maximum value of B_{pk} should always be less than a specified value to avoid significant drop in the cavity quality factor. This is the hard limit [66]. As it is mentioned earlier, for a 650 MHz niobium made SRF cavity, a safe value for the B_{pk} can be typically taken as 70 mT. Also

from field emission consideration, the maximum value of E_{pk} on the cavity surface is typically limited to 40 MV m^{-1} . However, the maximum tolerable value of E_{pk} can be enhanced considerably, improving the surface finish and cleanliness of the cavity wall, as well as, following an appropriate surface processing technique. This limit is therefore called the soft limit. Here, we want to mention that the upper limit for $B_{pk} = 70 \text{ mT}$ is of course a safe value, but it may be found as a little conservative one. In the recent tests of 650 MHz cavities at FNL and 644 MHz cavities at MSU, it has been shown that it is possible to push this B_{pk} value, even beyond 90 mT [68], [69]. In fact, we have also obtained the similar result even theoretically through a rigorous magneto-thermal analysis, which will be described in Chapter 5. With enhancement in upper limit of B_{pk} , we should be able to operate the cavity at higher acceleration gradient, if required. This will be particularly helpful, if we need to operate a cavity at higher gradient, in case of failure of adjacent cavity in that period.

Another aim of such optimization may be to minimize the power loss P_c on the cavity wall. As it is shown in Eq. 2.7, by maximizing the parameter $G(R/Q_0)$, we can minimize P_c [70]. This power loss which can be expressed in terms of G and R/Q_0 is as follows:

$$P_c = \frac{V_0^2}{R} = \frac{V_0^2 \times R_s}{G(R/Q_0)}. \quad (2.7)$$

Therefore, we need to maximize the parameter $G(R/Q_0)$ to minimize the power loss P_c .

As it is reported in the literature, these are the two approaches followed for optimization of the electromagnetic performance of an SRF cavity, especially the mid cell geometry. As mentioned earlier, the end cell has some added issues to be considered. The procedure that we have developed, performs the optimization, aiming at maximum achievable acceleration gradient. However, finally we will show that the geometry optimized following our methodology is moderately optimized, even for the minimum power loss.

In an RF cavity, the peak value of the electric field and the peak value of the magnetic field typically follow an inverse relation, *i.e.*, if we perturb the geometry to decrease the peak value of the magnetic field, the peak electric field increases. Hence, a higher accelerating gradient can be achieved for a relatively low B_{pk} on the cavity surface, if one is ready to tolerate more E_{pk} in the geometry and vice versa. Therefore, following our design recipe, the cavity geometry will be optimized to minimize the value of B_{pk}/E_{acc} below $(E_{pk,max}/B_{pk,max}) \times (E_{pk}/E_{acc})$ for the targeted value of E_{pk}/E_{acc} .

In the next subsection, we describe the geometry optimization of an SRF cavity mid-cell for a maximum achievable E_{acc} under the constraint imposed on the peak field values as we have discussed. Using this optimization technique, three sets of 5-cell 650-MHz elliptic cavities has been designed for the medium and high energy section of the ISNS linac. For the medium energy section, $\beta_g = 0.61$ cavity will be used and for the high energy section, we have the options to choose from either $\beta_g = 0.81$ or $\beta_g = 0.9$ cavity geometry. Later, in Chapter 6, we will discuss how we choose these β_g values.

2.3 Geometry optimization of an elliptic cavity midcell

We designed three sets of elliptic cavities, following the methodology that we have developed. Therefore, while describing different steps of this designed recipe, the reference will be drawn from the respective cavity sets, where it can be best explained.

As it is described, half-cell length $L = \beta_g \lambda / 4$ is a fixed parameter for the $TM_{010}-\pi$ mode. Therefore, for $\beta_g = 0.61$, $\beta_g = 0.81$ and $\beta_g = 0.9$, 650-MHz SRF cavities, L is equal to 70.336 mm, 93.400 mm and 103.77 mm, respectively. In this chapter, first, we explain our optimization of the mid-cell geometry for a fixed value of $R_{iris} = 44.000$ mm, and the optimization of R_{iris} will be presented in detail in the later part of this chapter. We set the targeted value of $E_{pk}/E_{acc} \leq 2.36$ for the $\beta_g = 0.61$ cavity. This choice should give an accelerating gradient of ~ 16.95 MV m⁻¹ under the constraint condition of $E_{pk} \leq 40$ MV

m^{-1} , provided the B_{pk} is below the maximum allowable value. As mentioned earlier, we kept the maximum allowable value of the surface magnetic field as 70 mT. Under similar conditions, a maximum of 18.6 and 20 MV m^{-1} can be achieved for the accelerating gradient in the $\beta_g = 0.81$ and $\beta_g = 0.9$ cavities for the targeted values of $E_{pk}/E_{acc} = 2.17$ and 2.25, respectively.

Next, we explain the design recipe for the optimization of mid-cell geometry, referring to the results we have obtained for $\beta_g = 0.61$ cavity. The starting geometry is the simplest one, where $a/b = A/B = 1$, and $\alpha = 88^\circ$. We would like to mention here, that the value of α is chosen based on the cavity fabrication experiences from the contemporary projects. This is because the upper limit of α appears as a mechanical constraint from cavity fabrication and cavity processing (chemical cleaning) point of view. Only one independent variable will then remain with these three constraints imposed on a/b , A/B and α . Hence, we choose B as ‘*that*’ independent variable. We have performed these simulations using a two-dimensional (2 D) electromagnetic eigenmode solver SUPERFISH [71]. In Fig. 2.2, values of B_{pk}/E_{acc} and E_{pk}/E_{acc} are plotted as a function of B . We have started these calculations from $B \approx L/2$. Such choice also sets the remaining optimization parameters A, a and $b \approx L/2$, thus the initial geometry turns out to be as the simplest **TESLA** type elliptical cavity geometry that one can imagine. As shown in Fig. 2.2, initially, at $B \approx 40$ mm, the corresponding value of B_{pk}/E_{acc} is ~ 5.5 mT/ (MV m^{-1}) which is high, whereas the corresponding value of E_{pk}/E_{acc} is moderate there (~ 2.8). Since the magnetic volume of the cavity enhances with a concurrent increase in the values of B and A , the ratio B_{pk}/E_{acc} decreases steadily, as we progress along the horizontal axis in the plot. This happens up to $B \sim 55$ mm, with a trivial increment in the value of E_{pk}/E_{acc} . Infact the values of B_{pk}/E_{acc} continue to decrease gradually beyond this point also, but, there the E_{pk}/E_{acc} values starts increasing significantly. Based on this observation, we stop at $A = B = 55.550$ mm, and we note the respective values of E_{pk}/E_{acc} and B_{pk}/E_{acc} as ~ 2.9 and ~ 4.31 mT/(MV m^{-1}), respectively, which shows that we are approaching close to our targeted values.

Therefore, fixing the value of $B = 55.550$ mm, we choose the geometry for further optimization. We are now left only with two independent variables A and a/b .

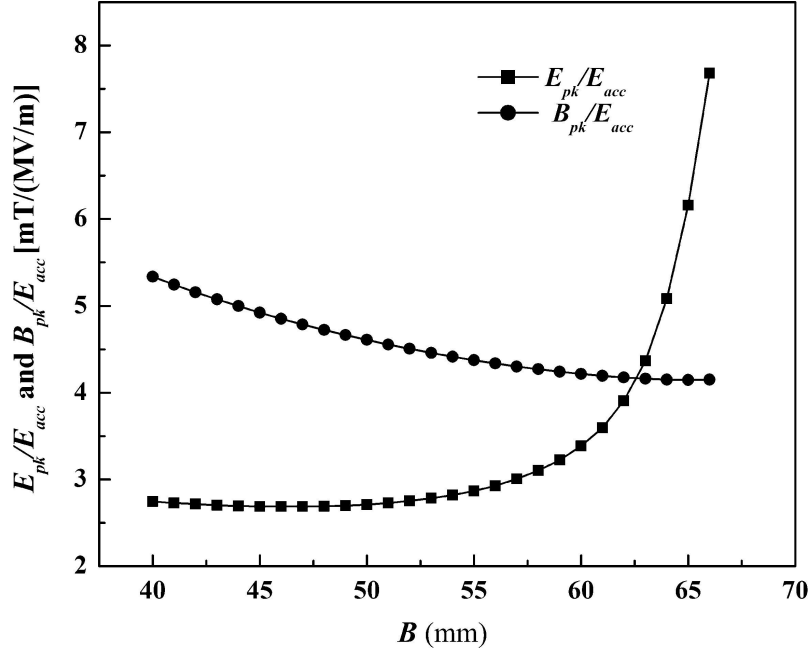


Figure 2.2: For the $\beta_g = 0.61$ cavity, variation of B_{pk}/E_{acc} , as well as E_{pk}/E_{acc} as a function of B , where, $a/b = A/B = 1$ and $\alpha = 88^\circ$.

Here, we want to emphasize that our initial optimization was started with four variables a , b , A and B . However, we chose the parameter B , and fixed its value. It is based on our observation that, up to the chosen limit, B has the minimum influence on the ratio of B_{pk}/E_{acc} and E_{pk}/E_{acc} of the cavity among these four parameters. This is probably because while changing B , the value of R_{eq} was adjusted simultaneously to keep the resonant frequency of the cavity unchanged. As an overall effect, the equatorial volume of the cavity geometry was not significantly affected by the change in the parameter B . As mentioned, we choose α as a constraint. Then to fulfil that target, a wrapper code was developed to generate the geometry of a cavity mid-cell, ensuring the ‘constant wall slope’ criteria by adjusting a and b , when we change the parameter B as well as R_{eq} . The wrapper code was developed using C-programming language.

In fact, from a given set of inputs describing the parametric geometry of an elliptical half-cell / cavity, the code SUPERFISH has an inbuilt module to generate the required

geometric input file of an elliptical half-cell or the half cavity for its own eigen mode solver. This module also provides a few parametric options to optimize the conventional geometry of the cavity. However, these options are limited in number. In order to address this concern, our wrapper code helps us to generate the geometry file of an elliptic half-cell /cavity for the eigen mode solver of SUPERFISH in a more customized manner with additional flexibilities. As an example, if we want to generate the geometric input file in the case, where, only the length of the end half-cells, will be changed keeping the ratios of a/b a A/B as well as the iris and equatorial radius constant throughout the cavity, options given in the SUPERFISH module will not be good enough. However, this type geometry can be easily generated using this wrapper code.

We have described the geometry optimization, considering $\alpha = 88^\circ$ in the above discussions. As mentioned earlier, cavity fabrication, mechanical strength of the cavity and other considerations like cavity cleaning, put a limit on the maximum value of α , which was chosen as 88° , based on the practical experience and a thorough literature review [37]. However, in the later part of this chapter, we will show that the electromagnetic performance of the cavity improves with increasing value of α .

We have targeted the value of $E_{pk}/E_{acc} = 2.36$ to obtain the desired accelerating gradient, and at this stage of the simulation, we are close to it. Therefore, the next steps of our optimizations were performed to minimize the value of B_{pk}/E_{acc} imposing a constraint on the value of $E_{pk}/E_{acc} = 2.36$.

Second stage of our optimization was performed by calculating the values of E_{pk}/E_{acc} as a function of the parameter A for a wide range of values of a/b varying between 0.2 and 1. From simulations, we have observed the monotonically increasing nature of E_{pk}/E_{acc} with A , for each value of a/b . However, the trend was opposite in the case of B_{pk}/E_{acc} as a function of A . These trends of E_{pk}/E_{acc} and B_{pk}/E_{acc} as a function of A are shown in Fig. 2.3 for a narrow range of a/b between 0.51 to 0.56. We have performed the calculation over a wide range of a/b values. However, in the figure, we show the

results only for this narrow range, because the parameters of our optimized geometry are anticipated to be lying in between these values. From Fig. 2.3(a), we choose those particular values of A for each a/b value, which gives the target value of our $E_{pk}/E_{acc} = 2.36$. In fact, in this process, we choose a set of cavity geometries, each having their corresponding value of a/b and A , and for which $E_{pk}/E_{acc} = 2.36$. Amongst all these geometries, the better one should correspond to the minimum value of B_{pk}/E_{acc} . Therefore, we calculate the corresponding values of B_{pk}/E_{acc} for each of these geometries from Fig. 2.3(b). In Fig. 2.4(a) and Fig. 2.4(b) we plot the corresponding values of B_{pk}/E_{acc} of each geometry as a function of A and a/b . Note that, these data points as shown in Fig. 2.4, are obtained considering the additional constraint of $E_{pk}/E_{acc} = 2.36$. Therefore, unlike Fig. 2.3(b), here the variation of B_{pk}/E_{acc} is non-monotonic.

From Fig. 2.4, we choose the final optimized mid-cell geometry, which corresponds to the minimum value of $B_{pk}/E_{acc} = 4.56 \text{ mT}/(\text{MV m}^{-1})$. Importantly, this value of B_{pk}/E_{acc} limits the value of achievable E_{acc} to 15.35 MV m^{-1} in this geometry, for the maximum peak surface magnetic field value of 70 mT . This gradient is less than the targeted value of 16.95 MV m^{-1} , which was mentioned earlier. In this geometry, $E_{pk}/E_{acc} = 2.36$, which indicates that for the maximum peak surface electric field of 40 MV m^{-1} , we can reach a gradient of 16.95 MV m^{-1} . However, in that case, exceeding the allowable limit of 70 mT , magnetic peak field value on the cavity surface, will reach a value of $\sim 77.29 \text{ mT}$. In this optimized mid-cell geometry, $A = 52.640 \text{ mm}$ and $a/b = 0.53$. For $\alpha = 88^\circ$, this geometry corresponds to $a = 15.280 \text{ mm}$ and $b = 28.830 \text{ mm}$. Optimized geometric parameters of the $\beta_g = 0.61$, 650-MHz cavity mid cell is summarized in Table 2.1, and the corresponding RF parameters (for the $\text{TM}_{010}\text{-}\pi$ mode) are specified in Table 2.2. As mentioned earlier, these values are obtained using the 2D electromagnetic design code SUPERFISH [71].

We conclude this discussion on the mid-cell geometry optimization describing an

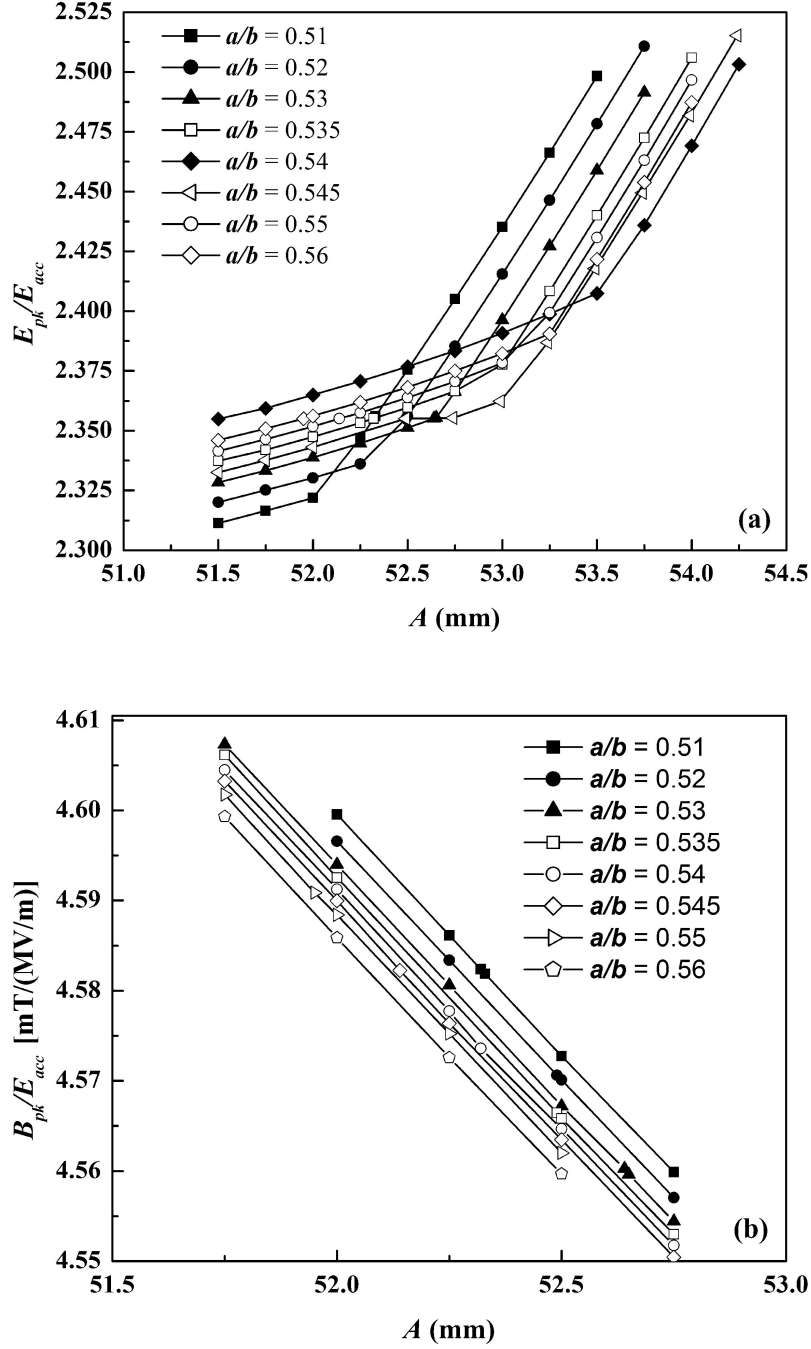


Figure 2.3: For the $\beta_g = 0.61$ cavity, variation of (a) E_{pk}/E_{acc} and (b) B_{pk}/E_{acc} as a function of A . In these simulations, the parameter B is kept fixed at 55.550 m for the $\beta_g = 0.61$ cavity. Here, $\alpha = 88^\circ$,

interesting observation noticed in the plot of E_{pk}/E_{acc} as a function of a/b for different values of A as shown in Fig. 2.5. As it is observed there, we can identify an optimum value of a/b for each value of A for which E_{pk}/E_{acc} shows a minimum. Interestingly, the distribution of the electric field on the cavity surface (E_s) becomes more uniform near

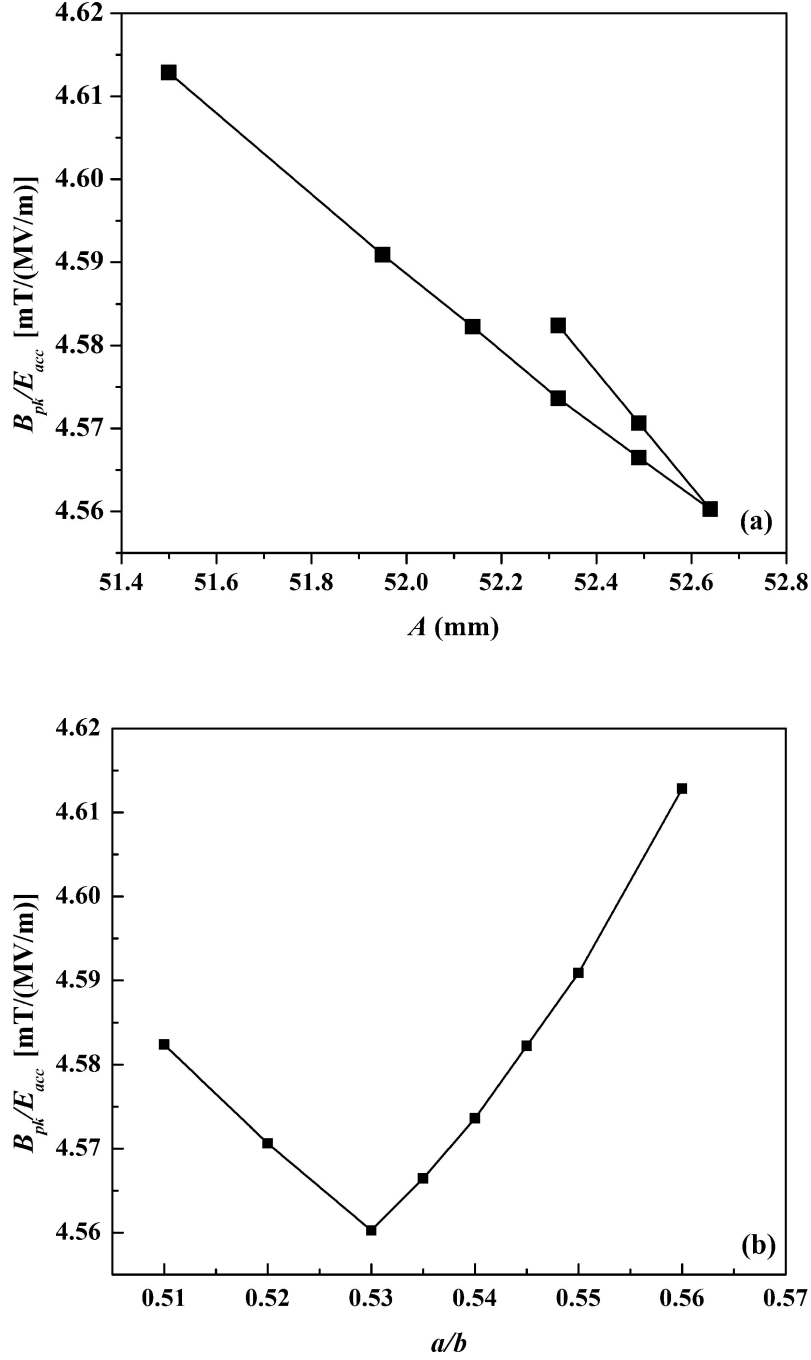


Figure 2.4: Plotting of B_{pk}/E_{acc} (a) as a function of A and (b) as a function of a/b for the $\beta_g = 0.61$ cavity. For each of these points, $E_{pk}/E_{acc} = 2.36$. Data for plotting these curves are taken from Fig. 2.3.

the iris region of the cavity when such minimum occurs. This is explicitly shown in Fig. 2.6. There we have plotted the value of E_s/E_{acc} along the cavity length. In this figure $z = 0$ indicates equatorial plane of the cavity. This observation justifies the selection of a/b as an optimization parameter.

Table 2.1: Geometrical parameters for the optimized mid-cell geometry of the $\beta_g = 0.61$ cavity.

Parameter	Magnitude	Unit
R_{iris}	44.000	mm
R_{eq}	195.59	mm
L	70.336	mm
A	52.640	mm
B	55.550	mm
a	15.280	mm
b	28.830	mm
α	88.000 ⁰	

Table 2.2: RF parameters for the optimized mid half cell in the $TM_{010-\pi}$ mode for the optimized $\beta_g = 0.61$ cavity. These values are calculated considering $R_s = 10 \text{ n } \Omega$.

RF Parameter	Magnitude	Unit
Frequency	650.0	MHz
Transit-time factor(T)	0.7675	
Q_0	1.332×10^{10}	
$R_s Q_0$ (Geometry Factor)	189.0	Ω
R/Q_0	32.66	Ω
E_{pk}/E_{acc}	2.355	
B_{pk}/E_{acc}	4.560	mT/[MV/m]
E_{acc}	15.40	MV/m

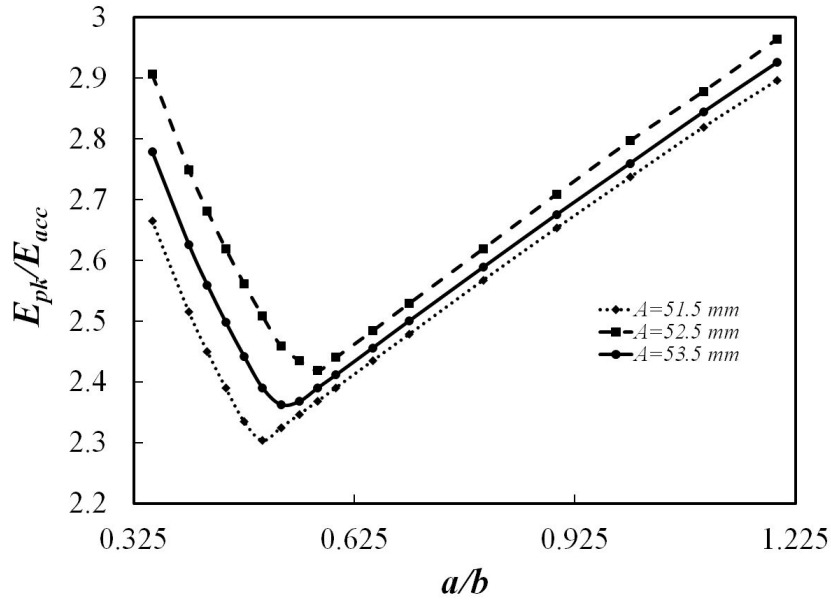


Figure 2.5: Variation of E_{pk}/E_{acc} as a function of a/b for different values of A for the $\beta_g = 0.61$ cavity. Note that $B=55.550$ mm in this figure.

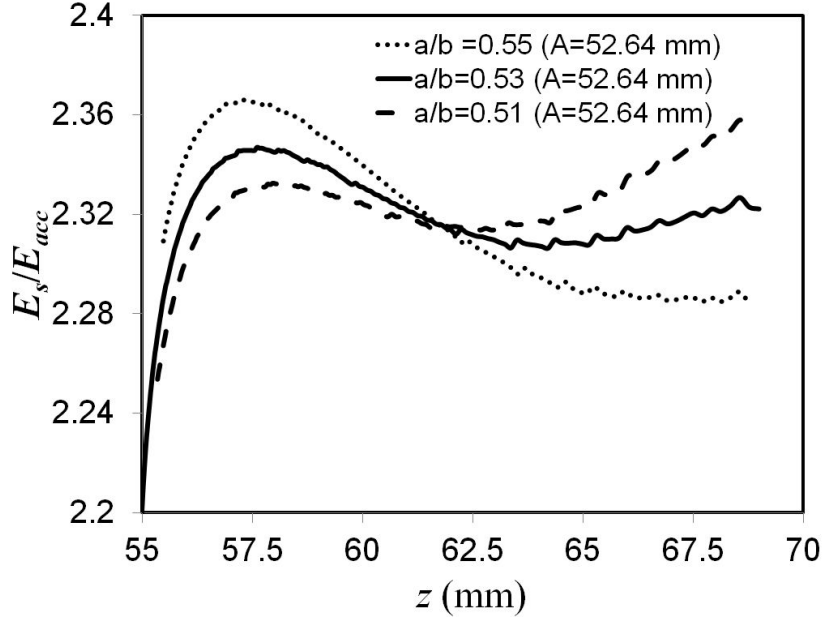


Figure 2.6: Plotting of E_s/E_{acc} as a function of z , where, the solid line corresponds to $a/b = 0.53$, for which E_{pk}/E_{acc} shows the minima in a $\beta_g = 0.61$ cavity geometry. Here, the other two curves are for $a/b = 0.55$ and 0.51 respectively, which peak at higher value of E_s/E_{acc} , and $z = 0$ corresponds to the equator plane.

In reality, for most of the cases, these cavities are comprised of multiple cells. Issues related to the multicell elliptic SRF cavity geometry are discussed in the next section.

2.4 Some aspects of multicell elliptic SRF cavities

Typically the multicell SRF cavities are used in a superconducting accelerator. Multicell cavities are more efficient because compared to a single cell cavity, here, we can obtain a higher value of the real estate or effective acceleration gradient. The primary parameter that needs to be decided in the case of multicell cavity geometry is the number of cells N in the cavity. This decision depends on several considerations. Among these, one consideration is the transit time factor T , which strongly affects energy gain ΔW obtained from a cavity. As discussed earlier, beam particle of velocity v ($= \beta c$) will gain maximum energy from a cavity when $\beta = \beta_g$. However, the β of the particle changes with acceleration along the length of the cavity. Dependence of T on β

is described by the following equation [57]:

$$T(N, \beta, \beta_g) = \begin{cases} \left(\frac{\beta}{\beta_g}\right)^2 \cos\left(\frac{\pi N}{2\beta/\beta_g}\right) \frac{(-1)^{(N-1)/2}}{N((\beta/\beta_g)^2 - 1)} & \text{where } N = \text{odd} \\ \left(\frac{\beta}{\beta_g}\right)^2 \sin\left(\frac{\pi N}{2\beta/\beta_g}\right) \frac{(-1)^{(N+2)/2}}{N((\beta/\beta_g)^2 - 1)} & \text{where } N = \text{even}, \end{cases} \quad (2.8)$$

Functional dependence of T on the normalized parameter β/β_g is shown in Fig. 2.7 for the $\beta_g = 0.61$ cavities for different number of cells N . As mentioned earlier, these cavities will be used in the approximate energy range between 160 MeV to 500 MeV in the ISNS linac. This energy range will correspond to a range of β from 0.51 to 0.76, which is between the two vertical lines shown in Fig. 2.7. As it is shown in Fig. 2.7, the transit time factor is mostly greater than 0.7 within this selected range of β/β_g . It will be the case if we choose the number of cells $N \leq 5$ in the $\beta_g = 0.61, 0.81$ and 0.9 650-MHz SRF elliptic cavities.

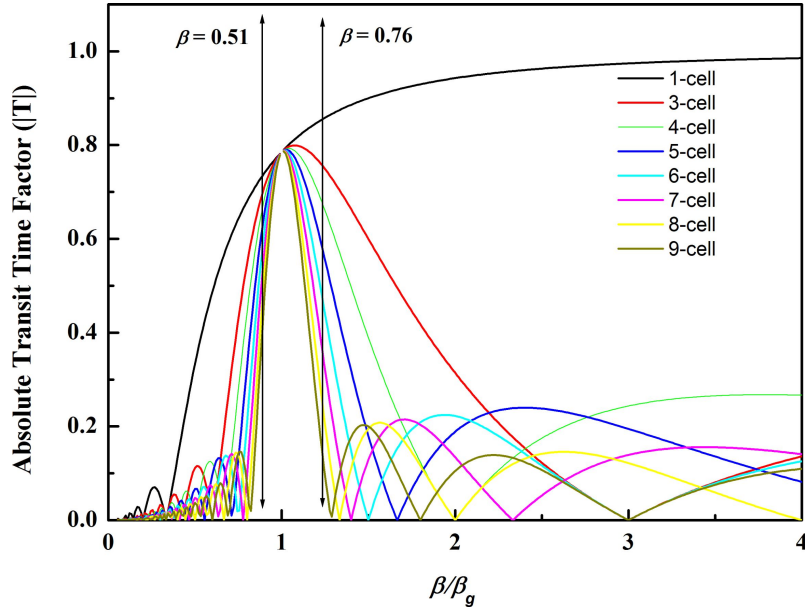


Figure 2.7: Variation of transit time factor T with the normalized parameter (β/β_g) for the 5 cell, $\beta_g = 0.61$ cavity. The two vertical lines correspond to $\beta/\beta_g = 0.85$ and 1.27 , which is explained in the text on the context of $\beta_g = 0.61$ multicell cavities.

Another important consideration in the cavity arises from the requirement of good field flatness while deciding the number cells per cavity. Field flatness η for a multicell cavity

is defined as follows [72]:

$$\eta = \left(1 - \frac{\sigma_E}{\mu}\right). \quad (2.9)$$

where, σ_E is the standard deviation of the maximum values of the electric field amplitudes in different cells, and μ is the mean value calculated from these maximum values of the electric field amplitudes. Field flatness is an important figure of merit of a multicell cavity. In a cavity with poor field flatness, the cell with higher electric field may quench or field emit first, even in a relatively low overall gradient of the cavity. The synchronization between the particle and the electromagnetic wave may also be affected by the poor field flatness. Thus, the field flatness plays a decisive role in the maximum achievable acceleration gradient of a multicell cavity geometry. A maximum value of η close to unity is therefore always desirable for a multicell cavity geometry. In addition to this, the external quality factor of a power coupler may also be affected by a poor field flatness.

In principle, for a cavity with an infinite array of perfectly identical cells, or for a cavity with finite number of perfectly matched cell, η should not depend on the cell number. However, in the presence of manufacturing errors in the individual cell geometries, the field flatness becomes a strong function of the number of cells N in a cavity, and κ_c , *i. e.*, the cell-to-cell coupling coefficient, as [73]

$$(1 - \eta) \propto \frac{\sigma_f}{f} \frac{1}{\kappa_c} N^2. \quad (2.10)$$

Here, σ_f/f denotes relative rms error in the resonant frequency of different cells, and achievable tolerance on the cavity dimensions in the cavity manufacturing process decides the quantity σ_f/f . For a cavity with N number of cells, and for a known achievable value of σ_f/f , Eq. 2.10 shows that the coupling coefficient κ_c will decide the field flatness η . Therefore, for further calculation, first, let us obtain an approximate estimation of the value of κ_c is shown in Table 2.3, calculated from the 0 and π mode frequencies of a cavity mid cell: As it is mentioned in the literature, cell-to-cell coupling $\kappa_c = 1.87\%$

Table 2.3: Calculation for the cell-to-cell coupling coefficient κ_c for the $\beta_g = 0.61$ cavity.

Mode	Resonant frequency (MHz)	Cell-to-cell coupling coefficient
π	$f_\pi=650.00$	$\kappa_c = 2 \times \frac{(f_\pi - f_0)}{f_\pi + f_0} \times 100 = 0.892\%$
0	$f_0=644.23$	

for a nine-cell 1.3-GHz **TESLA** cavity geometry, for which, an acceptable value of field flatness is achieved [61], [66]. Assuming that a similar value of σ_f/f is obtainable, following similar machining and cavity processing techniques, we anticipate similar field flatness (as it is reported in the case of a 9-cell **TESLA** cavity) for our elliptical cavities, if we choose $N = 9 \times (0.892/1.87)^{0.5} \leq 6$ number of cells per cavity. On the safer side, we limit the number of cells in a cavity to 5 in our design. In this regard, more justifications will be given later, when we discuss optimization of the iris radius.

Power handling capacity of the input power coupler is another consideration that influences the choice of the number of cells in a multicell cavity. In the medium and high energy section of the ISNS linac, beam will consume up to 200 kW of peak RF power from a 5-cell cavity. This can be supplied by the commonly used power couplers designed for the SRF cavities without hindrance [74].

Based on the above considerations, we opt for five cells in the elliptic cavities which will be used in the medium and high energy section of the proposed ISNS linac.

As mentioned, the terminal cells are known as end-cells in a multicell cavity geometry. Compared to the midcell geometry, end-cells are slightly different. In the next section, we will discuss electromagnetic design optimization of the end-cell geometry.

2.5 Optimization of the end cell-geometry

End-cells does not see symmetric boundary conditions at the two ends in a multicell cavity geometry. This is because, there are mid-cells at one end of an end-cell, and beam pipe on the other end. Hence, electromagnetic field terminates at the two ends

differently, even in the π mode. Therefore, if we take end-cell geometry exactly the same as the mid-cell geometry, cavity will resonate at a slightly different frequency and some more optimization steps become necessary to restore the resonant frequency to the design frequency.

In addition to this restoration of the resonant frequency, another important consideration for the end-cells is to ensure that none of the prominent higher order mode gets trapped within the multicell geometry. Therefore, further optimization is required to take care of the trapped mode in the end cell geometry, and this will be discussed in the next chapter. In this chapter, we focus on the primary optimization of the end-cell geometry, aiming at the frequency restoration.

Not only the overall resonant frequency of the cavity, but the resonant frequency of the individual end-cell will also be deviated from the design frequency of the cavity, if we use the geometry of an end-cell, exactly the same as the mid-cell geometry. An unequal accelerating gradient may appear in the consecutive accelerating cells as a consequence of such deviation in the resonant frequency. Therefore, restoration of the frequency is also necessary to achieve good field flatness in the cavity. For the optimization of end-cell geometry, our starting geometry is same as that of our optimized mid-cell. As shown in Fig. 2.8, one side of the end-cell is connected to the beam pipe. In this geometry, we modify only the half of the cell towards beam pipe end, keeping the other half undisturbed. To tune the mid-cell geometry R_{eq} was made to vary. However, this process is not suitable here. In fact, a fixed R_{eq} is a constraint here, because both the half-cells of the end-cell should have the same R_{eq} . Another possibility is to tune the length of the end-half cell L_e , which is performed here to restore the design frequency (*i.e.* the mid-cell frequency) in the end-cell. Following this technique, we found that the design frequency 650-MHz is restored with an elongated end-half cell length $L_e = 71.550$ mm in the $\beta_g = 0.61$ cavity. However, in comparison to the mid cell, the change in the end-cell is small and does not affect the synchronism condition. As it is mentioned earlier, the field flatness

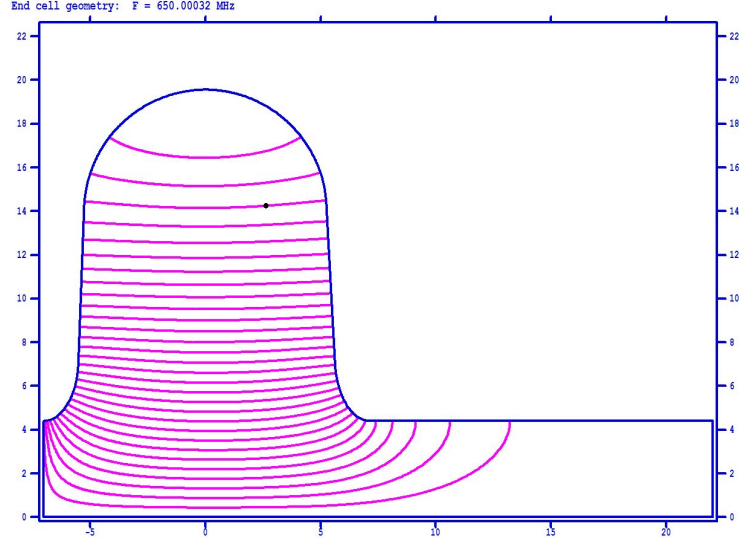


Figure 2.8: Geometry of the end-cell for the $\beta_g = 0.61$ cavity.

of the multicell geometry should improve with this restoration of the design frequency, which we have explicitly verified while optimizing, the end-cell geometry of the $\beta_g = 0.9$, 650-MHz cavity. In Fig. 2.9, we plot the variation of the end cell resonant frequency with the end-half cell length. Also, in the same figure, we show the field flatness of the 5-cell cavity geometry. As shown in the figure, resonant frequency of the end-cell increases monotonically with increasing value of L_e . Field flatness of the cavity also improves initially with the increasing end-half cell length and shows its maximum when the frequency is perfectly restored. If we increase the cavity length further, the resonant frequency of the end-cell continues to increase gradually, whereas the field flatness of the multicell cavity starts dropping monotonically.

In this simple approach, only the end-half cell length is tuned. Therefore, one can keep equator radius of the end-cell unchanged. This will help to keep the mechanical fabrication of the cavity simple. Else, different cavity forming ‘die’ should be designed for the mid-cell and the halves of the end-cell at the two ends. Beside the length and wall angle, in this optimization process, all other geometrical parameters of the end-half cell remains the same as the mid half-cell geometry.

In this context, we must mention another important issue related to the geometry

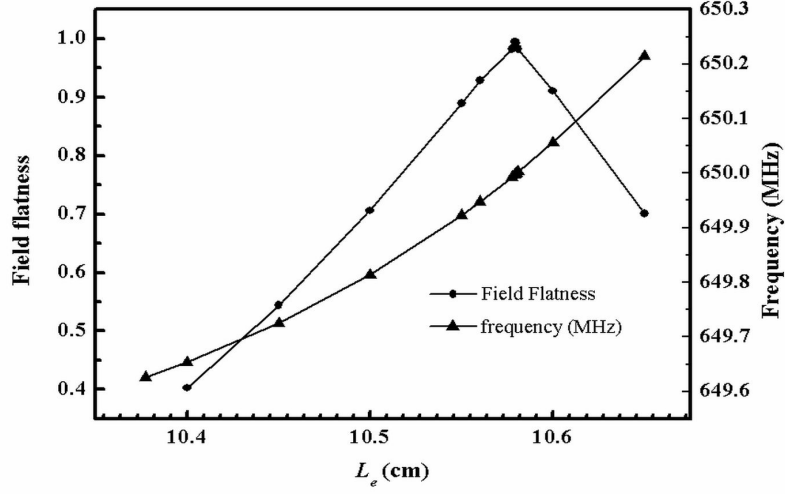


Figure 2.9: Field flatness and resonant frequency as a function of the $\beta_g = 0.61$ cavity end-half cell length L_e .

optimization of an end half-cell. We have optimized the end half-cell geometry with an R_{iris} , which will ensure the required value of the cell-to-cell coupling coefficient κ_c . However, a modification in the end half-cell geometry may be needed in future, when a power coupler will be incorporated in the geometry. As it is described in Ref [75], there the end half-cell geometries are modified with enhanced iris diameter. However, the optimization procedure, described in this chapter, is very general, and will be applicable in performing the required modification in that case.

As mentioned earlier, some advanced optimization of the end-cell may be required to take care of the trapped HOM. Another geometrical parameters of the end half cell also need to be varied there along with the end-half cell length. The details will be discussed in Chapter 3. In the next section, the remaining geometrical parameter, *i.e.*, the iris radius r_{iris} will be optimized.

2.6 Optimization of the iris radius

In the last sections, we have described the optimization of the mid cell and end cell

geometry, considering a constant value of the iris radius R_{iris} . In an RF cavity, R_{iris} plays an important role in deciding (a) the shunt impedance R of the cavity, which decreases with R_{iris} , as well as (b) the cell-to-cell coupling κ_c , which improves with increasing R_{iris} [37]. In Fig. 2.10, R and κ_c of a $\beta_g = 0.61$, 650-MHz cavity geometry are plotted as a function of the R_{iris} , which confirms the expected trends. On the plot, each of the five points represent an optimized cavity geometry, having a particular value of R_{iris} . For each of the different optimized multicell geometries, values of κ_c was calculated from the passband of the respective $TM_{010}-\pi$ modes. Here, we want to mention that for a required value of η , the value of $\kappa_c \propto N^2$, which is emphasized in Eq. 2.10 as well as in Ref. [76]. However, another reference [77] describes $N^{3/2}$ dependence for the same, which is more stringent. Following this conservative formula, we have calculated $\kappa_c \geq 0.775\%$, which is required to achieve the desired field flatness in a $\beta_g = 0.61$, 650-MHz, 5-cell cavity geometry. The first formula with N^2 dependence specifies a requirement of $\kappa_c \geq 0.6\%$ only. As shown in Fig. 2.10, the requirement $\kappa_c \geq 0.6\%$ can be satisfied even in a cavity with $R_{iris} = 39$ mm. However, following a conservative approach we select our $R_{iris} = 44$ mm for the optimized $\beta_g = 0.61$, 650-MHz 5-cell cavity geometry for which $\kappa_c = 0.81\%$.

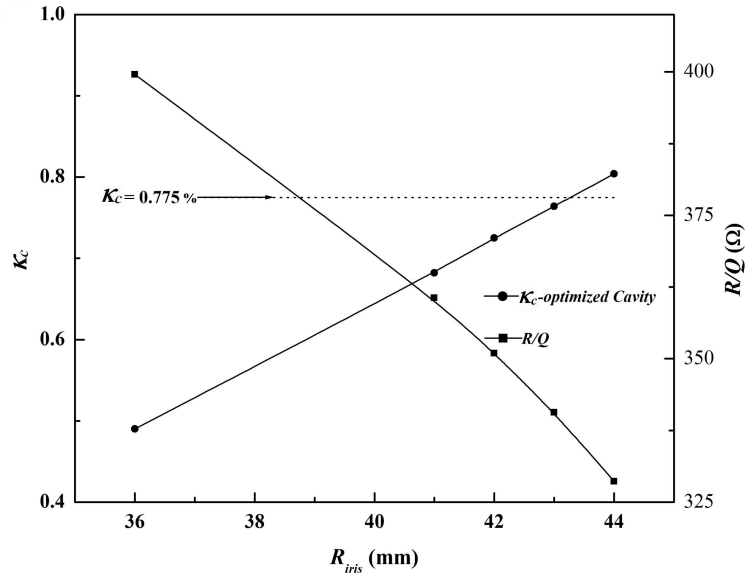


Figure 2.10: Variation of κ_c (in %) and (R/Q) with the R_{iris} , where the dotted line shows the value of $\kappa_c \sim 0.775\%$.

2.7 RF parameters obtained for the optimized multicell cavity geometry.

For the ISNS linac, optimization of 5-cell 650-MHz elliptic SRF cavity parameters for $\beta_g = 0.61$, $\beta_g = 0.81$ and $\beta_g = 0.9$ were performed following this design recipe, using the 2 D EM code SUPERFISH. We now present the RF parameters obtained from the simulations performed for optimized cavity geometries.

1. Simulated results for a $\beta_g = 0.61$, 650-MHz 5-cell SRF elliptic cavity geometry:

Table 2.4 shows the simulated RF parameters obtained for the $\beta_g = 0.61$ cavity. In this design, only the length of the end-half $L_e = 71.550$ mm is different compared to the mid cell length. Rest of the end-half cell geometry is identical with the mid-cell geometry, which we have described in Table. 2.1.

For the optimized multicell geometry, we have observed that there is a slight deviation of ~ 0.31 kHz in the frequency of the final cavity even after matching the frequency of the end cell with the mid cell. In Fig 2.11, we plot the absolute amplitude of the axial electric profile which was used to estimate the field flatness η of the cavity geometry. We have obtained $\eta > 99\%$ for the optimized geometry. Fig. 2.12 shows the field contours in one half of the multicell cavity. In Fig. 2.13, five normal mode frequencies of the 5-cell cavity are plotted as a function of their phase shifts. From this passband we have calculated cell-to-cell coupling coefficient $\kappa_c \approx 0.81\%$.

These cavities will be operated in their $\text{TM}_{010}-\pi$ mode. However, as shown in Fig. 2.13, for the 5-cell geometry, there will be five modes in the passband. We have calculated the corresponding R/Q values for these five normal modes as a function of β using the electromagnetic code SLANS [78], and these results are shown in Fig. 2.14. As it is shown there, the R/Q values for the π -mode at 650.0 MHz dominate within the operation of range β (from ~ 0.51 to ~ 0.76), for which

medium β cavities will be used. Maximum R/Q value for the π mode is $\approx 354 \Omega$ at $\beta \sim 0.65$. However, beyond this range, R/Q of the $4\pi/5$ mode resonating at 649.44 MHz frequency is large compared to the R/Q of the π mode.

2. Simulated results for a $\beta_g = 0.81$, 650 MHz, 5-cell SRF elliptic cavity geometry:

We summarize the geometry and the optimized RF parameters of our $\beta_g = 0.81$, 650-MHz, 5-cell SRF elliptic cavity in Table 2.5 and Table 2.6, respectively. Here, end-half cell length was calculated as $L_e = 94.830$ mm. Other design parameters of the end-cell are identical with the optimized mid-cell geometries.

3. Simulated results for a $\beta_g = 0.9$, 650-MHz 5-cell SRF elliptic cavity geometry :

Table 2.7 and Table 2.8 summarize the geometry and the optimized RF parameters respectively of the $\beta_g = 0.9$, 650-MHz 5-cell SRF elliptic cavity. For the optimized end-cell, we have obtained $L_e = 105.80$ mm. Other end-cell parameters are identical with the optimized mid-cell parameters.

Here, we want to mention that the optimized mid-cell of $\beta_g = 0.81$ and 0.9 elliptic cavities have longer half-cell length than the half-cell length of a $\beta_g = 0.61$ cavity. For these two cavities, we can accept even somewhat smaller wall slope in the optimized design still realizing the targeted acceleration gradient. Such relaxation in the wall slope will improve the mechanical strength of the cavity and will ease fabrication procedure ensuring the generation of the required field gradient. Therefore, we chose $\alpha \approx 85^\circ$ for these two cavities.

In the next section, we will briefly discuss the optimization based on another design approach, where the aim is to minimize the Ohmic loss in the design.

2.8 Geometry optimization for a low loss SRF cavity

So far, we have kept the wall angle of the cavity, *i.e.*, α as a constant. In this section,

Table 2.4: RF parameters for a 5-cell $\beta_g = 0.61$ cavity in the $\text{TM}_{010-\pi}$ mode.

RF Parameter	Magnitude	Unit
Frequency	650.0	MHz
Transit-time factor(T)	0.7094	
Acc. Gradient ($E_{acc} = E_0 T$)	15.40	MV/m
Q_0	1.333×10^{10}	
G	189.4	Ω
R/Q_0	327.4	Ω
E_{pk}/E_{acc}	2.370	
B_{pk}/E_{acc}	4.560	mT/(MV/m ⁻¹)

Table 2.5: Optimized geometry of a $\beta_g = 0.81$, 650-MHz cavity mid cell.

Parameter	Magnitude	Unit
R_{iris}	43.930	mm
R_{eq}	196.92	mm
L	93.397	mm
A	75.017	mm
B	69.000	mm
a	13.045	mm
b	20.781	mm
α	85.450 ⁰	

Table 2.6: RF parameters for a 5-cell $\beta_g = 0.81$ cavity in the $\text{TM}_{010-\pi}$ mode.

RF Parameter	Magnitude	Unit
Frequency	650.0	MHz
Transit-time factor(T)	0.7159	
Acc. Gradient ($E_0 T$)	18.38	MV/m
Q_0	1.7026×10^{10}	
$R_s Q_0$ (or G)	241.7	Ω
R/Q_0	556.4	Ω
E_{pk}/E_{acc}	2.170	
B_{pk}/E_{acc}	3.809	mT/(MV/m ⁻¹)

we will review the effect of α on the electromagnetic performance of the SRF cavity. These calculations are performed with $\beta_g = 0.9$ half-cell geometry. In Fig. 2.15, we show the variation of B_{pk}/E_{acc} for different values of α . The analysis shows that B_{pk}/E_{acc} of the half-cell reduces further for the higher values of α . It is in fact expected. Equatorial volume of the cavity cell increases with the increasing wall angle, and as a consequence, the energy density of the magnetic field in the cavity, reduces resulting in reduction of the

Table 2.7: Optimized geometry of a $\beta_g = 0.9$, 650-MHz cavity mid-cell.

Parameter	Magnitude	Unit
R_{iris}	50.000	mm
R_{eq}	199.93	mm
L	103.77	mm
A	83.275	mm
B	84.000	mm
a	16.788	mm
b	29.453	mm
α	85.000 ⁰	

Table 2.8: RF parameters for a 5-cell $\beta_g = 0.9$ cavity in the $TM_{010}-\pi$ mode.

RF Parameter	Magnitude	Unit
Frequency	650.0	MHz
Transit-time factor(T)	0.7169	
Acc. Gradient (E_0T)	18.60	MV/m
Q_0	2.395×10^{10}	
$R_s Q_0$ (or G)	257.6	Ω
R/Q_0	608.3	Ω
E_{pk}/E_{acc}	2.251	
B_{pk}/E_{acc}	3.754	mT/(MV/m ⁻¹)

peak value of the surface magnetic field B_{pk} there.

We have also plotted another parameter $G(R/Q_0)$ as a function of α in the same figure. Interestingly, it is observed that the value of the parameter $G(R/Q_0)$ increases slowly with increasing wall angle and nearly saturates for the higher values of α . These two observations clearly indicate that the cavity geometries corresponding to the higher values of α are optimized for the low loss as well as relatively higher accelerating gradients. In fact, in an elliptical cavity geometry, the volume, as well as the (inner) surface area of the equatorial dome increases with increasing α , *i.e.*, the slope of the cavity wall. In these cavities, volume inside the equatorial dome is the region, which is dominantly occupied by the magnetic field (energy). Therefore, with increasing dome volume, peak value of the magnetic field (as well as the surface current) on the inner wall of the cavity, reduces, resulting a reduction in the Ohmic loss. It is because heat loss is proportional to the square of the magnetic field value. It explains why one should prefer elliptical cavity geometry

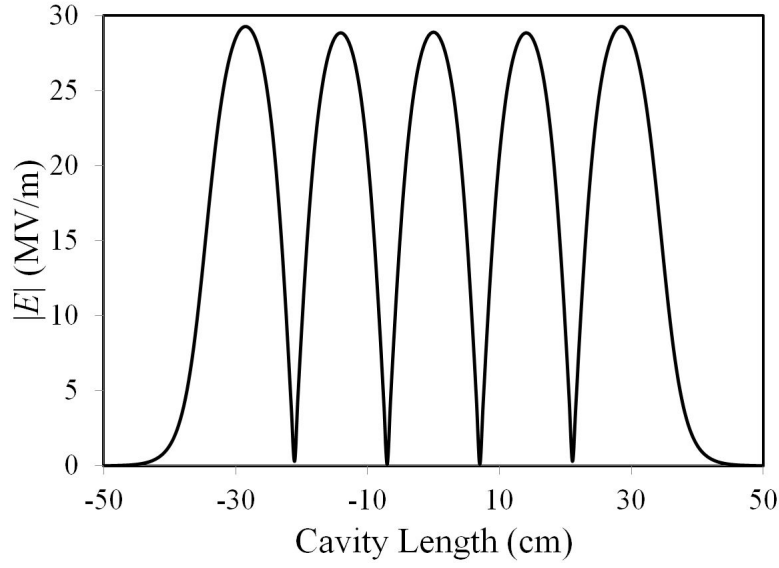


Figure 2.11: Variation of the magnitude of the axial electric field along the beam axis for the optimized $\beta_g = 0.61$ cavity.

with higher wall slope for the low loss operation.

On the other hand, an increase in α , does not change the shape and volume of the iris region of the cavity. Therefore, the peak value of the electric field, which occurs at the iris surface, remains nearly unperturbed in the geometry. As mentioned earlier, peak value of the surface magnetic field as well as the peak value of the surface electric field together, limit the electromagnetic performance of the cavity. However, for most of the cases, limitation imposed on B_{pk} on the surface is reached first, while performing the geometry optimization of an elliptical SRF cavity aiming at the maximization of E_{acc} . Again, in the optimized cavity, the cavity geometry fixes B_{pk}/E_{acc} and E_{pk}/E_{acc} . Therefore, a reduction in the peak value of the magnetic field on the inner wall of the cavity geometry optimized with higher values of wall slope, indicates an increase in the value of E_{acc} achievable under the peak magnetic field limit.

However, as mentioned above, with increasing wall slope, inner surface of the cavity, especially in the equatorial dome region, also increases. As we know, with increasing surface area, Ohmic loss increases proportionally, and such an increase in the Ohmic loss becomes comparable with its reduction due to the decreasing magnetic field value in the

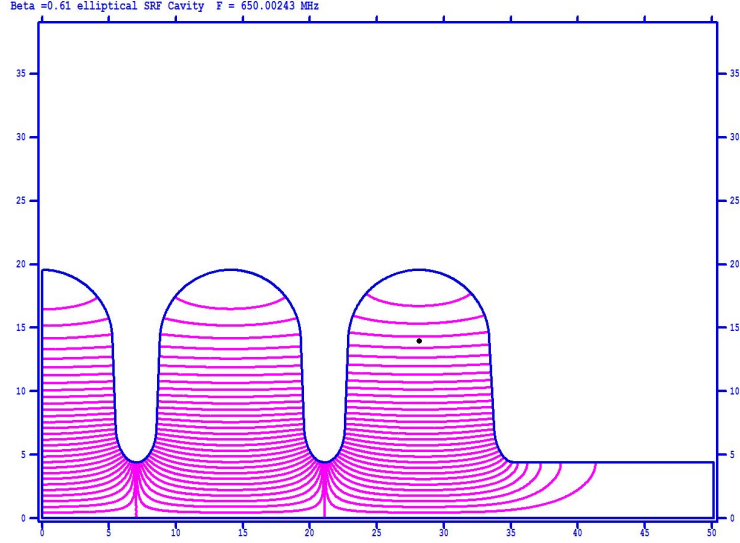


Figure 2.12: Field contours for one half of the $\beta_g = 0.61$ cavity.

cavity geometry with very high wall slope. As it is shown in the figure, for the higher values of α , $G(R/Q_0)$ as well as E_{acc} saturates in the cavity geometry.

However, it is inconvenient to manufacture multicell elliptic cavities with higher wall angle from the fabrication and cavity processing point of view. Especially, it turns out to be extremely challenging for the cavities with α values more than 90° . These cavities are called the re-entrant cavities. Although re-entrant type of cavities are superior choice for achieving higher E_{acc} as well as minimum cavity loss, yet for the above mentioned complexities, these designs are not well accepted for the fabrication of multicell elliptic SRF cavities.

2.9 Summary and conclusion

In this chapter, we have described a design recipe for the geometry optimization of multicell elliptic SRF cavities. Following this step-by-step, one dimensional methodology, we have optimized three sets of 5-cell 650 MHz elliptic cavities, which will be used in the medium and high energy sections of the superconducting linac for the proposed ISNS project. For the elliptic SRF cavity, the optimized parameters are chosen,

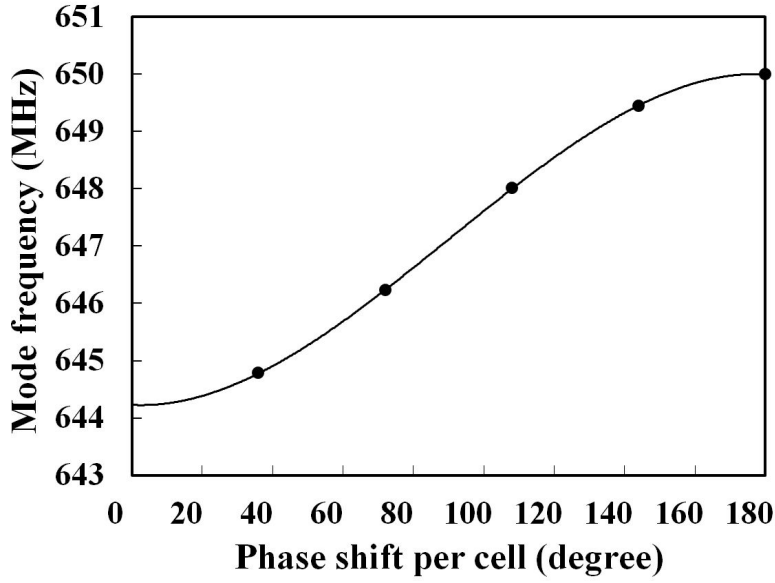


Figure 2.13: Dispersion curve for the $\text{TM}_{010}\text{-}\pi$ mode of the $\beta_g = 0.61$ cavity.

using a generalized procedure which is summarized as follows:

1. In this methodology, we reserve R_{eq} to tune the cavity to its design frequency for each simulation, and from the synchronization point of view, we choose the half-cell length $L = \beta_g \lambda / 4$. For the time being, we keep the value of R_{iris} fixed.
2. Keeping in mind the practical constraint, we choose the permissible maximum possible value for α .
3. Based on the above considerations and constraints imposed on L , R_{eq} and α , we are left with three independent parameters A , B and a/b . Our optimization starts by choosing B , which minimize the value of B_{pk}/E_{acc} , restricting E_{pk}/E_{acc} within a reasonable limit. Parameters like A , a and b are chosen to achieve the minimum value of B_{pk}/E_{acc} , and a target value of E_{pk}/E_{acc} .
4. End cells are optimized to restore the design frequency and field flatness, and there L_e is used as the tuning parameter.
5. Finally, we choose the value of R_{iris} based on the requirement of κ_c .

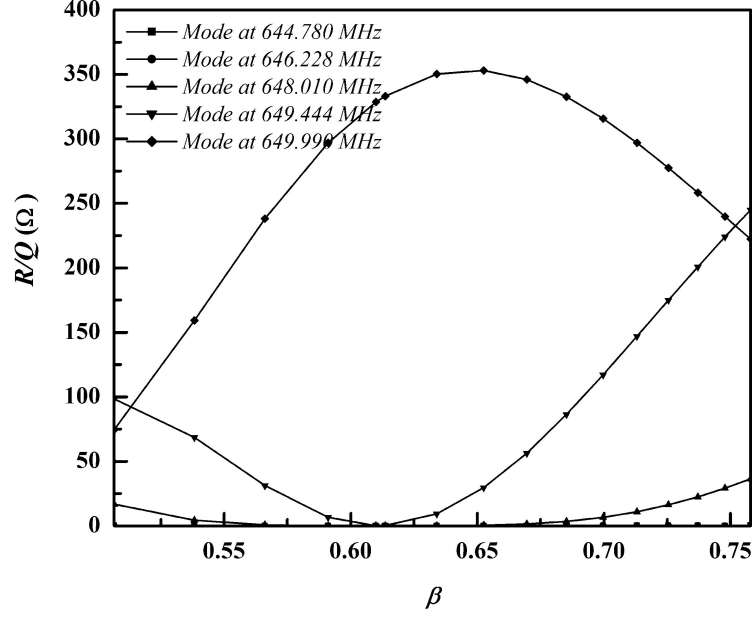


Figure 2.14: R/Q values of the monopole modes are plotted as a function of β for the 5 normal mode frequencies of the first pass band.

We have developed a new and generalized logical approach towards the design optimization of a multicell SRF cavity. Following this, the geometry of an elliptic cavity can be optimized for maximum achievable acceleration gradient. This approach is a step-by-step, one dimensional methodology. The conventional SRF cavity optimization techniques are essentially multidimensional technique. To compare our methodology with the conventional multidimensional optimization process reported in the literature (*e.g.*, in Ref. [61], [70]), we plot the optimized values of B_{pk}/E_{acc} as a function of α in Fig. 2.16, calculated using our methodology for the **TESLA** geometry. Then we compared it with the plot reported in Ref. [70], where the plot is obtained using a multidimensional optimization technique. Figure 2.16 shows similar trend for the two plots. The proximity between these two plots justifies the effectiveness of our optimization technique, compared to the multivariable optimization technique that has been followed worldwide. In addition to this, the data point corresponding to the experimentally obtained value of the cavity geometry described in Ref [61] designed for the **TESLA** project is also shown in the same figure, which too confirms the effectiveness of our design recipe. Before we conclude this Chapter, it will not be

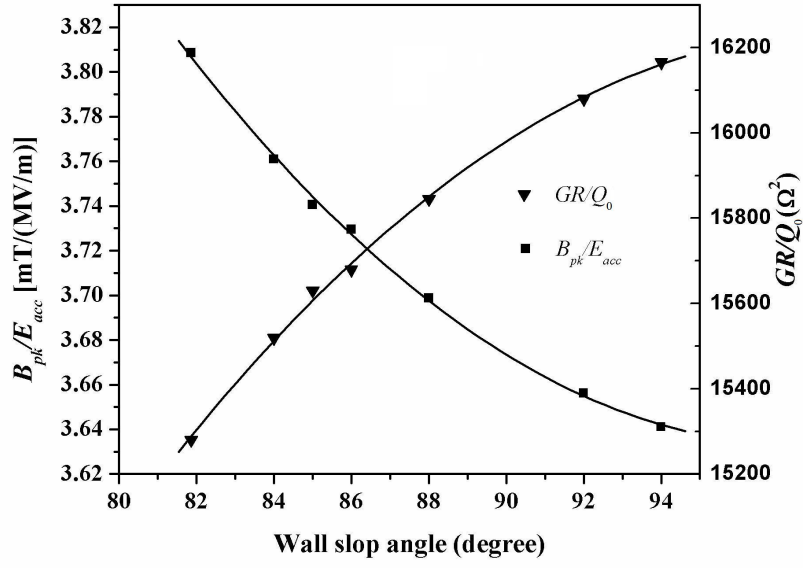


Figure 2.15: Optimum values of B_{pk}/E_{acc} as a function of α . Here the value of E_{pk}/E_{acc} is kept fixed at 2.0 for each data point.

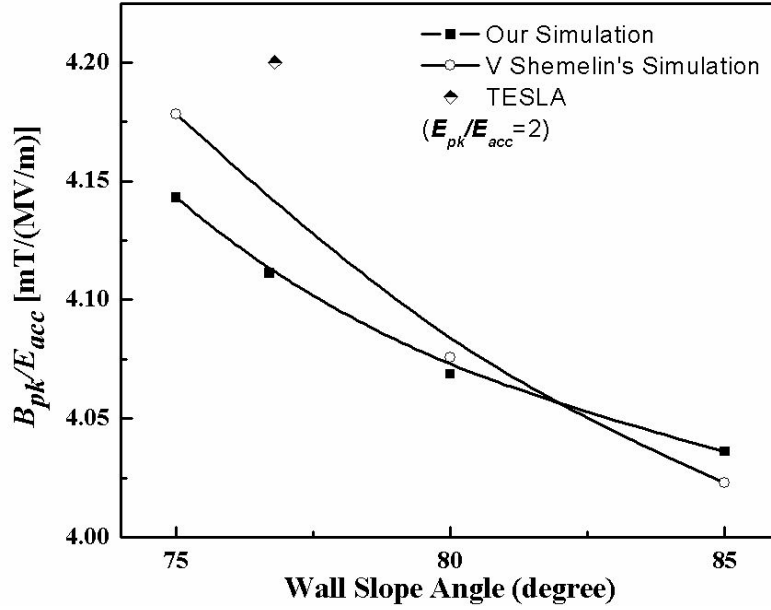


Figure 2.16: Optimized value of B_{pk}/E_{acc} as a function of wall angle α using (i) our step-by-step one dimensional optimization procedure, as well as (b) the conventional multi-variable optimization technique, for the **TESLA** design. Also here, we have shown the data point which correspond the design used for the **TESLA** project.

inappropriate to discuss the following point on the choice of the wall slope α for the three set of cavities. For the **TESLA** type elliptical cavity, α is a parameter which has a

profound influence on the accelerating gradient of a cavity. Cavities with larger value of α offers more gradient. And in the design of a cavity with $\alpha \geq 90^\circ$, *i.e.*, a reentrant type cavity, accelerating gradient will be more. However, for the multicell elliptical cavities, designed for the medium / low beta range, depending on β_g value, its length reduces, E_{pk}/E_{acc} value increases and effectively its acceleration efficiency reduces. Therefore, in order to increase the efficiency, there one plays with α and increase its value as large as possible. Again, for an elliptical cavity, the choice of α is dominated by the chemical cleaning and cavity fabrication view point. Realizing this tradeoff, in the $\beta_g = 0.61$ case, we set the value of $\alpha = 88^\circ$ based on the experience and feedback of the contemporary projects, and the cavity fabrication team. However, for the high beta cavities, acceleration efficiency is indeed not that bad because of the moderate or relatively small value of E_{pk}/E_{acc} , and the choice of α is a bit relaxed there. Therefore, for the $\beta_g = 0.9$, and 0.81 elliptical cavities, we choose $\alpha = 85^\circ$ and 85.45° , respectively.

Chapter 3

Study on Higher Order Modes (HOMs) and wake-fields in elliptic SRF cavities

If we want to push the value of the operating beam current limit up in a linear accelerator, then something unwanted, but interesting, happens there. For instance, beam becomes unstable beyond a threshold value of the current. Certainly, these phenomenon are very much troublesome from the operation point of view. In fact, such a occurrence plays a decisive role, and ultimately sets the limit on the high-energy, high-current operation of a frontier accelerator. However, many a times, such challenges also open up opportunities to learn, develop and widen the horizon of beam physics, and eventually push the state of the art accelerator technologies to a new level.

Typically, RF cavities in a linac are made to operate with their fundamental mode, *i.e.* the mode with lowest resonant frequency. Particles in a beam bunch gain energy while interacting with cavity fields developed in that electromagnetic mode.

In addition to the fundamental mode, in an accelerator, beam can generate and interact with higher order modes also. The higher order modes (HOMs) extract energy mostly from the beam. In fact not only thrive on the beam, but HOMs also act back on it leading to different beam instabilities. In some special circumstances, energy stored in these

modes may result in a significant heat load for the cryogenic cooling system of an SRF accelerator. Studies on HOMs, along with their effect on the electromagnetic performance of the cavity, and the resulting beam stability become therefore indispensable while designing a high power accelerator.

In the previous chapter, detailed methodology has been described for the design optimization of the medium and high β multicell elliptic SRF cavities for its operation in the fundamental ($\text{TM}_{010}-\pi$) mode. And in this chapter, we will explore the interaction between HOMs developed in those cavities, with the beam. First, we will analyze HOMs supported in these elliptical cavity geometries, and then we will explore the impact of wakefield, which is yet another aspect of the beam cavity interaction.

3.1 Studies on HOMs in a multicell elliptic SRF cavity

An RF cavity can support a number of resonantly excited electromagnetic modes inside the cavity. The fundamental mode has typically the lowest resonant frequency among all of these modes, and rest of these modes are therefore called higher order modes or HOMs in short.

3.1.1 Classification of HOMs and other general considerations

Electric field, *i.e.*, the \mathcal{E} field and magnetic field, *i.e.*, the \mathcal{B} field lines in the fundamental mode configuration of an elliptic radio-frequency cavity preserve azimuthal symmetry around the cavity axis, which is usually the beam axis. In the fundamental mode, the axial component of the electric field $E_z(r, z, \theta, t)$ is the only non-zero electric field component inside the cavity, except at the iris location and near the beam pipe. There the other non-zero field component is the azimuthal magnetic field $B_\theta(r, z, \theta, t)$. In this context, here, we use the subscript z and θ to denote the axial and azimuthal field components, respectively. In the other modes, also falling in the TM category, magnetic

field components are non-zero only in transverse planes with respect to the axis of the cavity. However, field components may vary azimuthally in these TM type HOMs. Variation of electromagnetic fields in the azimuthal direction (*i.e.*, in θ) can be expressed in terms of $e^{im\theta}$, where, m is an integer such that its value may be 0, 1, 2 \dots , and $i = \sqrt{-1}$. Such modes can be expressed as TM_{m10} class, following the common nomenclature. In this nomenclature, $m = 0$ indicates modes, where electromagnetic fields show no variation in θ . Such modes are called the monopole modes. For example, the fundamental mode, *i.e.*, the TM_{010} mode developed in an elliptic RF cavity is a transverse magnetic monopole mode. Similarly, $m = 1$ modes are called the dipole modes. Contrary to the monopole modes, dipole modes do not produce any axial component of the electric field along the beam axis. Modes with $m = 2, 3$ or $4 \dots$ are known as the quadrupole, sextupole and octupole \dots modes, respectively. Similar classification is applicable for the transverse electric (TE) type modes also [65].

In the next subsection, we will study a very important and useful concept used in analyzing the effect of HOMs in a particle accelerator. This is called the **Panofsky-Wenzel theorem** [65], [79]. In fact, this theorem interestingly underlines that only the higher order monopole and dipole modes can significantly influence the dynamics of well collimated beam particles. In a well focused beam bunch, beam particles remain nearly confined within a small transverse size and divergence throughout the linac. Paraxial approximation therefore turns out to be an useful technique there to simplify the related calculations.

3.1.2 Energy exchange between beam particles and HOMs

Following equation describes Lorentz force experienced by a beam particle traversing through the electromagnetic environment of an RF cavity:

$$\mathcal{F} = \frac{\Delta p}{\Delta t} = q(\mathcal{E} + \mathbf{v} \times \mathcal{B}), \quad (3.1)$$

where, q and v are the respective charge and velocity of the beam particle. The change in energy $\Delta\xi$ introduced due to the change in momentum under the influence of this force on a beam particle can be written as, $\Delta\xi = m_0c^2\beta\Delta(\gamma\beta) = c\beta|\Delta p|$, where c is the speed of light in vacuum, and $\beta = |v|/c$.

3.1.2.1 Energy exchange with the on-axis field components:

In an RF cavity, we can calculate the total change in energy of a particle traversing along the cavity axis from Eq. 3.1 as [65],

$$\xi_{\parallel} = qV_{\parallel} = c\beta|\Delta p| = q \int_{s_i}^{s_f} \mathcal{E} \cdot d\mathbf{z} = q \int_{s_i}^{s_f} E_z dz, \quad (3.2)$$

where V_{\parallel} is the axial voltage developed in the cavity, as the particle traverses from the position s_i to s_f . These two positions s_i to s_f can be chosen far enough beyond the end walls of the cavity, where cavity fields get attenuated completely. In the above equation, V_{\parallel} represents effective voltage V_0 for a TM_{010} mode as it is described in Chapter 2. We have estimated there the shunt impedance R of the cavity from V_0 . Alike TM_{010} mode, shunt impedance as well as the parameter R/Q can also be identified as a figures of merit for higher order TM monopoles. Interestingly, except for the monopole mode, strength of the axial electric field is zero on the beam axis for all other higher order TM modes. Another category of modes, *i.e.*, the transverse electric or TE modes have no axial electric field components. Therefore, neither TE modes nor TM dipole modes ideally participate in this energy exchange with a well collimated on-axis beam.

3.1.2.2 Energy exchange with off-axis field components:

Depending on their electromagnetic field configurations, few modes in the RF cavity, can also produce transverse deflection of the beam particles. Such deflections are undesirable in the case of a typical accelerating cavity. Electromagnetic forces that deflect the beam particles from their axial position, yield a change in the transverse

momentum, and to calculate the amount of change introduced in the momentum, one can use Panofsky-Wenzel theorem.

Transverse R/Q calculation from Panofsky-Wenzel theorem [65], [79], [80]

While traversing through the electromagnetic environment of an RF cavity, a beam particle may experiences a change in its transverse momentum Δp_{\perp} , which can be obtained from the following equation:

$$\Delta p_{\perp} = \frac{q}{c\beta} \int_{s_i}^{s_f} |\mathcal{E} + \mathbf{v} \times \mathcal{B}|_{\perp} dz. \quad (3.3)$$

The above equation is derived based on the assumption that the change in velocities of the beam particles is insignificant within the cavity.

In the RF cavity, electromagnetic fields oscillate at the resonant frequency of the electromagnetic mode. There, the following expression of Δp_{\perp} can be derived for the beam particles traversing through the cavity, from Eq 3.3 using Panofsky-Wenzel theorem:

$$\Delta p_{\perp} = -\frac{iq}{\omega} \int_{s_i}^{s_f} d\mathcal{E}_{\perp} + \frac{iq}{\omega} \int_{s_i}^{s_f} \nabla_{\perp} E_z(r, z, \theta, t) dz. \quad (3.4)$$

In the above equation, \mathcal{E}_{\perp} denotes orthogonal component of the electric field of the electromagnetic mode developed in the cavity, resonating at an angular frequency ω . For good reason, therefore, in this formulation, the electromagnetic field components are assumed to have $e^{i\omega t}$ harmonic time dependence. We choose the two position s_i and s_f deep in the beam pipe, up to which all electromagnetic field components of corresponding mode completely get attenuated completely. Hence, omitting the first term from RHS, Eq. 3.4 can be written in the following simple form:

$$\Delta p_{\perp} = \frac{iq}{\omega} \int_{s_i}^{s_f} \nabla_{\perp} E_z(r, z, \theta, t) dz. \quad (3.5)$$

Equation 3.5 explains why neither the TE modes, nor the TM monopole modes can deflect

on-axis beam particles. It is because, only the TM dipole modes have non-zero $\nabla_{\perp} E_z$ on the cavity axis.

For the beam particles, change in the transverse momentum also indicates energy exchange between particles and corresponding electromagnetic mode. Therefore, similar to our earlier discussion on shunt impedance in the case of a monopole mode imparting acceleration to the beam particles, here also, one can introduced a figure of merit for the dipole modes producing transverse deflection of the beam particles in terms of transverse shunt impedance R_{\perp} . For azimuthally symmetric cavities, formula for R_{\perp}/Q of the n^{th} order dipole mode is given as follows:

$$\left. \frac{R_{\perp}}{Q} \right|_n = \frac{1}{\omega_n U_n} \left| \int_{s_i}^{s_f} \nabla E_z(r, z, \theta, t) \cdot d\mathbf{z} \right|^2. \quad (3.6)$$

Here the subscript ‘ n ’ denotes corresponding parameters of the n^{th} order dipole mode. This is the equation, which is followed by the computer code SLANS to calculates R_{\perp}/Q value for an electromagnetic mode developed in the given geometry of a cavity [78].

Based on the above discussion, mostly the TM type monopole as well as dipole modes can influence a well-collimated on-axis beam, and we may ignore the effect of all other modes on the beam in a cavity, except at both the ends, where those ‘other’ modes may have small axial field contributions. Now we present a brief discussion on the regenerative beam break up (BBU) instability [81], [82].

Regenerative beam break up instability and threshold current calculation:

With the increasing beam current in a linac, a threshold value is reached, such that beyond this limit, beam becomes unstable. This phenomenon was observed for the first time in late 1950’s during the development of linacs [83], [84]. Later, it was identified as regenerative beam break-up instability. The threshold current limits maximum obtainable beam power from a particular linac. A formula for the threshold current calculation was

derived by Wilson *et. al.* [85]. In fact, this work was an extension of the Backward Wave Oscillator analysis on TM₁₁₀ type dipole modes [85], [86]. More rigorous analysis was performed later by Gluckstern *et. al.* on the calculation of threshold current for a standing wave accelerating structure [87]. Following their work, we have performed a detailed derivation to understand BBU instability [88].

TM type dipole modes can be generalized in terms of Hybrid electromagnetic (HEM)₁₁ mode with x polarization. For these modes, using paraxial approximation, one can write the non-zero synchronous part of the space harmonic components of the electromagnetic field as [83], [84],

$$\begin{aligned} E_x &= \xi_x \sin(kz) \cos(\omega t), \\ E_z &= x \zeta_0 \cos(kz) \cos(\omega t), \\ H_y &= \mathcal{H}_y \cos(kz) \sin(\omega t). \end{aligned} \tag{3.7}$$

In the above expression, ω is the angular frequency and k is the wave vector of the corresponding electromagnetic mode, whereas ξ_x , ζ_0 and \mathcal{H}_y are the amplitude of the respective field components. In the electromagnetic theory, it is a common practice to represent the electromagnetic field components by complex number. Accordingly we can write the z -component of the electric field as

$$\xi_z = x \zeta_0 \cos(kz) e^{i\omega t}, \tag{3.8}$$

such that $E_z = \mathcal{R}e\{\xi_z\}$.

From Panofsky-Wenzel theorem, one can formulate the following equation for describing the trajectory of a beam particle traversing through the electromagnetic field of a higher order dipole mode excited in a cylindrically symmetric RF cavity:

$$\mathcal{X}_0(z) = \frac{iq}{\omega} \int_0^z \frac{dz'}{p_z(z')} \int_0^{z'} \frac{\partial \xi_z}{\partial x} dz''. \tag{3.9}$$

In the above expression, p_z is the momentum in the z direction. Here, the real part of

$\mathcal{X}_0(z)$ represents the transverse position $x_0(z)$ of the particle. The off-axis beam particles experience non-zero E_z field of a dipole mode and exchange energy with the field and the dipole mode get energized. Such energetic dipole mode then provides stronger transverse kick to the beam particles and pushes them more and more off axis. In this positive feedback process, the amount of power P_{beam} swapped from the beam to a dipole mode can be calculated as follows:

$$P_{beam} = -I_b \int_0^L E_z(x = x_0(z), y, z, t) dz = -I_b \int_0^L x_0(z) \frac{\partial E_z(x, y, z, t)}{\partial x} dz, \quad (3.10)$$

where, I_b is the beam current, and L is the total axial length of the structure. Here the negative sign indicates that we are calculating the power lost by the beam.

In order to evaluate the above expression (*i.e.*, Eq. 3.10), we require a closed form expression of $x_0(z)$ and $\partial E_z/\partial x$ explicitly in terms of the variable z . Therefore, let us rewrite the term $\partial \xi_z/\partial x$ replacing t with $t_0 + z/\beta c$ as

$$\frac{\partial \xi_z(x, y, z, t)}{\partial x} = \frac{1}{2} \zeta_0 (e^{ikz} + e^{-ikz}) e^{\frac{i\omega z}{\beta c}} e^{i\omega t_0}, \quad (3.11)$$

where t_0 indicates *the time* at which the particle was at the entrance of the cavity. Also we have considered the entrance of the cavity coinciding with $z = 0$.

In Eq. 3.11, the wave vector k can be written as $k = \omega/v_p$, where v_p denotes the phase velocity of the electromagnetic wave of the corresponding dipole mode. It can be argued that in this energy exchange process, the contribution of the second term alone in the RHS of Eq. 3.11, will be significant when synchronism (or near synchronism) is achieved between the velocity of the particle and phase velocity of the wave. Accordingly, the above equation can be approximated as

$$\frac{\partial \xi_z}{\partial x} = \frac{\zeta_0}{2} e^{-i(\delta\beta)z} e^{i\omega t_0}, \quad (3.12)$$

where $\delta\beta = 1/v_p - 1/\beta c$. Substituting Eq. 3.12 in the equation of \mathcal{X}_0 , we obtain

$$\mathcal{X}_0(z) = \frac{iq}{\omega} \int_0^z \frac{dz'}{p_z(z')} \int_0^{z'} \frac{\zeta_0}{2} e^{-(\delta\beta)z''} e^{i\omega t_0} dz''. \quad (3.13)$$

In the light of the above discussion, it is clear that both of these complex quantities in Eq. 3.13 have $e^{i\omega t_0}$ dependence, where the initial time t_0 will be different for different particles in the beam, as because they will enter the cavity with different initial phases. Therefore, to estimate the total amount of power lost by the beam, it is required to take average over all t_0 in the calculation. And finally we need to substitute real values of the two quantity $\mathcal{X}_0(z)$ and $\partial E_z/\partial x$ in Eq. 3.10 to calculate P_{beam} . Multiplying the complex conjugate of the first quantity, *i.e.*, $\mathcal{X}_0^*(z)$ with second one, then dividing by 2 and taking the real part, we obtain the following form of the expression for P_{beam} :

$$P_{beam} = -i \frac{qI_b \zeta_0^2}{8\omega p_z} \Re e \left[\int_0^L dz \int_0^z dz' \int_0^{z'} dz'' e^{i\delta\beta(z-z'')} \right], \quad (3.14)$$

and after performing few more mathematical steps, finally we derive

$$P_{beam} = \frac{qI_b \zeta_0^2 L^3}{2\pi^3 \omega p_z} g(\psi). \quad (3.15)$$

In the above equation (Eq. 3.15), $g(\psi)$ represents the degree of synchronization between the velocity of a beam particle and the phase velocity of the electromagnetic wave established because of a respective dipole mode. Following this formulation, one can explicitly show that $g(\psi) = \frac{1}{2} \left(\frac{\pi}{\psi} \right)^3 \left(1 - \cos \psi - \frac{\psi}{2} \sin \psi \right)$, where $\psi = L \left(\frac{1}{v_p} - \frac{1}{\beta c} \right)$.

Like the other electromagnetic modes, these dipoles also loose part of there power P_c dissipated on the metalic wall of the accelerating structure, and from this Ohmic heat loss, we can calculate the transverse shunt impedance R_\perp for the respective mode as

$$R_\perp = \frac{1}{P_c} \left[\int_0^L dz \frac{\partial E_z}{\partial x} \right]^2 = \frac{1}{P_c} \left[\int_0^L \zeta_0 \cos(kz) e^{i\omega t} dz \right]^2. \quad (3.16)$$

Above equation as well shows the dependency between the transverse shunt impedance R_{\perp} of a dipole mode and the speed of the beam particle. From the above equation, following expression for P_c can be obtained

$$P_c = \frac{1}{4} \frac{\zeta_0^2 L^2}{R_{\perp}}. \quad (3.17)$$

Here, we want to mention that the transverse shunt impedance is calculated at the phase velocity of the dipole mode.

Summarizing we can say that the dipole mode gains energy from the beam and simultaneously it also loses its energy in the form of Ohmic heat dissipation on the cavity wall. Therefore, the respective mode (dipole) will grow only when P_{beam} of the mode becomes more than P_c . Hence, equating P_{beam} and P_c , we can calculate a threshold value of the beam current I_{th} , above which the dipole will grow and beam will become unstable. The expression for threshold beam current is obtained as

$$I_{th} = \frac{\pi^3 \times (cp_z) \times k \times \beta}{2q \times g(\psi) \times \frac{R_{\perp}}{L} \times L^2}. \quad (3.18)$$

In the above formulation, we presumed that a respective dipole mode will lose energy only because of Ohmic heat dissipation on the cavity wall. In this regard, we must point out that the scenario may change significantly if we take into account of the contribution of HOM couplers in the design. Strength of the HOMs (including dipoles) established in the cavity will be radically reduced because of the out coupling of power in presence of HOM couplers. As a consequence, threshold values of the beam current may improve significantly.

As mentioned earlier, the above mechanism acts like a positive feedback process, *i.e.*, with the increasing beam current ultimately the dipole mode will be strong enough to kick the beam in such a way that the beam will hit the cavity chamber and will be lost. This is called regenerative beam breakup instability, and to avoid such instability for a

pulsed linac, the *cw* average current needs to be smaller than the threshold current given by the above formula [88]. This calculation will be very important for the accelerators dedicated for ADS application, whereas the accelerators designed for SNS application, regenerative BBU instability may not be that much vulnerable.

At the end of this discussion, we want to highlight that the phenomenon of regenerative BBU is associated with single cavity, whereas in the case of multiple cavities, stacked one after another, there the cumulative contribution of the individual cavities will decide the ultimate deflection of the beam. Such mechanism may generate another type of beam break-up instability, known as the cumulative BBU instability. Both monopole and dipole HOMs may get induced because of this cumulative beam break-up [65]. Cumulative BBU shows profound dependence on the temporal signature of the beam bunch as well as their charge, which shows saturation in the case of a sufficiently long beam bunch (in time), and then the threshold current remains nearly unchanged. As it is shown in Refs. [89] and [90], threshold current corresponding to the cumulative BBU instability is sufficiently large in the case of typical accelerators dedicated for SNS. Therefore, we did not calculate threshold current corresponding to cumulative BBU for the ISNS elliptic cavities.

Along with this, we have also calculated the resonantly excited heat generation and the corresponding heat load due to collective contribution of monopole HOMs. It will be presented in the later part of this chapter.

3.2 HOMs in the medium and high β elliptic cavities

Ideally, an RF cavity supports infinite number of HOMs, along with the fundamental mode. However, beam pipes attached to its both ends, act as waveguides for the electromagnetic modes excited in the cavity geometry. This defines an upper cutoff frequency for a particular cavity geometry. Modes having frequency more than this

cutoff frequency f_c starts travelling through the beam pipe.

Such cutoff is determined by the beam pipe radius. For a cylindrical beam pipe, f_c is decided by the resonant frequency of a TE_{11} mode. However, some of the cavity modes having frequency even more than this cutoff still may remain inside because of their field configurations. Hence, we performed the HOMs analysis for our medium and high beta elliptic cavities, up to the cutoff frequency of the TM_{11} mode in the beam pipe.

HOM analysis were performed for all the three families of 650 MHz, multicell elliptic SRF cavities. However, we will describe our analysis, along with the simulated results, mainly obtained using $\beta_g = 0.61$, 650-MHz, 5-cell cavity. For this cavity, beam pipe radius is 44 mm. Accordingly, the cutoff frequencies corresponding to the TE_{11} and TM_{11} modes, are ~ 2 GHz and ~ 4.2 GHz, respectively. Hence, HOM analysis was performed up to 4.2 GHz frequency.

3.2.1 Higher order monopole modess in the multicell elliptic cavities

For the monopole mode, an important figure of merit is the parameter R/Q . This parameter primarily quantifies “efficiency of acceleration per unit stored energy” of the fundamental mode, as described in Chapter 2. In the cavity, a higher order monopole mode with high R/Q value, may turns out be a potentially dangerous HOM. Therefore, we have analyzed all monopole modes in the cavity up to the cutoff frequency f_c . We described this analysis and elaborate the simulated results obtained using $\beta_g = 0.61$, 650 MHz 5 cell cavity geometry.

Simulation shows the presence of three pass-bands in this multicell geometry up to frequency $f_c = 4.2$ GHz. Among them, the first one corresponding to the fundamental mode (TM_{010} mode), has been described in the previous chapter. In this $\beta_g = 0.61$ cavity geometry, highest R/Q value was obtained as about 354Ω for the π -mode configuration at $\beta = 0.65$. In this context, we want to recapitulate that these cavities will be used for range

of β - from ~ 0.51 to ~ 0.76 . We have calculated an approximate value of the cell-to-cell coupling coefficient $\kappa_c = 0.8\%$.

For the second pass band, calculated R/Q values were considerably small compared to the values obtained for the π or $4\pi/5$ mode of the first pass band. Cell-to-cell coupling coefficient κ_c for this pass band was obtained to be approximately 1.65%.

The third pass band shows an approximate $\kappa_c = 0.74\%$, which is the smallest value of the cell-to-cell coupling coefficient among the three pass bands. Interestingly, such small κ_c may indicate the likelihood of a mode configuration trapped within the multicell cavity geometry. With this anticipation, a thorough analysis was carried out for all five modes of this third pass-band. Calculated R/Q of the constituent modes of this pass-band are shown in Fig. 3.1, as a function of β . The mode resonating at 1653.2 MHz frequency shows a gradually increasing pattern of R/Q with increasing β , which approaches a value $\sim 20 \Omega$ at about $\beta = 0.76$. To verify if the mode is trapped, the axial electric field values of this mode is plotted along the length of the multicell cavity in Fig. 3.2. As it appears in the figure, the overall field amplitude shows maximum near the middle of cavity and falls gradually as we move towards the cavity ends, and its values significantly drops near the cavity end. Couplers are usually located on the beam pipe in a multicell SRF cavity, and such a coupler can not efficiently out-couple the above mentioned trapped mode from the cavity. Therefore, such confined field configuration of the corresponding HOM evidently indicates the trapped nature of the mode.

Trapped mode analysis and final optimization of the end-cell:

Any trapped mode can be categorically classified as the mode with poor field flatness. As addressed in Chapter 2, good field-flatness for a mode can be achieved and restored typically by tuning the individual end-cells of the cavity. However, the implementation is a little tricky here - since a good field-flatness must always be kept ensured for the fundamental mode. To meet these two simultaneous requirements, one end-cell of the

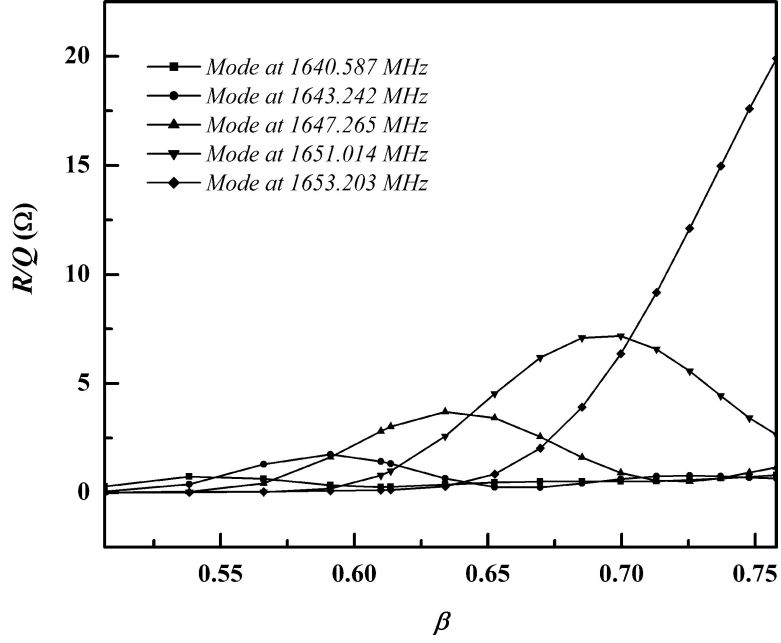


Figure 3.1: Plot of R/Q of the monopole modes as a function of β , for the five modes of the third pass-band.

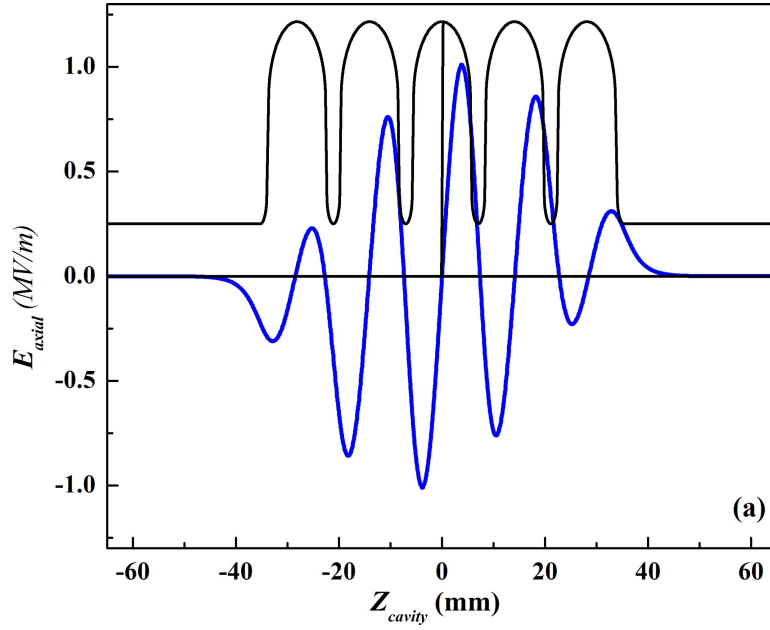


Figure 3.2: Plot of the axial electric field amplitude along the length of the cavity, for the HOM at 1653.2 MHz in this unmodified geometry.

cavity is fine-tuned to resonate at a frequency of 650 MHz for the fundamental mode, as well as for the trapped mode oscillating at a frequency 1653.2 MHz. Accordingly, corresponding end half-cell dimension is adjusted iteratively by tuning the end half-cell length L_e and the semi major axis A_e .

In Fig 3.3, we plot the axial electric field amplitude along the cavity length, obtained from simulation performed with the modified cavity geometry. This figure clearly shows a shifting of the field amplitude towards one end of the cavity. This confirms that the mode is no longer trapped inside the cavity, and because of the axially shifted field configuration, it will be possible to out-couple this mode with the HOM coupler.

In Figs. 3.4(a) and 3.4(b), field contours obtained in the modified end-cell geometry are shown for the operating mode, resonating at 650 MHz, as well as for the HOM resonating at 1653.2 MHz. In this modified geometry, the values of L_e and A_e were found to be 71.24 mm and 52.12 mm, respectively. Geometric parameters of this modified end half-cell, i.e., “End Cell (A)” are summarized in the table 3.1, along with the other (unmodified) end half-cell i.e., “End Cell (B)”.

Table 3.1: Optimized geometric parameters for the modified end half-cell.

Parameters	End Cell-A	End Cell-B	Unit
R_{iris}	44.000	44.000	mm
R_{eq}	195.59	195.59	mm
L	71.240	71.550	mm
A	52.120	52.640	mm
B	55.550	55.550	mm
a	15.280	15.280	mm
b	28.830	28.830	mm

3.3 Dipole HOMs in the multicell elliptic SRF cavities

Higher order dipole modes were simulated and analyzed up to a frequency of 4.2 GHz in the $\beta_g = 0.61$, 650-MHz, 5-cell cavity geometry. We found four dipole passbands below 4.2 GHz in this geometry. This analysis was also performed within the range of β values for which these cavities will be operated. We have used the computer code SLANS to perform this analysis.

Among these passbands, we found that the corresponding modes of the first passband

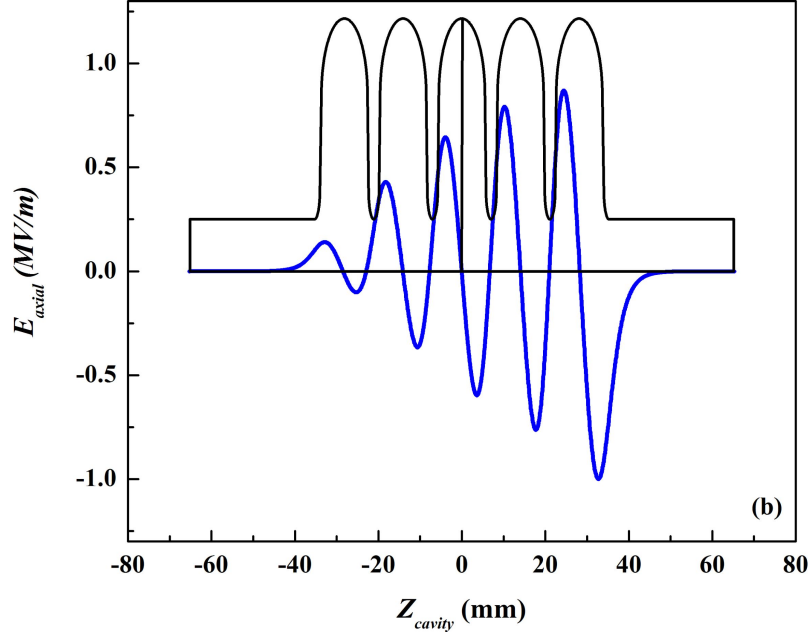


Figure 3.3: Amplitude of the axial electric field of the mode at 1653.2 MHz along the cavity length, for the geometry with modified end cell at one side.

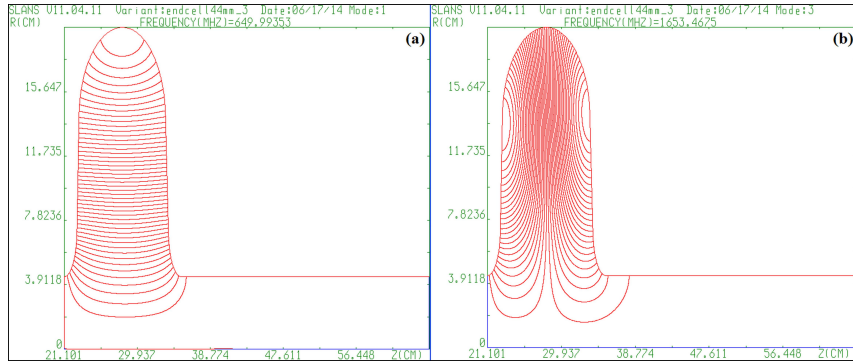


Figure 3.4: Plot of (a) field contour for the fundamental mode at 650.0 MHz, and (b) field contour for the HOM at 1653.2 MHz, for the modified end-cell.

were the most prominent. The dipole mode resonating at 961.98 MHz frequency shows highest value of $R_{\perp}/Q \approx 4.43 \times 10^4 \Omega/m^2$ at $\beta = 0.76$. For this first passband, Fig. 3.5 represents the values of R_{\perp}/Q as a function of β . The detailed parameters of few prominent dipole modes with significant R_{\perp}/Q values are summarized in Table 3.2.

Here we must emphasize that the code SLANS calculates dipole modes considering the cavity wall as PEC (perfect Electrical Conductor). SLANS then performs post-processing, where wall loss is calculated using the property of copper (Cu), and accordingly the code calculates the value of the quality factor Q . As we know, Q

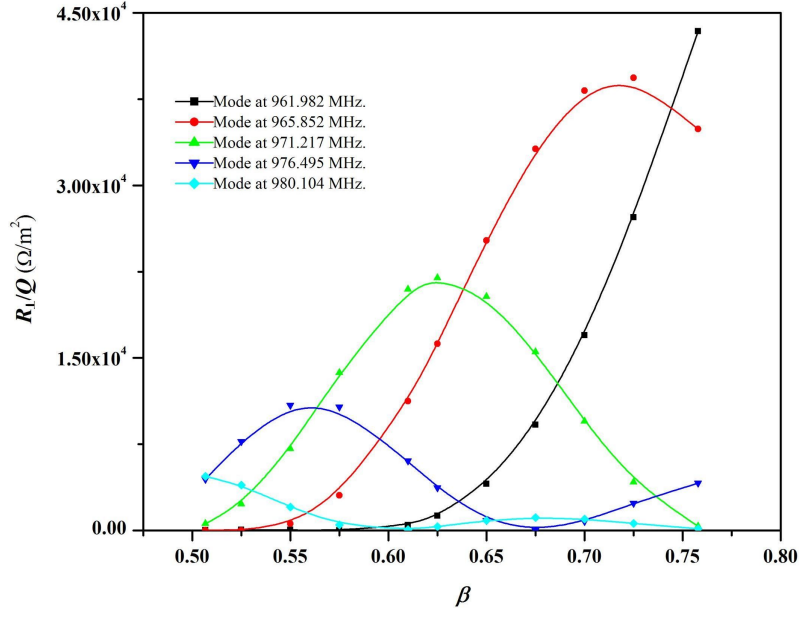


Figure 3.5: R_{\perp}/Q values of five dipole modes of first passband plotted as a function of β .

depends inversely on the surface resistance of the cavity material. Therefore, we have reprocessed the Q values multiplying with a scale factor $R_s|_{Cu}/R_s|_{Nb}$ to obtain the correct value of the quality factor for the Nb SRF cavities. Here $R_s|_{Cu}$ and $R_s|_{Nb}$ represents the surface resistance of copper and niobium respectively and the values were calculated at the corresponding dipole mode frequencies.

Regenerative BBU and the threshold current calculation:

As discussed earlier, calculation of the threshold current I_{th} for the excitation of regenerative BBU instability constitutes an important part of the design of a high average power linac.

We have obtained the details of all dipole modes up to the frequency 4.2 GHz from SLANS simulations. As it is shown in Eq. 3.18, threshold current calculation also requires the phase velocities v_p values of the corresponding dipole modes. Therefore, we have plotted dispersion diagram for the first few dipole-pass bands in the figure 3.6. Phase velocity of the corresponding mode was calculated from there.

Values of the corresponding mode frequency were obtained directly from SLANS

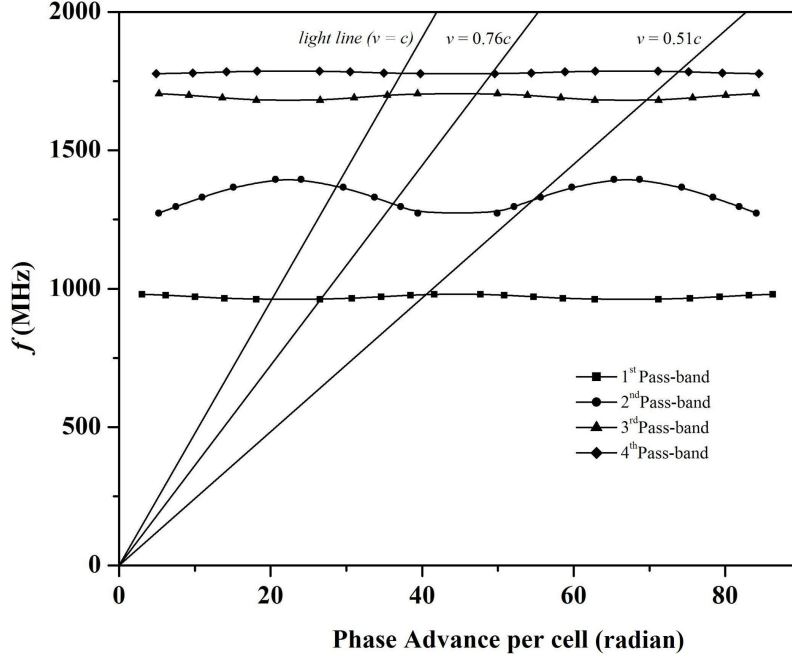


Figure 3.6: Dispersion diagram for the first four dipole passbands is shown here. Mode frequencies are plotted with respect to the corresponding values of phase advance per cell.

simulation. However, calculation of the phase advance per cell ϕ (say) is not straight forward. We have calculated the same following the procedure given in Ref. [91], using the following formula,

$$\cos(\phi) = \frac{E_z(r, z + L_{cell}) + E_z(r, z - L_{cell})}{2 \times E_z(r, z)}. \quad (3.19)$$

where we considered $E_z(r, z) = e^{i\phi} E_z(r, z + L_{cell})$ based on Floquet condition [65] for an infinitely periodic structure.

It is important here to note that the on-axis axial electric field $E_z(r = 0, z)$ is zero for a dipole mode. Hence, to estimate ϕ from the above expression, we have considered $E_z(r, z)$ values at a slightly off-axis position ($r \sim 1$ mm). The $\beta_g = 0.61$ cavities will be operated for the β values ranging 0.51 to 0.76. Therefore, in this dispersion diagram, the modes located in between the lines $v = 0.76c$ and $v = 0.51c$ may show high probability of interaction with the beam. Hence, we perform the threshold current calculation for these selected modes only. Threshold current values calculated for the corresponding dipole

modes are given in the Table 3.2. From calculation, we found that for the dipole mode resonating at 965.85 MHz, the value of I_{th} will be minimum, which is around 0.5 mA. This is less than the designed *cw* average beam current of 1 mA in our case¹.

Figure 3.7 shows the dependence of $g(\psi)$ as a function of β for the most prominent dipole mode, resonating at 965.85 MHz. Also for this mode the variation of I_{th} is plotted as a function of β in Fig. 3.8.

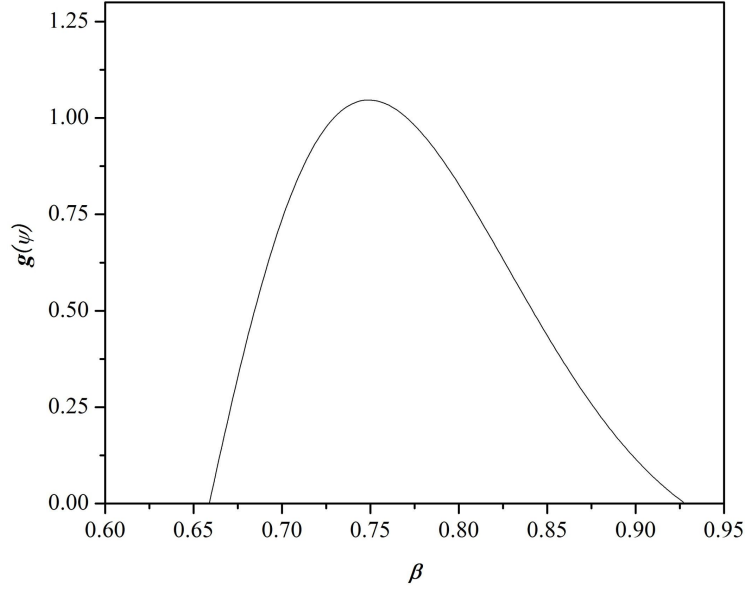


Figure 3.7: Here $g(\psi)$ values plotted as function of β for the dipole mode resonating at 965.85 MHz.

Table 3.2: Few prominent dipole modes supported in the $\beta_g = 0.61$ cavity geometry. Here, β_m indicate β value at which corresponding m^{th} dipole shows the maximum R_{\perp}/Q value.

Mode frequency f (MHz)	β_m	Q	R_{\perp}/Q Ω/m^2	I_{th} (mA)
961.98	0.760	2.165×10^{10}	44314	0.805
965.85	0.659	2.229×10^{10}	28280	0.516
971.22	0.588	2.335×10^{10}	16987	0.570
976.50	0.532	2.465×10^{10}	8869.0	0.779
980.10	0.494	2.574×10^{10}	4606.5	1.18
1296.3	0.731	2.165×10^{10}	19224	1.86

We would like to emphasize that in this calculation, we have assumed the total HOM power confined within the cavity only. In a realistic scenario, there will be a fair chance

¹In this calculation, we took a value of 10 n Ω residual resistance for the cavity material. More details on residual resistance is will be described in Chapter 5.

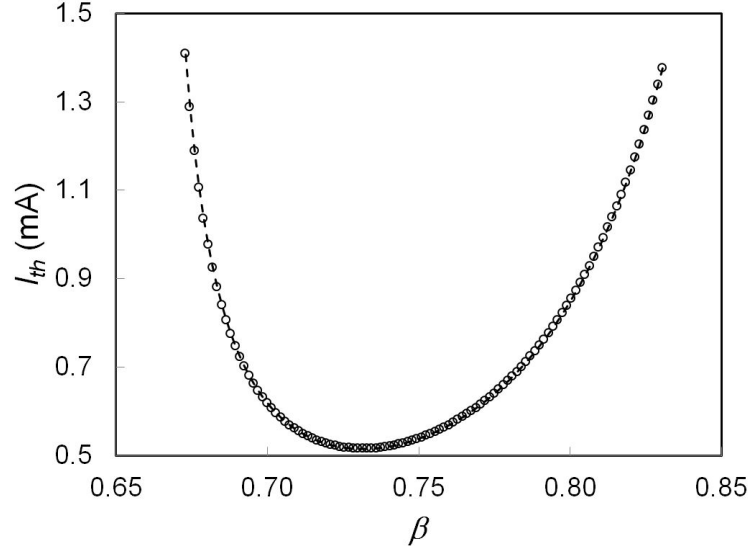


Figure 3.8: Threshold current values are plotted as a function of β for the dipole mode resonating at 965.85 MHz.

of the partial reduction of this HOM power in presence of beam pipes and other coupler ports. Even, addition of the fundamental mode power coupler may change the scenario significantly, and augmentation of any coupler in the design will profoundly increase the threshold value of the beam current for the regenerative BBU instability. Considering all these aspects, in future, we will assess whether inclusion of a dedicated HOM coupler is required to achieve the desired value of the of the threshold beam current.

As we saw in the preceding section, it is the beam which excites higher order modes in an RF cavity, and sometimes, if favourable conditions are fulfilled, these modes may gain energy cumulatively and become stronger. Energy stored in these modes develops HOM fields in the cavity. These HOM fields are also called retarded or wakefields, as because most of the cases they interact with following beam bunches. Some of these wakefield interactions will be studied in the next section.

3.4 Wakefield analysis of multicell elliptic SRF cavities

Particles in a beam bunch interact with each other, as well as with their image charges

(currents) developed on the wall of the vacuum chamber. The first type of interaction is typically between the particles within the beam bunch itself, and is known as the *space-charge effect*; whereas, in the second type, electromagnetic field generated by the beam, produces a retarded action on the tail particles of the same beam bunch or the beam bunches traveling down the linac, and is known as the *wakefield*. Depending on their phases, trailing particles or bunches may get acceleration or deceleration due to the wakefield, which results in an energy spread in the beam bunch. In addition, wake energy may produce Ohmic dissipation on the cavity wall, and thus may add to the cryogenic heat load².

3.4.1 Calculation of the wake Loss factor in these SRF cavities

As we have already explained, beam-cavity interaction is the source of the wake-energy. If a point charge q loses U_n amount of energy into the n^{th} mode of an empty cavity mode, following Ref. [55] we can write

$$U_n = k_{n0} q^2, \quad (3.20)$$

where the parameter k_n is known as loss factor, which quantifies the amount of energy lost by a point particle of unit charge. For the n^{th} order monopole HOM, the loss parameter k_{n0} can be explicitly written as $k_{n0} = \omega_n R|_n / 4Q_n$, where ω_n , $R|_n$ and Q_n represent angular frequency, shunt impedance and quality factor, respectively, for the monopole mode. Note that, $R|_n$ is calculated for the speed of the charge particle.

In the above formulation, k_{n0} is defined for a point charge. However, following the formulation given in Ref. [55], we can obtain a modified form of the formula for loss

²Please note that, the calculations presented in this section, were performed considering 0.4 mA *cw* average beam current in the linac, which corresponds to ≈ 18.9 pC charge per micro-bunch. It was the earlier design specification of the ISNS linac. However, as mentioned, in the present design, the *cw* average beam current is increased to 1 mA, which corresponds to ≈ 47.25 pC charge per micro-bunch. Although, with this specification, procedure described in this section will remain unchanged but, few results presented in this section, particularly where the charge (of a micro-bunch) is used, should be scaled accordingly.

factor of a Gaussian beam bunch as

$$k_n = k_{n0} \times e^{-(\omega_n^2 \sigma^2)/(\beta^2 c^2)}, \quad (3.21)$$

where σ is the *rms* length of the Gaussian beam bunch. We define an integrated loss factor \mathcal{K} which is summed-over all k_n values.

As discussed previously, shunt impedance R of a mode becomes dependent on the velocity of the beam particle via transit time factor. Therefore, the loss factor also shows a strong dependence on β . The conventional wake field solver code ABCI [92] can calculate the loss factor only for the cases where $\beta \sim 1$. However, the respective β values at the entrance and exit of the elliptic cavity sections of the linac, will be around 0.51 to 0.87. Therefore, ABCI simulation will not be able to predict the loss factor for these cavities accurately. Hence, we have developed the following alternative way.

As the name suggested, integrated loss factor \mathcal{K} can be estimated by summing up the loss factors of the individual HOMs [93]. Based on it, we have developed a semi-numerical method.

In Chapter 2, we defined shunt impedance of a cavity as $R = ZT^2(\beta)$, where $Z = (E_0 L)^2 / P_c$ is a quantity independent of β . First we have obtained the values of Z and Q for each of the monopole modes from SUPERFISH simulation. In the next step, the variation of the transit time factor T with β was obtained from the same code. From Z and beta dependent transit-time factor $T(\beta)$, R/Q values were calculated for different β values using Eq. 3.21. This exercise was repeated for nearly 200 monopole modes. Finally, the integrated loss factor was calculated from the summation of the individual k_n at each β values. Fig. 3.9 shows the integrated loss factor \mathcal{K} plotted as a function of β as a blue colored continuous line. The other smooth lines represent total loss factor for the first, second and third monopole pass bands, respectively. From the calculation we found $\mathcal{K} \approx 2.6$ V/pC at $\beta \sim 1$. We have also simulated the same structure, using the code ABCI

to verify this result at $\beta \sim 1$. Result obtained using ABCI is shown in Fig. 3.10. We found \mathcal{K} values at $\beta \sim 1$, calculated using these two techniques are comparable.

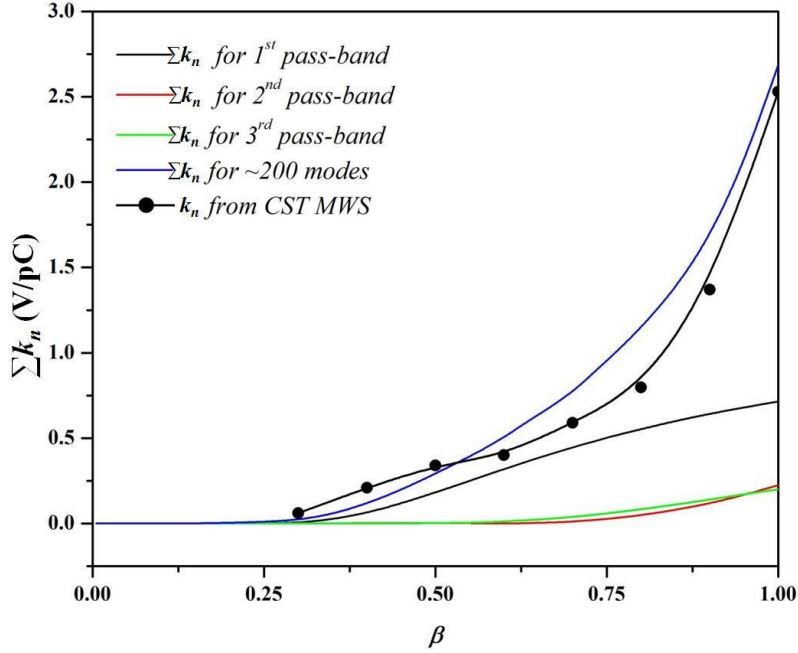


Figure 3.9: Integrated loss factor $\mathcal{K} = \sum k_n$ is plotted as a function of β . The blue line here is generated by summing over the individual loss factors of ~ 200 modes.

Using three-dimensional electromagnetic solver software CST-PS [94], calculation of \mathcal{K} is little involved for the $\beta \leq 1$ cases. For $\beta \leq 1$ cases, space-charge effect is also very much prominent along with the wakefield effect. These two effects cannot be handled separately by the wakefield solver of CST-PS. Therefore, following post-processing [95] is required there to calculate the value of \mathcal{K} .

Effect of space charge remains associated with the beam throughout the linac, whereas wakefield confines mostly within the cavity geometry. Based on this fact, two consecutive simulations were performed using the wakefield solver available with CST-PS for two different cases. These two cases correspond to two geometries of the same cavity connected to the beam pipes having small differences in their length. It is expected with a little approximation that the total space charge effect will be proportional to the cavity length, and it will be different for the two cases. On the other hand, the effect associated with the wakefield would remain same in both of these

geometries. From the two simulated results, contribution associated with the wakefield alone was calculated following the procedure given in Ref. [95] and the calculated values are shown in Fig. 3.9. Also, these values agree with the results we obtained using SUPERFISH and ABCI. We found that the value of \mathcal{K} at $\beta \sim 0.61$ is approximately 0.531 V/pC from Fig. 3.9.

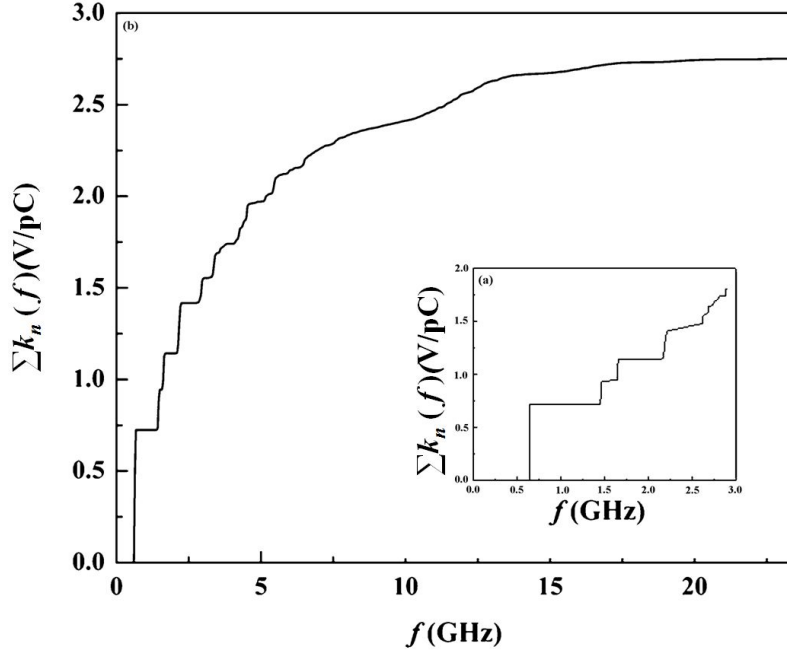


Figure 3.10: Integrated loss factor $\mathcal{K} = \sum k_n$ as a function of the frequency f , calculated (a) following semi-numerical method for $\beta \rightarrow 1$, and (b) calculated using ABCI, for a beam bunch with Gaussian distribution of rms bunch length $\sigma \sim 5$ mm.

3.4.2 Parasitic heat loss and the calculation of the wake potential

Part of the energy in the wakefield may produce parasitic heat loss, and in that case, such loss will be an added heat load dissipated on the surface of the cavity along with the regular head load of the operating mode. Therefore, this will also be an added load to the cryogenic plant. The total power P_0 deposited as parasitic heat load can be calculated as

$$P_0 = N_0 \times q^2 \times \mathcal{K}. \quad (3.22)$$

In the above equation, N_0 denotes the number of micro-pulses per second, and

$q = 18.9$ pC is the total charge of a micro-bunch. Hence, for $\mathcal{K} = 0.531$ V/pC, we estimated the dissipated cw average power as 0.4 mW. Here, we assume that wake-fields from different micro-pulses are adding incoherently within a macro-pulse. This assumption will be appropriate in case the frequency of a significant HOM supported in the cavity is neither an integral multiple of micro-pulse repetition rate, nor of midi-pulse repetition rate. The rate of heat loss becomes significantly large if one or more HOMs has their frequency as integral multiple of the micro bunch repetition rate. We conclude this section by presenting the calculation of the energy spread in the beam bunch, introduced by the wakefield.

Figure 3.11 shows wake-potential $W(s)$ developed in a $\beta_g = 0.61$ cavity. We used CST-PS wakefield solver to calculate $W(s)$ [95]. We calculated maximum energy spread $\delta\xi$

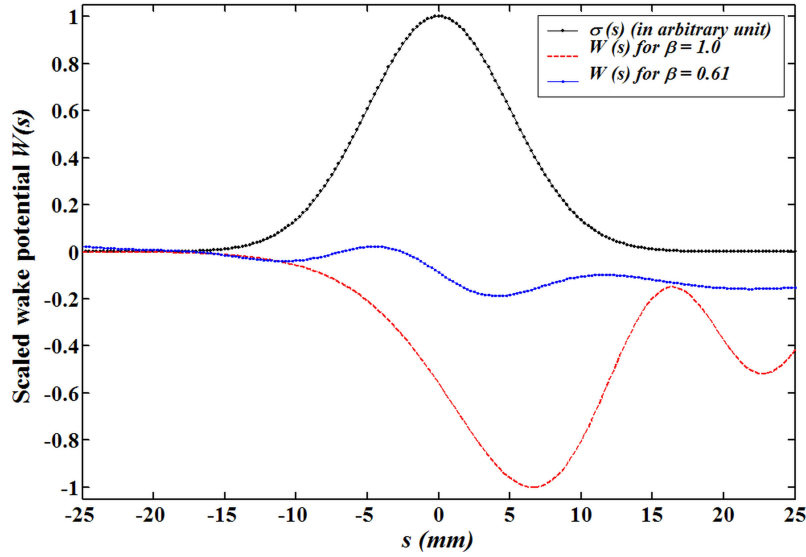


Figure 3.11: Longitudinal wake potential generated by a Gaussian bunch having 1 pC charge passing through the optimized 5-cell cavity.

induced in a single beam bunch due to wakefield using the formula give in Ref. [96]:

$$\delta\xi = -q \sqrt{\int ds \times \rho(s) \times W^2(s) - \mathcal{K}^2}, \quad (3.23)$$

where $\rho(s)$ represents normalized line charge density and s is the distance from the bunch centre. From Fig. 3.11, we observe that the $W(s)$ at $\beta = 0.61$ is less compared to the

$W(s)$ calculated for the $\beta = 1$ case. We obtain $\delta\xi = 6.53$ eV from the above equation. The typical energy gain for a single $\beta_g = 0.61$ 5-cell cavity is ~ 11 MeV. Therefore, the relative spread in the beam energy due to wakefield will be negligible. In the next sub-section, we will calculate the parasitic heat load due to resonant excitation of HOMs.

3.4.3 Heat load due to resonant excitation of HOMs

The beam has a multiple time-structure in a typical hadron linac. The time-structure of the beam in the proposed ISNS linac is shown in Chapter 1 (in Fig. 1.2). Details of the time structure are summarized here in the Table 3.3. For the ISNS, macro-pulse train will repeat with a PRR of 50 Hz. Inside the macro-pulse, there will be a train of midi-pulses repeating with a frequency of 1 MHz and within the midi-pulse, there will be the pulse train of 325 MHz micro-pulses.

Following the procedure given in Ref. [97], Fourier series representation of this typical time structure was calculated, and it is shown in Fig. 3.12. In case a cavity mode frequency coincides with any of the frequency component present in the Fourier spectrum of the beam, fields in that particular mode will add coherently from each of the beam bunch, traversing through the cavity. Fourier coefficient corresponding to the frequency component decides the fractional beam energy gained by the mode. In a real cavity, energy in the mode will decay through Ohmic heat dissipation, as well as being out coupled through beam pipe / coupler. However, if the corresponding Fourier coefficient is sufficiently strong, energy will build up in the mode, depending on the energy decay rate.

In a loss free cavity, an on-axis Gaussian micro beam bunch will excite n^{th} monopoles HOM with the following induced voltage:

$$V_q = \frac{\omega_n R}{2Q_0} q e^{i\omega_n t} = \bar{V}_q e^{i\omega_n t}. \quad (3.24)$$

Table 3.3: Beam time structure for the ISNS injector linac

Time Spacing between micro-bunches, $T_{\mu b}$	3.07 ns (325 MHz)
Midi-pulse period, T_m	1 μs (1.0 MHz)
Midi-pulse gap length, T_{mb}	0.65 μs (1.0 MHz)
Average current in T_{mb}	~ 6 mA
Macro-pulse period, T_M	20 ms
Macro -pulse gap length, T_{MG}	18 ms
Number of micro-bunches in one mid-pulse, N	211
Number of mid-pulses in one macro-pulse, M	2000
Average current in, T_M	0.40 mA

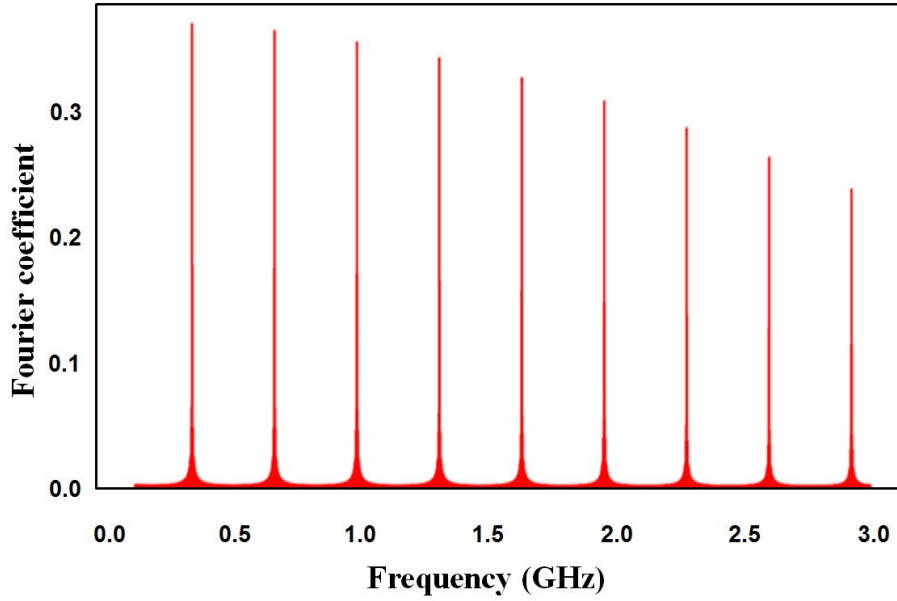


Figure 3.12: Fourier components of ISNS beam pulse and the coefficients at different frequencies.

Considering an external quality factor Q_{ext} for the n^{th} HOM, we can calculate the decay time constant $T_d = 2Q_{ext}/\omega_n$. Note that, the decay time constant will depend on the total quality factor Q_{tot} of the cavity assembly, and in presence of couplers, $Q_{tot} = (Q_0^{-1} + Q_{ext}^{-1})^{-1}$. As we know, for a superconducting cavity $Q_0 \gg Q_{ext}$. Therefore, for an SRF cavity assembly, Q_{tot} will become approximately equal to the Q_{ext} . With this decay time, an expression for the net induced voltage can be written as $V_q = \bar{V}_q e^{(i\omega_n t - t/T_d)}$.

Let us now consider a time instant t_1 by which n_1^{th} micropulse has already passed through the cavity. Hence, we can express $t_1 = n_1 T_{\mu b} + t$, where, $0 \leq t \leq T_{\mu b}$ and n_1 may

represent any number between 1 and N . Now the total voltage induced in the cavity is

$$\begin{aligned} V(t) &= \bar{V}_q \sum_{n_i=1}^{n_1} e^{[i(n_i-1)\omega_n T_{\mu b} - (n_i-1)T_{\mu b}/T_d]} e^{(i\omega_n t - t/T_d)} \\ &= \bar{V}_q \left[\frac{1 - \exp\{n_1(-T_{\mu b}/T_d + i\omega_n T_{\mu b})\}}{1 - \exp(-T_{\mu b}/T_d + i\omega_n T_{\mu b})} \right] e^{(i\omega_n t - t/T_d)}, \end{aligned} \quad (3.25)$$

With a similar argument, total voltage induced in the cavity after the exit of m_1^{th} midipulse at a time instant $t_2 = m_1 \times T_m + t$, where, $0 \leq t \leq T_m$ and $1 \leq m_1 \leq M$ is

$$\begin{aligned} V(t) &= \bar{V}_q \left[\frac{1 - \exp\{N(-T_{\mu b}/T_d + i\omega_n T_{\mu b})\}}{1 - \exp(-T_{\mu b}/T_d + i\omega_n T_{\mu b})} \right] \\ &\quad \times \left[\frac{1 - \exp\{m_1(-T_m/T_d + i\omega_n T_m)\}}{1 - \exp(-T_m/T_d + i\omega_n T_m)} \right] e^{(i\omega_n t - t/T_d)}. \end{aligned} \quad (3.26)$$

Finally, after the exit of p^{th} macropulse at a time instant $t_3 = p \times T_M + t$, where, $0 \leq t \leq T_M$, total voltage induced in the cavity can be calculated as

$$\begin{aligned} V(t) &= \bar{V}_q \left[\frac{1 - \exp\{N(-T_{\mu b}/T_d + i\omega_n T_b)\}}{1 - \exp(-T_{\mu b}/T_d + i\omega_n T_{\mu b})} \right] \\ &\quad \times \left[\frac{1 - \exp\{M(-T_m/T_d + i\omega_n T_b)\}}{1 - \exp(-T_m/T_d + i\omega_n T_m)} \right] \\ &\quad \times \left[\frac{1 - \exp\{p(-T_M/T_d + i\omega_n T_b)\}}{1 - \exp(-T_M/T_d + i\omega_n T_M)} \right] e^{(i\omega_n t - t/T_d)}, \end{aligned} \quad (3.27)$$

Eq. 3.27 clearly shows the signature of three resonances in the total induced voltage $V(t)$, which is also a function of Q_{ext} . Therefore, if we need to restrict the induced voltage below some defined limit, we must choose the value of Q_{ext} accordingly with the deployment of a suitable HOM coupler.

In Fig . 3.13 , we plot normalized HOM power $P(t)$ as a function of time for different values of Q_{ext} in the steady state. For the n^{th} HOM, the normalized power is defined as

$$P(t) = \frac{V(t)^2}{(R/Q)_n Q_{ext}}. \quad (3.28)$$

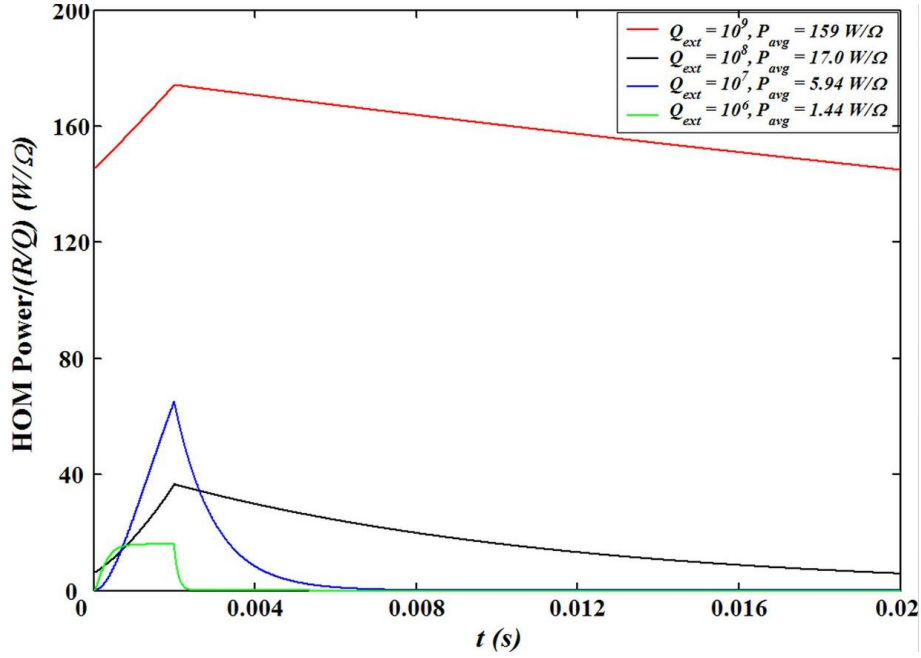


Figure 3.13: Normalized HOM power in the steady state, plotted for different values of Q_{ext} at an HOM frequency of $f = 1.625$ GHz, which is the 5th harmonic of the micro-pulse repetition rate, and 1625th harmonic of the midi-pulse repetition rate.

As mentioned, $P(t)$ is the power coming out through the HOM coupler with a given Q_{ext} . Again, for the n^{th} mode, the power dissipated on the cavity, which will appear as heat load to cryoplant will be given by $P(t) \times Q_{ext,n}/Q_{0,n}$. If we keep on reducing the value of Q_{ext} , the normalized HOM power, *i.e.*, $P(t)/(R/Q)$ reduces, and so does load to cryoplant. As we know, for any mode, $V(t)$ is proportional to R/Q , and from the above argument, we can say that the HOM power $P(t)$ is also proportional to R/Q . It is therefore, we normalized $P(t)$ with respect to R/Q to make the curves given in Fig. 3.13 as universal curves for a given time structure of pulses, the HOM frequency and Q_{ext} .

Figure 3.14(a) and (b) show the plots of normalized steady state HOM power as a function of Q_{ext} for the HOM frequency of 1625 MHz and 1626 MHz respectively. The HOM resonating at a frequency of 1.626 GHz is the 1626th harmonic of the 1 MHz which is the midi-pulse repetition rate of the beam.

From Fig. 3.14(a), it is clear that for these cavities if we fix $Q_{ext} = 10^8$, the normalized

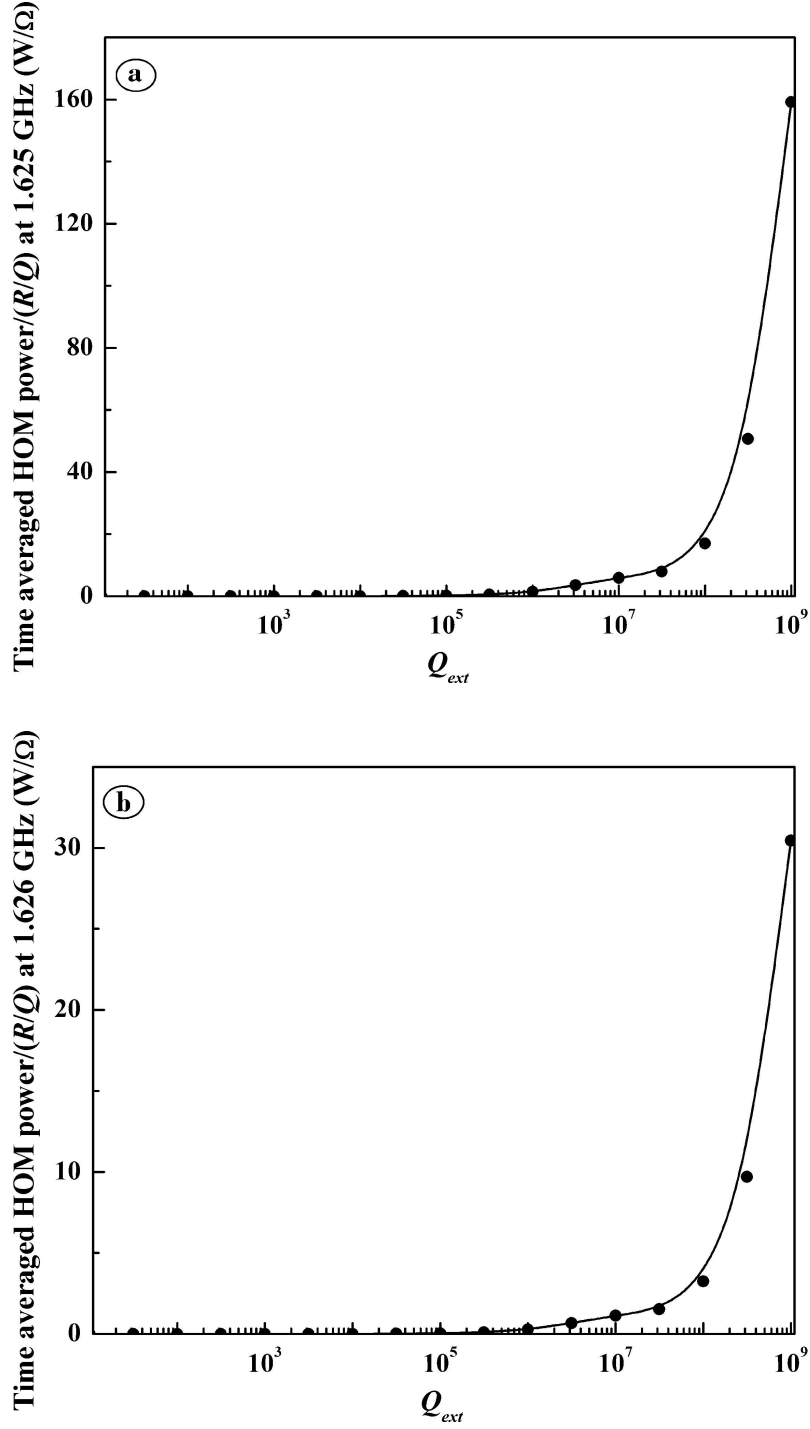


Figure 3.14: Time averaged HOM power (P_{avg}) plotted as a function of Q_{ext} . (a) Here the HOM frequency is 1.625 GHz, hence micro and midi-pulses both are in resonance, (b) Here HOM frequency is 1.626 GHz, therefore only midi-pulses are in resonance.

HOM power \bar{P}_{HOM} will be $< 17 W/\Omega$ for the higher order mode resonating at 1.625 GHz. Again, for a value of $Q_{ext} = 10^7$, \bar{P}_{HOM} will further reduce to $\sim 5.94 W/\Omega$. As expected, for the frequency 1626 MHz, the resonance is relatively weak.

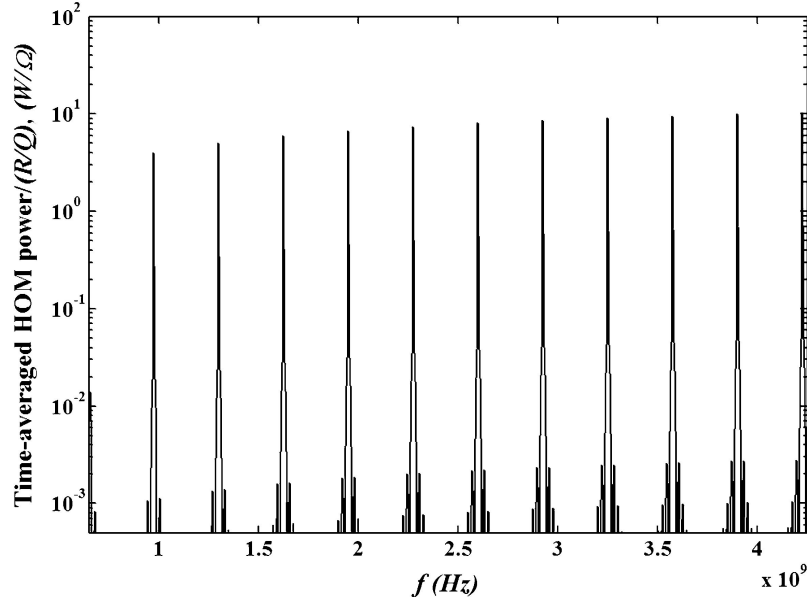


Figure 3.15: The normalized time averaged HOM power plotted as a function of HOM frequency. Here we took $Q_{ext} = 10^7$.

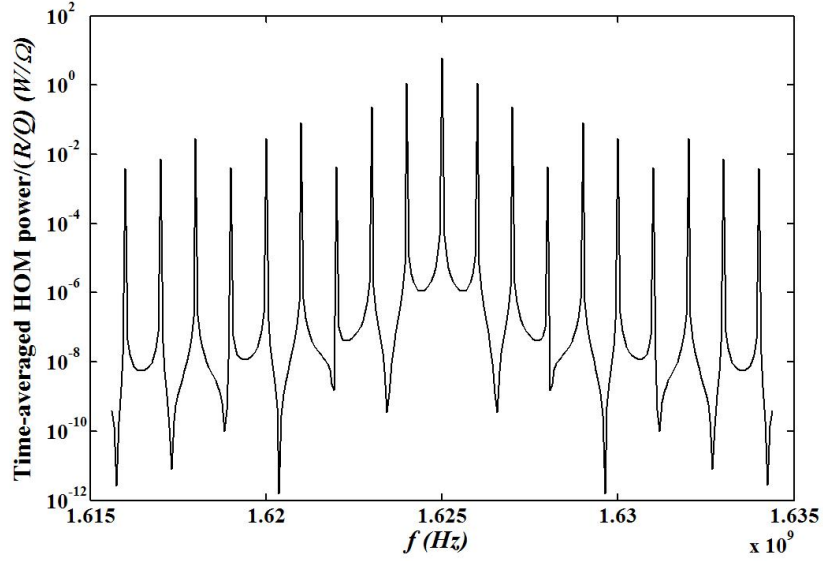


Figure 3.16: Normalized time-averaged HOM power from the beam time structure near $f = 1.625$ GHz which is the fifth harmonic of the micro-pulse repetition rate. Here $Q_{ext} = 10^7$.

Fig. 3.15 shows the normalized time-averaged HOM power up to 4.2 GHz frequency, and $Q_{ext} = 10^7$. Similar values of \bar{P}_{HOM} is noticeable there for other micro-pulse resonance peaks.

In the figure Fig 3.16 we plot the values of \bar{P}_{HOM} for around $f = 1.625$ GHz for a small range of frequencies. Fig 3.16 shows the signature of the midi-pulse resonances along with the micro-pulse resonating at 1.625 GHz. From Fig 3.16, we also observe that, while in resonance, the micro-bunch frequency gives rise to the strongest resonance.

Based on this analysis, we conclude that the value of Q_{ext} should be kept below 10^8 in order to reduce the cryogenic heat load due to resonant excitation of HOMs considerably.

3.5 Summary and conclusion

In this chapter, we have described studies on HOM and wakefield generated in the optimized elliptic cavities for the ISNS linac. An HOM with a field configuration trapped inside the optimized medium beta cavity is reported here, which is followed by a discussion on the procedure for the successful removal of the same. A rigorous analysis on the regenerative BBU instability and threshold current calculation is also discussed here. Accordingly, we found that the medium beta elliptical cavities will limit the maximum value of the *cw* average beam current below 0.516 mA. However, as mentioned, threshold values of the beam current are calculated here in the absence of HOM dampers since we have taken unloaded Q for all HOMs. In presence of HOM couplers, or even the fundamental mode power coupler, the loaded Q will be significantly less than the unloaded Q , and as a consequence, there, the threshold current limits will increase several times. As it is discussed in this chapter, threshold value of the beam current strongly depends on the velocity of the beam particles, and the minimum value of the threshold beam current corresponds to that particular velocity, for which synchronism between the velocity of a beam particle and the phase velocity of the electromagnetic wave is a maximum. For a particular dipole mode, such condition is satisfied only within one or two cavities in the linac. Therefore, even in the absence of HOM dampers, there will be a fair chance that the instability produced in those cavities may die out eventually in the subsequent sections of the linac. In this chapter, we have

also calculated the heat load arises due to resonant excitation of the monopole HOMs. However, such analysis only gives an idea about the extreme scenarios. An alternative approach for the estimation of the parasitic heat load generated in the elliptical cavities, is elaborated in Ref. [98]. Following the methodology given in reference, one can calculate the total heat load due to the higher order electromagnetic modes supported in the cavity geometry.

Chapter 4

Study on the Lorentz Force Detuning (LFD) in elliptic SRF cavities

Radiofrequency fields of an electromagnetic mode produce an electromagnetic self-force on the inner wall of an RF cavity. This force is known as the Lorentz force. This force has the potential to deform the cavity. As a consequence of this deformation, resonant frequency of the operating mode gets detuned from its designed value. This is called the Lorentz force detuning.

We have described electromagnetic design optimization of multicell elliptic SRF cavity geometries in the previous chapters. The design has been optimized for maximum achievable acceleration gradient. Owing to their extremely high Q -value, frequency bandwidth for these SRF cavities is stringently small. Therefore, even a small detuning in these cavities is enough to cause a large reflection of the input power. The situation is even more stringent for a pulsed machine. The scenario may get worse there in case the structural mode frequency of the cavity assembly starts resonating with the pulse repetition rate (PRR) of the input RF pulse.

As described in previous chapters, the proposed ISNS accelerator will be a pulsed machine, and elliptic SRF cavities will be used there in the medium and high energy

section of the superconducting linac. Study of LFD is therefore extremely important for these cavities.

4.1 General discussion on the Lorentz force detuning

In a cavity resonator, time varying electric and magnetic fields of an electromagnetic mode remains confined inside the cavity wall, where these oscillating fields induce surface current and surface charge density. The current and charge density thus induced, interact with the electromagnetic fields of the mode to give rise to Lorentz force on the cavity wall [99], which deforms the cavity wall [36], [100]. On a conducting plane with a surface charge density, the pressure produced because of this Lorentz force will act in the outward direction from the surface, *i.e.*, inwards to the cavity, whereas due to the surface current, such force will be inward, *i.e.*, outwards to the cavity.

In an RF cavity, electric and magnetic field of a mode oscillate with the resonant frequency f_0 . However, cavity wall will effectively experience a pressure, averaged over an RF period T_p , due to slow mechanical response of the cavity material. The time averaged Lorentz pressure \mathcal{P} acting on the resonator wall can be calculated from the following expression [36], [100], [101]:

$$\mathcal{P} = \frac{1}{4}(\epsilon_0 E_{pk}^2 - \mu_0 H_{pk}^2). \quad (4.1)$$

Here ϵ_0 and μ_0 denote permittivity and permeability of the free space. In the equation, E_{pk} and H_{pk} represent peak value of the electric field and magnetic intensity respectively. Also, as we know, in the free space, magnetic field $\mathbf{B} = \mu_0 \mathbf{H}$ [99].

For a TM_{010} mode, \mathbf{E} -field dominates near the iris region of an elliptical cavity and \mathbf{B} -field dominates at the equatorial surface. Accordingly, Fig. 4.1(a) shows the typical distribution of the Lorentz pressure on the inner surface of an elliptic cavity wall. As

a consequence of this pressure, iris region deforms inward, whereas, in the equatorial region, the deformation is in the outward direction; which is shown in Fig. 4.1(b). As a result of this deformation, resonant frequency of the cavity reduces and gets shifted to f_L from the design frequency f_0 . The deviation in the resonant frequency $\Delta f = |f_0 - f_L|$ is known as the Lorentz force detuning [66].

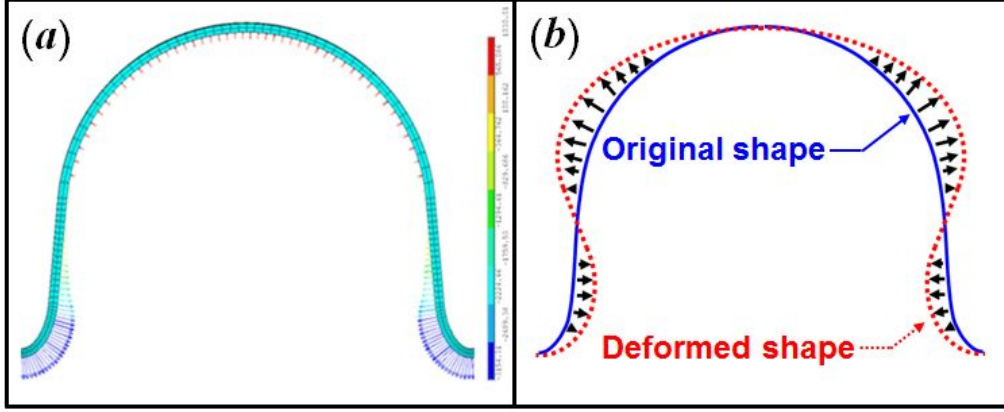


Figure 4.1: (a) Typical Lorentz pressure distribution on the inner wall of an SRF cavity half-cell, and (b) the corresponding deformation (Not to scale).

As it is shown in Eq. 4.1, value of the Lorentz pressure \mathcal{P} depends on the square of amplitude of the peak electric field and magnetic field value. Therefore Lorentz pressure will generate a static deformation in the cavity shape for an accelerator operating in a cw mode. Such static detuning, which is a result of this static deformation is known as *static LFD* [16], [66].

For a pulsed mode of operation, Lorentz pressure \mathcal{P} also becomes periodic, following the temporal pattern of the periodic input RF power pulse. Then, as mentioned, some of the structural mode frequencies of a cavity assembly may get resonantly excited by this periodic Lorentz pressure pulse train. This may lead to a dynamic amplification in the deformation of the cavity shape. The detuning introduced by this resonant amplification is known as the *dynamic LFD* [102].

Here we would like to emphasize that these structural modes are decided not by the cavity alone, but by the entire cavity assembly, which includes stiffener rings, as well

as the helium vessel [101]. Schematic of a typical SRF cavity - stiffener rings - helium vessel assembly is shown in Fig. 4.2. As explained, electromagnetic field of a resonant mode will apply a radiation pressure on the inner surface of the niobium cavity wall and as a consequence of this pressure, the cavity shape might get deformed. Niobium rings are therefore welded, connecting the outer wall of the niobium cavity cells, to reduce this deformation. These rings are called stiffener rings. Assembly of cavity and stiffener rings is inserted into a cylindrical titanium vessel. In an SRF accelerator, these vessels remain filled up with liquid helium (usually at 2 K) and hence known as helium vessel also. In this assembly, a thin ring-like niobium titanium (55Ti-45Nb) transition piece is used to facilitate the joining between titanium vessel and niobium cavity end-groups [103].

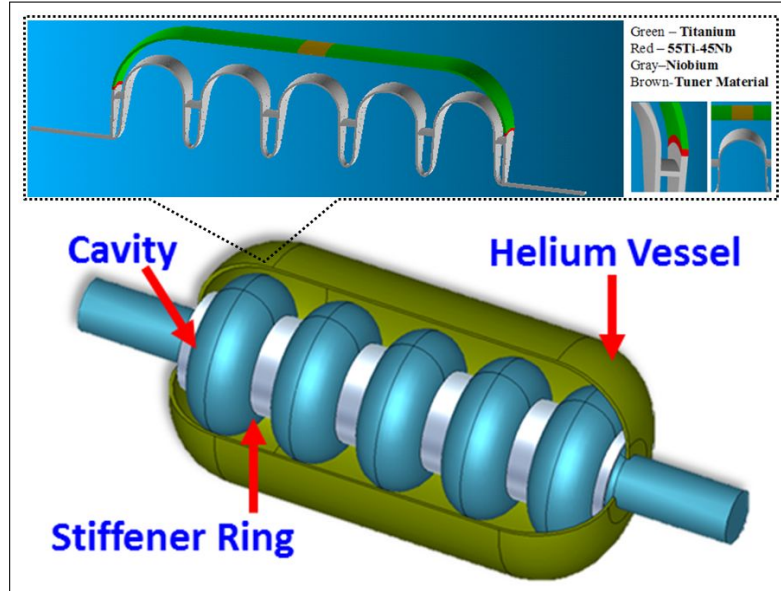


Figure 4.2: (a) Schematic of a multicell SRF cavity along with helium vessel and stiffener rings. (b) Inset is the 15° sector model of the cavity assembly.

Lorentz Force Detuning analysis is indeed a coupled-physics problem. We need to perform both electromagnetic and structural analysis in order to compute Lorentz pressure, cavity deformation and the detuned frequency. These calculations were performed using the single environment of a finite element based simulation software ANSYS™ [104], [105], [106]. Subroutines were developed there using ANSYS™ parametric design language (APDL) which is a seamless programming interface available with the software [106].

4.2 Static and dynamic LFD in an elliptic SRF cavity - a theoretical framework

In order to feed RF power to an RF cavity, impedance matching is essential between the cavity and the RF power coupler. Such matching is ensured between cavity and power coupler at design frequency f_0 of the operating mode of an RF cavity. The requirement on the RF power to be fed to the cavity becomes nearly doubled if the resonant frequency of the cavity is detuned by $\delta f = f_0/2Q_L$ [107]. Here, Q_L is the loaded quality factor of the cavity, which is expressed in terms of coupling coefficient (β_c) as $Q_L = Q_0/(1 + \beta_c)$. We need to set $\beta_c = 1 + P_B/P_c$ in the case of a critical coupling in the presence of beam, where P_B denotes beam power in the expression of β_c [65]. In case of an SRF cavity, P_c is considerably less than that of the P_B . With a little approximation, therefore the parameter Q_L can be calculated from the formula $Q_L \approx Q_0/\beta_c = Q_0/(P_B/P_c)$. In terms of the beam current I_B and R_{sh} , *i.e.* the shunt impedance of the cavity, finally one can derive $Q_L \approx Q_0/(R_{sh} \times I_B/V_0)$.

The average beam current in a pulse will be around 10 mA for the ISNS linac. Therefore, Q_L for the $\beta_g = 0.9$, 650 MHz elliptic SRF cavities will be around 3.2×10^6 , which corresponds to the typical bandwidth of the cavity, *i.e.*, $f_c/Q_L \approx 200$ Hz [36]. Therefore, analysis and compensation of this Lorentz force detuning is extremely essential in the case of an elliptic SRF cavity used in the ISNS injector linac.

4.2.1 Static Lorentz force detuning in an elliptic SRF cavity.

As mentioned, static LFD is the constant deviation in resonant frequency in an accelerator operating in the continuous mode. Following Refs. [102], [101], we define a parameter k_{LFD} , which is known as Lorentz force detuning coefficient. This parameter relates static detuning δf in the resonant frequency of the cavity with the accelerating

gradient E_{acc} as

$$\delta f = -k_{LFD} E_{acc}^2, \quad (4.2)$$

where k_{LFD} has the unit Hz (MV/m)^{-2} . As it is shown in Fig. 4.1(a), due to Lorentz pressure, there is a reduction in the volume of an elliptic cavity, where electric field dominates and the expansion in the cavity volume occurs in the magnetic field region. Therefore, from Slater perturbation theory, it can be shown that such deformation in the cavity volume will lead to a reduction in the resonant frequency of the cavity. This explains the negative sign in Eq. 4.2.

4.2.2 Periodic Lorentz pressure and the Dynamic LFD in an elliptic SRF cavity.

As explained, Lorentz pressure originates from electromagnetic fields of the cavity mode, and we can derive Lorentz pressure pulse shape from shape of the cavity voltage using Eq. 4.1. Figure 4.3 describes the temporal shape of the RF voltage, as well as the corresponding Lorentz pressure pulse, where the beginning point t_1 of the 2 ms flat top (from t_1 to t_2) indicates starting time of the 2 ms beam pulse [37]. The rising and falling part of the voltage pulse is decided by the loaded quality factor of the cavity.

Following the cavity voltage, the Lorentz pressure pulse will be repeated with a PRR of 50 Hz [37]. Therefore, we will explore the structural response of the cavity under the influence of this periodic pressure pulse in the next subsection.

Theoretical formulation for the dynamic LFD [100]

Figure 4.3 shows the temporal profile of the Lorentz pressure pulse within the time period 20 ms (PRR^{-1}). In response to this time-dependent Lorentz pressure \mathcal{P} , one can explain the vibration of the cavity wall in terms of its normal mechanical modes of vibration. This is described in brief as follows.

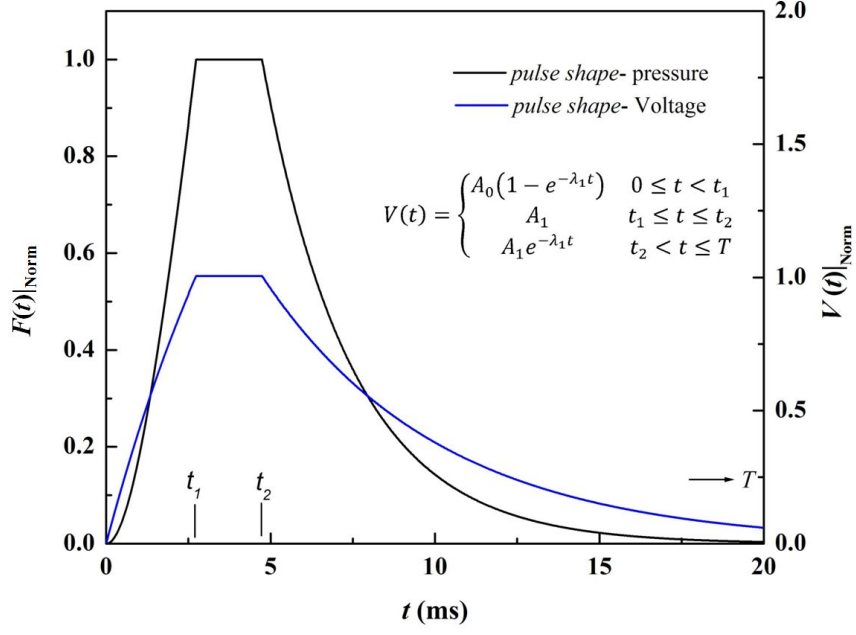


Figure 4.3: Temporal profile of the amplitude of the normalized cavity voltage (in blue), and the amplitude of the normalized Lorentz pressure pulse (in black).

We can parametrize the cavity surface in the form of two appropriately defined variables u and v . Following this parametric representation using variables u and v , any point on the cavity surface (x, y, z) can be denoted as $x = x(u, v)$, $y = y(u, v)$, and $z = z(u, v)$. Let us define a variable $\chi(u, v, t)$ representing the displacement of any point on the cavity wall surface due to mechanical vibration at a time instant t . Any such displacement can be decomposed into eigenmodes of vibration. Therefore, one can write $\chi(u, v, t) = \sum_m \phi_m(u, v) \eta_m(t)$, where, $\phi_m(u, v)$ and $\eta_m(t)$ represents shape function and amplitude of the m th orthonormal eigenmode, respectively. For these eigenmode shape functions, we define the orthonormality condition as follows:

$$\iint_S \phi_m(u, v) \phi_n(u, v) dS = S \delta_{mn}, \quad (4.3)$$

where, dS denotes an elementary area on the total cavity surface area S and δ_{mn} is the Kronecker delta function representing the condition $\delta_{mn} = 1$ if $m = n$, and $\delta_{mn} = 0$ for the cases $m \neq n$.

An RF cavity may perform damped harmonic oscillation in the absence of any external

force. We can calculate the time evolution of the displacement of a point on the cavity surface as

$$\begin{aligned}\ddot{\chi} &= \sum_m \phi_m(u, v) \ddot{\eta}_m(t) \\ &= -2 \sum_m \xi_m \omega_{0m} \phi_m(u, v) \dot{\eta}_m(t) - \sum_m \omega_{0m}^2 \phi_m(u, v) \eta_m(t),\end{aligned}\tag{4.4}$$

in that damped oscillation condition. Here ‘ $\dot{}$ ’ and ‘ $\ddot{}$ ’ denote first order and second order derivatives respectively w.r.t. time. In the above equation, the first term in the right hand side containing $\dot{\eta}_m(t)$, specifies the damping. The second term indicates the restoring force. In the above equation, ξ_m describes fraction of the critical damping in this damped harmonic oscillation equation [108].

However, an RF cavity will perform forced oscillation in the presence of Lorentz force. In this case, r.h.s. of Eq. 4.4 will be modified with an addition of the term $[\mathcal{P}(u, v, t)d\mathcal{S}]/[m(u, v)d\mathcal{S}]$ as follows:

$$\begin{aligned}\ddot{\chi} &= \sum_m \phi_m(u, v) \ddot{\eta}_m(t) \\ &= -2 \sum_m \xi_m \omega_{0m} \phi_m(u, v) \dot{\eta}_m(t) - \sum_m \omega_{0m}^2 \phi_m(u, v) \eta_m(t) + \frac{P(u, v, t)}{m(u, v)},\end{aligned}\tag{4.5}$$

where, $m(u, v)$ is the mass per unit area of the cavity wall.

Multiplying the both sides of the above equation with $\phi_n(u, v)$ and performing integration over the entire surface \mathcal{S} , we get

$$\begin{aligned}\iint_{\mathcal{S}} \sum_m \phi_m(u, v) \ddot{\eta}_m(t) \phi_n(u, v) d\mathcal{S} &= -2 \iint_{\mathcal{S}} \sum_m \xi_m \omega_{0m} \phi_m(u, v) \dot{\eta}_m(t) \phi_n(u, v) d\mathcal{S} \\ &\quad - \iint_{\mathcal{S}} \sum_m \omega_{0m}^2 \phi_m(u, v) \eta_m(t) \phi_n(u, v) d\mathcal{S} \\ &\quad + \iint_{\mathcal{S}} \frac{P(u, v, t)}{m(u, v)} \phi_n(u, v) d\mathcal{S}.\end{aligned}\tag{4.6}$$

Considering that the mass per unit area $m(u, v)$ of the cavity wall is a constant quantity which is not getting affected by the Lorentz pressure induced deformation of the cavity, $m(u, v)$ can be taken outside the integration. Hence, applying orthonormality condition,

Eq. 4.6 can be simplified into the following form of a familiar forced harmonic oscillator equation:

$$\ddot{\eta}_m(t) + 2\xi_m\omega_{0m}\dot{\eta}_m(t) + \omega_{0m}^2\eta_m(t) = \frac{1}{M} \oint_S \mathcal{P}(u, v, t)\phi_m(u, v)dS, \quad (4.7)$$

where, M is the mass of the total mass of the cavity.

In this forced oscillation equation, Lorentz pressure \mathcal{P} is the source of excitation, which can be written as,

$$\mathcal{P}(u, v, t) = F(t)\mathbb{P}(u, v) = \frac{F(t)}{S} \sum_n A_n\phi_n(u, v), \quad (4.8)$$

where, $F(t)$ and $\mathbb{P}(u, v)$ independently represent the time and space dependent parts of the pressure function \mathcal{P} , and spatial part of the pressure function has been expanded in terms of Eigen modes of mechanical vibration.

Substituting the series expansion of $\mathcal{P}(u, v, t)$ in Eq. 4.7, we obtain

$$\ddot{\eta}_m(t) + 2\xi_m\omega_{0m}\dot{\eta}_m(t) + \omega_{0m}^2\eta_m(t) = F(t)A_m/M. \quad (4.9)$$

It is an ordinary forced harmonic oscillator equation, here $F(t)$ describes time-variation of the excitation force.

As explained, $F(t)$ will be a periodic pulse train for the case of ISNS linac, and will repeat with a PRR of 50 Hz. Hence, in terms of Fourier series we can write $F(t) = \sum_n \mathcal{F}_n \sin(n\omega_M t + \theta_n)$, where, ω_M represents $2\pi \times$ PRR with $n = 0, 1, 2, \dots$. Absolute values of the Fourier coefficients of the forcing function are shown in Fig. 4.4 for different frequencies $\omega/2\pi$. Here, resonance will occur only when any of the structural mode frequency (angular) meets the condition $\omega_{0m} = n\omega_M$. Figure 4.4 also shows that the contributions from the structural mode frequencies higher than 250 Hz are progressively lower in the total response. In fact, the ratio of amplitudes corresponding

to frequencies 250 Hz and 0 Hz, is $\leq 1/20$.

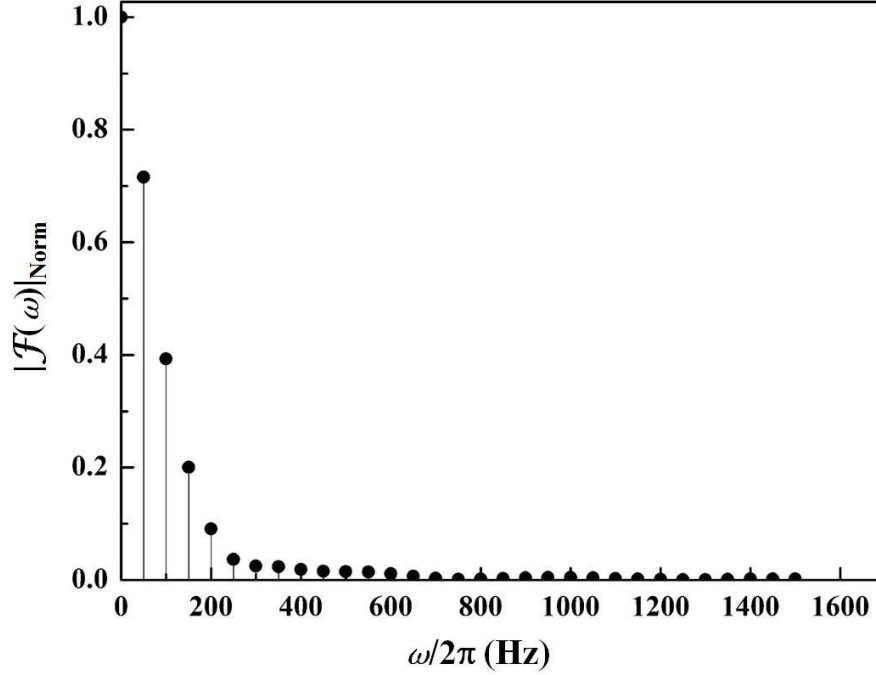


Figure 4.4: Fourier series representation of the normalized Lorentz Pressure Pulse Shape. Here $\mathcal{F}(\omega)|_{\text{Norm}}$ denotes normalized amplitudes corresponding to the participating frequencies.

Therefore, based on this analysis, we can conclude that the contribution in building up the resonance in the case of a forced oscillation will be significantly less for the participating structural modes having frequencies higher than 250 Hz.

In the next section, we will discuss the details of modelling of the problem under study, based on finite element method.

4.3 Discussion on the Finite element model

So far, we have identified the Lorentz force detuning analysis as a multiphysics problem. We need \mathbf{E} and \mathbf{B} -field of the electromagnetic mode resonating in the cavity to calculate the radiation pressure. Calculated pressure is then applied to the cavity wall and the corresponding deformation in the geometry is calculated by performing the

structural analysis. Depending on the type of analysis required, we need modules like static or transient solver for structural analysis and eigenmode solver for electromagnetic analysis. Therefore, we picked the FEM based code ANSYSTM to perform entire analysis under the same software environment.

Geometric details of the 650-MHz medium and high β multicell elliptic SRF cavities are described in Chapter 2. Based on studies performed on a similar cavities, the thickness of the cavity wall has been selected as 4 mm [100].

Inner wall of these elliptical cavities will experience azimuthally symmetric Lorentz pressure in a $TM_{010-\pi}$ mode configuration. On the basis of Eq. 4.7, we can expect that this pressure will excite only azimuthally symmetric structural modes in the cavity. Hence, we modelled only a 5° sector of the full cavity - helium vessel assembly in the azimuthal direction, to take into account all the modes excluding the torsional or flexure ones. This model is shown in Fig. 4.5. In the assembly of a dressed SRF cavity, electron beam welding (EBW) is used to integrate the stiffener rings in the design. Stiffener rings can be made of reactor grade niobium for which the advantage of 1.3 times higher yield strength can be taken; therefore the thickness of the stiffener rings has been reduced to 3 mm only. This also helps in reducing the heat input during EB welding of the stiffener ring with the cavity wall, which in turn reduces the distortion caused by welding shrinkage. Material properties used in the calculations were taken from the Ref. [109]. Fig. 4.5 also shows the small transition piece of 55Ti-45Nb in between the niobium and titanium plates of the end cover of the helium vessel. As mentioned, this transition piece facilitates the joining between two dissimilar materials - niobium and titanium. However, this transition piece in general reduces the stiffness of the cavity-helium vessel assembly due to its lower elastic modulus compared to Nb or Ti. Therefore, the width of this ring shaped transition piece is kept as small as possible, ensuring the manufacturing requirement.

It is mainly the boundary stiffness and the radiation pressure, which determine the structural modes of a structure. In the work reported in Ref. [101], the stiffness was

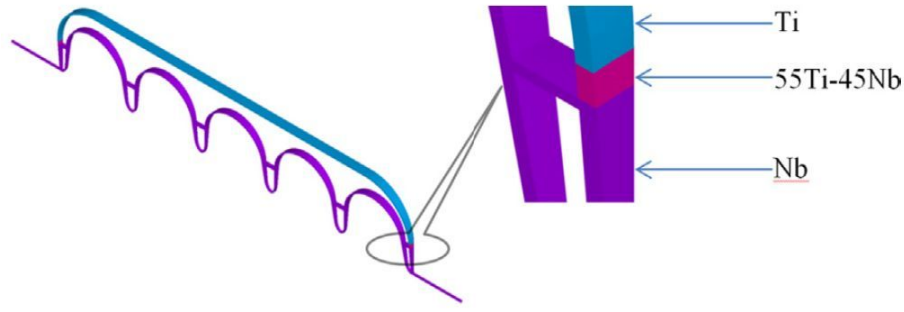


Figure 4.5: Figure shows the 5° sector model of the cavity-helium vessel assembly.

modelled by springs without including helium vessel. Our simulations were performed on an integrated model of the cavity helium vessel assembly. It is therefore expected that our model will represent the bending stiffness of the end cover more realistically. However, the dedicated tuner arrangement was not included in this analysis.

Stiffness of the helium vessel depends on the two principal considerations - (a) bending stiffness of the end cover, and (b) axial / membrane stiffness of the cylindrical wall [100], [110]. Among these two, the later one is far more than the former. Bending radius of the end cover and the wall thickness of cylinder were optimized for a desired stiffness of the helium vessel. The bending stiffness is less compared to membrane stiffness (*i.e.*, the stiffness offered by a plane with finite thickness), therefore it influences structural modes in the cavity-helium vessel assembly more than the membrane stiffness. The tuner assembly is mounted in the mid of the cylindrical part of the helium vessel in a typical configuration. Therefore, inclusion of the tuner assembly might change the stiffness of the cylindrical membrane of the vessel. However, as explained in the end of this chapter, it would have no significant effect on the result of our analysis.

As mentioned, this analysis was performed using the FEM based software ANSYSTM-MULTIPHYSICS. The software ANSYSTM uses vector finite element method (VFEM) for the computation of electromagnetic eigenmodes and electromagnetic fields. VFEM ensures the accuracy in the computation by enforcing continuity of the electric field on the inter-element boundaries [106]. In this study, the

volume enclosed inside the cavity wall was the domain for the electromagnetic analysis. Accurate computation of the radiation pressure requires precise estimation of the electromagnetic field values at the inner surface of the cavity wall. Therefore, a fine mesh density was created near the metallic boundary of the cavity. A refined mesh density was also created along the cavity axis to ensure an accurate calculation of the accelerating gradient E_{acc} . Lorentz pressure was calculated using Eq. 4.1 from the electric and magnetic field values obtained at the metallic boundaries for each of the nodal points on the cavity inner wall. ANSYSTMAPDL was used extensively for this computation. In the subsequent operation, deformation in the cavity geometry was computed through a structural analysis.

Numerical computations were performed on the nodal points for structural analysis and we perform the discretization accordingly. Each of the discrete mass points can be considered connected to all other points through imaginary springs. Based on that assumption, the structure can be visualized like a system with multiple degrees of freedom (MDoF). However, one principal bottleneck here is that the theoretical modeling of an actual damping is very difficult in the case of a MDoF system.

Hence, to incorporate the damping in the structural computation, we have used an established mathematical model, which is called Rayleigh proportional damping model [111], [112]. Commensurate with the experimentally obtained result, reported in Ref. [101], in our semi-numerical approach, we have assumed that for each of the modes, the amount of damping present was 0.3% of their critical damping. Here, critical damping is defined as the smallest damping coefficient above which the transient response shows a non-oscillatory asymptotic behavior [108].

We have performed the structural transient calculation, following the mode superposition method. Transient simulation was run for 4 seconds (equivalently up to 200 RF pulses) as it was observed that this time was enough for the run to yield a steady repeatable response. We chose a time step size $\Delta t = 50 \mu s$, which is less than (1/20)th of

the time period of the largest frequency of natural modes of vibration that may get excited during the pulse [106].

In the analysis, we have generated fully compatible finite element mesh at the interface, which ensures a one-to-one correspondence between calculated electromagnetic fields and applied Lorentz pressure on the structural elements.

In the next section, we will present the result of our analysis, which was performed on $\beta_g = 0.61$ and $\beta_g = 0.9$, 650 MHz SRF elliptic cavities designed for the proposed ISNS.

4.4 LFD analysis of elliptical cavities designed for ISNS

Based on the above theoretical framework, a sequential design methodology was developed. Lorentz Force Detuning analysis were performed on the medium and high β elliptic multicell SRF cavities, following this methodology. In this section, we will describe the methodology based on the results obtained from Lorentz force detuning analysis of the $\beta_g = 0.9$, 650-MHz multicell elliptical SRF cavity geometry. This will be followed by a brief description of results obtained from the $\beta_g = 0.61$, 650 MHz SRF cavity. Considerations like the tunability of the cavity and the probable effect on the LFD due to the inclusion of a tuner will be emphasized there.

4.4.1 LFD analysis on $\beta_g = 0.9$ 650 MHz 5-cell elliptical SRF cavity

The detailed geometry of this cavity has been described in Chapter 2. From the parametric cavity geometry, FEM model of the ‘cavity helium vessel assembly’ was created in ANSYSTM [36], [100].

As mentioned, the design gradient for this cavity is 18.6 MV m^{-1} . To achieve this gradient, a maximum of around 200 kW RF power will be fed into the structure. We have calculated the corresponding bandwidth as $\sim 200 \text{ Hz}$ for these cavities.

As mentioned, ISNS accelerator is a pulsed mode machine. Therefore, dynamic Lorentz force detuning will be a crucial issue for the cavities. However, we start with analyzing the static LFD as the helium vessel geometry is optimized based on the static analysis.

Analysis on the static Lorentz force detuning: Our starting geometry of the helium vessel was simple. It was a 1.1 m long titanium cylinder with inner diameter 504 mm, terminated with flat end covers at both ends. A small curvature of 35 mm radius was assumed at the junctions of the cylinder and end covers. This radius is called the ‘torus-radius’. Configuration of this cavity helium vessel assembly is shown in Fig. 4.6.

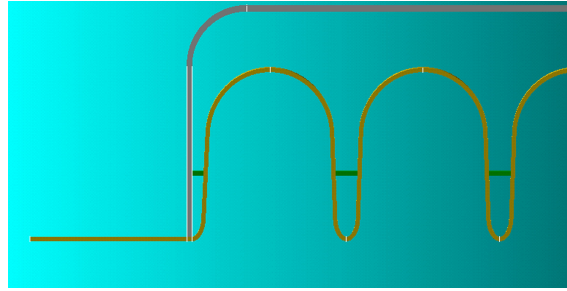


Figure 4.6: Starting geometry of the cavity and the ‘tori-flat’ helium vessel assembly. Torus radius of the helium vessel is 35 mm in this configuration.

Stiffness of the helium vessel plays an important role in controlling the detuning due to Lorentz force. Vessel stiffness can be enhanced (i) by increasing torus radius, or (ii) by increasing the wall thickness of the cylinder. However, maximum value of this torus radius is limited by the cavity volume, maximum radial position of the stiffener rings and the radial position of the 55Ti-45Nb transition material. The transition piece is kept in the flat portion of the end cover for ease of welding. With the increasing thickness of the cylinder wall, the helium vessel will become heavy. This also increases the sag of the assembly, and the material cost. Therefore, reduction in the LFD by increasing the stiffness of the helium vessel is an expensive option, and needs suitable optimization.

Thickness of the titanium cylinder wall of the helium vessel was varied within a range of 3 to 5 mm, and the torus-radius from 35 to 200 mm. The stiffness of the helium vessel

were calculated for the different combinations of wall thickness and torus-radius. We have used Hook's law to calculate the stiffness of the helium vessel in this analysis. Figure 4.7 shows a reduction in the static LFD with increasing stiffness of the helium vessel. As it is seen in the figure, the absolute value of the detuning reduces from 2.6 to 1.1 kHz, when we increase the vessel stiffness from 2.3 to 6.5 kN/mm. In the same plot, corresponding values of Lorentz force detuning coefficient $-K_{LFD}$ are shown. These calculations were performed in absence of the stiffener ring.

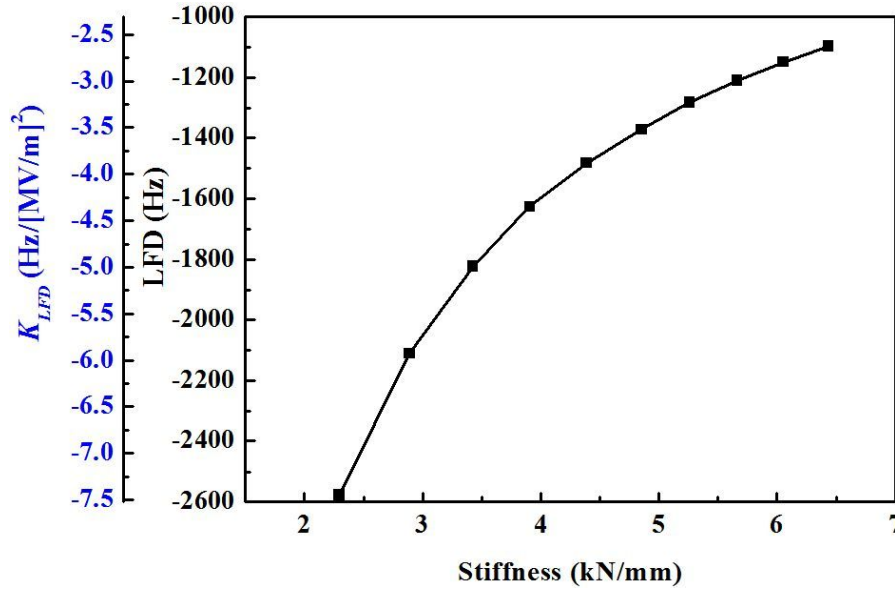


Figure 4.7: LFD as a function of the stiffness of the helium vessel. Here calculations were performed without including stiffener rings in the design. Also, the values of $-K_{LFD}$ is shown here.

It can be seen from Fig. 4.7 that the stiffness of the helium vessel alone cannot completely nullify the LFD. In fact, increasing helium vessel wall thickness makes the structure stiff, but it has minimal influence on the deformation of individual cavity cells. Therefore stiffener rings were integrated with the model to reduce the detuning further. In this analysis, we have calculated the LFD by varying the radial positions of the stiffener rings, for different values of the helium vessel stiffness. A reduction in the values of static detuning with increasing radial position of stiffener rings is shown in Fig. 4.8. Stiffener rings constraint the deformation of the cavity wall. Its effectiveness increases, as we move towards radially outward location, and finally, when the stiffener

rings reach nearly the top of the equatorial dome of the cavity, its effectiveness saturates. As it is shown in Fig. 4.1, the intensity of the Lorentz force reduces near the cavity equator. We have also shown the corresponding values of K_{LFD} in the same figure. Accordingly, the reducing trend of the detuning saturates for the higher radial position of the stiffener ring.

Figure 4.8 shows that the static LFD (absolute) attains its minimum for the configuration, which corresponds to a reasonable high value of the radial position of stiffener rings. In this configuration, minimum LFD value of $\sim 550\text{Hz}$ was obtained for a radial position of stiffener rings around 170 mm. Helium vessel stiffness was kept fixed at 4.9 kN/mm in this calculation.

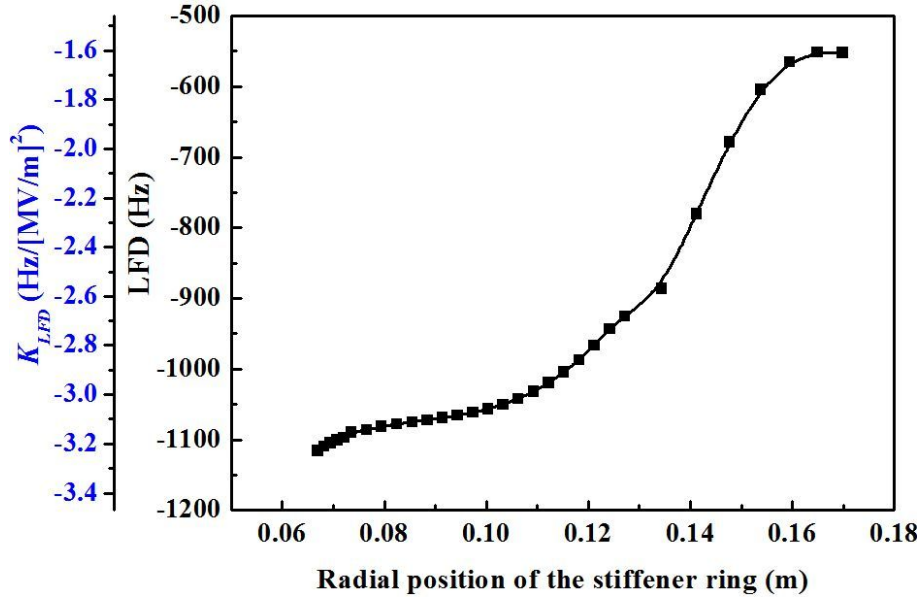


Figure 4.8: LFD is plotted as a function of the radial location of the stiffener rings. Helium vessel stiffness was kept fixed at 4.9 kN/mm in this calculation. Values of $-K_{LFD}$ is shown here.

Above analysis shows that the stiffener rings reduce the detuning considerably, yet proper tuning is required for complete elimination of LFD. In this tuning process, the cavity is subjected to an axial elongation (or contraction) with the help of a tuner system.

In the next part of our analysis, calculations were performed for the tuning requirement for different radial positions of stiffener rings for the complete

compensation of the static LFD. Complete compensation of LFD with the help of proper tuning was studied for different values of the helium vessel stiffness. Moreover, based on the practical considerations, like the maximum allowable value of the stiffener radius and the limitation on the maximum tuning range, finally we have selected the design of the helium vessel, which can offer a stiffness 4.9 kN/mm. For this configuration, the thickness of the helium vessel was obtained as 5 mm with a torus radius of 120 mm. The detailed geometry of the helium vessel is summarized in Table 4.1. Without incorporating stiffener rings in the design, in the cavity-helium assembly, one can reduce the detuning due to LFD to a value of ~ 1300 Hz, which corresponds to a $|K_{LFD}|$ of ~ 4 Hz / [MV/m] $^{-2}$.

Table 4.1: The detailed geometry of the helium vessel.

Diameter (mm)	Thickness (mm)	Torus radius (mm)	Stiffness (kN/mm)
504	5	120	4.9

Figure 4.9 shows that static LFD can be fully compensated with a pre-stretching of ~ 9.5 μ m, if we set the radial location of the stiffener rings around 80 to 110 mm. Such a pre stretching in fact provides a small axial elongation to the cavity volume. Since, this elongation increases mostly the volume of the electric field region of the cavity near the iris, cavity frequency increases slightly.

One more constraint arises in the LFD analysis regarding the positioning of the stiffener rings. An increasing radial position of the stiffener rings makes the tuning difficult. Being an additional constraint, stiffener rings make the cavity assembly more rigid and the structure becomes more and more rigid with the increasing radial location of stiffener rings. However, finally, the cavity requires an elongation to completely compensate for the LFD, and this elongation is provided by the tuner. Tuning turns out to be difficult with the increasing rigidity of the cavity assembly. It will be explained later in this chapter with the help of simulated results, when we present the LFD analysis performed on $\beta_g = 0.61$ cavities. Increasing the radial position of stiffener rings also

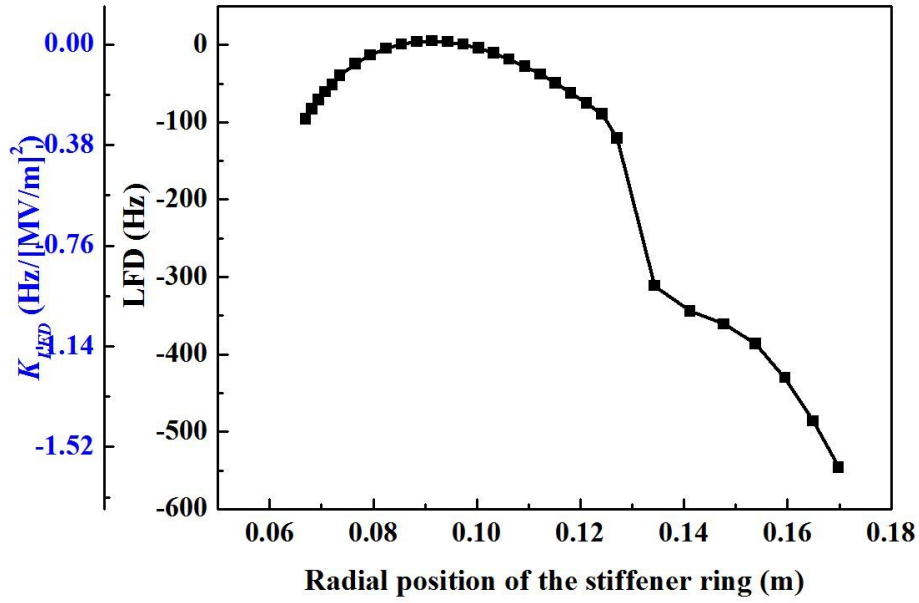


Figure 4.9: LFD as a function of the radial locations of the stiffener rings. Here, the stiffness of the helium vessel is 4.9 kN/mm. In the vessel, an axial elongation of $9.5 \mu\text{m}$ was considered in this simulation. Corresponding values of K_{LFD} is also shown here.

affects another important figure of merit of a multicell cavity, which is the field flatness η . One of the important optimization criteria in designing a multicell cavity geometry was to maximize the field flatness. Chapter 2 shows that 99.4 % field flatness was achieved in the optimized $\beta_g = 0.9$, 650 MHz 5-cell cavity geometry. There, stiffener rings were not considered in that optimization work. As it shown in Fig. 4.10, field flatness starts deteriorating if we increase the radial position of stiffener rings. In a multicell elliptic cavity geometry, the end cells are supported directly by the helium vessel, which is relatively stiff compared to the cavity cells. Therefore, mid-cells deform more compared to the end-cells with the increasing stiffener location. As a result, the different cells of the cavity accrue different deformation. Therefore, resonant frequencies of the individual cell become different, which results in a degradation of the cavity field-flatness. Figure 4.10 also shows that this reduction will be rapid if we push the radial position of the stiffener approximately beyond 100 mm.

Therefore, positioning of the stiffener rings will be a compromise between the field flatness and LFD. Among the contemporary projects, as it is described in the Ref. [113],

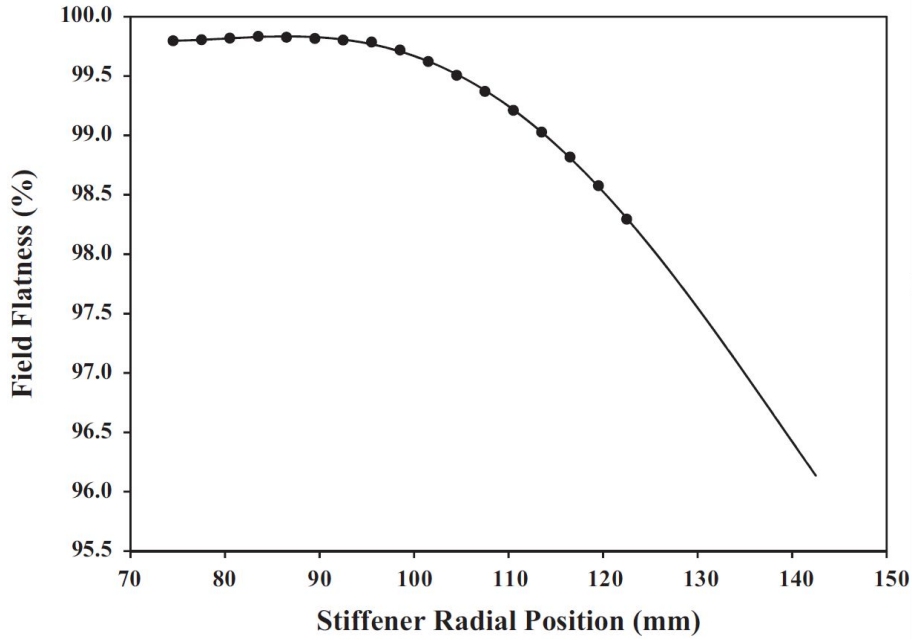


Figure 4.10: Reduction in the field flatness with increasing radial position of the stiffener rings.

SNS project at Oak Ridge has targeted 98% field flatness as their design goal, whereas, for the SNS cavities, the requirement was set as $\eta \geq 92\%$ [114]. We have set a target of 98% field flatness in the final elliptic cavity geometry.

Finally, we would like to clarify that the radial position of all the stiffener rings was kept the same in our analysis. It is because, the asymmetric placement of stiffener rings will produce an uneven change in the individual cell geometry, particularly when the cavity will go through the tuning. As observed in the simulation, asymmetric placement of the stiffener rings leads to a loss of field flatness.

Static LFD is a predictable and slow phenomenon, and in the steady state, deformation and the detuning remain constant. Therefore, following this deformation pattern, a pre-calculated stretching of the cavity with a slow mechanical tuner can compensate this static detuning effectively.

Above analysis shows that, in the case of our $\beta_g = 0.9$, 650 MHz 5-cell elliptic cavity, stiffener rings can be positioned anywhere in between the radial range of 80 to 100 mm

to compensate the static LFD with an axial elongation of $9.5 \mu\text{m}$, and because of such positioning, field flatness of the multicell cavity will remain almost unaffected. However, as mentioned, ISNS injector linac will be operated in the pulsed mode. In that case, as mentioned, there the optimized positioning of the stiffener rings can only be finalized based on the feedback obtained from the dynamic Lorentz Force Detuning study. In the next subsection, we present the dynamic Lorentz force detuning analysis for the $\beta_g = 0.9$ cavity.

Analysis on the dynamic Lorentz force detuning: For a pulsed linac, there is a possibility of unwanted coupling between structural mode frequencies and the PRR of the input RF pulse, and the undesirable outcome may be the dynamic amplification in the detuning, *i.e.*, the dynamic LFD.

Dynamic LFD analysis was also performed using ANSYSTM, and the required subroutines to change the stiffener locations and to incorporate the pressure pulse in the simulation *etc.* were developed in ANSYSTMAPDL.

Table 4.2 summarizes the results obtained from the simulation. Static and dynamic LFD values of few prominent structural modes are tabulated there for different radial locations of the stiffeners. Corresponding stiffness values of the cavity - stiffener ring - helium vessel assembly are also included in the table. In this dynamic LFD analysis also, we have kept the thickness of niobium stiffener rings fixed at 3 mm. Our observations and results are explained in the following paragraphs.

Our analysis shows that if we keep the radius of the stiffener rings more than 113.5 mm, all the structural mode frequencies of the cavity assembly will be beyond 250 Hz. As it is shown in Table 4.2, for most of the cases, such choice also ensure the amplification ratio between the static and dynamic Lorentz force detuning nearly unity. This in fact corroborate the theory discussed earlier, where it was shown that the amplitude of the Fourier components present in the pressure pulse goes down significantly beyond 250 Hz. For example, if we choose the radial position of the stiffener at 122.5 mm, we found two

of the structural mode frequencies close to multiples of 50 Hz. Even then, our analysis shows that there will not be any amplification subjected to dynamic LFD. Similarly, if we fix the radial position of stiffener above 116.5 mm, sensitivity of the LFD towards stiffener radial position becomes less. In fact, beyond this radial position, both static and dynamic LFD almost saturate. The dynamic LFD for the configuration with a mean value of the stiffener location at 119.5 mm is shown in Fig. 4.11, during one time period after the achievement of the steady state. Tuning requirement and the other important figures of merit corresponding to this configuration is given in Table 4.3. Here, the tuning efficiency of a tuner arrangement can be calculated from the dynamic LFD value and the required tuning range. For example, as it is shown in Table 4.2, if we choose the radial position of the stiffener at 119.5 mm, the corresponding dynamic detuning produced in that case will be -652 Hz, and to compensate the same, one can calculate the required elongation of $5.3 \mu\text{m}$ in the tuning arrangement from the tuning efficiency data given in Table 4.3. There the cavity sensitivity is another parameter, which is an indirect measure of the actual elongation in the cavity length required to compensate the LFD. Based on the data given there, compensation of -652 Hz dynamic detuning requires approximately $3.1 \mu\text{m}$ in the cavity length. Figure 4.13 shows that, the same detuning provides an approximate axial displacement of $1.68 \mu\text{m}$ in the half of the cavity length, which substantiates the calculated value of the $3.1 \mu\text{m}$ elongation in the cavity length to compensate the detuning fully.

In the simulation, corresponding to the mean value of the radial position of stiffener rings 80.5, 101.5 and 113.5 mm, respectively considerable dynamic amplifications were observed. As expected, we found that the structural mode frequencies are close to the multiples of 50 Hz for each of these cases and as it appears in Table 4.2, these mode frequencies are considerably less than 250 Hz for these cases. Among these cases, maximum dynamic LFD of 11480 Hz is reported for the configuration with mean location of the stiffener at 80.5 mm. The reason is the perfect resonance between the corresponding structural mode frequency at 150 Hz and the PRR, *i.e.* 50 Hz.

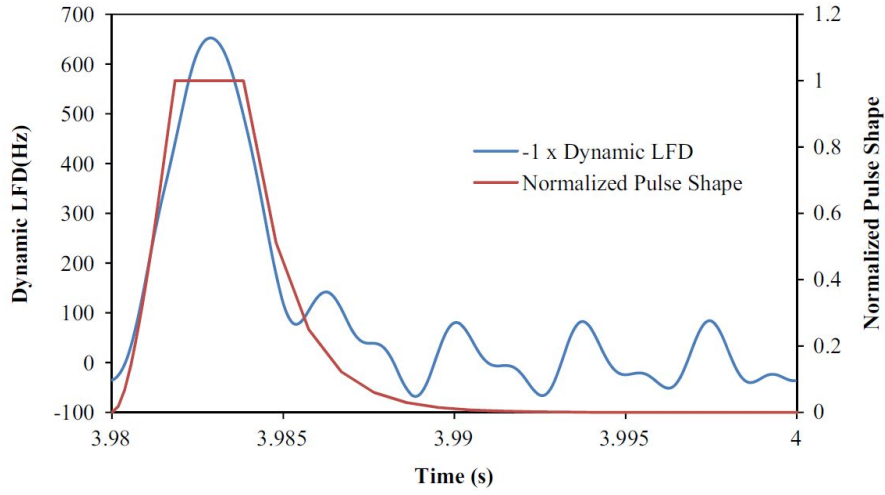


Figure 4.11: Dynamic LFD with mean radial position of the stiffener rings at 119.5 mm.

As mentioned earlier, radiation pressure deforms the cavity shape. Consequently the length of the cavity changes (squeezing or elongation). We observed that the change in length is more important in determining the detuning compared to the radial deformations. To verify this observation, we have simultaneously recorded the displacement of a point (node) on the beam pipe (close enough to the end closure of the helium vessel) and the LFD value with time during a single RF pulse after attaining the steady state. These two results are shown in Fig. 4.12 in their normalized forms. It is evident from the figure that the two curves follow each other. Therefore, transient displacement of the selected node on the beam pipe can very well give an estimation of the dynamic LFD. We also obtained a scale factor between the the dynamic LFD and change in the cavity length to be 170 ± 5 Hz/ μm for the $\beta_g = 0.9$ cavity. We found the scale factor is independent of the radial position of the stiffener.

Figs. 4.13 to 4.16 show the transient displacement of a particular node of the cavity located at the end. These figures correspond to the four different radial locations of the stiffener rings. Figure 4.13 shows the transient longitudinal displacement of the above mentioned node with a mean radial position of stiffener at 119.5 mm. Similarly, Fig. 4.14 to 4.16 show transient displacements with mean radial positions of stiffener at 113.5 mm, 101.5 mm and 80.5 mm respectively. In these three cases the resonance

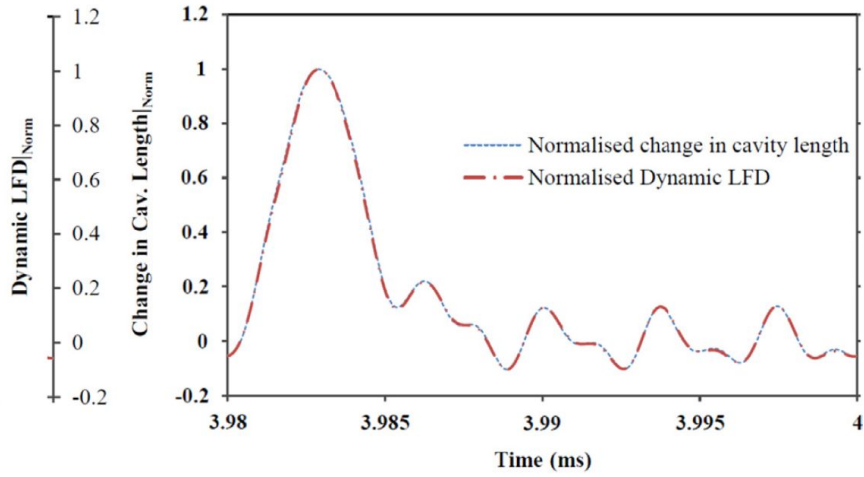


Figure 4.12: Normalized dynamic LFD and change in the cavity length with a mean radial position of the stiffener ring at 119.5 mm during a single pulse.

conditions are satisfied between structural mode frequencies and the PRR. Hence, displacement amplitudes show clear signatures of the dynamic amplification.

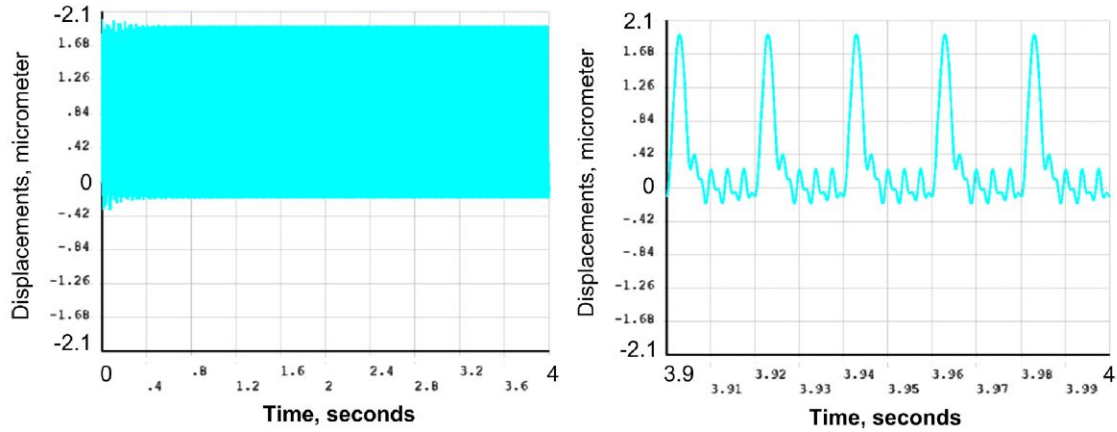


Figure 4.13: Longitudinal displacement of the cavity w.r.t. its central plane as a function of time, with mean radial position of stiffener at 119.5 mm.

To attain the stabilized transient response using the mode superposition method, we have calculated the transient displacements up to 200 RF pulses. There the last pulse was taken for our computation of the dynamic LFD.

Compared to static LFD, the cavity tuning required to compensate for the detuning becomes more challenging in the case of dynamic LFD. Pre-stretching cannot compensate the detuning here. Hence, we need a piezo crystal based tuner system.

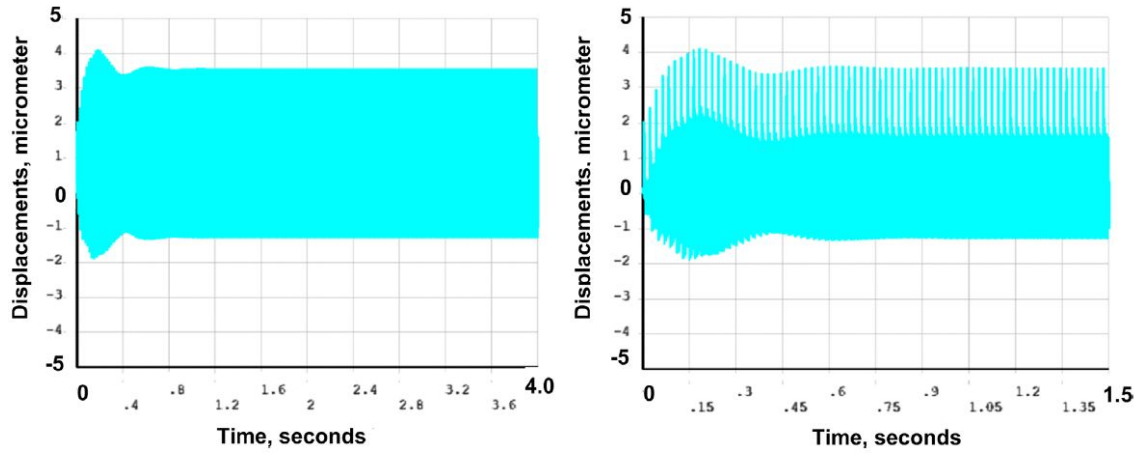


Figure 4.14: Resonant conditions corresponding to a mean radial position of stiffener at 113.5 mm, where the displacement is calculated w.r.t. central plane of the cavity.

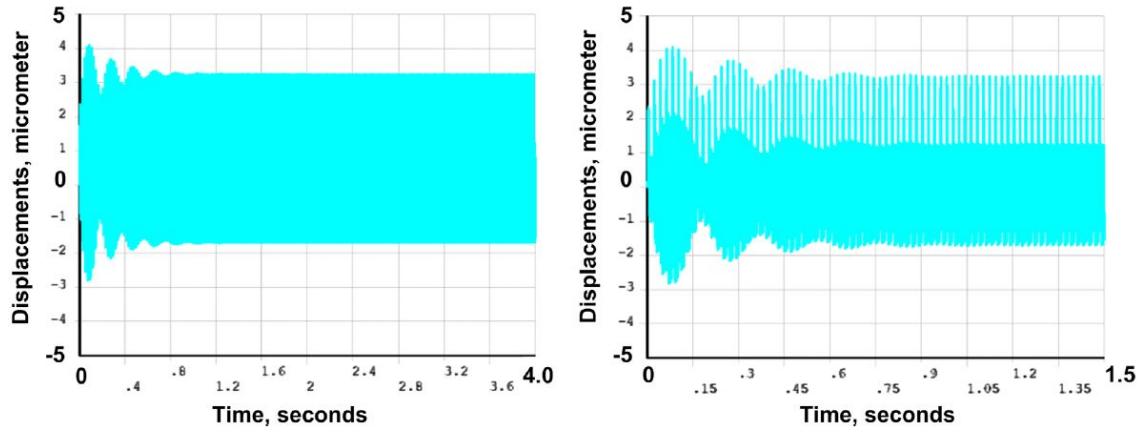


Figure 4.15: Resonant conditions corresponding to a mean radial position of stiffener at 101.5 mm, where the displacement is calculated w.r.t. central plane of the cavity.

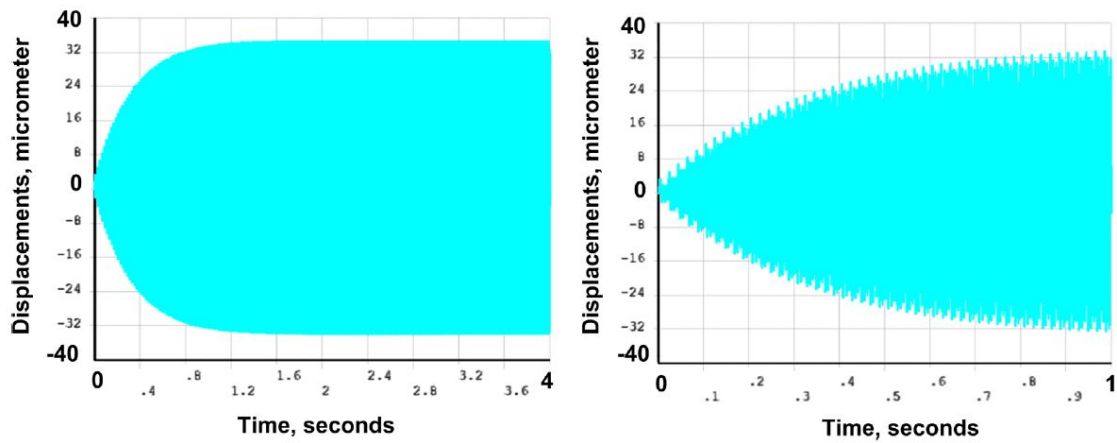


Figure 4.16: Resonant conditions corresponding to a mean radial position of stiffener at 80.5 mm, where the displacement is calculated w.r.t. central plane of the cavity.

Instead of a single crystal, multiple piezo crystals are used in a stacked form to produce sufficient force required to provide an exact change in cavity length. Here, we want to mention that the presently available stacks of PZT give up to $100\text{ }\mu\text{m}$ of movement range at the room temperature and $10\text{ }\mu\text{m}$ at operating temperature [115]. With a feed-forward programming, the piezo tuner can compensate the LFD within the pulse duration. In this design, as expected, we have kept the required range of the maximum axial elongation (or contraction) to tune the cavity to be less than $10\text{ }\mu\text{m}$.

In the next subsection, we will present LFD analysis performed on the $\beta_g = 0.61$, 650 MHz SRF elliptical cavity geometry. There, we will elaborate only those points which are different compared to the procedures already discussed.

Table 4.2: Static and dynamic LFD for different radial positioning of the stiffener rings.

No.	Stiffener mean radius (mm)	Structural frequency of symmetric longitudinal modes (Hz)	Static LFD (Hz)	Dynamic LFD (Hz)	Cavity stiffness (kN/mm)
1	122.5	296,551,757,882,925	-660	-794	17.84
2	119.5	280,534,745,787,932	-654	-652	15.67
3	116.5	266,515,733,877,939	-649	-656	13.85
4	113.5	252,493,721,876,943	-647	-1229	12.27
5	110.5	239,471,711,874,945	-648	-648	10.89
6	107.5	227,449,701,869,942	-653	-923	9.70
7	104.5	216,427,691,862,937	-659	-800	8.68
8	101.5	205,407,680,853,929	-669	-1120	7.78
9	98.5	195,387,669,843,918	-682	-670	7.01
10	95.5	186,369,657,832,906	-699	-877	6.34
11	92.5	178,352,645,820,892	-719	-815	5.75
12	89.5	170,336,633,807,878	-742	-916	5.23
13	86.5	163,322,621,795,864	-768	-1098	4.78
14	83.5	156,308,609,783,850	-796	-1574	4.39
15	80.5	150,296,597,771,836	-828	-11480	4.04
16	77.5	144,284,586,760,823	-862	-1177	3.73
17	74.5	139,273,575,749,810	-898	-781	3.45

4.4.2 LFD analysis of a 650 MHz, $\beta_g = 0.61$, 5-cell elliptic SRF cavity

Geometrical, as well as other required parameters for the $\beta_g = 0.61$, 650 MHz, 5-

Table 4.3: Figures of merit of a design with mean radial position of stiffener at 119.5 mm

No.	Figures of merit	Value
1	Required total tuning range for dynamic LFD compensation	5.3 μm
2	Field flatness after 1 mm movement of tuner	98.58%
3	Cavity end sensitivity while tuning ($\Delta f / \Delta \text{cavity}$)	208.29 kHz/mm
4	Tuning efficiency ($\Delta f / \Delta \text{tuner}$)	123.83 kHz/mm

cell elliptical cavity are described in Chapter 2. Design value of E_{acc} for these cavities is 15.4 MV/m. It is to be noted that the design frequencies for both $\beta_g = 0.61$ and $\beta_g = 0.9$ cavities are the same, *i.e.*, 650 MHz; hence, the cavities will have nearly the same diameter. Although $\beta_g = 0.61$ cavity will be a little shorter in length. For the helium vessel, length of the cylinder does not influence the stiffness much. Therefore, helium vessel used for the both the cases will be identical, except for the length. Helium vessel modelled for the $\beta_g = 0.61$ cavity case will offer a stiffness around 4.9 kN/mm.

Analysis on the static Lorentz force detuning: Figure 4.17 shows the LFD as a function of the radial positions of the stiffener rings, for the case, where the static detuning is compensated by providing a longitudinal elongation of 8.3 μm to the cavity length. In this compensated configuration, radial position of the stiffener rings can be varied from 70 to 110 mm.

For the $\beta_g = 0.61$ cavity also, the temporal profile of the RF pulse will be the same. Therefore, as it is described for the $\beta_g = 0.9$ cavities, similar dynamic analysis can be carried out here. However, avoiding repetition, we only give a qualitative presentation of the dynamic LFD here.

Analysis on the dynamic Lorentz force detuning: Based on our previous discussions, we conclude that the amplification in the detuning due to dynamic LFD can be avoided for a structural mode of the cavity -

- (1) if the mode frequency is not a multiple of the PRR; and more importantly
- (2) if the mode frequency is more than 250 Hz.

For the $\beta_g = 0.61$ cavities, Table 4.4 shows the five lowest order structural modes for

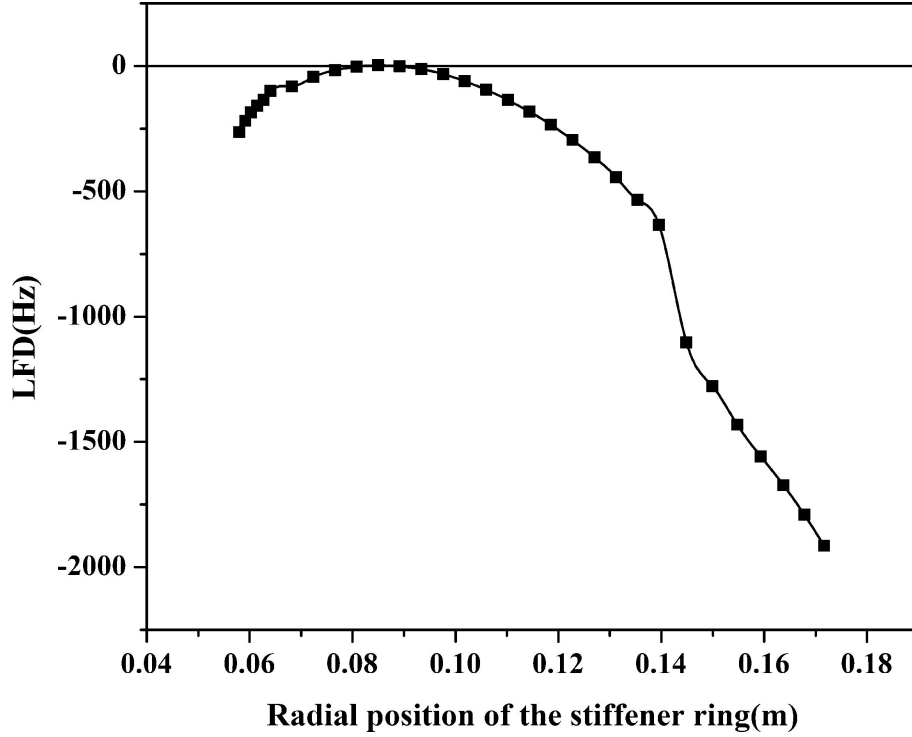


Figure 4.17: Static LFD as a function of the radial position of the stiffener rings. The compensation due to cavity elongation provided by an axial elongation of $8.3 \mu\text{m}$ of the cavity-helium vessel assembly is taken into account.

few radial position of the stiffeners. As it is shown in the table, the lowest order structural mode frequencies will be more than 250 Hz for the configuration with radial location of the stiffener rings on or above 124 mm. Therefore, on or beyond this radial location the resonant amplification of dynamic LFD will not take place.

Table 4.4: Participating structural modes of the 5-cell $\beta_g = 0.61$ cavity

$r_{\text{stiffener}}$ (mm)	f_1 (Hz)	f_2 (Hz)	f_3 (Hz)	f_4 (Hz)	f_5 (Hz)
124.00	265.07	426.48	576.19	713.59	749.42
120.00	244.87	414.74	564.03	696.97	759.72
116.00	226.00	397.09	550.89	681.37	760.72
112.00	208.76	375.45	538.55	662.98	750.70
108.00	193.18	352.27	526.39	641.40	732.29

As it is shown in Table 4.2, stiffness of the cavity helium vessel assembly also increases with the increasing radial position of the stiffeners. Anticipating that this will make the tuning inefficient, we have calculated the required displacement to compensate the detuning for different radial position of the stiffener rings for the $\beta_g = 0.61$ cavity. As

expected, Fig. 4.18 shows that with the increasing radial position of the stiffener, larger displacement of helium vessel is required to compensate for the LFD. Here, we just want to clarify that the helium vessel displacement signifies its stretching only. We therefore stopped at 124 mm for the mean radial location of the stiffener rings. This configuration requires a $7.35 \mu\text{m}$ elongation of the helium vessel to compensate fully for the LFD.

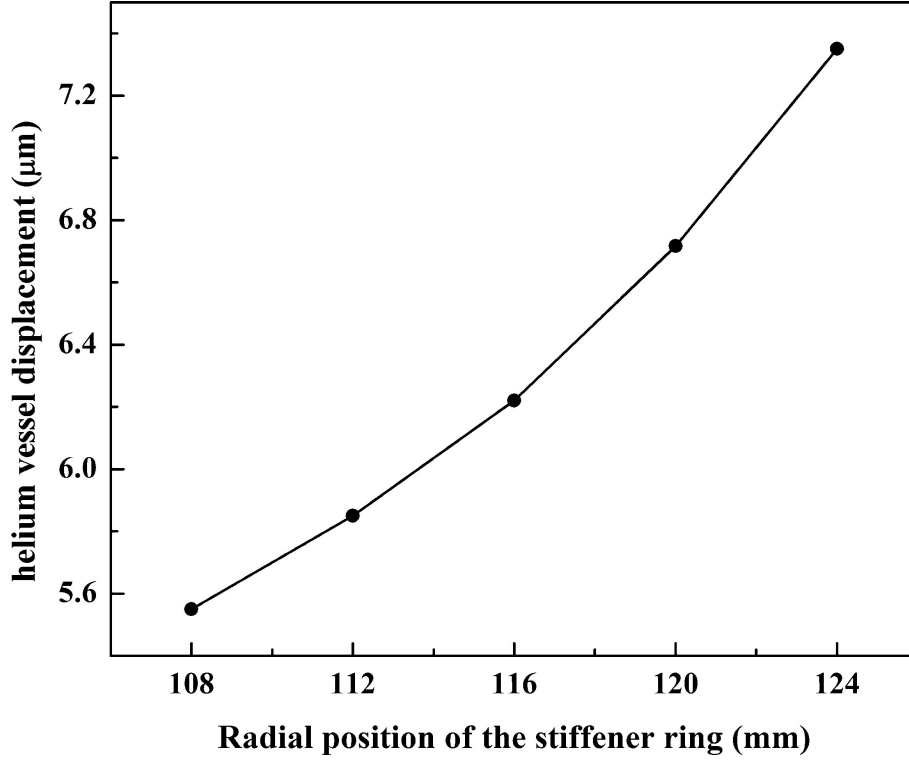


Figure 4.18: Helium vessel displacement required to compensate for LFD, as a function of the radial position of the stiffener rings.

In this analysis, we have studied the LFD by assuming tuner placed at the mid-length of the cavity, where its own stiffness does not influence the LFD. However, PIP-II (FNAL) [116], ESS [117] and MSU [118] have taken a pragmatically different approach. They have chosen two stiffener rings to reduce LFD values to be so small that they need little fast online tuning during their operation. They have also placed the tuner at the flat end of the helium vessel so that it supplements the lower stiffness of the end cover to reduce the LFD further. They have not presented their estimate of dynamic LFD. In such scenario, the LFD strongly depends on the tuner rigidity for a multicell elliptic SRF

cavity geometry. According to their observation made on $\beta_g = 0.65$ cavities, LFD can be minimized at the tuner /end cover / helium vessel rigidity >40 kN/mm, and two stiffener rings instead of one stiffener, may therefore be an effective choice. However, as it is shown in Fig. 4.18, with the increasing rigidity of cavity assembly, even offline tuning will be very difficult. Therefore, further analysis is required for our cavities also to corroborate the importance and effectiveness of the adaptation of two stiffener schemes.

4.5 Discussion and conclusion

A discussion on the static and dynamic Lorentz force detuning analysis is presented in this chapter. Simulations were performed using ANSYSTM on the assembly of $\beta_g = 0.61$ and $\beta_g = 0.9$ elliptical cavity, integrated with stiffener ring and helium vessel. Calculations were performed on the requirement of the elongation in the cavity length for the full compensation of LFD. However, as mentioned, in this analysis, we did not directly include the tuner arrangement in the design but modelled its influence.

To realize the effect of tuner arrangement on the stiffness of the helium vessel, a simple analysis was performed. Instead of the tuner, in the middle of the helium vessel, we modelled an annular section approximately, where the conventional tuner will be attached. This section is shown in Fig. 4.2, where it is demarcated in brown colour. As mentioned in Ref. [100], in the case of longitudinal structural mode excitation, cylindrical part of the vessel will remain stationary, whereas the bending of the end cover alone will produce mode shapes. Therefore, absence of tuner in our analysis has little impact on the final outcomes. To verify this point, stiffness and density of the selected annular section in the helium vessel were varied, and simultaneously, structural mode frequencies were calculated. As shown in Fig 4.19, the variation in the structural mode frequency with the density and stiffness of the material is negligible. We repeated the analysis by varying the length of the annular ring from 3 to 20 mm, but no significant

changes were observed in the result.

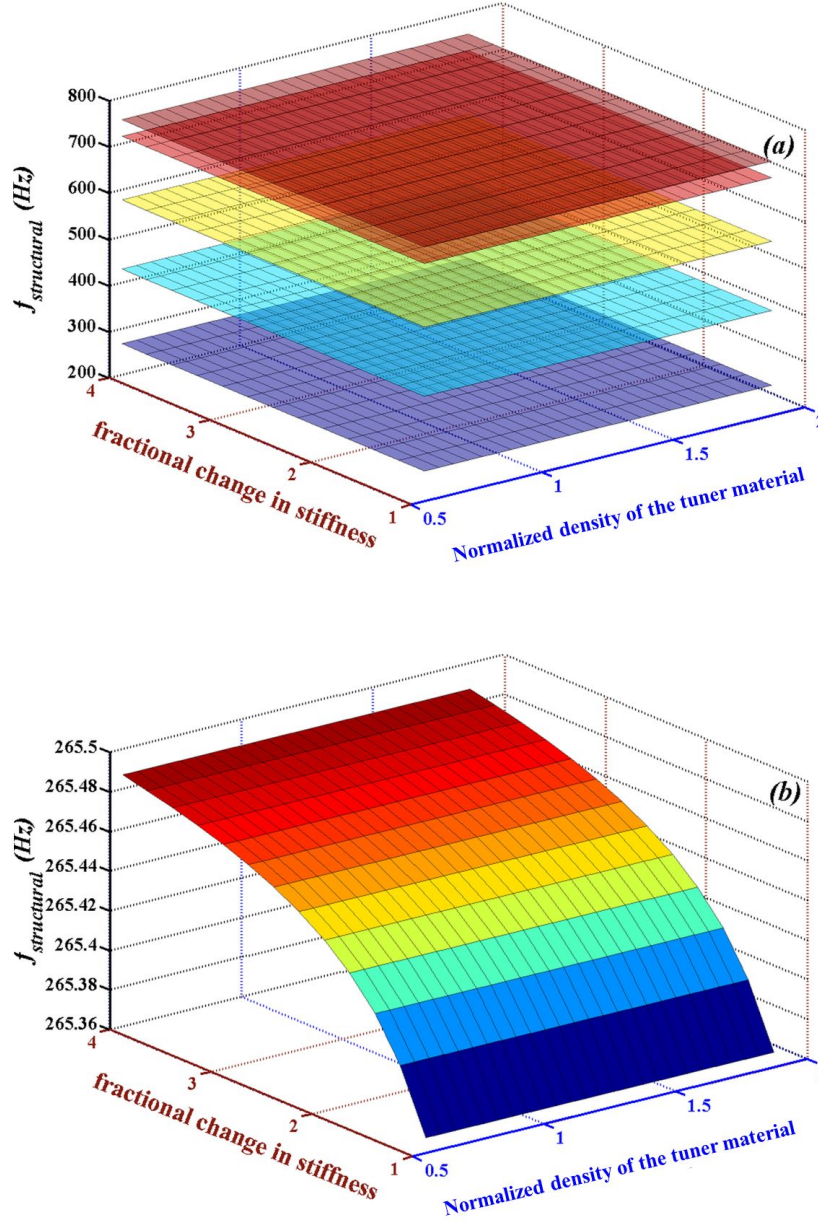


Figure 4.19: . (a) Structural mode frequencies ($f_{\text{structural}}$) as a function of the stiffness and density of the tuner material (normalized with respect to the density of titanium) for five structural modes, and (b) enlarged view of the plot of the lowest order structural mode frequency. Here, the length of the annular tuner material is taken as 20 mm.

We would like to clarify that our LFD analysis was performed considering a single stiffener arrangement. As it is shown in Fig. 4.8, single stiffener alone cannot drastically reduce the LFD; and one needs a piezo based tuning arrangement to compensate for the

same completely. However, the reliability of piezo tuner is not very well proven. Therefore, one can go for double stiffener rings [117] if fast tuning is absent. Certainly the double stiffener arrangement will increase the stiffness of the cavity assembly, and therefore the LFD will be reduced considerably; however, such stiff arrangement will be very difficult to tune, and there will be a possibility of a small amount of uncompensated LFD [117]. Such scenario may be acceptable, if one can afford to put more input RF power, and tolerate more reflection. Another interesting observation can also be made regarding the tuner arrangement. Figure 4.2(b) shows the 15° sector model of our cavity-stiffener-helium vessel assembly. Although, we did not model the tuner explicitly, but the annular cross section of the helium vessel (tinted in brown) in the model shows the probable location of the tuner arrangement, where a conventional blade type tuner will be mounted. Such a tuner and its operation are described in Ref. [119]. In this arrangement, a bellow will be there, connecting the two cylindrical halves of the helium vessel. After performing off line (slow) tuning there, the movement of the bellow will be restricted rigidly with an arrangement of nut and bolts. However, for fast tuning the piezo actuator is excited in a programmable manner as per requirement. It is placed in series with slow tuner mechanism. During slow tuning piezo element is a passive element.

In the tuned arrangement, the overall stiffness will be determined by the membrane stiffness of the helium vessel cylinder, and thus in the (slow) tuned scenario, tuner arrangement will add some more mass in the cavity-stiffener-helium vessel assembly, but will not influence the stiffness of the assembly very much, as it is shown in the above figure (Fig. 4.19). In this context, we want to mention that in our study, the tuner is placed at the mid length of the cavity. Therefore, the bending stiffness, which is quite less than the axial membrane stiffness of helium vessel's cylindrical portion, determines the magnitude of Lorentz force detuning. However, there could be another design approach, where the effect of low bending stiffness of end covers is mitigated by placing the tuner at the end of the cavity, so that it stiffens the end cover.

Chapter 5

Influence of material properties on the performance of Nb based SRF cavities

In a normal conducting RF cavity made of copper, when used in continuous mode of operation, the typical value of the achievable acceleration gradient is limited to a maximum of 2 MV m^{-1} [62]. To generate even this much gradient, normal conducting cavities have to withstand huge power dissipation on the cavity wall. Roughly 100 kW power is deposited per meter as heat loss on the normal conducting cavity wall to generate a typical gradient of 2 MV m^{-1} . Removal of such a large amount of heat load from an RF cavity is inherently difficult, therefore, for a high power accelerator used in the *cw* mode or high duty factor operation, Superconducting Radio-Frequency (SRF) cavities are the only choice. A typical gradient of 15 MV m^{-1} can be easily achieved even in the continuous mode of operating in such cavities [61]. Since Ohmic wall loss is remarkably small in an SRF cavity, heat load is not the bottleneck there. This gives an additional liberty of compromising with the shunt impedance of the cavity to optimize the shape of the cavity. For example, an SRF cavity with a large beam pipe radius is extremely advantageous for a hadron machine, where limiting the loss of beam particle in the linac is the most important goal.

However, this journey of high power and high gradient SRF cavities has spanned nearly half of a century. From Stanford Hansen Experimental Physics Laboratory (HEPL) cavities to the contemporary state-of-art SRF cavities, dedicated effort has been made to choose the suitable material, the appropriate pre and post processing techniques and certainly the optimized cavity shape. Today's SRF cavities for high power, high gradient application are mostly of niobium. However, generating an appropriate specification of the cavity material (niobium), in terms of its purity and other properties, which influences the achievable gradient and Ohmic loss of the SRF cavity immensely, has been an active field of research.

In this chapter, we will emphasize on the material aspects of an SRF cavity, and we will study how these material properties can influence the electromagnetics of a state-of-the-art niobium based high gradient SRF cavity. In Chapter 2, we have discussed how the geometry optimization of an accelerating cavity can improve its accelerating gradient E_{acc} . Here, we will show that the properties of the material may also need optimization to realize the high gradient dream at an economical cost.

5.1 Introduction

Chapter 2 shows how the electromagnetic design of the cavity has been optimized, aiming for the maximum achievable E_{acc} , under the constraint of upper limit on the fixed peak electric and magnetic field values on the surface. As mentioned there, the maximum value of the electric field E_{pk} developed on the cavity surface is limited by the field emission, whereas, the breakdown of the superconducting property of the SRF cavity material depends on the peak value of the magnetic field B_{pk} on the cavity surface.

Ohmic heat dissipation on the cavity wall raises the temperature of the cavity material. This dissipation is exceptionally small in the SRF cavities due to an extraordinarily small value of superconducting surface resistance R_s [65]. Yet in the low operating

temperature ($T \leq 2$ K) realm, extraction of this small amount of heat turns out to be a challenging problem because of the low value of thermal conductivity κ [66]. Thus R_s and κ become the primary parameters to determine the steady state temperature profile in the cavity material. However, these two parameters themselves are also strong functions of the temperature. We will show that these dependencies play a very important part in this analysis. In addition to temperature, purity of the material and the surface field B_a influence R_s and κ strongly.

Increasing the purity of a Nb made SRF cavity improves the thermal conductivity κ . At the same time, around the purity zone of our interest, R_s also shows an *increasing* trend with the increasing purity of Nb. These two trends indicate towards an optimal selection of the purity level of the cavity material niobium, for which the temperature rise in the cavity material will be minimal. It is therefore expected that cavity made of material of optimized purity level will withstand higher B_{pk} value before the initiation of magnetothermal breakdown in the superconductivity.

Purity of a material (niobium here) in the SRF community is typically characterized by the parameter called RRR *i.e.*, the residual resistivity ratio [66]. It is defined as the ratio of the resistivity of the material at room temperature and the normal state resistivity at a low enough temperature which is below the superconducting transition temperature T_c of the same material. Purity level of $RRR = 300$ has been set by the contemporary SRF community as the most recommended choice for the niobium material for SRF cavity fabrication [66]. Experimental observations are in favour as well as against this empirical choice of $RRR = 300$ standard [120]. Therefore, in this chapter, we will present a rigorous self-consistent magnetothermal analysis in the quest of an optimal choice of purity of the SRF cavity material Nb.

5.2 Material properties and the performance of the superconducting cavities

Generalities:

Low loss feature of the state-of-art SRF cavities makes them nearly a unique choice for high energy - high current accelerators operating in the continuous wave (cw) or long pulse mode [66], [120]. The Ohmic loss P_c is proportional to R_s in an RF cavity. The quality factor of an SRF cavity is a ratio of the geometry factor G and R_s , where the geometry factor is a parameter solely dependent on the cavity geometry [65]. This inverse relation between Q_0 and R_s explains why an SRF cavity shows such extraordinarily high value of quality factor ($Q_0 \sim 10^{10}$) [66]. This is why these cavities are universally the most suitable choice for the low loss-high gradient operation.

Today's SRF community widely accepts niobium (Nb) as the material for making SRF cavities to realize this low loss, high gradient goal. This choice is supported by the fact that, among the elemental superconductors, Nb has the highest value of superconducting transition temperature or critical temperature $T_c \sim 9.2$ K [121]. Along with this, relative abundance, ease in availability, formability, machinability, weldability and adequate mechanical strength even at the low operating temperature make this metal as the most suitable material for manufacturing the SRF cavities. Typically niobium is a Type-II superconductor, offering reasonably high value of the lower critical magnetic field B_{c1} [121]. Here, we want to mention that, for the type -II superconductor niobium, the typical values of B_{c1} and B_{c2} can be taken as 180 mT and 240 mT, respectively [66].

Cavities made of bulk niobium show a typical trend of Q_0 with the increasing field strength B_a . In the low field region ($B_a \sim 0 - 20$ mT), Q_0 of the cavity increases slightly. Then Q_0 shows gradually decreasing trend in the medium field region ($B_a \sim 20 - 80$ mT), which is called Q_0 slope and finally, a sharp fall occurs at higher values of the RF field ($B_a \sim 80 - 180$ mT). This sharp fall is identified as the Q_0 drop,

which indicates breakdown of superconductivity in the SRF cavity material [122], [123]. The corresponding field strength B_a at which this breakdown phenomenon occurs is denoted as the threshold magnetic field B_{th} . In fact, this is the peak RF magnetic field value B_{pk} achievable in an SRF cavity on its surface. As it has been shown in Chapter 2, ratio of B_{pk} and E_{acc} is a constant quantity for the design, *e.g.*, for our $\beta_g = 0.9$ and $\beta_g = 0.61$ cavities, B_{pk}/E_{acc} will be 3.76 and 4.56 mT/[MV/m], respectively [36], [37]. Therefore B_{th} also becomes a parameter, deciding the achievable maximum electric field gradient E_{acc} possible in the SRF cavity.

There is a constant quest in the contemporary SRF community to push the threshold magnetic field value B_{th} [121], [124] of Nb to B_{c1} (or beyond) to achieve the maximum possible gradient. In order to make the high gradient accelerator economically more viable, there is a simultaneous urge to push the value of Q_0 as high as possible.

This threshold limit B_{th} observed experimentally for an SRF cavity depends on the purity level of the cavity material as well as the processing techniques followed during cavity manufacturing. In today's scenario, a standardized recipe is followed mostly to perform the 'pre' and 'post'-processing of Nb based superconducting cavities in different SRF laboratories. Interestingly, an exact correlation between the purity level of the niobium material, and the threshold magnetic field value B_{th} is yet unknown, even after following such standardized recipe. A broad variation in B_{th} is reported by different laboratories, but most of them have chosen RRR~ 300 grade highly pure niobium as a material for manufacturing today's SRF cavity for high gradient operation.

To explain these experimental results as well as to predict an exact correlation between the achievable threshold field B_{th} and the purity of the cavity material, ample amount of theoretical works have been reported in the literature, and various models have been proposed. But these studies performed in bits and pieces in different laboratories can only explain experimental results, mostly in a case specific manner. We have performed a rigorous magnetothermal analysis, considering the functional dependence of R_s and κ

on the material purity, temperature and the applied field B_a . Aim of this study was to try to understand the requirement of the highly pure (RRR \sim 300) Nb in the high gradient operation, as well as to find out the feasibility of relatively low-purity, low-cost Nb as a choice of material for the SRF cavity.

Before we go to the main topic, let us present a brief discussion on material purity, especially the points associated with niobium. For niobium, defects and impurities are classified mostly in two types—(i) impurities due to metallic (*e.g.*, Ta, Fe, Sn etc.) or non-metallic (*e.g.* O, H etc.) inclusions, and (ii) various kinds of material defects including dislocations [125]. Through an expensive processing and purification process, metallic impurities like Ta, Ti, W and Fe are reduced to the ppm level in the Nb material [126]. Amongst them, the main metallic impurity is Ta embedded in niobium. Since it is a substitutional impurity, it should not have much influence on the electronic properties of the bulk niobium. Besides, small Ta beads surrounded by the Nb Sea might not affect the superconducting property of the bulk Nb due to proximity effect. The second type of impurities, *i.e.*, defects and dislocations are inevitable even in an ultra-pure Nb material. In fact, the process of half-cell formation of a niobium made elliptical SRF cavity may induce more defect and dislocations in the formed cavity. Therefore, the level of impurity present in the final shape of a Nb-SRF cavity may be significantly different from the impurity level of the starting Nb material. Previously, as a measure of the impurity in the superconducting material, we discussed about RRR, which is the ratio of the resistivity (ρ_{300K}) at 300 K to the normal state resistivity (ρ_{no}) at a lower temperature. We now discuss about another important parameter here - the electronic mean free path l_e , which shows a proportional relationship with the metallic purity level [66], [127], [128], [129]. For a metallic sample, ρ_{no} can be estimated from the value of the electronic mean free path l_e . Following Ref. [125] for Nb at $T_c = 9.2$ K, relation between l_e and ρ_{no} can be expressed as $l_e = 3.7 \times 10^{-16} \Omega \text{ m}^2 / \rho_{no}$. Interestingly, for the normal electrons, the values of ρ_{no} and l_e remain almost unaltered at a temperature below T_c . Both RRR and l_e vary inversely with ρ_{no} . Hence, these two parameters will be proportional to each other.

In the next two sub-sections, we discuss explicitly the functional form of R_s and κ and their dependence on the Nb purity, T and B_a .

Electrical surface resistance (R_s) :

In the presence of an RF electromagnetic field, a superconductor shows a non-zero but small resistance at a temperature below T_c (however, $T \neq 0$). Cooper pairs of a superconductor lag behind the field when subjected to an oscillating electromagnetic field, and the consequence is a partial screening of the electromagnetic field within the superconductor. Normal electrons present in the superconducting state are exposed to the field and give rise to this finite resistance. Considering their functional dependence, the non-zero surface resistance can be written as follows:

$$R_s(l_e, B_a, T) = R_{BCS}(l_e, T) \times \mathcal{F}(\bar{B}_a + C_1 \bar{B}_a^2 + C_2 \bar{B}_a^3 \dots) + R_i. \quad (5.1)$$

In the above equation, $R_{BCS}(l_e, T)$, denoted as the BCS resistance [121], shows a strong dependence on the purity level of the material. The field dependent, dimensionless multiplication term $\mathcal{F}(B_a, T)$ is a non-linear enhancement factor here, and $\bar{B}_a = B_a/T$. In the equation, R_i is the residual resistance [66], [128].

Purity of the material has a strong influence on the surface resistance and as mentioned, material purity can be measured from the electronic mean free path l_e . With the increasing purity, electronic mean free path in a material becomes quite large at a very low temperature. In that scenario, R_{BCS} reveals the true nature of the *non-local* field response of the superconductor, and this non-locality becomes prominent, when the field varies considerably within the radius l_e around a position \mathbf{r} [66], [130], [131]. This is the situation in the clean limit, where l_e is much greater than the zero field coherence length ξ_0 of the superconductor [66], [121]. In the dirty limit, where, $l_e \ll \xi_0$, electromagnetic field shows only a small variation in the length scale l_e , and the material responds locally to the field. Considering this true response of a superconductor in an RF electromagnetic

field, Mattis and Bardeen have derived the expression for the superconducting surface current $\vec{J}(\vec{r})$ from BCS formulation (including the contribution from the normal electrons as well as cooper pairs), and the superconducting surface impedance in the extreme anomalous limit [130], [132]. Based on this formulation, Reuter and Sondheimer [133] and Hook [134] have derived a generalised form for the superconducting surface impedance $Z_s = R_{BCS} + iX_s$. Following their work, we have developed a subroutine in MATLAB [135] to calculate $\mathcal{R}e(Z_s) = R_{BCS}$. Fig. 5.1 shows BCS resistance at 2 K, as a function of the purity level of the material Nb.

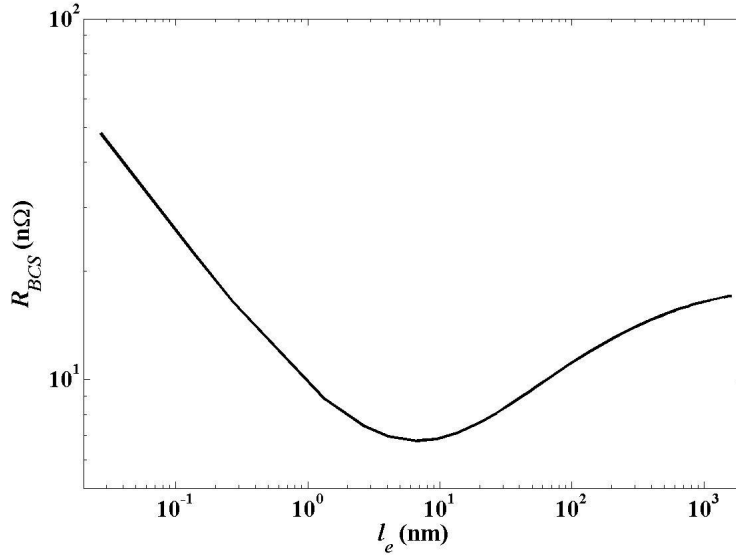


Figure 5.1: R_{BCS} (calculated using the nonlocal response of electric field) at 2 K plotted as a function of l_e for niobium, where, $\lambda_0 = 39$ nm, $\xi_0 = 32$ nm and $\Delta = 1.9k_B T_c$.

In our calculation, we took the two important parameters London penetration depth λ_0 and coherence length ξ_0 for niobium as 39 nm and 32 nm, respectively, with superconducting band gap $\Delta = 1.9k_B T_c$. Here, London penetration depth signifies the distance in depth of the material from the surface required to die down to e^{-1} times the externally applied electromagnetic field, and the other characteristic length of a superconductor is the coherence length which is the distance between two electrons in a cooper pair. As it is shown in Fig. 5.1, $R_{BCS}(l_e, T = 2 \text{ K})$ becomes minimum at around $l_e \approx 10$ nm. The value of R_{BCS} increases gradually with l_e beyond this minimum.

Interestingly, in the dirty limit, R_{BCS} values calculated from this formulation are very close to the values obtained using the local field response of the superconductor. On the other hand, in the clean limit, the deviation is significant in the value of R_{BCS} calculated using these two approaches. For an example case of Nb, with $l_e = 270$ nm, if we calculate R_{BCS} assuming local response of the material, the value will be nearly double of the value estimated from Fig. 5.1. Results obtained from our subroutine has been benchmarked with the results obtained from **SRIMP** code [131], [136] which also evaluate $R_{BCS}(l_e, T)$ values solving the BCS formulation and including the non-local field response of the material.

In the above formulation, values of $R_{BCS}(l_e, T)$ have been calculated for an electromagnetic field oscillating at 650 MHz frequency. However, here the calculations have been performed assuming that the superconducting surface resistance is not at all influenced by B_a (i.e., as if $B_a \rightarrow 0$). As the form of $R_s(l_e, B_a, T)$ is shown in Eq. 5.1, field dependent *non-linear* function $\mathcal{F}(B_a, T)$ may incorporate an enhancement in R_s subjected to the applied magnetic field B_a . This enhancement in the superconducting resistance happens due to the field induced reduction in the superconducting band gap. Applied field B_a normally increases the chances of *pair-breaking* of few quasi particles like Cooper pairs. For a Type-II superconductor (like Nb) in the clean limit¹, the closed form of the enhancement factor can be taken as [138],

$$\mathcal{F}(B_a, T) = \frac{8}{\pi\beta_0^2} \int_0^\pi \sinh^2\left(\frac{\beta_0}{2}\cos\tau\right)\tan^2\tau d\tau, \quad (5.2)$$

where the quantity $\beta_0 = \frac{\pi}{2^{3/2}} \frac{B_a}{B_{c1}} \frac{\Delta(T)}{k_B T}$.

Fig. 5.2 shows calculated values of the enhancement factors $\mathcal{F}(B_a, T) = R_s/R_{BCS}$ as a function of β_0 . From Eq. 5.2 the values of the factor $\mathcal{F}(B_a, T)$ were calculated considering the value of the critical magnetic field $B_{c1} = 200$ mT.

¹A pragmatically different formulation for the dirty superconductors is described in Ref [137], where the field-induced suppression of the superconducting surface resistance is explained in an excellent way.

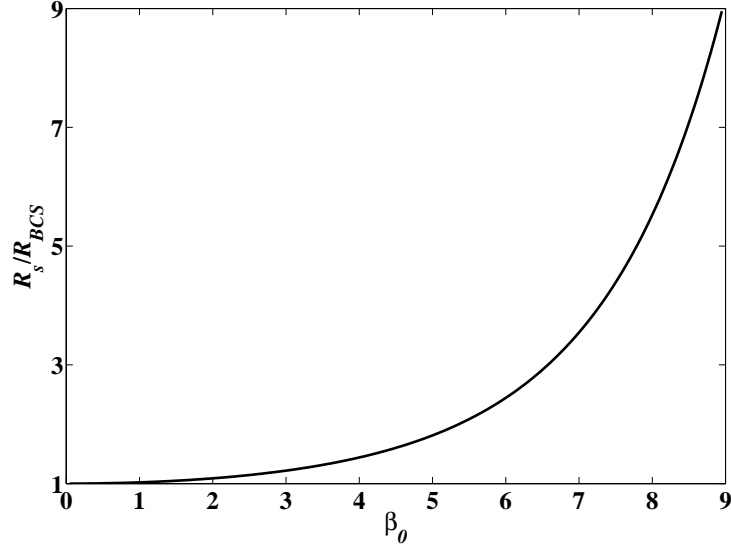


Figure 5.2: Enhancement factor $\mathcal{F} = R_s/R_{BCS}$ plotted as a function of β_0 .

In this analysis, the value of the residual resistance was kept fixed at $R_i = 5 \text{ n}\Omega$. As it is realized, R_i is a part of the superconducting surface resistance, which is present in the superconducting material even at $T = 0 \text{ K}$. This value remains nearly unchanged up to the critical temperature T_c . Probable origins of the residual resistance are the trapped magnetic flux or the formation of the Nb-H, etc. [128]. We performed this analysis with experimentally observed value of R_i . However, in a more rigorous calculation, one may consider the weak dependence of the residual resistance on the temperature, B_a or even on the purity level of the material. Based on the above formulations, a subroutine was developed to calculate $R_s(l_e, B_a, T)$.

For the magnetothermal analysis, thermal conductivity κ is another important parameter. We will discuss the functional form of κ and its dependence on parameters like material purity on the temperature in the next paragraph.

Thermal conductivity of the SRF cavity material (κ):

In a metal, heat is propagated primarily via diffusion. Heat energy is transported due to the microscopic movement of two types of carriers-the conduction electrons, and the lattice vibrational modes, *i.e.*, phonons [129]. Hence, summarizing the contributions from

these two carriers, we can express the total thermal conductivity of κ of a metal as $\kappa(T) = \kappa_{en}(T) + \kappa_L(T)$ [139], [140], where, suffixes ‘en’ and ‘L’ indicate respective contributions from electrons and phonons. In the diffusion process, contribution from the conduction electrons dominates in a typical metal. Phonon modes are usually suppressed as a result of their scattering from the electrons, impurities and material defects. Though at a very low temperature, phonons may contribute noticeably to the heat transport. This will be discussed later.

Usually, scattering of the carriers limits the thermal conductivity of a metal. Thermal carriers may scatter from impurities, material defects and other thermal carriers. Scattering from the impurities influences electronic contribution in the thermal conductivity. In the normal conducting state, Wiedemann-Franz law correlates this contribution κ_{ei} with the normal state conductivity σ_{n0} as $\kappa_{ei} = L_0 \sigma_{n0} T$ for a metal [140], where L_0 is the Lorentz number. Accordingly, the quantity κ_{ei} is proportional to σ_{n0} and improves monotonically with the increasing purity of the material. This is the impetus, which instigates the SRF community to use high RRR material. Scattering of free electrons from lattices also limits the electron’s contribution in the thermal conduction. The corresponding thermal conductivity $\kappa_{el} = 1/aT^2$ commensurates well with experimental results. The parameter a here is an estimation of the amount of momentum transfer with the lattice vibrations. Analyzing electron-phonon interaction, theoretical value of a can be calculated from the formula $a = (6/\pi^2) 2^{1/3} N_a^{2/3} I_5(\infty) \cdot [K_e(295K) \cdot \Theta_D^2]^{-1}$ [140], where Θ_D and N_a denote Debye temperature and the effective number of conduction electrons per atom, respectively. Here, $I_5(\infty) \approx 124.4$ is the fifth order Grüneisen integral. For Nb, considering $N_a = 1$, $\Theta_D = 275$ K and $K_e(295K) = 54$ W m⁻¹ K⁻¹ as given in Ref. [140], analytically we can estimate $a = 2.3 \times 10^{-5}$ m W⁻¹ K⁻¹. As it is reported in Ref. [140], measured value of a is found to be significantly smaller than that of this analytically estimated value. In our analysis we have used $a = 7.52 \times 10^{-7}$ mW⁻¹K⁻¹ [139], measured for a BCP treated Nb sample reported in the Ref. [139].

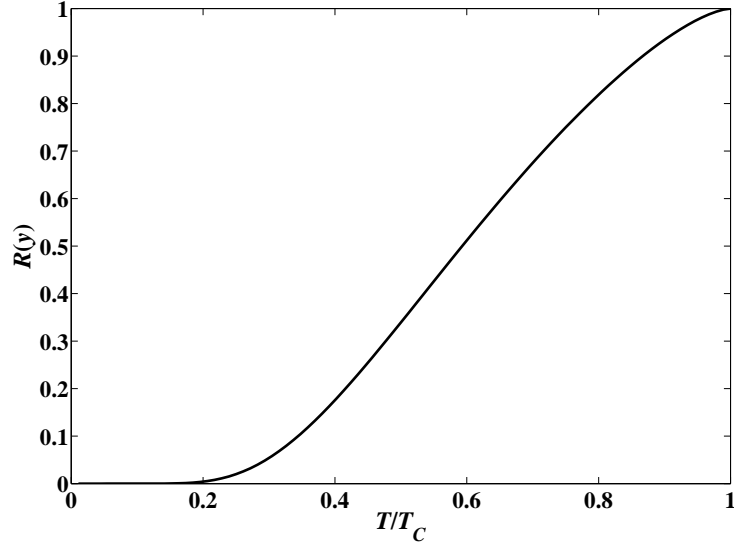


Figure 5.3: Plot of $R(y)$ as a function of T/T_c .

Number of free electrons in a metal decreases steadily with decreasing temperature. Particularly, in the superconducting state of a material, there is a drastic reduction in the number of free electrons because of the formation of Cooper pairs [121]. Analytical estimation of the thermal conductivity considering reduction in the number of free electrons was performed by Bardeen *et. al.* [141]. Following their work, we have estimated the scaled-down contribution in the electronic thermal conductivity κ_{es} from κ_{en} in the superconducting state of a material as follows:

$$\frac{\kappa_{es}}{\kappa_{en}} = R(y) = \frac{1}{f(0)} \left[f(-y) + y \ln(1 + e^{-y}) + \frac{y^2}{2(1 + e^{-y})} \right], \quad (5.3)$$

where $f(-y)$ is the Fermi integral, and is defined as $f(-y) = \int_0^\infty (z/[1 + \exp(z + y)])dz$, and $y = \Delta(T)/(2\kappa_B T)$. As it is shown in Ref. [141], the value of $R(y)$ tends to 0 as T tends to 0, and approaches unity as the temperature approaches towards the transition temperature, (i.e. $T \rightarrow 9.2$ K). Variation of this scale factor $R(y)$ is shown in Fig. 5.3 as a function of the temperature $T \leq T_c$.

Next, we discuss the contribution κ_L arising from the crystal lattice. Lattice or

phononic contribution in the thermal conductivity is primarily influenced by the two scattering mechanisms- (i)scattering of phonons by the electrons, as well as (ii) by the impurities, defects or lattice dislocations. For a metal in the normal conducting state, scattering of phonons from the electrons give rise to a thermal conductivity $\kappa_{l-e}(T) \propto T^2$ in the low temperature regime [140]. On the other hand, in the superconducting state, such contribution will be enhanced considerably with the decreasing number of free electrons, and we write $\kappa_{l-e}(T) = DH(y)T^2e^y$. In the range $0 < T/T_c < 1$, $H(y)$ shows a flat maximum value of 1. Again, Scattering of phonons from the impurities limits the conductivity $\kappa_{l-i}(T) = Bl_{ph}T^3$, where B is a constant depending on the material parameter, and l_{ph} is the phonon mean free path. Including all the contributions, we write the expression for the total thermal conductivity $\kappa(T, l_e)$ as follows:

$$\begin{aligned}\kappa(T, l_e) &= \kappa_{es}(T) + \kappa_L(T) \\ &= R(y) \left(\frac{1}{L\sigma_{no}T} + aT^2 \right)^{-1} + \left(\frac{1}{DT^2e^y} + \frac{1}{Bl_{ph}T^3} \right)^{-1}.\end{aligned}\tag{5.4}$$

Interestingly, at a very low temperature, phononic contribution plays an important part in deciding the total thermal conductivity $\kappa(T, l)$ of a superconductor. For a defect /dislocation free highly pure metal, there is the likelihood of a phonon peak at a very low temperature, which can result in an enhancement in $\kappa_L(T)$. For Nb, phonon peak improves the conductivity (thermal) at a temperature around $T = 2$ K. However, the likelihood of this enhancement of κ almost entirely depends on the types of post-processing that an SRF cavity has undergone. It is because the cavity forming processes normally introduce ample defects and dislocations in the cavity geometry, causing a considerable reduction in the phonon mean free path l_{ph} as well as in the height of the phonon peak, which affects κ_{l-i} . In this context of post-processing of the cavity, annealing in particular may restore this phonon peak partly or sometimes completely. Fig. 5.4 explains the importance of a typical post-processing of SRF cavities. In this figure, we have shown the variation of $\kappa(T, l_e)$ of Nb with temperature for three different

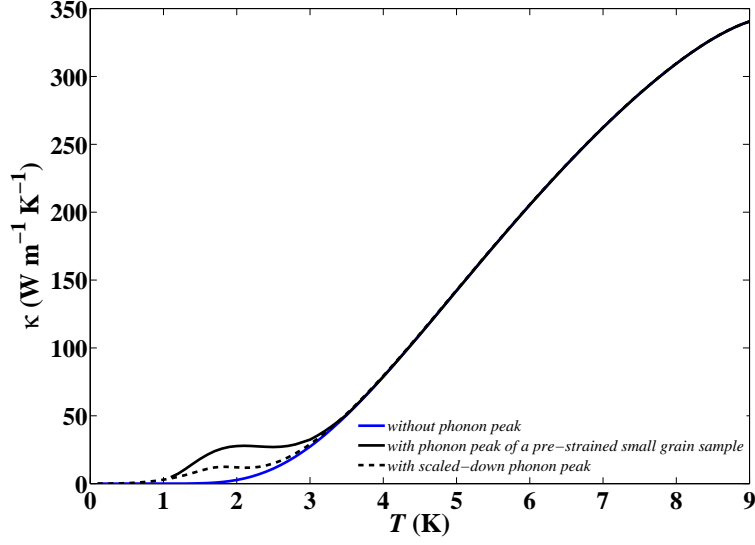


Figure 5.4: Total thermal conductivity κ of RRR 300 graded niobium plotted as a function of temperature T . Here the blue curve represents the case without the phononic contribution. The enhancement in κ due to phonons at low temperature is observed in a pre-strained, small grain niobium sample [126], which is shown in the continuous black curve. Here the dotted black curve represents the case with reduced phonon peak in $\kappa(T)$, in commensurate with the experimental observation in Ref. [127] for an SRF cavity.

cases of post processing. First case is a pre-strained small grain sample of Nb. There, $\kappa(T)$ is enhanced near 2 K, showing the signature of a phonon peak. To generate this plot from Eq. 5.4, we have considered $D = 350 \text{ mK}^3\text{W}^{-1}$ and $Bl_{ph}=0.25 \text{ mK}^4\text{W}^{-1}$ [142]. The other case shows the thermal conductivity without considering any phononic contribution. Also, in Fig. 5.4, the third case represents a practical situation where the phonon peak is not completely destroyed, but it is suitably scaled down according to the experimentally observed results at 2 K as is reported in Ref. [143].

For a superconductor, normally the phonon peak appears at a very low temperature (around $T = 2 \text{ K}$). Therefore, enhancement in κ will be effective mainly in the case where liquid helium bath temperature is kept at a value $T_B \leq 2 \text{ K}$ in particular. If we want to operate the cavity, keeping the bath temperature $T_B = 4.2 \text{ K}$, which is the boiling point of helium, there the phononic contribution will show almost no effects.

In the next sub-section, we will discuss another important contributor of thermal resis-

tance, especially in this low temperature regime, that is ‘Kapitza resistance’ which plays an important part in deciding the heat diffusion in the case of an SRF cavity.

Kapitza Resistance(R_s) : To some extent, Kapitza resistance R_k is a strange thermal resistance, which develops at the interface of two materials [66]. Until now, there is no universal model available explaining Kapitza resistance completely, yet origins of this resistance are mostly due to scattering and reflection of the phonons from interface as well as the difference amid the acoustic properties of the media. Niobium-based superconducting cavities are typically operated at a temperature close to 2 K and there the heat is diffused from metallic wall to the insulator i.e. the superfluid helium. In this low temperature regime, Kapitza resistance contributes prominently, causing a temperature jump $\Delta T = (T_S - T_B)$ across the phonon mediated interface, where T_S denotes the temperature of the cavity outer wall. This difference in temperature determines \bar{Q} i.e. the heat flow through per unit area of interface per unit time and is estimated as $\bar{Q} = h_k(T_S - T_B)$. Here the quantity $h_k(= R_k^{-1})$ is denoted as the Kapitza conductance. Following Ref. [144], for the ~ 2 K operation, h_k is estimated in units of ‘W m⁻² K⁻¹’ as

$$h_k = 200T_S^{4.65} \left[1 + \frac{3}{2} \left(\frac{T_S - T_B}{T_B} \right) + \left(\frac{T_S - T_B}{T_B} \right)^2 + \frac{1}{4} \left(\frac{T_S - T_B}{T_B} \right)^3 \right]. \quad (5.5)$$

So far, we have discussed the required theoretical background relevant to our analysis. In the next section, we will present our work and findings, but before that, we perform a brief review on the contemporary work and several interesting theoretical analyses reported in the recent past.

5.2.1 A review on the contemporary works

Amongst the contemporary work, Refs. [145] and [146] report analyses where the approach followed is relatively simple, R_s is assumed to be a function of temperature

alone. In comparison, more realistic models were proposed by Weingarten [127] and Gurevich [138]. These models perform thermal breakdown calculations, integrating the field dependent nonlinear BCS surface resistance in the analysis. Incorporating this non-linear BCS resistance model in their analysis, Bauer *et. al.* [143] proposed their thermal feedback model (TFBM) and attempted to explain few experimental results for different SRF cavities. However, in their TFBM model, non-linearity in the BCS surface resistance is introduced in the form of a truncated scale factor $\tilde{\mathcal{F}}(B_a, T) = (\bar{B}_a + C_1 \bar{B}_a^2)$. Also, they have used the parameter C_1 as a free parameter, which we found rather arbitrary, to attain a proper match with the experimental data. Due to this arbitrariness, this model cannot be used in our calculation directly. In the work reported in Refs. [127] and [138], non-linear BCS surface resistance is calculated in a more sophisticated way. However, like the previously explained TFBM, here too the heat load is calculated considering local Ohmic relation only. Arbitrariness of the TFBM was avoided with a fixed value of $C_1 = 2$ in the magnetothermal analysis performed by Vines *et. al.* [147]. They have included the influence of non-local response of the electromagnetic field also, while calculating the surface resistance, and have studied the trend for the medium field Q_0 slope considering a few values of RRR. Although, they have not calculated B_{th} values, noticeably the increasing trend of the threshold magnetic field with the reduced value of RRR is observed in their analysis, which corroborates with our results obtained based on a rigorous magnetothermal analysis. Nonlocal response of the electromagnetic field was included in the model described in Ref. [148]. However they have calculated the R_s without considering the field dependency in their calculation.

In our magnetothermal breakdown analysis, Ohmic heat load has been calculated using the formula of R_s , which includes the intricacies of the nonlocal, as well as the nonlinear response to the applied field. Non-locality was studied here also as a function of the purity level of the material. In the calculation of thermal conductivity κ , we have considered proper dependence on temperature and the purity level of the material. Before we complete this review, we must mention the recent work of Gurevich [137],

where he proposed a new model of non-linear superconducting surface resistance based on density of state (DOS) smearing. Using this model, he has explained experimental results obtained from Ti or N-treated Nb cavities. It is excellent that the field induced suppression of surface resistance in Ti or N-treated Nb cavities can be explained by this model. Our analysis is restricted only to the cavities made of medium and high purity (bulk) niobium, and we did not consider the effect of doping. Therefore, the formulation developed by Gurevich [137] is not directly applicable for our purpose.

5.3 Numerical calculations and analysis of results

In this section, we will present the result of our calculations with appropriate analyses. In an SRF cavity, Ohmic heat load will be generated on the inner wall of the cavity exposed to the RF electromagnetic field. The generated heat will diffuse through the thickness of the metallic wall, will finally experience Kapitza resistance at the Nb-He interface and finally will be deposited in the helium bath maintained at a temperature $T_B = 2$ K. In the steady state, the heat balance can be written as

$$\frac{1}{2\mu_0^2} R_s(T_{s0}, B_a, l_e) B_a^2 = -\kappa(T, l_e) \nabla(T) = h_k(T_S - T_B), \quad (5.6)$$

where T_{s0} denotes the steady state temperature of the cavity inner wall. This temperature reduces to T_S after crossing the Kapitza resistance developed in the solid-liquid contact layer.

In this numerical calculation, we have evaluated $R_s(T, B_a, l_e)$ and $\kappa(T, l_e)$ from the model described in Sec. 5.2. Our analysis considered the purity level of the material as an important input parameter. The purity level is indicated by the electronic mean free path l_e . An appropriate model for Kapitza conductance $h_k(T_S, T_B)$ is described in the subsection 5.2. All these parameters have been calculated considering their functional dependence on the temperature to ensure self-consistency. Therefore, in every step of

this numerical analysis, T is calculated accurately and is updated as an input to the parameters depending on it.

This analysis has been performed in a sequential manner, as described below:

1. Purity level of the material is assumed in terms of l_e
 - (a) Steady state value of $R_s(B_a, l_e, T)$ is estimated iteratively from a predicted value of the temperature as a function of the applied field B_a for that purity level,
 - (b) For the cavity, Q_0 value is calculated from the steady state value of $R_s(B_a, l_e, T)$, and
 - (c) The above two sequence is repeated with the increasing value of B_a until the breakdown is observed. (Here, breakdown is indicated by a sudden rise in the value of R_s .) Corresponding B_a value at the breakdown denotes the threshold value of the magnetic field B_{th} .
2. All the sequences are repeated for another value of purity level of the material.

Benchmarking calculations were first performed, where the study on dependence of the threshold field on the purity level of the material, considering the well-known TESLA cavity with resonant frequency 1.3 GHz [61]. In the second part of this analysis, calculations were performed using geometries, as well as properties, of the optimized ISNS cavities. In this calculation, the frequency value, wherever required, was considered equal to the resonant frequency of ISNS cavity, which is 650 MHz [36] [37].

Model used in the simulation:

For the first phase of our calculation to benchmark our methodology for analyzing the dependence of B_{th} on the purity level of the material, we have considered a 2.8 mm thick infinite Nb slab with planer geometry. One side of this slab is considered to be exposed to a spatially uniform RF electromagnetic field resonating at 1.3 GHz. This is the heat

generation surface. Increasing electromagnetic field strength will increase the steady state temperature of the surface. Another side of this infinite slab is considered to be in contact with liquid helium maintained at $T_B = 2$ K. As described, because of Kapitza resistance, surface temperature of this side of the slab T_S will be more than T_B . This simple model is described in Fig. 5.5.

In the real case, cavity and the magnetic field are essentially three-dimensional. Therefore, the simple model used here, might appear to be far from reality. However, because of the small thickness compared to curvature radius, the heat propagation through the cavity wall is mostly in the direction normal to the wall surface. Therefore, the realistic situation can be very well approximated with the model we have proposed. In this infinite slab with planer surfaces, heat will flow in one-dimension (1 D). However, in order to crosscheck the assumption, we have also performed the analysis for few cases with the three dimensional (3 D) geometry of the cavity using ANSYSTM. Results obtained using 3 D model were within a margin of 2 to 3 % deviation from the results obtained using the calculations performed with this 1 D model. In order to analyze this 1 D simple geometry, a code was written in MATLAB, using subroutines, which we have described in Sec. 5.2 to calculate $R_s(T, B_a, l)$ and $\kappa(T, l)$.

Numerical calculations: process benchmarking:

In our detailed magnetothermal analysis, converged values of R_s , κ and Q_0 were calculated in the steady state, considering three different phononic contributions in the total thermal conductivity as described in Fig. 5.4. Also, as mentioned, material parameters were taken as important input parameters in the analysis.

First, we performed the calculation for a fixed value of $\sigma_{no} = 2.069 \times 10^9 (\Omega m)^{-1}$. For a Nb sample, this corresponds to a value of $RRR \sim 300$. Fig. 5.6 shows the variation of Q_0 as a function of B_a , obtained from this magnetothermal analysis. For this calculation, we have considered a value of the residual resistance $R_i \sim 5 n\Omega$.

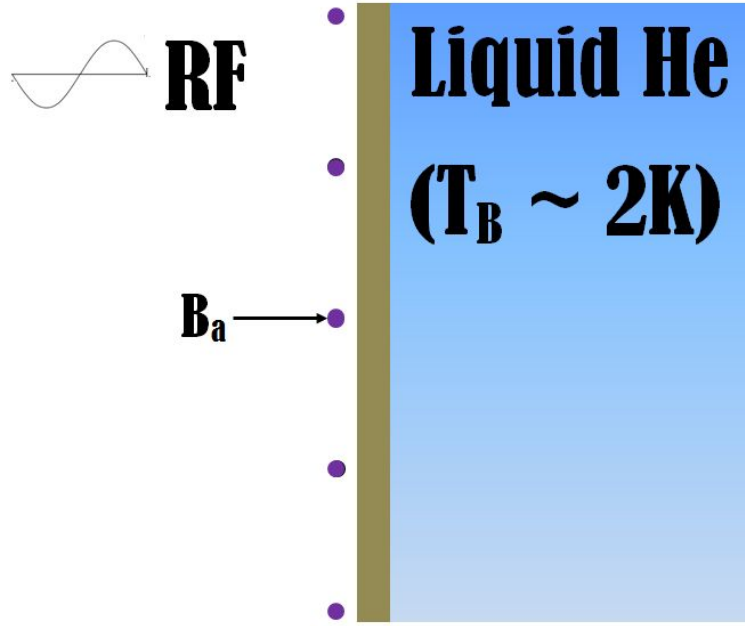


Figure 5.5: Model of a 2.8 mm thick infinite Nb plate geometry. Applied magnetic field B_a on the surface is denoted by the ‘dot’s. Inner surface of the plate is in vacuum, whereas the outer surface of the plate is immersed in a liquid helium bath at 2K.

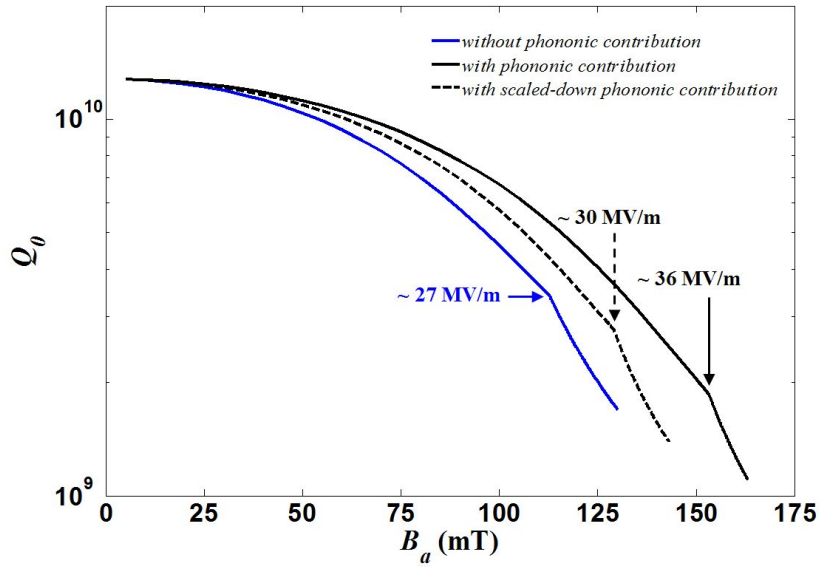


Figure 5.6: For 1.3 GHz TESLA cavity made of RRR 300, Q_0 is plotted as a function of B_a , considering three possible variations of $\kappa(T)$ described in Fig. 5.4.

As observed in Fig. 5.6, the corresponding Q_0 values drop down sharply beyond a certain value of the applied field B_a . This value is recorded as the threshold value of the magnetic field B_{th} . Among these three plots, the results that we have generated without including phononic contribution in the thermal conductivity κ , shows a sharp decrease of Q_0 , which starts approximately at a value of $B_{th} = 114$ mT; whereas the curve calculated considering full phononic contribution gives the corresponding value of $B_{th} \approx 154$ mT. Another calculation with κ corresponding to a scaled down phononic contribution, results in a $B_{th} \approx 130$ mT. Here the 2.8 mm thick Nb-slab, which we have chosen, corresponds to the wall thickness of the 1.3 GHz TESLA cavity, as described in Ref. [61]. From the same reference, for a value of $B_{pk}/E_{acc} = 4.22$ mT/[MV/m], we have calculated E_{acc} values corresponding to these three threshold magnetic field values as 27, 30 and 36 MV m⁻¹. Interestingly, the gradient calculated without considering phononic contribution in κ , is in good agreement with the experimental result reported in Ref. [61]. Figure 12 of that reference, describes the plot of Q_0 vs. B_a i.e., the applied field with a similar trend as observed in our calculation. For the same TESLA geometry, another reference (Ref. [143]) gives a value of $E_{acc} \sim 40$ MV m⁻¹, which is close to the theoretical value obtained considering full phononic contribution in this magnetothermal analysis. Reasonable proximity between these analytical results and the experimental values certainly benchmarks the approach followed in this analysis.

Here, we want to point out one interesting observation. Near breakdown, when the applied field approaches B_{th} value, corresponding temperature of the cavity inner-wall goes well beyond the region where phononic contribution is significant in the thermal conductivity κ . In the analyses, still the threshold field values differ depending on the different phononic contributions. Apparently the above argument and the observation may seem to contradict each other, however, the reason is the high sensitivity of cavity surface temperature with magnetic field near the breakdown.

Numerical calculations considering the influence of the impurities :

In the next part of our analysis, we repeat the same procedure for different values of

the purity level of the material. We can visualize as if we are doing calculation for different niobium samples with different levels of purity (which corresponds to samples with different σ_{no} values). We performed this analysis for a range of impurity values. We have calculated the corresponding breakdown limits for niobium material with different purity values. Figure 5.7 describes the scenario, where the three curves represent the results calculated considering three different phononic contributions in κ - no phononic contribution case, scaled down phononic contribution case and full phononic contribution case.

Among these three plots shown in Fig. 5.7, results obtained without considering the phononic contribution in the calculation of κ shows a rapid increment primarily with the increasing purity level of the material. Here, the purity is represented by the σ_{no} values shown in the horizontal axis in a logarithmic scale. Afterwards, the rise in the corresponding threshold values comparatively reduces with the increasing value of the purity. As it is shown in the figure, B_{th} value reaches from 92 to 115 mT when corresponding σ_{no} value changes from $6.89 \times 10^8 (\Omega \text{ m})^{-1}$ to $2.07 \times 10^9 (\Omega \text{ m})^{-1}$. These two values of σ_{no} actually represent RRR values of 100 and 300 respectively. In the other two curves, corresponding to the scaled down and the full phononic contribution in κ , the trend is a bit interesting. There, B_{th} value increases with the increasing purity level of the material and at around $\sigma_{no} = 1.724 \times 10^7 (\Omega \text{ m})^{-1}$, these two curves attain the corresponding maximum values of B_{th} . These B_{th} values are ~ 125 mT and ~ 176 mT, respectively for the cases considering the scaled down and full phononic contribution. Interestingly, for the higher values of σ_{no} , threshold magnetic field values nearly saturate. In the Table 5.1, B_{th} values corresponding to the RRR 100 and 300 material are given for the three cases of phononic contributions.

Above observation leads to an interesting corollary. Proton or H^+ accelerators dedicated for the ADSS or SNS application accelerates *cw* /pulsed beam mostly up to an energy 1 to 1.5 GeV. There, depending on the velocity of the beam, cavities are required

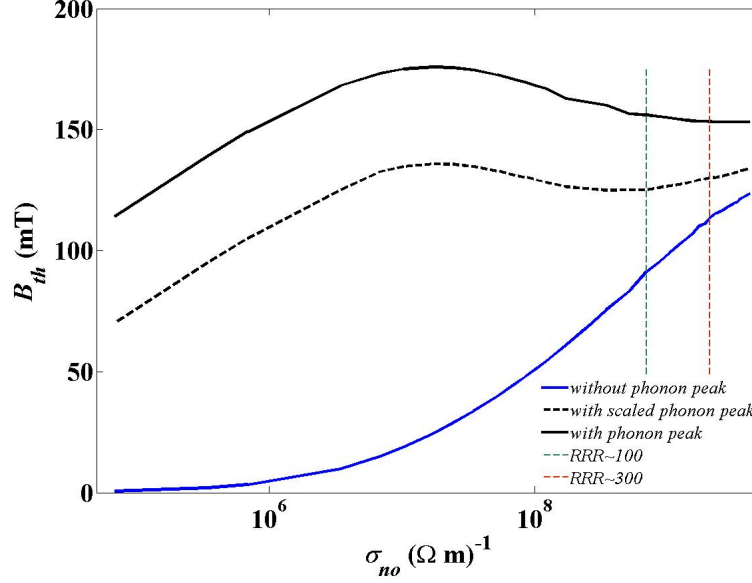


Figure 5.7: For 1.3 GHz TESLA cavity, B_{th} values are plotted as a function of σ_{no} . Here, the blue curve represents the case where phononic contribution is not considered. The continuous and the dotted black curves here represent the cases of full and scaled down phononic contribution, respectively.

Table 5.1: Q -values at B_{th} for 1.3 GHz TESLA cavity.

	RRR 300 Niobium		RRR 100 Niobium	
	$B_{th}(\text{mT})$	$Q(B_{th})$	$B_{th}(\text{mT})$	$Q(B_{th})$
without phonon peak	115	3.28×10^9	92	4.94×10^9
with scaled phonon peak	131	2.67×10^9	126	3.35×10^9
with phonon peak	154	1.84×10^9	157	2.04×10^9

to produce a typical accelerating gradient of 20 MV m^{-1} . Our analysis shows, this gradient is easily obtainable from the cavities made of RRR~100 grade Nb, because RRR~100 grade Nb-cavities will give similar performance as cavities made of RRR~300 grade material. Purity level of the material has important consequences in the cost reduction and mechanical strength point of view. For the above analysis have taken $R_i = 5 \text{ n}\Omega$.

Now we will discuss the implication of this material purity issue on the 650 MHz SRF cavities, which will be used in our ISNS program, as well as in the projected Indian ADSS program. There will be two families of 5-cell elliptical SRF cavities, i.e., $\beta_g = 0.61$

cavities for medium energy and $\beta_g = 0.81$ or $\beta_g = 0.9$ for high energy section of the ISNS linac. We have done the same analysis, as discussed for the previous work, on these cavities. The only difference is that, these cavities will not be operated up to that gradient corresponding to the breakdown limit. Instead, we will stop at a value of B_a , when the Q_0 value reduces to 50 % of the zero field value. These results are described in Fig. 5.8, where the three curves correspond to the three different contributions from the phonon peak used in the calculation of this magneto-thermal analysis. Here the dotted line shows $Q_0 \approx 7.18 \times 10^9$ which is the half value of the zero field Q_0 . As shown in the figure, the three curves representing the null, scaled-down and full contribution of the phonons in κ , reach $Q_0 \approx 7.18 \times 10^9$ at 109, 129 and 140 mT value of the peak / applied magnetic field value, respectively. Following Ref. [37], at a design value of $B_{pk}/E_{acc} = 4.56 \text{ mT}/(\text{MV}/\text{m})^{-1}$, these peak magnetic field values will correspond to an accelerating gradient of $\sim 24 \text{ MV m}^{-1}$ achievable in the case of niobium made ISNS SRF cavities made of RRR ~ 100 material, even in the case of a zero phononic contribution in κ . We close this discussion summarizing threshold magnetic field limits and corresponding quality factor values achieved in the case of RRR 100 and 300 graded niobium material in Table 5.2.

Not only the cost reduction, another major advantage we can anticipate in case of a RRR ~ 100 cavity in comparison to the RRR ~ 300 cavity is that we can achieve 10% higher value of Q_0 . The implication is that the heat load in these cavities will be less i.e. comparatively less load will be transferred the cryogenic plant.

Table 5.2: Q -values at B_{th} for 650 MHz ISNS cavity.

	RRR 300 Niobium		RRR 100 Niobium	
	$B_{th}(\text{mT})$	$Q(B_{th})$	$B_{th}(\text{mT})$	$Q(B_{th})$
without phonon peak	134	5.20×10^9	109	7.27×10^9
with scaled phonon peak	154	3.92×10^9	147	5.00×10^9
with phonon peak	180	2.46×10^9	184	2.64×10^9

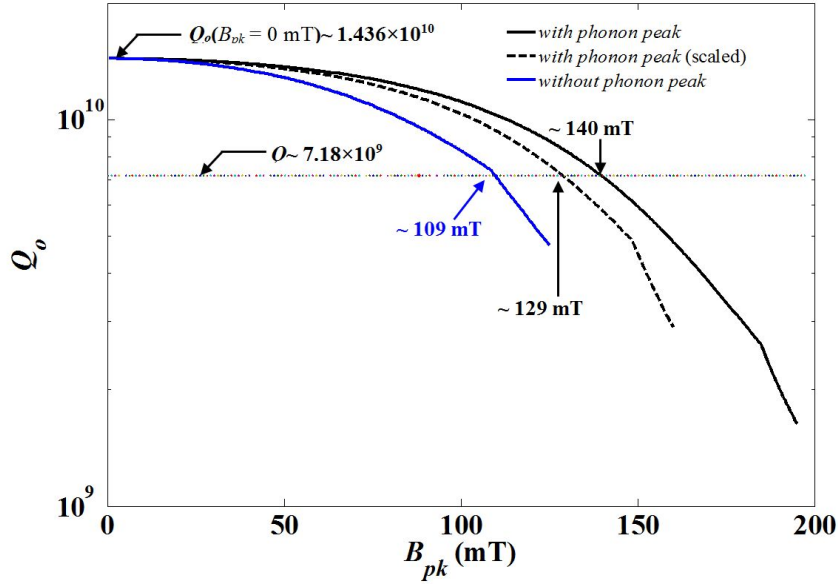


Figure 5.8: Plot of Q_0 as a function of B_a , as obtained from the analysis performed on an ISNS cavity [36] for a fixed value of RRR 100 grade Nb, for three possible variations of $\kappa(T)$. For these calculations, we considered 4 mm thick plate geometry. We have taken $R_i = 10 \text{ n}\Omega$ in this analysis.

5.4 Conclusions

In this chapter, we have discussed a rigorous magnetothermal analysis of a Nb-based SRF cavity immersed in a liquid helium bath kept at a fixed temperature 2 K. In a sense, this analysis is an extended review on the correlation between purity level of the SRF cavity material, *i.e.* niobium and the threshold magnetic field value B_{th} . In this analysis:

- (1) σ_{no} was used as an indicator of the purity level of Nb material.
- (2) R_s and κ were evaluated as a function of B_a , T and the purity level of the material.
- (3) Kapitza resistance was calculated as a function of T_B and T_S .

The analysis shows that relatively less pure niobium of RRR 100 can be an interesting alternative for the SRF cavities designed for the SNS or ADSS application. This choice will reduce the material cost of the cavity, as well the cavity will produce less heat load to the cryogenic plant. As per the ‘Table-4 of ASTM B393’ standard, another advantage of this reactor graded (RRR 100) niobium is around 30% higher value of the mechanical

strength compared to the highly pure RRR 300 graded niobium. Therefore, one can consider a reduction in the thickness of the cavity wall and based on this thickness reduction, two major improvements can be possible:

- (i) this will reduce the material requirement; hence cost will be further reduced.
- (ii) reduction in the wall thickness will reduce the thermal resistance of the material, and we may go for higher accelerating gradient.

Based on our analysis, we have generated a specification of the material for niobium based SRF cavities in terms of the three basic parameters σ_{no} , κ and α respectively, where the diffusivity $\alpha = \kappa/(\rho \times C_p(T))$. This corresponds to RRR 100 graded niobium with typical values of $\sigma_{no} \sim 6.89 \times 10^8 (\Omega\text{m})^{-1}$, and $\kappa \sim 138.68 \text{ Wm}^{-1}\text{K}^{-1}$ and $\alpha \sim 0.005 \text{ m}^2\text{s}^{-1}$. Here $C_p(T \sim 9.3 \text{ K}) = 3.36 \text{ J Kg}^{-1}\text{K}^{-1}$ [149]. These parameters are specified at a temperature 9.3 K.

In this chapter, we presented an argument that because of the small thickness of the cavity wall compared to its curvature, heat will diffuse mainly in the direction perpendicular to the wall surface. This magnetothermal analysis was also extended for the three-dimensional (3D) model and calculations were performed for a few cases. Though final conclusions were no different, this 3D analysis can give extra information in terms of the temperature profile along the inner surface of the cavity wall. One example is presented in the following paragraph.

As mentioned earlier, for this magnetothermal analysis of an infinite niobium slab, computer programs were written in MATLAB to solve the 1 D heat diffusion equation. Again, to estimate the steady state three dimensional solutions for the converged values R_s and κ , another computer programs were written in ANSYSTM, using ANSYSTM APDL. For this calculation, we have considered the bath temperature $T_B = 4.2 \text{ K}$. This is because, in this case, contribution from the phonon peak will not affect much the calculation of κ . Keeping the azimuthally symmetric field configuration in the $\text{TM}_{010-\pi}$ mode, and the other symmetries in mind, we modelled a 5° sector model of this cavity half-cell for the

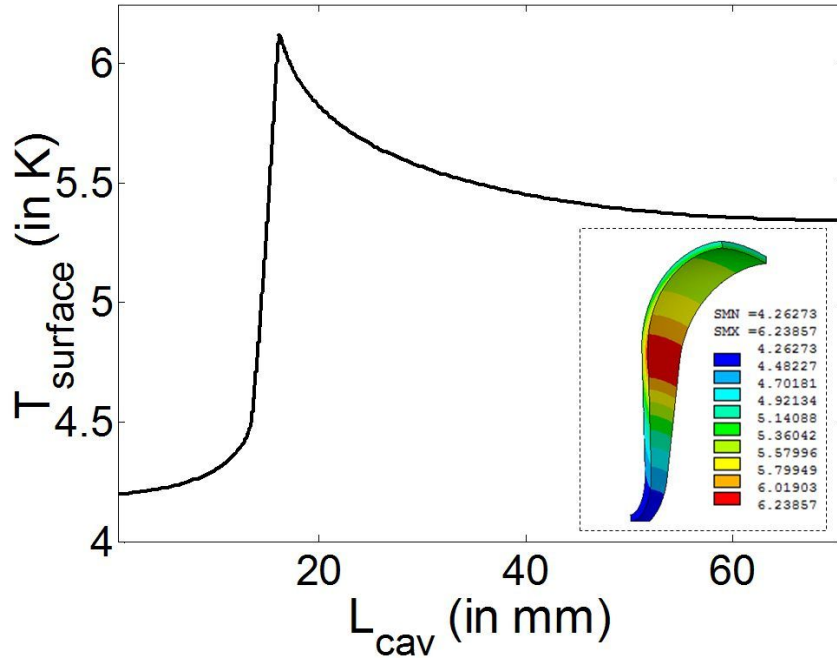


Figure 5.9: Surface temperature variation along the length of the cavity, obtained from a three-dimensional analysis. Picture shown in the inset is the ANSYSTM generated surface profile of the temperature.

3D analysis. Of course, we have considered the same wall thickness of 2.8 mm for both the cases.

In this example, the analysis was performed for a value $\sigma_{no} \sim 6.89 \times 10^8 (\Omega m)^{-1}$ (which corresponds to the RRR 100 graded material). From the 3D and 1D analyses, threshold magnetic field values were obtained around 117 mT and 123 mT respectively. Figure 5.9 shows the temperature profile at the inner wall surface of the cavity, obtained from the 3D analysis. At the threshold, estimated temperature value of the cavity inner surface obtained from this 3 D analysis was nearly 6.2 K, and the highest value of the temperature estimated from 1D analysis was around 6.24 K.

Before we conclude, we would like to mention that our analysis certainly highlights that the promise of relatively less pure reactor graded (RRR 100) niobium as the material for cavities dedicated for SNS or ADSS accelerators is worth considering, compared to the conventional choice of highly pure RRR 300 graded niobium material. In this work,

our principal focus was to study the dependence of the electromagnetics of SRF cavities on the purity level of the cavity material. We want to mention here that RRR 100 graded niobium material is a popular choice for the nuclear reactors. However, other aspects of the RRR 100 graded niobium, and substantial R&D experience on development of SRF cavities with RRR 100 material will be required before implementing this choice for future projects.

Chapter 6

Lattice design and beam dynamics of the 1 GeV H^- linac for ISNS

As discussed in Chapter 1, nuclear spallation was discovered even before the discovery of nuclear fission, yet the dream of a spallation neutron source (SNS) was realized only in the late 1980s. The concept of SNS was implemented in Los Alamos in 1985, after the commissioning of the proton storage ring. As mentioned in Chapter 1, one major reason for this was the challenge and complications associated with the development of a high average power hadron accelerator. In a typical linac based spallation neutron source, a pulsed beam of H^- ions is boosted up to an energy of around 1 GeV. Several stringent beam dynamics criteria need to be satisfied, while designing such a high power linac. The foremost criterion is to restrict the beam loss below a stringent limit of 1 W/m [56], [150]. The lost beam particles can introduce the hazard of permanent radioactivity in the structure. In addition, another important design target in such a mega budget project is to make the linac compact.

In this chapter, we will discuss the lattice design and beam optics studies of a 1 GeV, 1 MW H^- injector linac for the proposed Indian spallation neutron source [41]. In this linac, five sets of SRF cavities will be used to boost the beam energy approximately from 3 MeV

to 1 GeV. Amongst them, there will be 650-MHz multicell elliptic cavities in the medium and high energy range of the linac. The geometry of these two families of 650 MHz, 5-cell elliptic SRF cavities have been finalized for the maximum achievable accelerating gradient (E_{acc}), following a procedure discussed in Chapter 2. Rigorous analyses on the higher order modes were performed and described in Chapter 3, which ensures that the targeted beam current will not introduce instabilities during the operation of the machine. In this chapter, a methodology will be described, following which, one can perform the design optimization of the lattice of a compact megawatt class SRF linac.

A *non-equipartitioned* design concept [151] was implemented in this design methodology to set the accelerating gradient and focusing strength values of the SRF cavities and solenoid / quadrupole magnets, respectively. As described in the previous chapters, the breakdown of superconductivity of the cavity material will set a limit on the maximum achievable E_{acc} in these cavities; whereas, Lorentz stripping will restrict the maximum allowable field strength of the external focusing magnets.

We will start our discussion with a quick description on the normal conducting front end of the proposed linac in the next section. Proposed layout of the accelerator for Indian Spallation Neutron Source is shown in Fig. 1.1.

6.1 Layout of the front end linac and some general considerations

Front-end of the proposed injector linac will have a 50 keV, RF antenna type, multi cusp H^- ion source, followed by a 325 MHz RFQ accelerator. The ion source will be operated with a pulse repetition rate (PRR) of 50 Hz, and will produce an H^- beam of 2 ms pulse width, and 15 mA pulse current. The H^- ion beam from the ion source will be transported and matched to the required input of the RFQ through a Low Energy Beam Transport

(LEBT) line [42]. There will be a provision of chopping the beam to a pulse width of 650 ns @ 1 MHz in the LEBT line. Beam chopping is essential to avoid the beam loss while injecting the beam into the accumulator ring. However, chopping will reduce the *cw* average of the beam current from 15 mA to 10 mA, within the 2 ms macropulse. We would like to mention here that while performing the beam dynamics studies of LEBT line, we have assumed about 80 % space charge compensation everywhere in the line, except in the chopper box. Schematic of the 1.9 m long LEBT line is shown in Fig. 6.1, along with the transverse beam envelope. In the LEBT line, the 50 keV beam will be transversely focused by the two numbers of 294 mm long solenoids, and we will utilize the inter solenoid gap of ~ 0.8 m to place diagnostic devices, and two steering magnets. This arrangement will introduce $\leq 0.1\%$ energy spread at the LEBT line exit.

Beam will then be accelerated in the RFQ [43]. There, the beam will develop a normalized rms longitudinal emittance of 0.45 mm-mrad, while accelerating up to an energy of ~ 3 MeV.

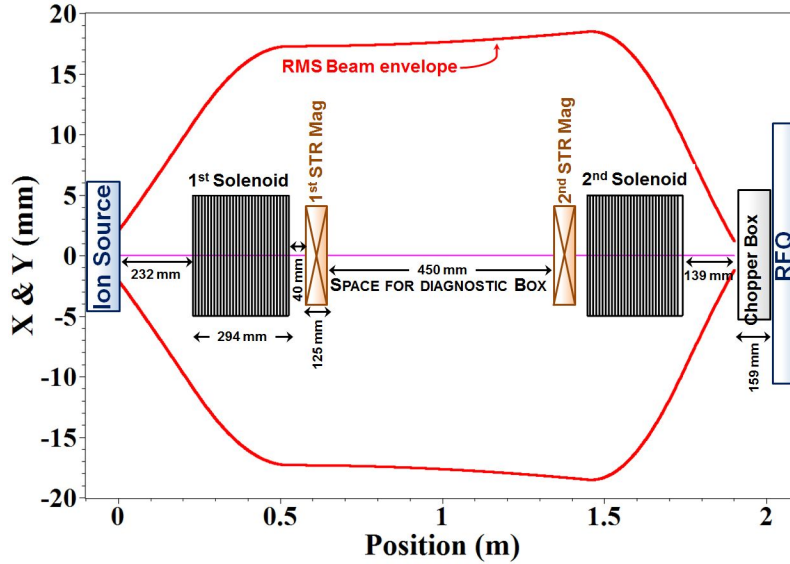


Figure 6.1: Schematic and RMS beam envelope calculated in the 1.9 m long LEBT line (not to scale). Two solenoids with strength ~ 0.196 T and ~ 0.235 T, respectively, will be used to shape the beam there.

Beam from the RFQ will now be transported and matched to the entrance of the 1 GeV

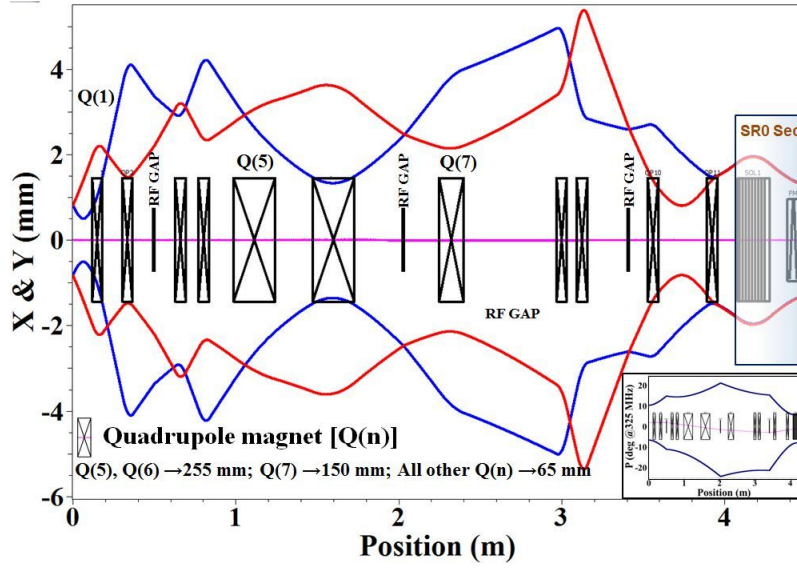


Figure 6.2: Schematic of the ~4 m long MEBT line (not to scale), along with the RMS beam envelopes. The blue and red curve represent the horizontal and vertical beam envelope, respectively. Inset shows the longitudinal beam envelope.

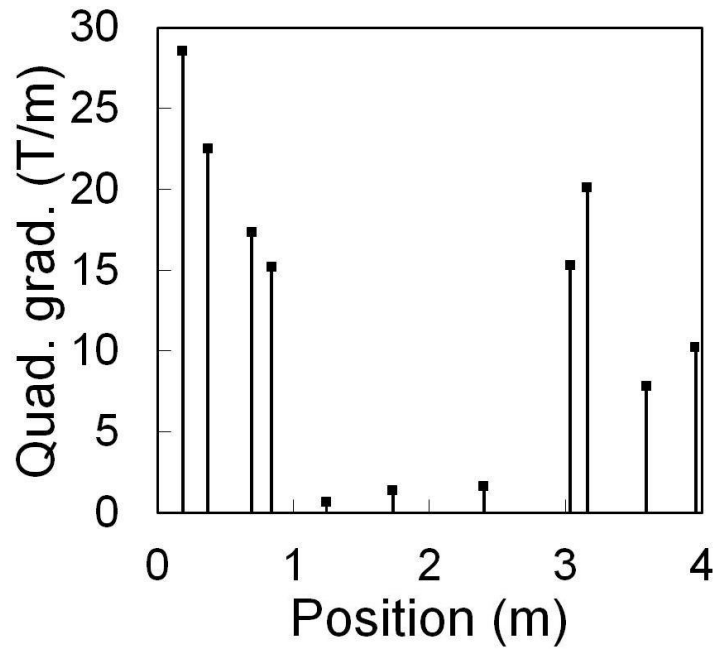


Figure 6.3: Required field gradient of the eleven quadrupole magnets, shown along the length of the MEBT line.

SRF linac, through a Medium Energy Beam Transport (MEBT) line [44]. Layout of the MEBT line along with the beam envelopes, is shown in Fig. 6.2. Optimized MEBT line will consist of eleven quadrupole magnets and three buncher cavities. The design gradient of these eleven quadrupoles is shown in Fig. 6.3. There is a plan to install a traveling wave chopper in the aperture of the fifth and sixth quadrupole. This will reduce the rise time of the chopped beam to nanosecond. In the MEBT line, gap voltage of the three buncher cavities will be kept below 100 kV.

Beam will now be accelerated through the 1 GeV, 1 MW superconducting injector linac. In this main linac, the beam loss should be kept strictly below the limit of 1 W/m, which is the maximum allowable value. In the following section, we will discuss the dynamics of the beam particles, and this will be followed by a description of the linac lattice.

6.2 Basic beam dynamics considerations and the lattice layout of the 1 GeV 1 MW H⁻ linac

The long injector linac will consist of several lattice periods, through which the beam will traverse, maintaining a matched beam size throughout the length of the linac. In an accelerator, the lattice is a typical periodic arrangement of RF cavities, focusing magnets and drift sections, *etc.* For a periodic lattice, the matched beam size is an important concept. In principle, it is the magical beam size that repeats itself after every period. Thus, matched beam size at the entrance of an arbitrarily long accelerating section will ensure constant average beam size in all periods throughout an accelerator. However, the perfectly matched beam is an idealized concept. In practice, the actual beam size will always have deviation from the matched beam size. Therefore, through an appropriate design of the lattice, it should be ensured that the perturbations associated with a real beam does not grow exponentially, and the overall beam does remain stable. We will discuss the basic beam dynamics considerations in the next subsection, which must be

addressed while designing a suitable lattice for the proposed injector linac. Based on these considerations, the evolution of the linac lattice will be discussed further, along with a detailed description on the layout of its lattice. In the following section, we start our discussion with the dynamics of a single beam particle in the beam bunch.

6.2.1 Single particle dynamics and envelope equations in presence of space charge

In an RF linac, the dynamics of a single particle in the beam bunch under the influence of the linear forces due to space charge, RF and focusing magnetic field is described by the following equation [60], [65], [152]:

$$\zeta'' + \frac{\gamma'}{\gamma\beta^2}\zeta' + k_{\zeta 0}^2(s, \gamma)\zeta - K_{\zeta}^{sc}(I_B, a_x, a_y, a_z, \gamma)\zeta = 0. \quad (6.1)$$

Here the variable ζ represents x , y or z coordinates of a particle in the beam bunch, relative to a reference particle traversing along the z -axis. In the above equation, “’” and “''” denote the single and double derivatives, respectively with respect to s . Here the variable s represents instantaneous position of the reference particle in the linac. In the equation, the second term denotes damping, which is introduced in an accelerator because of relativistic effect. The third term represents the net restoring force on a beam particle. This net force arises due to contributions from magnets (*e.g.*, quadrupole and solenoid magnets) and from the RF cavities. Typically the third term, *i.e.*, $k_{\zeta 0}^2$ is a periodic term in a periodic lattice configuration. However, under smooth approximation, this term is replaced suitably with an s -independent, equivalent focusing term denote by $\bar{k}_{\zeta 0}^2$, where $\bar{k}_{\zeta 0}$ represents zero current phase advance per unit length. Finally, the fourth term K_{ζ}^{sc} in the above equation represents defocusing contribution from the space-charge forces.

Space charge contribution is difficult to calculate for an arbitrary distribution of the

beam particles in an arbitrarily shaped beam bunch. However, for an ellipsoidal beam bunch with uniform distribution and rms beam sizes a_x , a_y and a_z along x , y and z direction, respectively, K_ζ^{SC} can be calculated analytically in terms of the beam current I_B , using the formula given in Ref. [65]. Under smooth approximation, we can define a net focusing term $\bar{k}_\zeta^2 = \sqrt{(\bar{k}_{\zeta 0}^2 - \bar{K}_\zeta^{sc})}$, where, \bar{k}_ζ will represent the phase advance per unit length in presence of beam current. Here we introduce another parameter known as tune depression μ_ζ , which is a ratio $\bar{k}_\zeta/\bar{k}_{\zeta 0}$. Eq. 6.1 represents a set of three coupled differential equations. Here, coupling is generated because of the space-charge forces and the electromagnetic field of the radio frequency cavity.

Above equation describes the dynamics of a single particle in an ellipsoidal beam bunch. Using the single particle equation of motion, we derive the equation representing the collective motion of all particles in the beam bunch. The evolution of the rms beam size a_ζ is called the envelope equation, which is [65],

$$a_\zeta'' + \frac{\gamma'}{\gamma\beta^2}a_\zeta' + k_{\zeta 0}^2(s, \gamma)a_\zeta - \frac{\epsilon_{\zeta\zeta'}}{a_\zeta^3} - K_\zeta^{sc}(I_B, a_x, a_y, a_z, \gamma)a_\zeta = 0. \quad (6.2)$$

Here $\epsilon_{\zeta\zeta'}$ denotes an un-normalized rms beam emittance in the $\zeta\zeta'$ plane. Multiplying this un-normalized rms emittance value with $\beta\gamma$ and $\beta\gamma^3$ we can obtain respectively the normalized value of transverse and longitudinal rms emittances.

For an ideal case, we have introduced the concept of a matched beam. Accordingly, for a periodic lattice, we can calculate matched rms beam sizes $a_{\zeta m}(s)$ which satisfies Eq. 6.2. Being a matched solution, the rms beam size $a_{\zeta m}(s)$ as well as its first order derivative $a_{\zeta m}'(s)$ should be identical at the entry and exit of each period. If the beam size is matched throughout the linac, it ensures minimum variation in the rms beam size. However, in the real cases, both the beam size and the lattice deviate from their ideal condition of matched size and perfect periodicity. Considering these perturbations, the rms beam size for a real beam bunch can be written as $a_\zeta(s) = a_{\zeta m}(s) + \Delta a_\zeta(s)$, where, $\Delta a_\zeta(s)$ denotes the small mismatch. Using Eq. 6.2, one can calculate a linearized differential equation describing

the evolution of $\Delta a_\zeta(s)$ as [60],

$$\Delta a_\zeta'' + \frac{\gamma'}{\gamma\beta^2} \Delta a_\zeta' + k_{\zeta 0}^2(s, \gamma) \Delta a_\zeta - 3 \frac{\epsilon_{\zeta\zeta'}}{a_\zeta^4} \Delta a_\zeta - \sum_{\zeta} f_\zeta^{sc} \Delta a_\zeta = 0. \quad (6.3)$$

In this linearized differential equation for envelope mismatch, $f_\zeta^{sc}(I_B, a_{xm}, a_{ym}, a_{zm}, \gamma)$ denotes the coefficient of the space-charge term. Through the beam dynamics design, it is essential to ensure that any mismatch in the beam size should not grow exponentially, and to avoid the chances of beam loss, beam envelope should be confined well within the available aperture of the machine. For a two dimensional coasting beam, several authors have reported their analyses on the growth rate of the mismatch in beam size. Based on their analyses, a conclusion has been drawn that the oscillations due to mismatch does not grow if $\sigma_{\zeta 0}$, i.e., the zero current phase advance per period is less than or equal to 90 degree in all three planes. The parameter $\sigma_{\zeta 0}$ is defined as $\sigma_{\zeta 0} = \bar{k}_{\zeta 0} \times L$, where, L is the period length [60] [153]. The authors did not include the effect of RF cavity field in their stability analysis. Therefore, we have revisited these issues for a three-dimensional beam bunch, including the effect of RF field. Results of this analysis will be elaborated in Section 6.3.3. We will show later in this chapter that the growth in the mismatched envelope oscillation can be explained as resonances occurring between mutually orthogonal beam envelope oscillations, coupled through space charge forces (confluence resonances), as well as between the lattice and each of the three orthogonal beam envelope oscillations.

Similarly, as it can be shown using Eq. 6.1, unwanted resonance can get triggered between an individual beam particle and the stable beam envelope oscillation, which can arise in both case - without mismatch, or with mismatch. Single particle in a beam bunch may experience a periodic variation in $K_\zeta^{sc}(I_B, a_x, a_y, a_z)$, because of the space-charge force varying with the oscillating rms beam sizes. Beam particle will experience periodic excitations due to the periodically varying space charge forces, and under suitable conditions, this may lead to parametric resonance for some of the particles. As a

consequence of this parametric resonance, these beam particles start performing large amplitude oscillations, which results in the formation of beam halo [65]. For a given lattice, different values of mismatch will produce different periodicity in the mismatched envelope oscillation. In fact, this happens due to amplitude dependence of oscillation frequency, arising due to the nonlinear space charge. For envelopes with different values of mismatch, the maximum extent of halo particles will be different. Considering smooth focusing approximation, Wangler et. al. [55] have developed a model called Particle Core Model (PCM), which calculates the maximum extent of the halo particle for different values of mismatch. In their analysis, they have reported the typical extents of halo particles between 6 to 8 times of the rms beam size. This is important, because it helps us in deciding the minimum aperture radius of an accelerator, and accordingly, the aperture radius should be more than 6 to 8 times the rms beam radius. We have extended the PCM analysis, explicitly including the periodic variation of the specific lattice that we have designed, as well as their corresponding matched beam parameters.

In the preceding discussion, we have characterized the beam only in terms for the rms beam size. However, an important consideration for a beam bunch is also its distribution in real and phase space, taking into account the space charge forces, which affect the dynamics of the beam particles. From previous studies [60], it is known that for a beam bunch having dissimilar temperature in three degrees of freedom along x , y and z , the emittance may be exchanged among different degrees of freedom. This may grow as an instability which leads to emittance growth in certain planes and eventually results in beam loss. This instability was studied extensively by Hofmann [151], based on which Hofmann diagram was developed. For a particular beam current, this diagram shows the growth rate of emittance exchange for a given ratio of normalized longitudinal and transverse emittance (ϵ_z/ϵ_{tn}), as a function of tune depression \bar{k}_t/\bar{k}_{t0} and tune ratio \bar{k}_z/\bar{k}_t . On the Hofmann diagram, a point representing the corresponding \bar{k}_t/\bar{k}_{t0} and \bar{k}_z/\bar{k}_t is defined as the ‘lattice footprint’ for a lattice period. The analysis performed by Hofmann indicates an important corollary that while designing a linac, one does not always need

to strictly satisfy the law of equipartitioning [151] *i.e.*, maintain equal temperature in all three degrees of freedom. Instead, one may suitably choose the design parameters to keep the linac compact and cost-effective, provided it is ensured from the Hofmann diagram that there is no emittance growth due to emittance exchange. Based on this philosophy, we have evolved a generalized methodology, to keep the linac design compact, and yet free from beam instabilities.

6.2.2 A brief review on the design recipe of a high power hadron linac

As emphasized earlier, objective of the design is two fold- (*a*) to make the injector linac compact, cost-effective and (*b*) to keep the beam loss strictly below permissible limit of 1 W/m. In order to realize this, the following design recipe [57] [59] is generally followed:

1. The variation of phase advance per unit length $k_{\zeta 0}$ has to be adiabatic along the linac. This is because a sudden change in $k_{\zeta 0}$ may result in large amplitude oscillations for some particles, and the consequence may be a large growth in the beam size.
2. The zero current phase advance per period or $\sigma_{\zeta 0}$ should be kept below 90° , to avoid envelope instabilities arising due to mismatch. It is desirable however, to check explicitly whether it is possible to choose a higher value of $\sigma_{\zeta 0}$ and still avoid envelope instabilities for the particular lattice adopted in the design. This is discussed in details in Section 6.3.3.
3. The net transverse focusing term $k_{\zeta 0}^2(s, \gamma)$ in Eq. 6.1 includes contribution from the electromagnetic field developed in the RF cavity, which depends on the longitudinal phase advance of the particle. In the cavity, beam particles undergo small amplitude synchrotron oscillation, and therefore, $k_{\zeta 0}^2(s, \gamma)$ shows a periodic variation with s . The coupling may give rise to parametric resonance when $\sigma_{\zeta 0} = n\sigma_{z0}/2$, n being an integer [154]. Such resonance has to be avoided.

4. Space charge induced collective instability can cause an emittance exchange between transverse and longitudinal planes, and to avoid this emittance exchange, lattice footprints throughout the linac should be carefully set in the resonance free zone on Hofmann diagram [151]. To realize this approach in the design, tune depression will be kept more than 0.5. Equipartition criterion is carefully violated in this approach. As mentioned, implimenting this concept, we have developed our methodology to make the linac compact.
5. In the case of a strong space-charge dominated beam, it is very difficult to keep the tune depression above 0.5. There, fulfilling the equipartition criteria turns out to be a useful way to reduce the chance of emittance exchange. Following the equipartition criteria, one has to ensure equal temperature due to the transverse and longitudinal motions in the beam frame. To implement this equipartitioning in the design, it is required to tune the lattice to maintain $k_t \epsilon_{t,n} = k_l \epsilon_{l,n}$ throughout the linac. This criteria can also be expressed in terms of zero current phase advances as $\frac{k_{t0}}{k_{z0}} = \left(\frac{3}{2} \frac{\epsilon_{l,n}}{\epsilon_{t,n}} - \frac{1}{2} \right)^{1/2}$ [60]. This formula is however valid in the strong space charge limit ($\mu_\zeta > 0.71$) only [60].
6. Minimum beam aperture radius of an accelerator should be kept larger than the maximum extent of halo particles. Based on our discussion in the previous subsection, minimum radius should be at least six times the rms beam size. In the longitudinal plane also, the rms phase width should not exceed one sixth of the synchronous phase. We have explicitly checked these criteria for our lattice designed for the injector linac. We will discuss this in Section 6.3.4.
7. Formation of beam halo is undesirable throughout the length of the linac, and as we have discussed, this is triggered by the oscillations in the beam envelope introduced by the beam mismatch. Therefore, to reduce the mismatch in beam size, appropriate beam matching should be ensured between two different sections of the lattice.
8. Last but not the least, the effect of intra-beam stripping of H^- ions has to be consid-

ered. The loss due to intra-beam stripping has a strong dependence on the density of H^- ions in the beam bunch [58]. This factor has to be taken into account, while choosing the beam size and beam emittance.

Before we delve on the lattice design and design schematic in the next section, here we would pause for a brief comparative discussion on the *equipartitioned* and *non-equipartitioned* design approach for our case. The normalized RMS longitudinal, horizontal and vertical emittance values at the entrance of the linac in our design, are 0.447 mm-mrad, 0.397 mm-mrad and 0.400 mm-mrad, respectively. By putting these numbers in the equipartitioning condition, finally we obtain the ratio $k_{(x,y)0}/k_{z0}$ as 1.114. This implies that, to satisfy the equipartitioning criterion, the longitudinal phase advance is required to be kept less than the transverse phase advance. However, σ_{z0} has to be limited to less than 90° to avoid envelope instability. Accordingly, the maximum possible value of transverse phase advance and longitudinal phase advance per period should be as 90° and 81° , respectively. On the other hand, if we choose to violate the equipartitioning condition by considering a higher value of longitudinal phase advance per period, it will be possible to choose a larger accelerating gradient, which will make the injector linac compact. Therefore, we have chosen the nonequipartitioned approach in our design, keeping in mind that a careful tuning throughout the linac is required to avoid the collective resonances in the design.

6.2.3 Lattice design and layout of the ISNS linac

In this section, we discuss the calculations and considerations on the basis of which the lattice of the ISNS linac is optimized. Schematic layout of the this optimized linac will also be described here. First, we discuss how to choose the optimum value of geometric beta (β_g) for different families of the accelerating cavities. A perfect synchronization between beam particles and the resonant field developed inside the RF cavity can be achieved if we vary the cell length of the cavity continuously, as the beam propagates

from one cavity to the other and gets accelerated. However, in practice, only a limited families or sets of cavities with fixed cell length (for each family) are designed for a linac, to keep the cavity manufacturing process simple and efficient. Typically, standing wave accelerating cavities are operated in the π -mode, to ensure a maximum shunt impedance. Hence, the cell length is kept fixed at $\beta_g \lambda / 2$. As mentioned earlier, β_g is known as the geometric beta. For a linac with limited number of the different type of cavity sets, the choice of β_g for each set and the transition energies from one set to another set of cavities in the linac become an important considerations while designing a compact linac. Here, we want to emphasize that along with physics requirements or optimization studies, other factors like economy as well as construction and manufacturing feasibilities also play a decisive role behind these choices. In the planning and implementation of such a mega project, a major attention is paid to minimize the time, effort and the uncertainty / risk factors. With this goal in mind, a thorough survey of similar contemporary projects like PIP-II [155], ESS [34], Chinese ADS [156] as well as SNS at Oak-Ridge [16] [157] *etc.*, was made.

As discussed earlier, ISNS is planned as a precursor to the Indian ADS [41] programme. The concept of ADS is based on a high-energy, high-current proton accelerator, which will be capable to deliver a cw power of around few tens of MW. And to realize such a high power cw machine, superconducting RF cavities are the only choice. Therefore, to acquire the skill as well as to acquaint ourselves with the SRF technology, for the ISNS linac, our current plan is to use SRF cavities in the injector linac immediately after the RFQ accelerator. Based on our review of the operational or ongoing SNS projects worldwide and Indian Institutions and Fermilab Collaboration (IIFC), we decided the use of five families of different superconducting RF cavities for the specified energy range of the ISNS injector linear accelerator, starting from ~ 3 MeV to around 1 GeV energy. We will use three sets of superconducting single spoke resonators in the low energy section, namely SR0, SR1 and SR2, having the respective β_g values 0.11, 0.22 and 0.42. In the low energy (beam energy < 200 MeV) region, superconducting spoke resonator is an excellent

choice based on the high accelerating gradient (E_{acc}) achievable, compact size as well as their cost efficient performance [150] [156]. On the other hand, in the medium and high energy range (energy > 200 MeV), multicell elliptic SRF cavities are the popular choice worldwide. Therefore, for the proposed ISNS linac also, two families of 5-cell 650-MHz elliptic SRF cavities have been planned to boost the energy from ~ 170 MeV to 1 GeV. Similar to the PIP-II project [155], it was earlier decided to use 5-cell 650-MHz elliptic cavities with $\beta_g = 0.61$ and $\beta_g = 0.9$ for the medium and high energy part of the superconducting injector linac proposed for ISNS. However, a thorough optimization study was performed later aiming to minimize the number of cavities. Based on this study, $\beta_g = 0.81$ cavities have been picked up for the high energy section of the linac. This study will be elaborated later in this sub-section. In this analysis, we denote $\beta_g = 0.61$ and $\beta_g = 0.81$ elliptic cavities as EC1 and EC2, respectively.

For performing the optimization study, one needs the information regarding maximum achievable acceleration gradient in an elliptic cavity geometry denoted as $E_{acc,m}$, as a function of β_g . Based on the formulation proposed by Eshraqi [158], one can calculate the value of $E_{acc,m}$ in terms of the geometric beta of the cavity from the following formula:

$$E_{acc,m} = \frac{E_{pk,m}}{\left(\frac{k_1}{\beta_g} + k_2 \times \beta_g\right)}. \quad (6.4)$$

which fits well with experimentally obtained data for different SRF elliptical cavities. Here $E_{pk,m}$ denotes allowable limit of the peak electric field maximum on the inner wall of the cavity (which was considered 40 MV/m in this optimization calculation). Based on the maximum achievable gradient of our optimized medium and high beta multicell elliptic SRF cavity geometry [36] [37], k_1 and k_2 values were adjusted to 1.84 and 1.17, respectively, following Ref. [159].

As required, in this analysis, σ_{j0} was kept $\leq 90^\circ$ throughout the linac. First step of this optimization analysis is in fact a study of longitudinal beam dynamics at zero current.

Here, the only active components are the RF cavities, which provide focusing and acceleration to the beam particles. Other lattice components like beam pipes or the transverse focusing elements contribute as drift spaces in this zero current longitudinal beam dynamics study. As a pre-requisite, first we set the number of cavities, solenoids or quadrupoles and drifts to complete the periods of the lattice. It is noteworthy that these cavities are independently phased cavities, which offer flexibility to the lattice in terms of their tunability. However, these lattices are typically longer compared to the normal conducting drift tube linacs, and this is a disadvantage particularly in the low energy spoke resonator (SR) sections.

In comparison with the medium and high beta elliptical SRF cavity sections, beam experiences much stronger de-focusing force due to space charge in the low energy SR section. Therefore, compact period of short length is advantageous in the SR section. To realize this objective, superconducting solenoids are the excellent choice as external focusing element in the low energy SR section. Therefore, keeping this in mind, one can mount superconducting solenoids inside the cryostat, which helps to make the period more compact [150], as it is desperately required in the low energy section. In the ISNS linac, beam energy will be only 3 MeV at the entrance of the SR0 section. For an H⁻ particles 3 MeV energy corresponds to a β value around 0.08. Hence, in each period of this SR0 section we restrict to one SR0 cavity only, along with one 20 cm long superconducting solenoid. Periods in the SR1 section are designed with two cavities and one 30 cm long superconducting solenoid in between, whereas, in the SR2 section, one 30 cm long superconducting solenoid is sandwiched between two SR2 cavity doublets forming the period.

As mentioned earlier, 650 MHz multicell elliptical SRF cavities will be used in the medium and high energy sections of the proposed injector linac. In this energy range, particles will become nearly relativistic. Therefore, we can afford moderately longer period length in these sections. Accordingly, normal conducting quadrupole triplets are

planned in this energy range to provide the transverse focusing. In the medium energy section, each period consists of one quadrupole triplet followed by three cavities. Similarly, we have proposed a configuration with one triplet followed by six cavities for the high energy section. These two periods, along with three SR periods are shown in Figure 6.4. Table 6.1 and Table 6.2 present the design details for the RF cavities and magnets, respectively, proposed in the five different energy ranges of the ISNS lattice. Detailed configuration of all the periods is summarized in Table 6.3. In the medium and high energy sections of the proposed linac, we have also explored another possibility to use quadrupole doublet for transverse focusing [16] [41]. However, in our design, we have adopted quadrupole triplet [156], considering an added important advantage that if any of the quadrupole magnets in the triplet configuration goes out of order, still we can achieve the required focusing in both vertical and horizontal planes, performing a minor adjustment of the remaining two quadrupoles. Also, compared to the doublet configuration, beam will remain closer to axi-symmetric in the lattice with triplet configuration. In this design, one aim was to minimize the number of cryomodules, especially in the spoke cavity sections. It is because in the low energy range, reduction in the number of cryomodules will also reduce the number of matching sections, and consequently the growth in the beam size and in beam emittance will be reduced. Moreover it will reduce the number of room temperature to 2 K transitions there. We mention the possible cryomodule lengths in Table 6.3, based on this physics design alone. However, this issue may need a revisit after the completion of the engineering design of the linac.

To minimize the total number of cavities in the medium and high β sections, a detailed optimization was performed on the choice of β_g for the two sets of elliptical cavities, and the transition energy using the code GENLINWIN [159]. Figure 6.5 describes the result of this analysis. Based on this study, we have obtained the optimized geometric beta values for the corresponding two sets / families of elliptic SRF cavity as $\beta_g \sim 0.61$ and $\beta_g \sim 0.81$, respectively. From this optimization calculation, corresponding transition energy

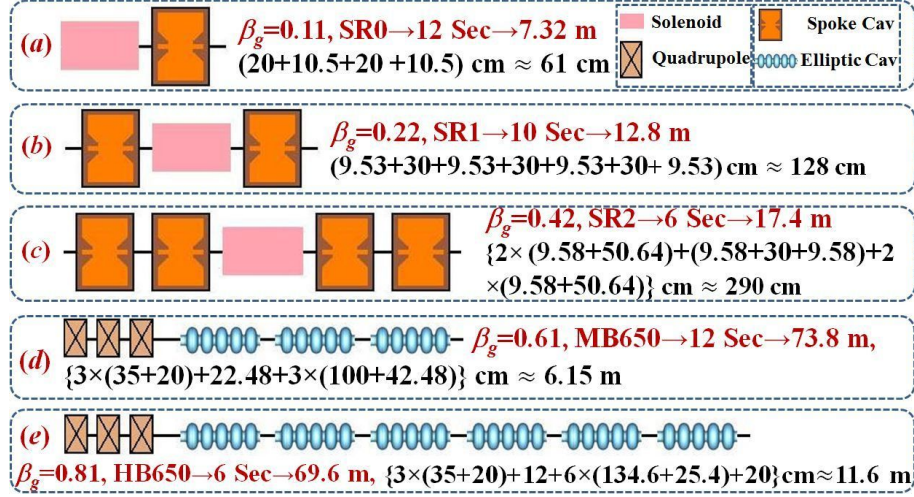


Figure 6.4: Schematic configuration of the lattice structures used in different energy sections of the injector linac: (a) $\beta_g = 0.11$ SR0 section, (b) $\beta_g = 0.22$ SR1 section, (c) $\beta_g = 0.42$ SR2 section, (d) $\beta_g = 0.61$ EC1 section and (e) $\beta_g = 0.81$ EC2 section.

between these two families was estimated as ~ 480 MeV. In the optimized configuration, 12 numbers of medium energy periods and 6 numbers of high energy periods will be used. Together, a total of 72 multicell elliptic SRF cavities will boost the energy from ~ 168 MeV to the final energy.

In this injector linac, superconducting cavities will be housed inside their respective cryomodules. Hence, unavoidably, the maximum length of a lattice section will be limited by the length of the cryomodule there. The maximum length of a cryomodule is decided from considerations imposed by the mechanical and thermal design. As it is shown in Table 6.3, the maximum cryomodule length is kept below 10 m in this design.

In this design, one objective was to keep the linac compact, and therefore, most of the RF cavities here will be operated with their maximum gradients. This consideration compels us to design small matching sections with few extra cavities and magnets to ensure proper beam matching during the transitions. Detailed configuration of the matching section is given as follows:

1. Dedicated for the matching purpose, two squeezed SR0 periods are used in between SR0 section and SR1(1) sections. Each of these periods is configured with one

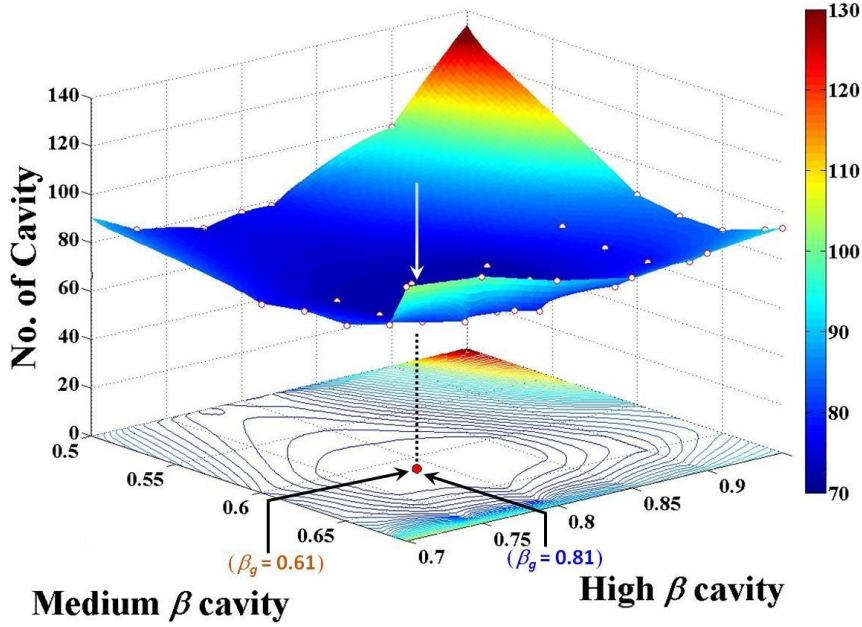


Figure 6.5: Total number of 5-cell, 650 MHz elliptic cavities required to accelerate the beam from 168 MeV to 1 GeV as a function of β_g plotted for both medium and high beta cavity sections.

SR0 cavity along with a 20 cm long solenoid, separated by a 10.5 cm drift space. Fig. 6.6(a) describes the details of this matching section. With a proper tuning of the cavity voltage and magnetic strength, a separation of 40 cm is ensured in between these two squeezed periods. This length will be sufficient to accommodate the end closures of the two cryomodules. In this configuration, the first cavity is used as an energy corrector, and the second one is used as a buncher cavity operating at $\phi_s \sim 90^\circ$.

2. Same configuration is repeated in between the SR1(1) and the SR1(2) section and also in between the SR1(2) and SR2(1) section.
3. Between SR2(1) and SR2(2) sections, part of the same configuration is used at the SR2(1) end, whereas at the beginning of the SR2(2) section only a single solenoid is used for the matching purpose, and there, an extra length in the beam pipe is added to keep the cryomodule design identical for the two SR2 sections. This configuration is shown in Fig. 6.6(b).

4. Matching between 325 MHz spoke resonator sections and 650 MHz medium energy elliptic cavity section is crucial, as because, we have a frequency doubling there. Therefore, with three SR2 cavities, one solenoid and 4 quadrupoles - a dedicated matching section is configured there. Among those elements, one solenoid and one SR2 cavity will be housed inside the SR2(2) cryomodule, whereas, another two SR2 cavities will be housed inside two dedicated cryo-jackets. With proper tuning of the cavities and magnets, we can manage there a gap of 60 cm in between these two cryo-jackets for the beam diagnostic and other necessary devices. Each of the four quadrupoles used here is similar to the regular quadrupoles, which will be used in the triplets. Configuration of this matching section is presented in Fig. 6.6(c).

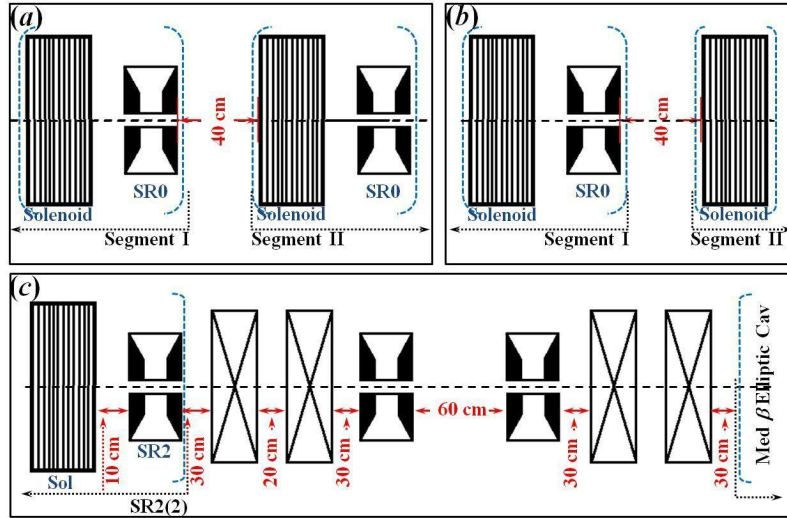


Figure 6.6: Dedicated matching sections used in between (a) SR0 and SR1(1) sections, (b) SR2(1) and SR2(2) sections, and (c) the SR2(2) section and medium energy EC1 section.

Table 6.4 summarizes the configuration details of these matching elements. It is noteworthy that the RF cavity used in the matching section in between SR2(1) and SR2(2) will be required to provide a voltage of around 3.1 MV for the matching. This might be challenging for an SR0 cavity. Keeping this in mind, we have also made an alternative design of this matching section, where an SR2 cavity will be used instead of the SR0 cavity. As it is shown in Fig. 6.6(b), space requirement will not be a limitation for this purpose.

At the transitions, adiabatic change in the phase advance per unit length will be ensured by these dedicated matching sections. These sections will also preserve constant longitudinal acceptance criterion [160]. Following the first criterion we write:

$$\left. \frac{E_0 T \sin(\phi_s)}{\lambda} \right|_{Section1} = \left. \frac{E_0 T \sin(\phi_s)}{\lambda} \right|_{Section2}. \quad (6.5)$$

Here, λ is the free space wavelength corresponding to the RF frequency in the cavity. In case, where the frequency gets doubled at the transition, synchronous phase ϕ_s should also require to be doubled in order to keep the geometrical bunch length acceptance unaltered. Introduction of these dedicated matching sections may be disadvantageous

Table 6.1: Design details of the RF cavities used in the proposed linac lattice.

Section	Cav Name	L (Field map)	Operating Range
$\beta_g = 0.11$	SR0	20 cm	~ 4.9 to 9.3 MV/m
$\beta_g = 0.22$	SR1	30 cm	~ 6.1 to 10 MV/m
$\beta_g = 0.42$	SR2	51 cm	~ 7.7 to 10.8 MV/m
$\beta_g = 0.61$	EC1	1.0 m	~ 10 to 15.4 MV/m
$\beta_g = 0.81$	EC2	1.36 m	~ 15 to 18.6 MV/m

Table 6.2: Magnets used in the linac lattice and their design details.

Section	Magnet Type	L (Hard edge)	Operating Range
$\beta_g = 0.11$	Solenoid	20 cm	~ 2.2 to 2.6 T
$\beta_g = 0.22$	Solenoid	30 cm	~ 1.9 to 2.8 T
$\beta_g = 0.42$	Solenoid	30 cm	~ 2.5 to 3 T
$\beta_g = 0.61$	Quad. (Triplet)	35 cm	~ 2.9 to 7.8 T/m
$\beta_g = 0.81$	Quad. (Triplet)	35 cm	~ 3.6 to 8.3 T/m

Table 6.3: Detailed lattice parameters of the injector linac.

Section	L_{period}	Focusing Type	β_{trans}	$\sim L_{cryo}$
$\beta_g = 0.11$	0.61 m	[Sol] (R)	~ 0.15	$\sim 7.8m$
$\beta_g = 0.22$	1.28 m	(R) [Sol] (R)	~ 0.32	$\sim 7.4m$
$\beta_g = 0.42$	2.90 m	$(2 \times R)$ [Sol] $(2 \times R)$	~ 0.50	$\sim 9.7m$
$\beta_g = 0.61$	6.15 m	[FDF] $(3 \times R)$	~ 0.74	$\sim 4.3m$
$\beta_g = 0.81$	11.6 m	[FDF] $(6 \times R)$	~ 0.87	$\sim 9.6m$

from the perspective of compactness. However, we would like to mention that it offers

more flexibility in the design. In a MW class hadron linac, it is extremely important to reduce the chances of emittance growth and the chances of halo formation, with the help of proper beam matching. These matching sections could be avoided, if we play with the readjustment of the cavity gradients and synchronous phases at the end of sections. However, increasing E_{acc} is not a feasible option in this ‘compact’ design. Another option might be to change the synchronous phase. Synchronous phase affects the phase acceptance. Therefore, it is not at all preferable to reduce the magnitude of synchronous phase substantially. In addition to this, dedicated matching section might be advantageous in the case of cavity failures in the adjacent regular accelerating sections. There, a limited compensation of the energy might be possible by readjusting the cavity-gradients of the matching section.

Table 6.4: Design and the detailed parameters of the matching sections.

Position (In between)	Cav Type	Focusing Element	Cavity ϕ_s	$E_0 L_{gap}$ (MV)
SR0, SR1(1)	2×SR0	2×Sol (20 cm)	$\sim -67.8^0$ $\sim -90.0^0$	~ 1.54 ~ 1.14
SR1(1), SR1(2)	2×SR0	2×Sol (20 cm)	$\sim -83.1^0$ $\sim -90.0^0$	~ 1.54 ~ 1.51
SR1(2), SR2(1)	2×SR0	2×Sol (20 cm)	$\sim -87.2^0$ $\sim -90.0^0$	~ 1.53 ~ 1.26
SR2(1), SR2(2)	1×SR0	2×Sol (20 cm)	$\sim -90.0^0$	~ 3.1
SR2(2), $\beta_g = 0.61$ sec	3×SR2	1×SoL (20 cm) 4×Quad (35 cm)	$\sim -90.0^0$ $\sim -90.0^0$ $\sim -90.0^0$	~ 1.64 ~ 3.32 ~ 3.77

We would like to emphasize that the optics design sometimes demands a reduced E_{acc} for the cavity. However, for the cavities, it is better to operate around their design gradient, to reduce the chances of multipacting. It may so happen that at lower value of E_{acc} , cavity will cross the multipacting barrier. In that case, multipacting will restrict the functionality of the cavity. We have taken care of this issue in the design. Although few of the SR0 cavities in this linac will be operated nearly at the half of their maximum acceleration gradient, we have checked that this gradient is still safe from the multipacting point of view. As we have discussed, transition energies should also be

optimized to minimize the total number of cavities. In this design, nearly for all the cavities, it is ensured that the normalized TTF (TTF / TTF_{max}) will be greater than 70%.

Fig. 6.7 also gives the confirmation that none of the cavities will be under-performing.

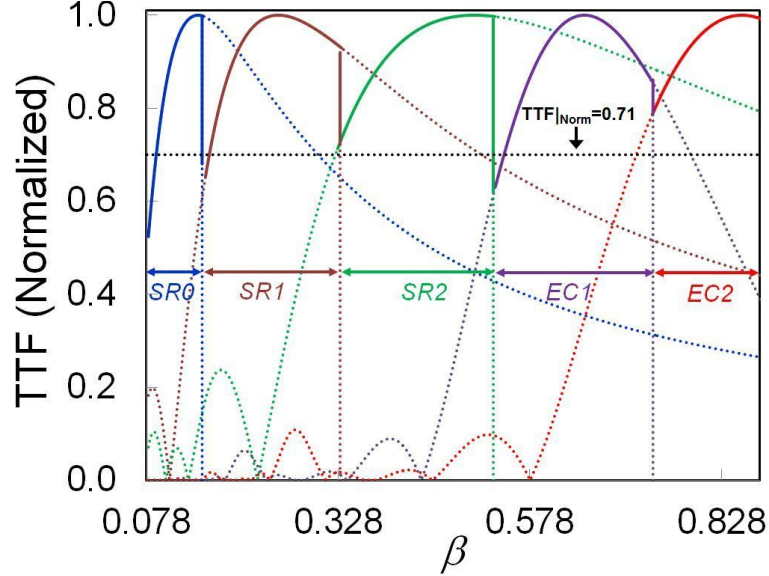


Figure 6.7: Transit time factors (TTF) normalized against their maximum values are plotted as a function of β for the five different lattice sections used in the injector linac. The straight lines show the transition β from one section to the other.

6.3 Beam dynamics calculations for ISNS linac

Lattice layout of the proposed injector linac for ISNS was described in the previous section. Beam dynamics calculations for the linac will be presented in this section. We start with a discussion on calculations performed to set the different lattice parameters (i.e., the synchronous phase ϕ_s and acceleration gradient E_{acc} in each RF cavity, as well as the focusing strength of the solenoid and quadrupole magnets). We will present the envelope and multi-particle beam dynamics calculations including the space charge effect in the Section 6.3.2. Section 6.3.3 will describe the detailed calculation of envelope instability for the beam bunch. Beam halo analysis will be presented in the Section 6.3.4. The discussion will be concluded with an estimation of the beam loss in the Section 6.3.5.

6.3.1 Beam optics calculations for the zero current

Discussion on the longitudinal beam dynamics calculations: Here, we will discuss the longitudinal beam dynamics studies performed with zero current. Based on this study, E_{acc} and ϕ_s values were set in each RF cavity. There are few computer codes available for such calculations. However, to the best of our knowledge, the detailed design procedure is not clearly described in the literature. Hence, we have evolved a methodology to set these values. We found a good agreement between our results and the results obtained using the computer code GENLINWIN. In this methodology, we consider a fixed value of ϕ_s and E_0 in all cavities in the same period. Here, we want to mention that although in this recipe, these two quantities are kept fixed for all the cavities in the same period, particle will gain different energies in each of the cavities. It is because the transit time factor T will varies as the particle gets accelerated. Therefore, energy value at the entrance of the next section will be carefully updated calculating the overall energy gain from the previous section. While moving from one period to the next, simultaneously, the values of ϕ_s and E_0 are calculated for the next period in such a way that the two quantities - (i) k_{l0} , i.e., the zero current phase advance per unit length, and (ii) the area of separatrix in the longitudinal phase space remain constant. As it is obvious, one constraint in this analysis is that the maximum allowable axial field value E_{max} in the cavity comes from the electromagnetic design of the cavity, and that limits E_0 . Hence, if the value of E_0 obtained in this methodology goes beyond E_{max} , we set E_0 for the corresponding cavity to E_{max} . As a consequence, we need to reduce the value of k_{l0} for the respective periods accordingly in the section, as we progress along the linac length. However, under all circumstances, we must ensure that the k_{l0} changes adiabatically. Constant or an adiabatically varying k_{l0} implies that the particle experiences restoring force due to constant or slowly varying spring constant as it moves down the linac. Maintaining a constant area of separatrix implies that a constant fraction of this area will be occupied by the beam, as the area of longitudinal phase space is conserved. Here, we consider the value of k_{l0} obtained after averaging over one lattice period.

We now discuss the basis on which we choose ϕ_s and E_0T at the entrance of the spoke resonator section, *i.e.*, at the beginning of our injector linac. Aiming at a compact linac, we try to achieve a design with maximum acceleration efficiency. Therefore, ϕ_s should be chosen as small as possible. However, as we know, phase acceptance is decided by the parameter ϕ_s only, and a small value of ϕ_s corresponds to a phase acceptance value of $3|\phi_s|$. Therefore, the selected value of ϕ_s must ensure that the beam bunch length from the preceding accelerating section will adjust well within the phase acceptance of the subsequent lattice section. In this case, preceding section is the RFQ and the beam will enter from there to this subsequent sections, *i.e.*, the SR0 lattice. Next, we elaborate about the choice of E_0T . In an accelerating cavity, k_{l0} limits maximum allowable value of E_0T (of course, E_0 needs to be kept smaller than E_{max}). Accordingly, the aim is to choose the highest possible value of k_{l0} that will ensure the use of a maximum gradient in the cavity. In addition, the maximum value of zero current longitudinal phase advance σ_{l0} should always be kept below 90° , to avoid envelope instabilities.

We choose the value of σ_{l0} in the first period of the SR0 section as 89° and accordingly we fix the value of E_0T in the first cavity. Such a choice of the value of $\phi_s = 45^\circ$, shows that at the entrance of the spoke resonator section, RMS longitudinal beam bunch length is less than one-fourth of ϕ_s . Although this value is well below the phase width of the separatrix there, which is $3 \times |\phi_s|$, yet, it is bigger than the RMS beam size of one-sixth of ϕ_s , as it is mentioned in the recipe described in Sub-section 6.2.2. From multiparticle simulation, for this design we have ensured that in spite of this choice of $\phi_s = 45^\circ$ at the entrance, it is possible to restrict the RMS longitudinal beam size less than one-sixth of ϕ_s mostly throughout the linac. The value of ϕ_s and E_0 is updated in the subsequent sections, following the procedure that we described earlier.

Discussion on the transverse beam dynamics calculation: Based on similar arguments, as adopted while discussing the longitudinal dynamics, focusing magnetic strengths is decided by the zero current transverse phase advance (k_{t0}) value in the case

of transverse dynamics. For the entire linac, it is required that all lattice footprints should always be in the resonance free zone on the Hofmann diagram in presence of beam. In fact, this is followed as the main guiding principle in the design of a *non-equipartitioned* compact linac. Accordingly, we calculate the transverse focusing strength of the solenoid and quadrupole magnets in the lattice such that the lattice footprints fall in the resonance free zone of the Hoffmann diagram. Especially, we have targeted to place the footprints in the wide resonance free zone, which exists between the third and fourth order even resonance peaks. Such placement of the lattice footprints ensures the absence of collective instabilities, which may arise because of the exchange of emittances among different planes.

We have already argued that the zero current phase advance per period (σ_{t0}) in the transverse plane should be kept below 90° to avoid transverse envelope instability. Therefore, this will be a constraint in our calculation, while deciding for the maximum design value of the zero current phase advance per unit length (k_{t0}) in the transverse plane. Also, as described, k_t/k_{t0} should be in the resonance free zone on the Hofmann diagram. Based on these two considerations we set the value of k_{t0} for each lattice. In the calculation, the following relationship between k_t and k_{t0} as well as between k_t and k_{t0} is used [65]:

$$k_t = k_{t0} \sqrt{1 - \frac{3q\lambda I_B \mathcal{F}}{20 \sqrt{5} \pi \epsilon_0 \gamma^3 \beta^2 m c^3 a_x a_y a_z k_{t0}^2}}, \quad (6.6)$$

$$k_t = k_{t0} \sqrt{1 - \frac{3q\lambda I_B (1 - \mathcal{F})}{20 \sqrt{5} \pi \epsilon_0 \gamma^3 \beta^2 m c^3 (a_x + a_y) a_{x,y} a_z k_{t0}^2}}. \quad (6.7)$$

Here $I_B = 14.5$ mA is the macropulse beam current, q is the magnitude of the charge of an H^- ion and the term λ denotes free space wavelength of the corresponding RF frequency at which the beam is bunched. As described in Ref. [65], the parameter \mathcal{F} is called the form factor, which depends on the shape of the bunch in the beam frame.

Pushing the value of transverse focusing strength or k_{t0} to its maximum is always

preferable in the design to minimize the transverse beam size (keeping in mind the possibility of intra-beam stripping). Limiting the maximum value of $\sigma_{t0} \leq 90^\circ$, we might have chosen the initial value of the zero current transverse phase advance per period (σ_{t0}) as 89° , which is same as the initial value of σ_{t0} . Accordingly, Eqs. 6.6 and 6.7 give the value of $k_l/k_t = 1.12$ at the beginning of the linac for an average value of the typical rms beam size of $a_x = a_y = 1.7$ mm and $a_z = 2.0$ mm. If we plot $k_l/k_t = 1.12$ on the Hofmann diagram, it will certainly be in the resonance free zone, but very close to the edge of the fourth order resonance peak. Therefore, it is preferable to set a value of $k_l/k_t > 1.12$. Such choice will categorically help us to move away from the resonance, and as a consequence the chances of emittance exchange between different planes will be reduced further. Interestingly, if we want to move sufficiently away from the width of the fourth order resonance peak by setting the ratio k_l/k_t to some higher value, the value of σ_{t0} will be reduced further from 90° , resulting in a further reduction in the transverse focusing strength. Therefore, we chose the initial value of $k_l/k_t \approx 1.2$. This choice ensures a satisfactory value of the transverse focusing strength, as well as a sufficient distance from the resonance peak. We have tried to maintain this ratio by suitably choosing the field strength of the focusing magnets throughout the linac. One point here we want to mention is that: ISNS lattice will be an emittance dominant design, *i.e.*, in this design, space charge issues will not be that severe. Hence, while designing the lattice, we have targeted to keep the tune depression values around 0.7.

We would like to emphasize that in this design, we have implemented the design approach suggested by Hofmann *et. al.* [151]. This is the non-equipartitioned design approach, where emphasis is more on making the linac compact. In the nonequipartitioned design, the chances of emittance exchange is reduced by limiting the lattice footprints to the safe zone of Hofmann diagram through appropriate tuning of the lattice parameters. Beam has asymmetric emittance values in longitudinal and transverse planes at the entrance of the SRF injector linac in our design. We found there the ratio of $\epsilon_{l,n}/\epsilon_m \approx 1.12$. Such a design where $\epsilon_{l,n} > \epsilon_m$, will be robust even in the case of an

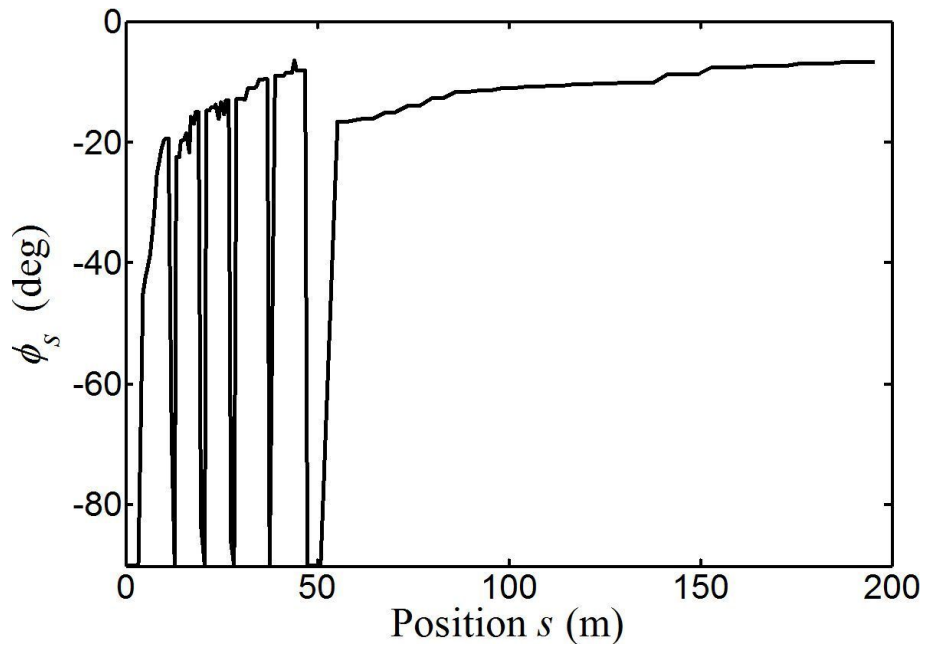
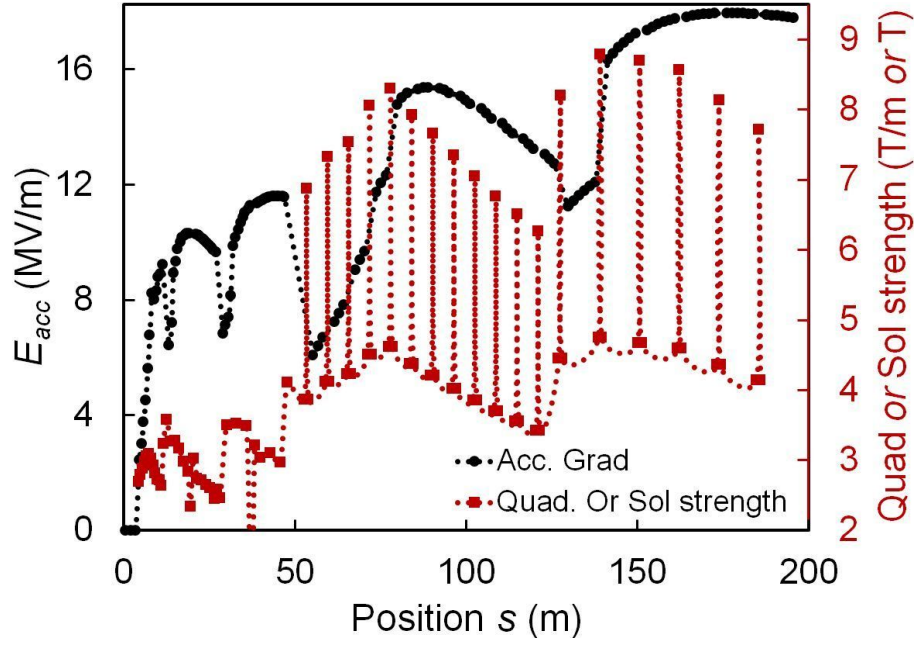


Figure 6.8: Figure on top shows the calculated acceleration gradient (E_{acc}) in the RF cavities and the required strength of solenoid / quadrupole magnets along the length of the linac. In the bottom, calculated variation in the synchronous phase ϕ_s of all RF cavities is shown.

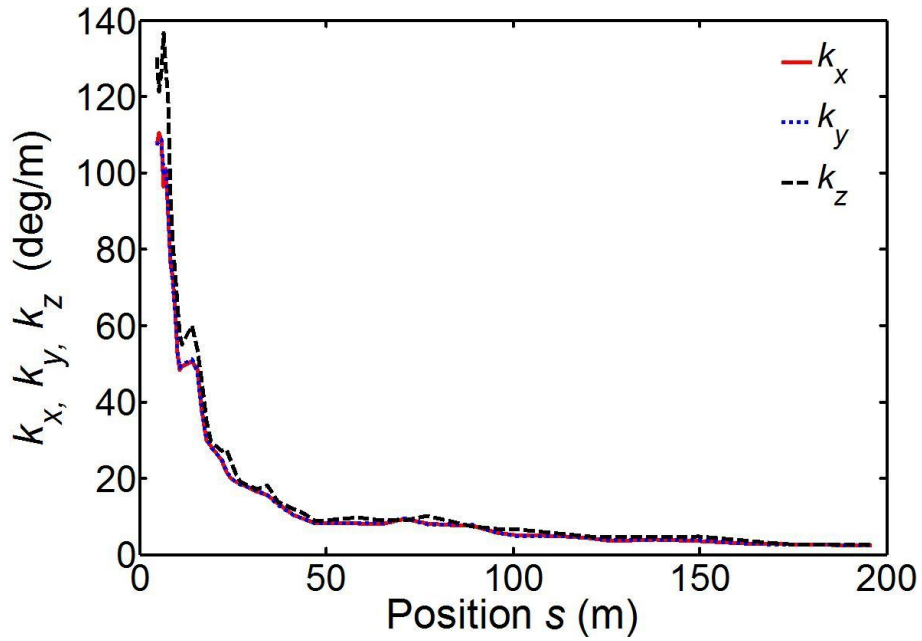
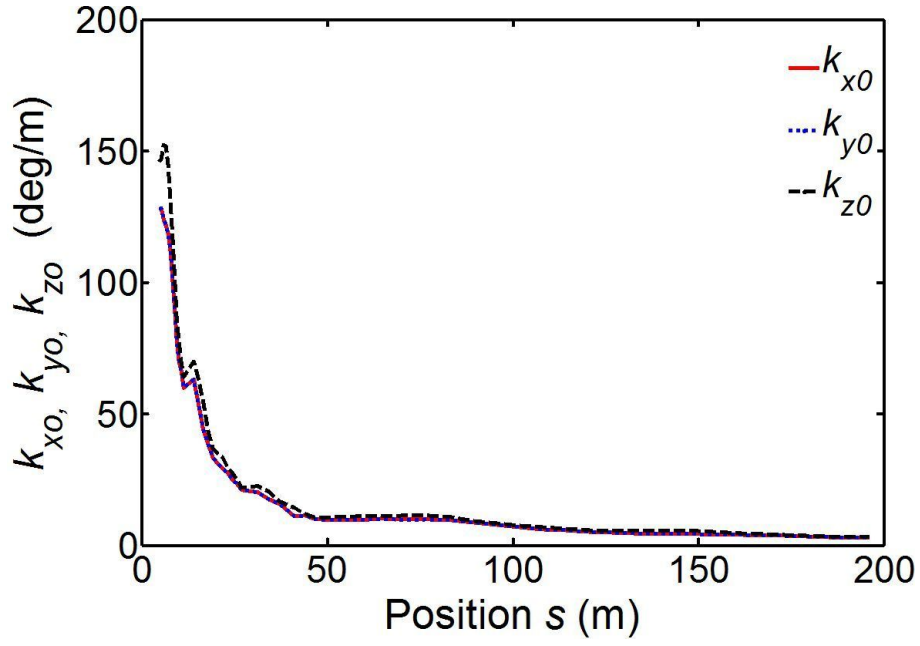


Figure 6.9: Longitudinal (black dashed line) and transverse phase advance (horizontal: solid red line and vertical: dotted blue line) per unit length is plotted along the length of the linac without space charge (top) and with space charge (bottom) for the designed value of a beam current of around 14.5 mA.

emittance exchange compared to the design with $\epsilon_{l,n} < \epsilon_m$. It is because in the case of $\epsilon_{l,n} > \epsilon_m$, reduction in the longitudinal emittance will divide equally between the two transverse planes. As a result, low emittance growth will be expected in the design. However, this choice will be disadvantageous compared to the other choice of $\epsilon_{l,n} < \epsilon_m$ in case we adopt the equipartition conditions in the design by keeping $k_l \epsilon_{l,n} = k_t \epsilon_{t,n}$. For an equipartitioned design and for $\epsilon_{l,n} > \epsilon_{t,n}$, we need to set relatively small value of k_{l0} , compared to the *non-equipartitioned* design that we described, which will limit the E_{acc} in the cavities to a relatively lower value. As a consequence, the linac will become longer [150]. Hence, to avoid this scenario, we followed a *non-equipartitioned* design approach. Among the contemporary projects, this philosophy is also adopted in designing a 1.5 GeV linac proposed for Chinese ADS program [156].

Calculated values of $E_0 T$ and ϕ_s in each of the cavities in the linac, as well as the focusing strengths of each magnet are plotted in Fig. 6.8. For this lattice, beam dynamics calculations were performed for the beam envelope using the code TRACEWIN [159], including the effect of space charge. As it is observed from the figure (Fig. 6.8), accelerating gradients remains low in the few initial cavities in almost each section of the linac. This happens due to the limitation coming from the longitudinal phase advance criterion. The set values of $E_0 T$ increases to higher values, as the beam energy increases in the linac, and finally gets limited by the maximum achievable acceleration gradients in the RF cavities. As we move from one section to the another, Transit time factor drops, and therefore, an initial dip is observed in the accelerating gradient, which later increases and ultimately saturates to the maximum achievable gradient values. In the design, absolute value of ϕ_s reduces constantly except at the transition between cryomodules. To accommodate the effect of frequency doubling at the transition from the SR sections to the elliptical cavity section, the $|\phi_s|$ jumps to double of its value. Figure 6.9 shows the signature of an overall smooth variation in the values of transverse and longitudinal phase advances per unit length throughout the linac.

6.3.2 Multi-particle beam dynamics simulations

We will now elaborate upon the multi-particle beam dynamics simulations for the lattice parameters finalized in the preceding subsection. We made extensive use of the beam dynamics computer code TRACEWIN. It calculates the space charge using a PIC based subroutine. Matched beam parameters were calculated for the design current of $I_B \sim 14.5$ mA at the entrance and exit of each ‘section’ of the linac. At this point, we want to discuss a bit more on the process of beam matching followed in general in designing a linac of this kind. There, the beam matching is performed carefully at the entrance of each section. It is because of two reasons: (1) different lattice periods are there in the separate sections, or (2) we need to include an extra length in the beam pipe in between two sections, mainly to incorporate beam diagnostic devices or the end closures of the cryomodules there. As an obvious consequence, regular periodicity of the linac breaks at the entrance of each section. It is therefore, dedicated matching is required there at the entrance of each section separately. In this design, the matching sections help in matching the output of previous section with the input of the section under consideration. As it is mentioned earlier, in the spoke resonator sections, we have considered the lattice periods inside each cryomodule as one ‘section’. However, in the elliptic cavity sections, all the lattice periods containing $\beta_g = 0.61$ cavities constitute a single section, and along the same line, all the periods consisting of $\beta_g = 0.81$ cavities constitute another single section.

End to end beam dynamics calculations were performed for the entire ISNS linac - starting from the exit of the RFQ to the end of the injector linac. Figure 6.10 shows the distribution of the input beam used in our calculation. This is the distribution obtained at the RFQ exit [43]. Input Twiss parameters for this distribution are listed in Table 6.5. As mentioned, the 4 m long MEBT line transports the beam from the RFQ to the entrance of the first section of the 1 GeV injector linac. In this design, we maintain the value of k_l/k_t to around 1.2, throughout the linac, based on the discussion in the previous subsection.

Required fine-tuning for the accelerating electric field strength and focusing magnetic field strength for each period were performed accordingly.

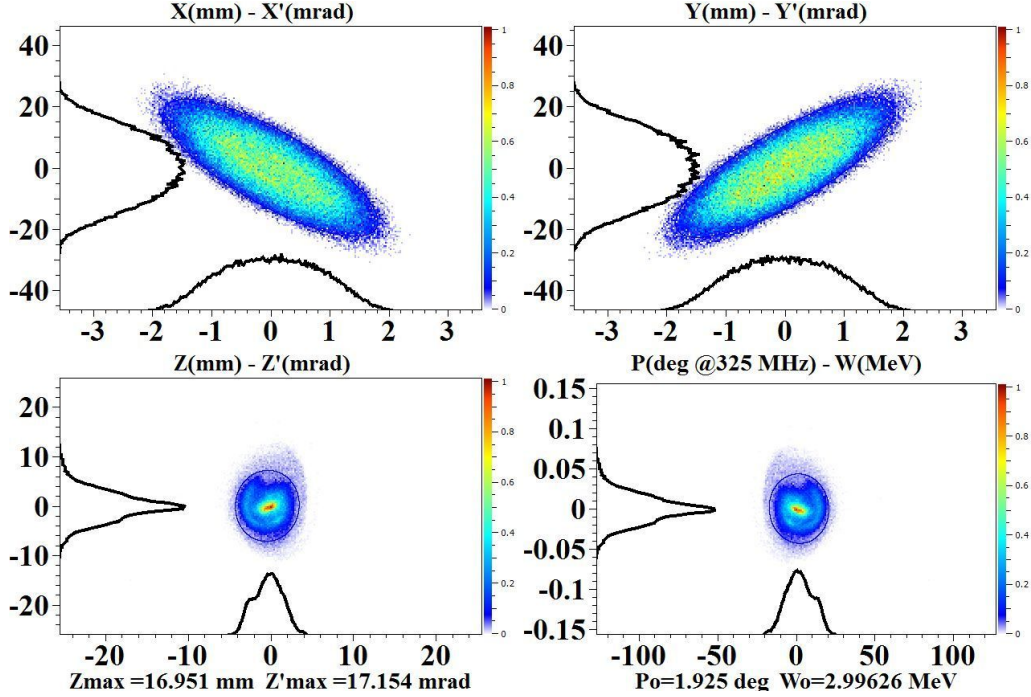


Figure 6.10: Beam distribution at the exit of Radio-Frequency Quadrupole (RFQ).

Table 6.5: Emittance values and Twiss parameters of the beam distribution at the exit of RFQ

Twiss Parameter	Values	Units
α_x	1.289	
β_x	0.1321	mm/mrad
ϵ_x	0.3973	mm-mrad
α_y	-1.3502	
β_y	0.1360	mm/mrad
ϵ_y	0.3996	mm-mrad
α_z	-0.0266	
β_z	0.5379	mm/mrad
ϵ_z	0.4467	mm-mrad

Now, we present the results of this end to end beam dynamics calculations. We have used one-dimensional field maps in the simulation for the longitudinal profile of electric field (*i.e.* $E_z(z)$) in the RF cavities, and have adopted hard-edge models for the calculation of the field strength in the solenoid and quadrupole magnets. Some details regarding the

field strengths and other parameters for the cavities and magnets are given in Table 6.1 and Table 6.2. Figure 6.11 shows the rms and actual beam envelopes for the longitudinal, as well as transverse directions. As observed from the figure, the transverse rms beam size is around 2 mm throughout the linac. In this linac, ratio of the transverse rms beam size to the minimum available aperture radius varies from 7 in the SR0 section to 10 at linac exit. Evolution of the synchronous phase along the linac length is shown in Fig. 6.12. It may be noted that we have found the rms phase width to be less than one sixth of the absolute ϕ_s along the length of the linac. As discussed earlier in Section 6.2.3, suitable matching sections have been designed between different sections of the linac. Detailed configurations of these matching sections, along with the rms beam envelopes obtained in these transition sections, are shown in Figs. 6.13(a) to 6.13(e).

Evolution of the three emittances values along the length of the linac is shown in Figure 6.14. As mentioned earlier, we have fine-tuned the lattice to control the emittance growth, while performing the multiparticle beam dynamics simulation with space charge. Figure 6.14 also shows an interesting feature. We notice that, all the three emittance values decrease simultaneously at a distance approximately between 80 to 110 m, which is contradictory to the Liouville's theorem. In order to explain this contradiction, it is relevant to mention here that the 2D emittance, $\epsilon_{\zeta\zeta'} = \sqrt{\zeta^2(\zeta'^2) - \zeta\zeta'^2}$ (where $\zeta \rightarrow x, y, \text{ or } z$) is actually only a projected emittance, and only the 4 of the 36 terms of a full beam matrix $[\Sigma][\Sigma]^T$ is represented by this. The column matrix Σ consists of six dimensional trace space coordinates x, x', y, y', z and z' . However, this decreasing trend concurrently persists in the linac at ~ 80 to 110 m, even in the 4 dimensional (4 D) and 6 dimensional (6 D) emittance plots with nominal fluctuations of $\pm 3\%$. This is shown in Fig. 6.15.¹ The cause of this behavior is concealed in the fact that the code TRACEWIN does not calculate emittance values from the canonical variables like $x, p_x,$

¹In TRACEWIN, the four dimensional (4D) and six dimensional (6D) emittances are defined as $\epsilon_{iir'} \times \epsilon_{jj'}$, where, $i, j \in \{x, y, z\}$, but $i \neq j$, and $\epsilon_{iir'} \times \epsilon_{jj'} \times \epsilon_{kk'}$, where, $i, j, k \in \{x, y, z\}$, but $i \neq j \neq k$. Coupling between x, y and z is thus not considered in the TRACEWIN results. Hence, in this calculation, contribution from off-diagonal elements of the Σ matrix is absent.

y , p_y , and z , $\delta p/p$. Rather, like the other usual multiparticle beam dynamics codes, it also uses trace-space variables like x , x' , y , y' etc. for emittance calculation [161]. The symplectic condition is therefore not satisfied there in the true sense, which seems to be the reason behind this minor discrepancy.

Variation of the tune values along the length of the linac is plotted in Fig. 6.16. In this linac, expected values of tune depression will be around 0.85 and lies in between 0.7 and 0.95. The beam is thus expected to be emittance dominated.

Figure 6.17 shows the lattice footprints on the Hofmann diagram, where, each point on the diagram corresponds to one lattice period. It can be very clearly inferred from the figure that all the lattice footprints are in the broad resonance free zone between the third and fourth order even resonance peaks, and their values will be scattered around $k_l/k_t \sim 1.2$ line. It is worth mentioning here that apart from ensuring lattice footprint in the resonance free zone, we have also ensured that the lines connecting consecutive footprints on the Hofmann diagram do not cross any resonance peak. This in turn helps to minimize emittance growth. Another point to be noted here is that in the medium and high energy section, the ratio of the average transverse to the longitudinal emittance values approaches unity. This is a favorable situation, as the fourth order even mode resonance peak in the Hofmann diagram reduces significantly in that case.

Apart from this, we have calculated the beam acceptance in the longitudinal and transverse planes using the computer code TRACEWIN, and the results are shown in Fig. 6.18. From the figure, the golf club kind of separatrix is seen in the longitudinal plane. The values of the longitudinal (full) and transverse (full) acceptances were obtained at around 160 mm-mrad and 318 mm mrad respectively, at the exit of MEBT.

Figure 6.19 plots the required rf power values to be fed to the different cavities, along the length of the linac. A margin of 25% has been kept in the rf power requirement calculations here to take into account the effect of any cavity detuning.

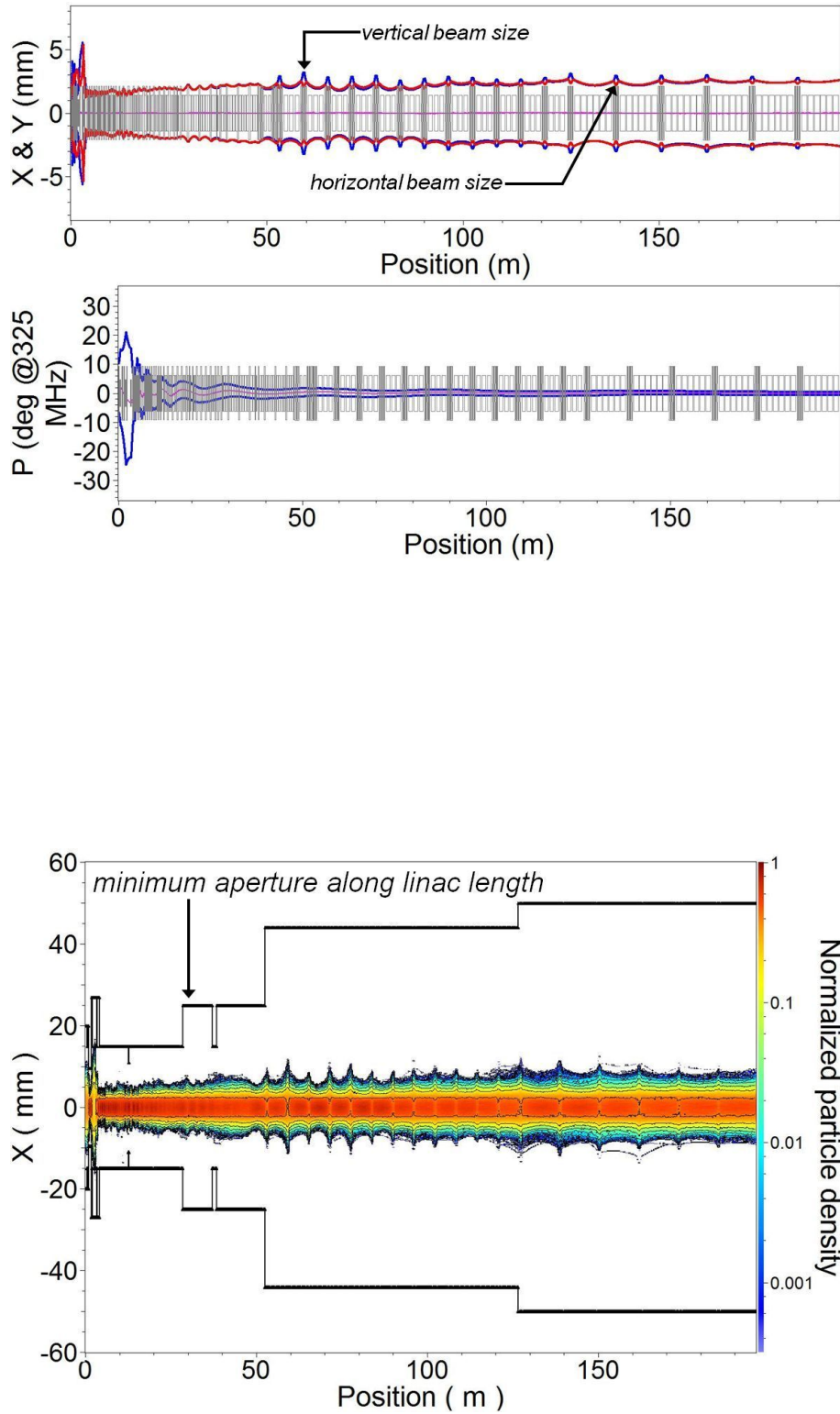


Figure 6.11: Horizontal (top, black), Vertical (top, blue) and longitudinal (middle, blue) rms beam size in the linac along the length. In the other figure (bottom) color map shows radial distribution of the normalized particle density throughout the linac, along with the available aperture (black).

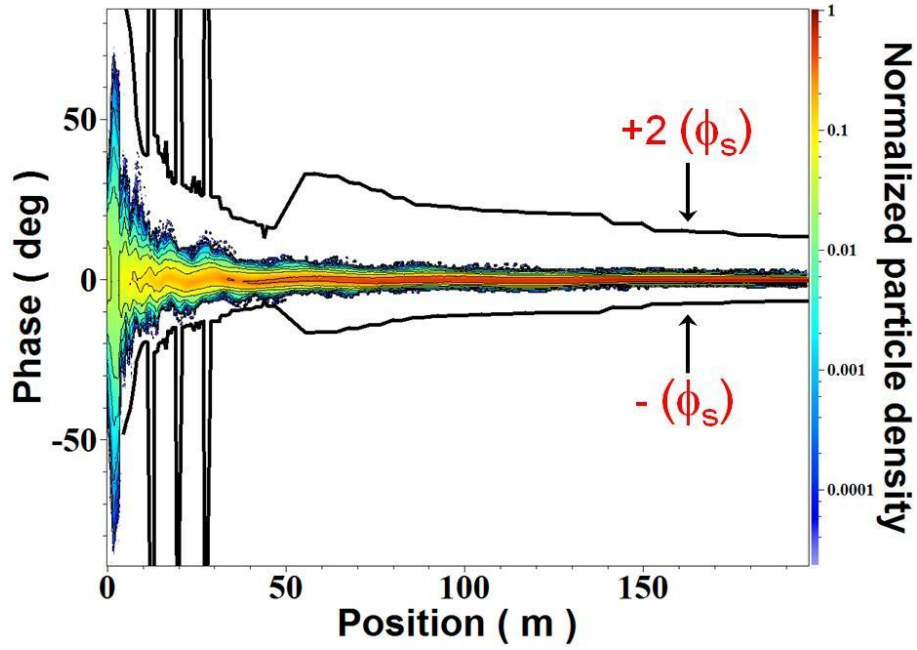


Figure 6.12: RF bucket boundaries at $+2|\phi_s|$ and $-|\phi_s|$ (black) are shown along with phase distribution in the linac.

6.3.3 Studies on the envelope instabilities

As it has been discussed, an actual beam bunch traversing through the linac is not the ideal or the matched one. Small mismatch or perturbation in the rms beam parameters is always there. Eq. 6.3 describes the evolution of the mismatched envelope ($\Delta a_z(s)$) of an intense beam bunch. This equation is a set of 3 coupled linear differential equations. Using Floquet theorem, one can calculate the most general solution in terms of eigenmodes with their eigenvalues for such a set of differential equations with periodic coefficients. Among them, if the modulus of any of the eigenvalues is greater than unity, solution will be unstable. Rigorous stability analysis for the case of a two dimensional coasting beam has been performed by Reiser and Stuckmire [60], as well as Lund and Bukh [153]. However, in their analysis, they have excluded the effect due to RF. In our work, this analysis is extended to the case of a three dimensional bunched beam, including the effect of acceleration and the transverse defocusing arising due to RF. The number of phase space variables is six in the case of a three dimensional beam bunch.

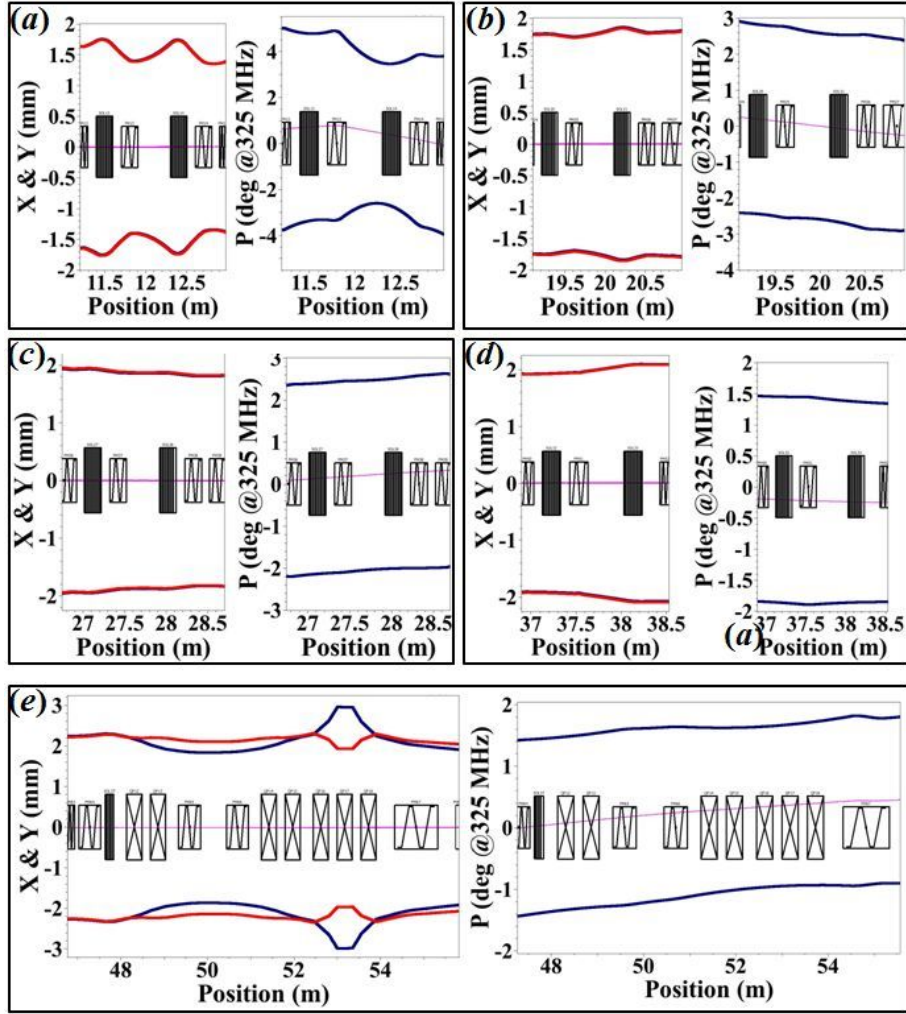


Figure 6.13: Longitudinal (right) as well as transverse (left) rms beam envelope across the transitions from (a) SR0 to SR1(1) section, (b) SR1(1) to SR1(2) section, (c) SR1(2) to SR2(1) section, (d) SR2(1) to SR2(2) section and (e) SR2(2) to EC1 section respectively.

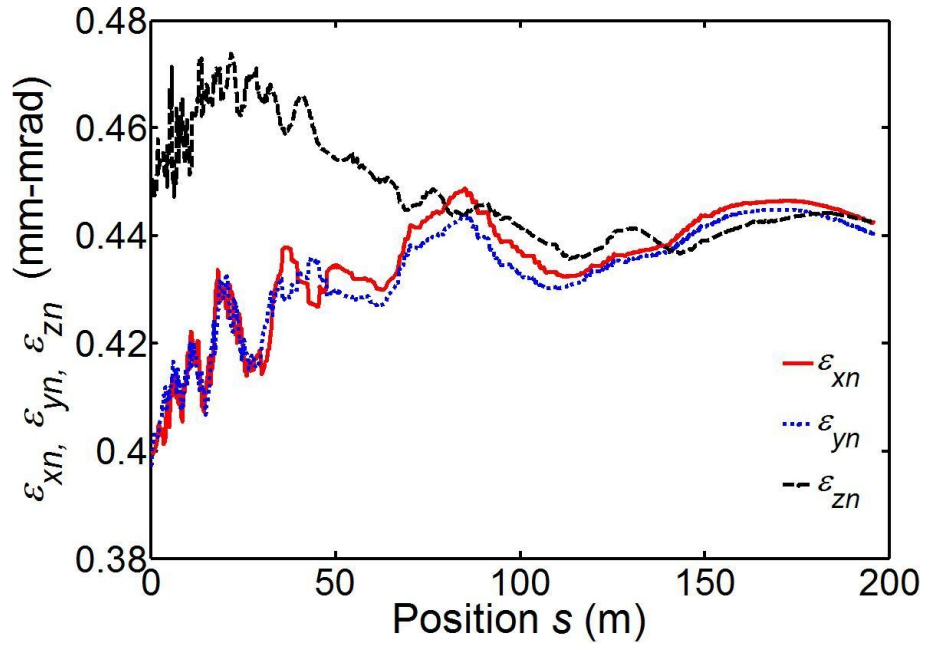


Figure 6.14: Evolution of the normalized rms beam emittance in the longitudinal (black broken line) direction, vertical (red solid line) direction and horizontal (blue dotted line) direction along the length of linac.

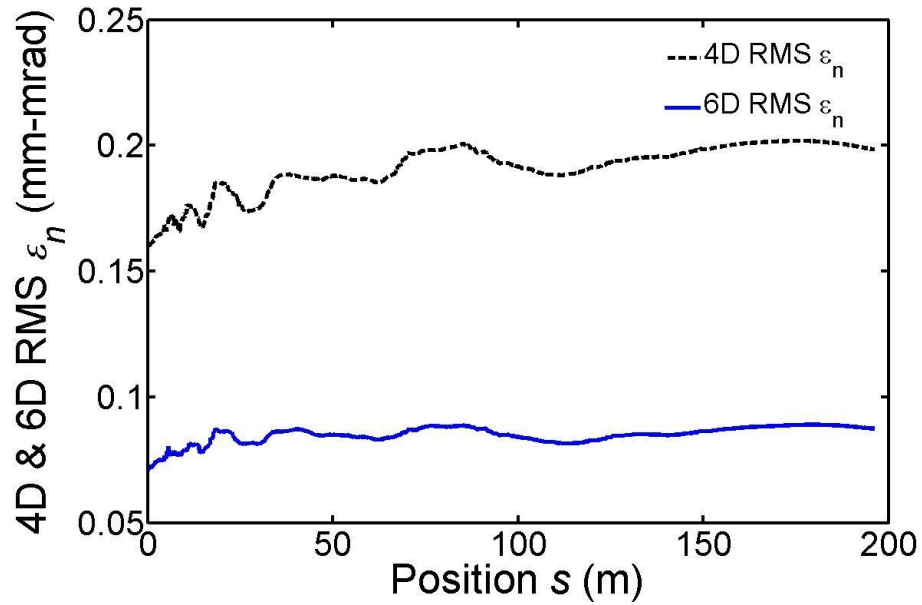


Figure 6.15: Evolution of the normalized transverse 4 D and the 6 D rms emittance values are plotted along the linac length.

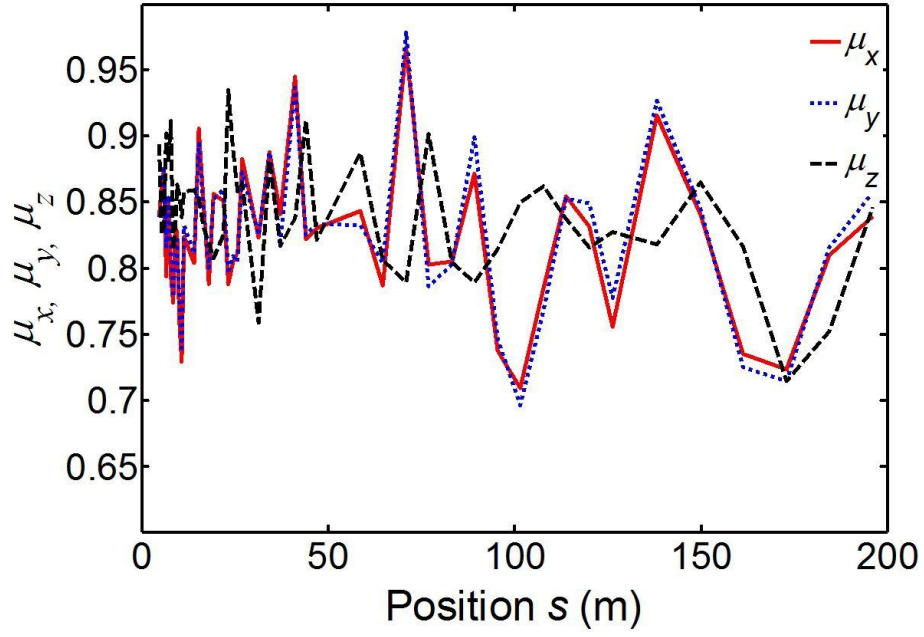


Figure 6.16: Longitudinal (broken black line), horizontal (dotted blue line) and vertical (solid red line) tune depression along the length of the linac.

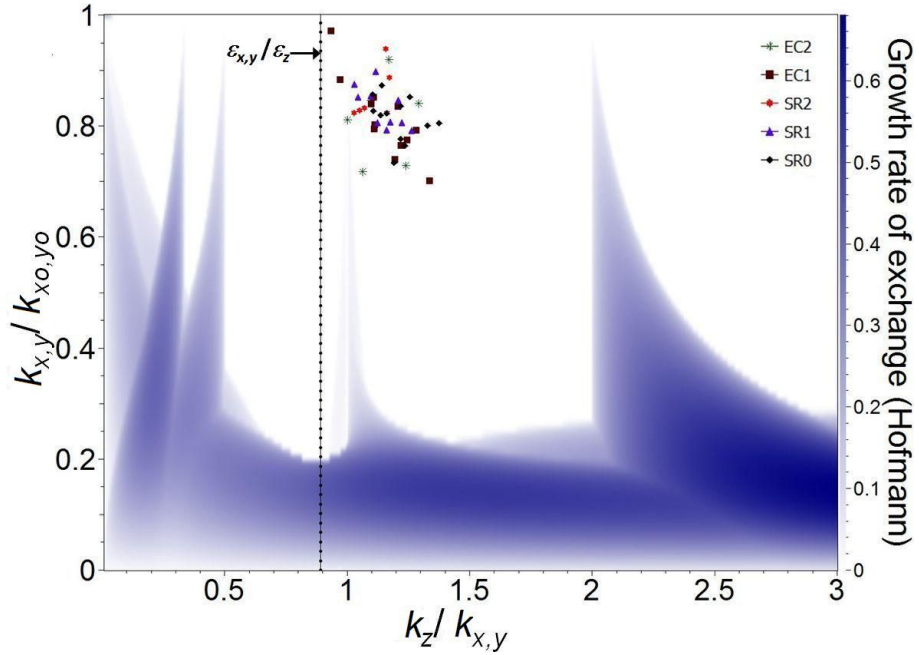


Figure 6.17: Lattice footprint are plotted on the Hofmann chart for ISNS injector linac with $\epsilon_z/\epsilon_x = 1.12$. Here $k_z/k_{xy}=1$ denotes fourth order even resonance, whereas, $k_z/k_{xy}=2$ denotes the third order even resonance. All lattice footprints (shown in coloured dots) are nearly confined in the resonance free zone of the Hofmann diagram, between these two resonances.

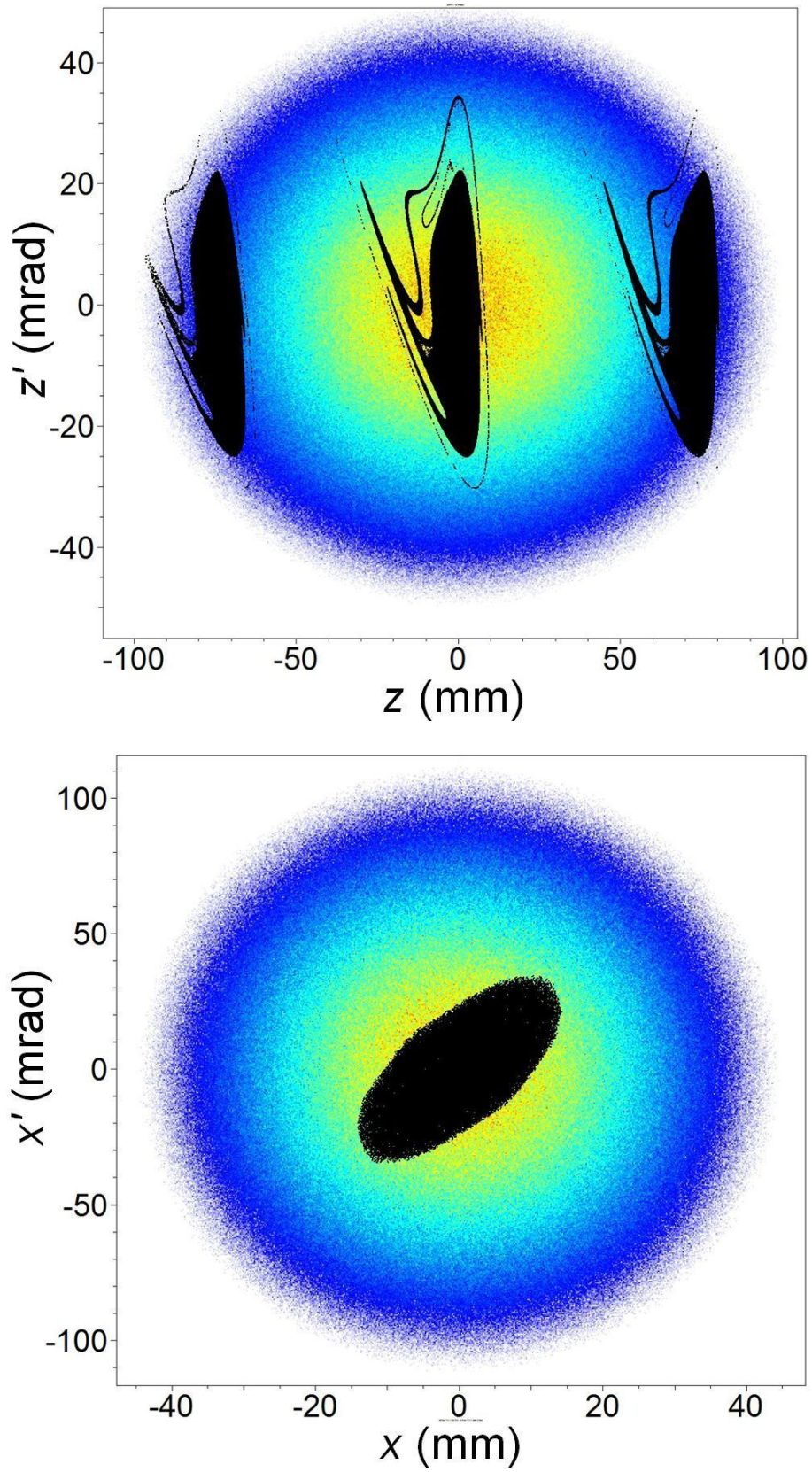


Figure 6.18: Longitudinal (top) and transverse (bottom) full unnormalized acceptance of the linac. Here background colour shows the input beam distribution, on which the acceptances are shown in black.

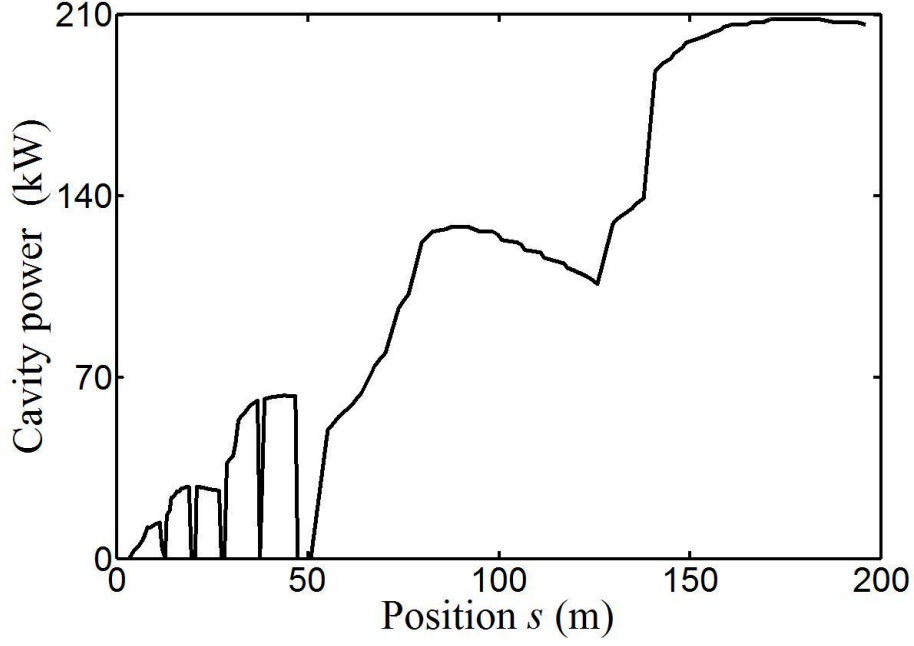


Figure 6.19: RF power requirement for the different cavities along the length of the linac.

Accordingly, six numbers of first-order, coupled linear differential equations with periodic coefficients are obtained. Solving these equations using Floquet theorem, we obtain six eigenvalues. However, as it is shown in Refs. [60] [153], with a two dimensional coasting beam, the authors have obtained four eigenvalues. In our analysis, the 6×6 transfer matrix corresponding to the six coupled differential equations, is symplectic, and it represents propagation of the phase space variables over one period. For this symplectic matrix, the calculated eigenvalues will be in reciprocal and complex conjugate pairs. Probable six scenarios are described below. Also, they are elaborated in Fig. 6.20:

- Case 1: Each of the three pairs of eigenvalues characterizes stable solution. All eigenvalues are complex here, and lie on the unit circle, i.e., $|\lambda| = 1$.
- Case 2: Among the three pairs of eigenvalues, one pair corresponds to unstable solution. For this pair, the eigenvalues are real with $|\lambda| \neq 1$ and $\phi = 180^\circ$. This corresponds to lattice resonance. Here, the remaining two pairs of eigenvalues characterize stable solutions with $|\lambda| = 1$.

- Case 3: Two among the three pairs of eigenvalues are in lattice resonance; hence, correspond to unstable solutions. These two unstable pairs correspond to $|\lambda| \neq 1$ and $\phi = 180^\circ$. For the third pair, solution is stable.
- Case 4: Each of the three pairs is in lattice resonance. Therefore, solutions are unstable here. For all these pairs corresponding $|\lambda| \neq 1$ and $\phi = 180^\circ$.
- Case 5: One pair corresponds to lattice resonance. The other two pairs (say, second and third pair) characterize $|\lambda_2|$ and $|\lambda_3| \neq 1$. Also, for these two pairs, $\lambda_2 = 1/\lambda_3$, $\lambda_2^* = 1/\lambda_3^*$ and $\phi_2 + \phi_3 = 360^\circ$. These two pairs perform confluence resonance. Here, solutions corresponding to all three pairs are unstable.
- Case 6: One of the three pairs corresponds to a stable solution, whereas, the other two are in confluence resonance.

For a perturbed beam bunch, the three pairs of eigenvalues represent the three normal mode of oscillation. Earlier analyses reported in Refs. [60] [153] describe growth rates of only two normal modes. On the contrary, this analysis performed for a three-dimensional bunched beam, discusses the growth rate of three normal modes. In their analyses presented in Refs. [60] [153], the authors have concluded that in the case of axisymmetric beam in a solenoid focusing channel, only one type of resonance, *i.e.*, the parametric resonance is possible, and confluence resonance is not possible in that case. This is because for an axisymmetric beam in a solenoid channel, their analysis reduces to one dimension in their case. However, for a three-dimensional beam bunch, even in the case of an axisymmetric beam in a solenoid focusing channel, the analysis will be two-dimensional. Here, the longitudinal dimension will be associated with each of the transverse dimension. Therefore, our analysis performed on an axisymmetric beam in a solenoid focusing channel shows confluence resonance also, in addition to parametric resonance.

We now present the results of our calculations performed to obtain the growth rate of

the three eigenmodes of three-dimensional rms mismatched envelope for the linac lattice. Mismatched envelope was analyzed for the different lattice sections, which were optimized for the different energy ranges of the linac. Through this analysis, we have ensured the stability of the beam by setting an upper limit on the zero current phase advance per period $\sigma_{\zeta 0}$. Analyses reported in Refs. [60] [153] suggest to set this limit as 90 degree for all three planes. Our three three-dimensional analysis is more generalized in nature. Therefore, in this three-dimensional analysis, we wanted to verify it explicitly, if we get a similar value of $\sigma_{\zeta 0}$, as reported in Refs. [60] [153]. Results of our analysis performed for the SR0 section are described in Fig. 6.21. As mentioned earlier, it is the only section, where the accelerating gradient in the cavity is limited by the maximum value of σ_{x0} , σ_{y0} and σ_{z0} . In line with our analysis, we therefore set $\sigma_{x0} = \sigma_{y0} = \sigma_{z0} = 89^0$, which is just below the limiting value of $\sigma_{\zeta,0} = 90^0$. For the envelope oscillations, phase advance per period of the three normal mode of envelope oscillations are shown in Fig. 6.21. These values were computed for different values of tune depression, corresponding to different values of beam current I_B . From the analysis, we found that the modulus of eigenvalues is unity, which is shown in Fig. 6.21. Also, this is independent of beam current. This shows that the envelope oscillations will be stable in this case. For the confirmation, beam dynamics simulations were performed explicitly for a beam bunch with 10% mismatch and the results are shown in Fig. 6.22. From the figure, it is evident that as expected theoretically, mismatch oscillations obtained from the simulations are stable.

To explore the behavior of the lattice for higher values $\sigma_{\zeta 0}$, another analysis was performed with $\sigma_{\zeta 0} = 105^0$, and the results are shown in Fig. 6.23. Here, we notice five distinct regions, which can be described as follows:

- Region 1: All three normal modes of oscillations are stable, which is represented as Case 1.
- Region 2: Lattice resonance is shown by the third normal mode. The other two

normal modes are stable, which are represented by Case 2.

- Region 3: Here the second normal mode is in resonance. Therefore, this region is similar to Region 2.
- Region 4: A confluence is observed between the first and second normal modes. Here, the third normal mode is stable. This characterizes Case 5.
- Region 5: It is similar to Region 2. The first normal mode is in resonance here.

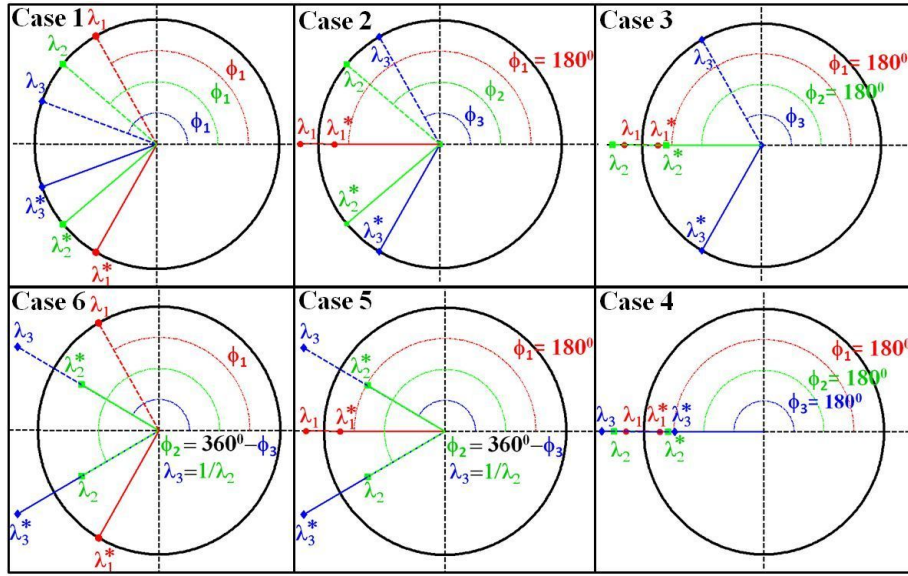


Figure 6.20: Along with the unit circle which is shown in black, eigenvalues of the envelope oscillations of a three-dimensional beam bunch in a periodic lattice are shown on the complex plane.

Region 4 in Fig. 6.23 shows the interesting occurrence of a confluence resonance in the solenoid focusing channel. This observation is commensurate with our earlier discussion, where we argued that such a case can only be observed in the three dimensional analysis of envelope mismatch, whereas, the two dimensional analysis of coasting beam described in Refs. [60] [153] does not derive this conclusion. Beside SR0 section, in the other sections of the lattice, we have specified the maximum value of $\sigma_{\zeta 0}$ considerably less than the limiting value of 90° in all three planes. These values are approximately 85° and 65° respectively, in the SR1 and SR2 sections. Similarly, $\sigma_{\zeta 0}$ is $\sim 68^\circ$ and 62° respectively,

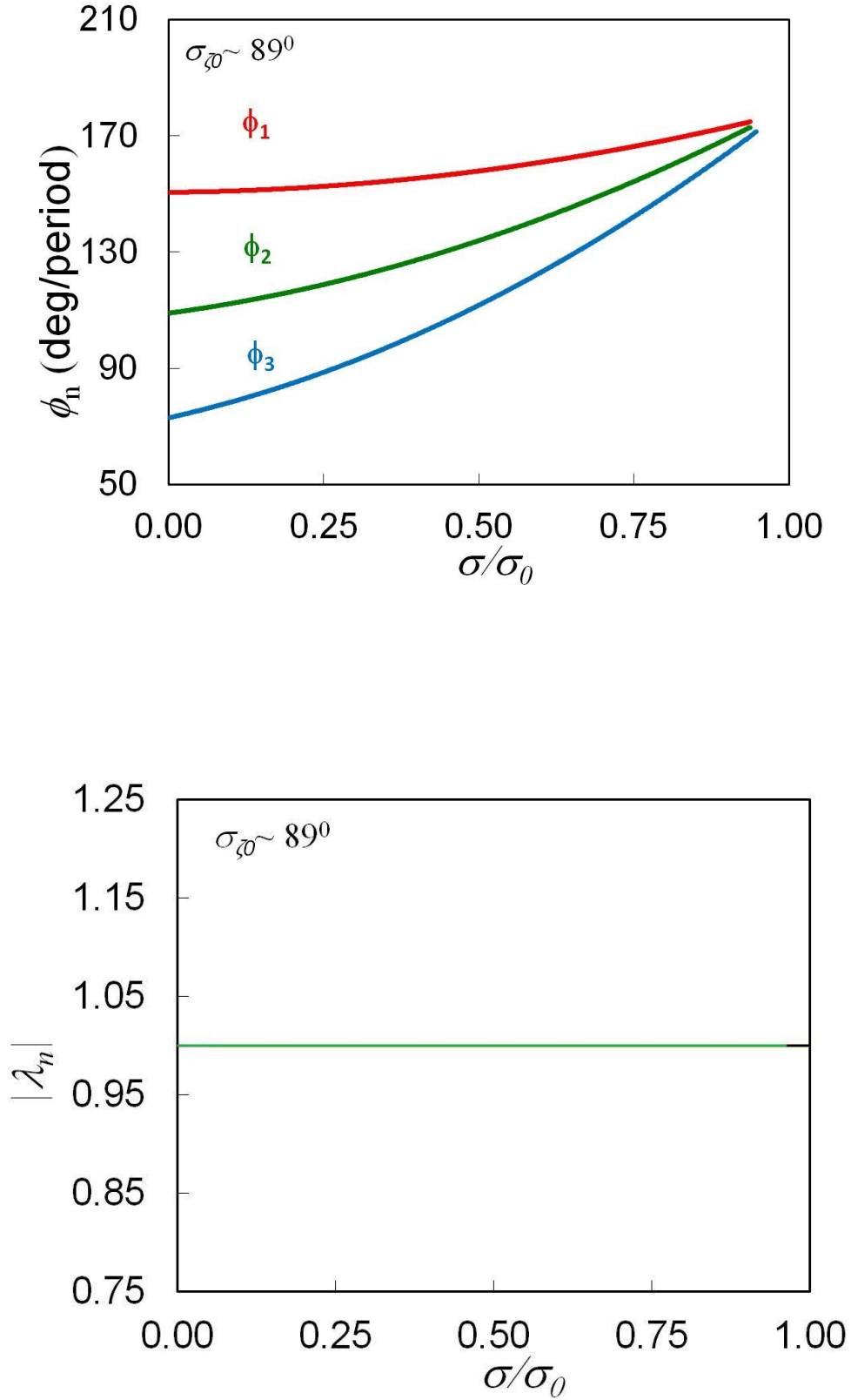


Figure 6.21: Phase advance per period ϕ_n (top), and modulus of eigenvalue of normal modes of mismatched envelope oscillation, plotted as a function of tune depression for $\sigma_{z0} = 89^\circ$. Note that in this case, eigen values could not be calculated accurately beyond a value of $\sigma = 87.5^\circ$, because of some numerical accuracy.

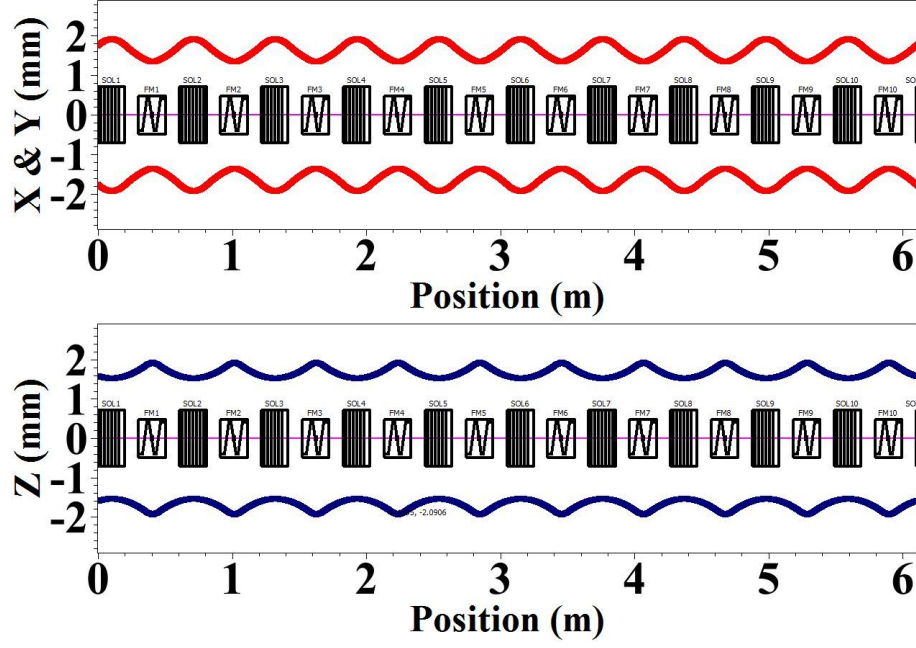


Figure 6.22: Oscillations in the beam envelope along x , y and z direction, as obtained from the simulation for 10% mismatch in the beginning, is shown for $\sigma_{\zeta 0} = 89^\circ$.

in the medium and high beta elliptic cavity sections. As it is expected, no resonance is observed there.

6.3.4 Analysis on the beam halo, using particle core model

In a high power hadron linac, another important loss mechanism is through halo formation. Average particles in the beam bunch perform stable oscillations within the beam envelope. In this context, oscillations performed by the halo particles are also stable but their amplitude is significantly larger compared to the average or core particles. As a consequence of this, beam size as well as beam emittance grows. In a typical accelerator for a spallation neutron source, halo particles are removed mostly in the High Energy Beam Transport (HEBT) section. Hence, these halo particles travel all the way throughout the linac, along with the core particles. In order to decide the minimum beam pipe aperture in a particular section of an accelerator, estimation of the maximum transverse extent of the halo particles is therefore extremely important.

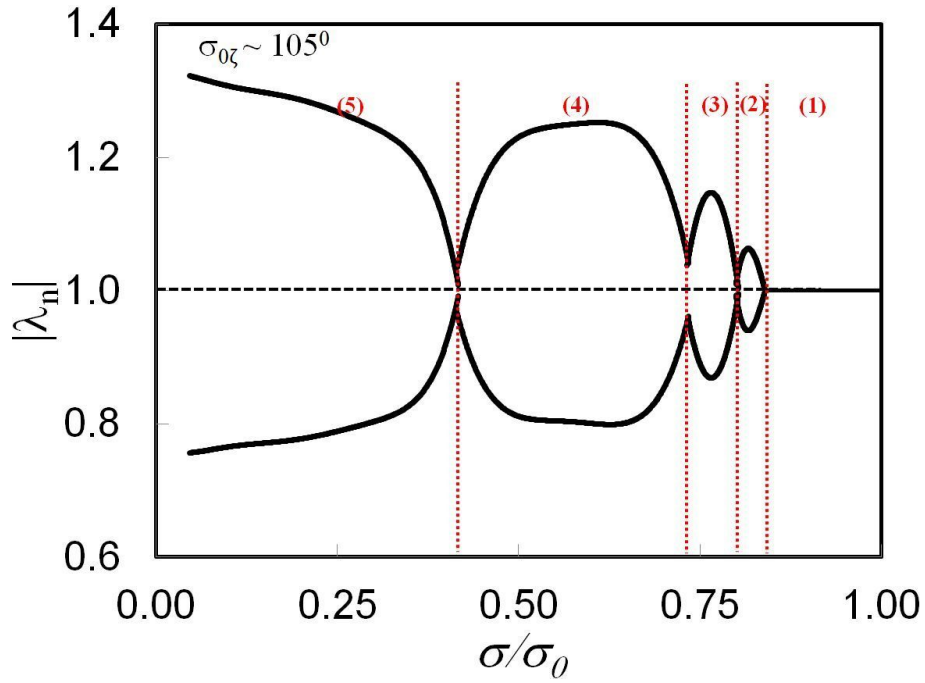
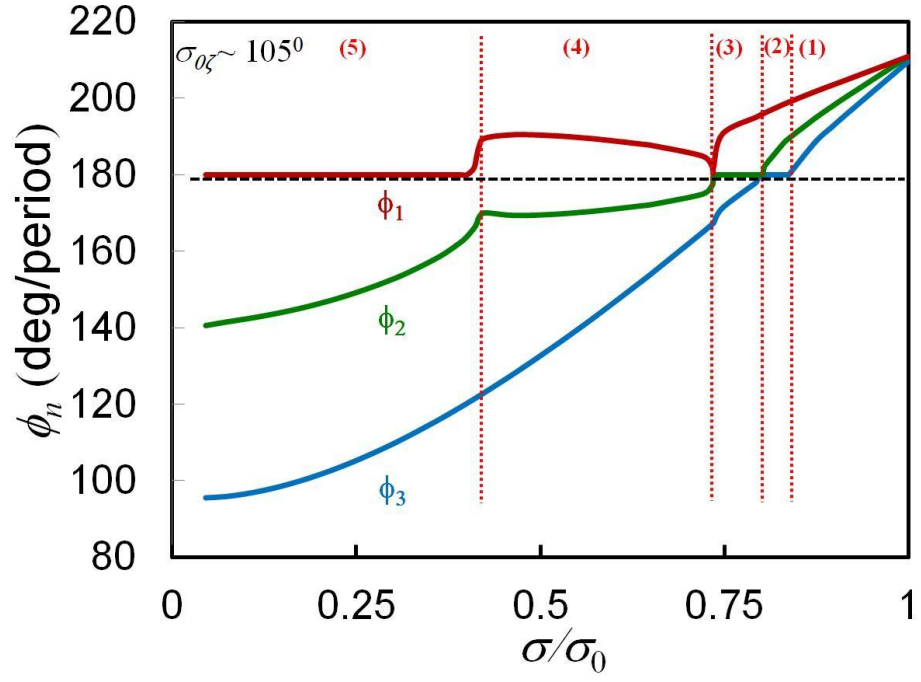


Figure 6.23: Phase advance per period ϕ_n (top) and modulus of eigenvalues of normal modes of mismatched envelope oscillation is plotted as a function of the tune depression for $\sigma_{\zeta 0} = 105^0$. In the figure we have marked five distinct regions as described in the text.

In-depth research has been performed on halo formation mechanism in the beam by several authors [55] [150]. It is widely believed that the parametric instability arising from the mismatch oscillations in the beam envelope is an important mechanism of halo formation. As a result of oscillations in the beam envelope arising due to mismatch, particles experience a periodic variation in the effective spring constant that corresponds to a net restoring force. The dynamics of such particles can be described using well-established Particle Core Model (PCM) based on the pioneering work reported in Ref. [55]. Implementing this concept, we wrote a subroutine in MATLAB, to solve the following equation of motion of a halo particle and calculate its maximum radial extent,

$$\zeta'' + k_{\zeta 0}^2(s)\zeta - f_{par}^{sc}(I_B, a_x, a_y, \zeta) = 0. \quad (6.8)$$

Along with this equation, following rms envelope equation was also solved simultaneously in the presence of a mismatch to calculate the rms beam size:

$$a_{\zeta}'' + k_{\zeta 0}^2(s)a_{\zeta} - f_{env}^{sc}(I_B, a_x, a_y)a_{\zeta} = 0. \quad (6.9)$$

Here we want to point out that, Eq. 6.8 and 6.9 are the simplified form of the Eq. 6.1 and 6.2. The dynamics of halo particles were calculated for the cw beam in absence of acceleration, where, position and angle of the single particle are described by ζ and ζ' . Perturbed beam size of the core is denoted by a_{ζ} . and space charge effect is introduced by the function $f_{env}^{sc}(I_B, a_x, a_y)$ in the above envelope equation. It is noteworthy to mention here that the space-charge term $f_{par}^{sc}(I_B, a_x, a_y, \zeta)$ acting on a single halo particle is linear only when the halo particle is inside the core and it decays outside the core. Such dependency makes $f_{par}^{sc}(I_B, a_x, a_y)$ a nonlinear function in ζ . Using the (electric) field expression(s) given in Ref. [162], space charge force experienced on the single particle is calculated inside, as well as outside the envelope.

The result of our analysis performed for the SR0 section, is shown in Fig. 6.24. Among

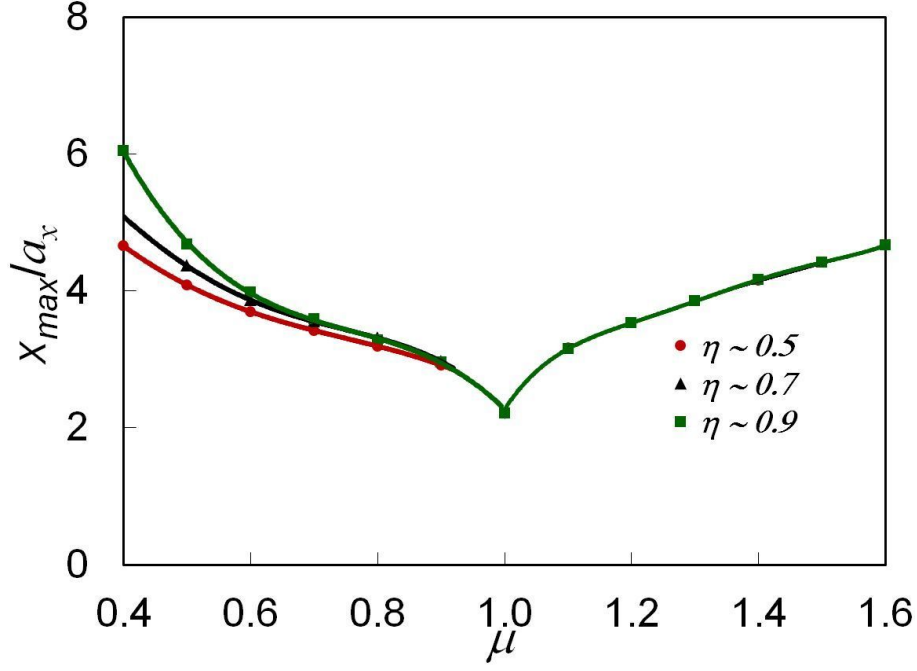


Figure 6.24: Maximum extent of the halo particles (x_{max}) in the transvers plane as a function of the beam mismatch (μ) for the proposed injector linac. Here, different curves corresponds to different tune values (η).

different sections of ISNS linac, aperture radius is lowest in the SR0 section. For different values of tune depression η , variation of the maximum extent of halo particle is shown in the figure, as a function of the mismatch parameter (μ). Here μ denotes the ratio of the mismatched and matched beam size at the entrance of the section. Calculations described in Ref. [55] was performed for an ideal condition, considering a ‘constant’ matched beam size a_x throughout the length s . In our calculation, we have considered the actual variation in a_x with s for a matched beam. Here, mismatched oscillations was taken as a perturbation, superimposed on the oscillating matched beam. In this analysis, maximum radial extent of the halo particles were estimated from the lattice with 5000 SR0 periods. At the entrance, the horizontal and vertical beam emittances were taken as at 0.3972 and 0.3996 mm-mrad, respectively. The two emittance values are nearly equal. Therefore, we have assumed that for this nearly circular beam, maximum extent of the halo particles will remain approximately independent of the azimuthal position of the particles.

In this analysis, we have estimated maximum transverse oscillation amplitude of the halo particles to be around 6 times that of the rms beam size a_ζ . It is noteworthy that for different tune values, we have observed nearly equal value for the maximum extent of the halo particles. Following Ref. [55], we have obtained the following expression for x_{max}/a_ζ as a function of mismatch factor μ by data fitting :

$$\frac{x_{max}}{a_\zeta} = 3.071 \times \ln(\mu) + 2.723. \quad (6.10)$$

Here, we want to emphasize that, in a real linac, number of periods are limited (*e.g.*, for the ISNS injector linac, in the SR0 section, only 12 periods will be there). As a consequence, effect of beam halo formation may not be severe for an individual section.

In this analysis, focusing or defocusing effect of RF in the lattice was not considered. Also as mentioned, we have considered a two-dimensional cylindrical beam instead of the realistic configuration of a three dimensional beam bunch. These considerations may deteriorate the scenario in the real case.

We have repeated the same analysis in the case of medium and high beta elliptical cavities sections also. There, beam pipe aperture (r_{bp}) is considerably larger compared to the SR0 and SR1 sections. Accordingly, we found there the ratio r_{bp}/a_ζ is even greater than or by 10 times.

6.3.5 Studies on the beam loss estimation of the optimized linac

In Chapter 1, we have presented a discussion on the issues and severity of the beam loss, particularly in the case of a high energy, high power H^- linac. In this chapter, a methodology has been described, following which, we have designed the optimized lattice for the 1 GeV, 1 MW injector linac for the proposed ISNS project. Our aim was to design a compact linac with low loss. We now present a discussion on the estimation of beam loss,

and also verify whether for this optimized design, the beam loss is within the acceptable limit. Using the optimized strength of focusing magnets, we first calculated the fractional loss due to Lorentz stripping, which was found negligible ($< 10^{-12} \text{ m}^{-1}$) throughout the linac. In Chapter 1, we also mentioned Intra-Beam Stripping (IBS), as another prominent loss mechanism, particularly important in an H^- linac. In this optimized linac, the loss due to IBS was calculated from the simulated beam size, divergence and beam energy. For this, we have followed the procedure outlined in Refs. [56] [163]. Besides, an elaborate discussion on the mathematical formulation for IBS is presented in the **Appendix A**. Calculated fractional beam loss due to IBS is shown in the Fig. 1.5. As it is shown there, the total allowable fractional beam loss demonstrates smooth decreasing trend with increasing beam energy, because the beam size and divergence are nearly constant along the linac. Calculated power loss per unit length of the stripped particle due to IBS, as well as the integrated power loss along the length of the linac is also shown in Fig. 6.25. Based on our calculation, we have observed that the maximum loss due to IBS is around 0.03 W/m in our design, which is significantly less than the stringent loss limit of 1 W/m.

The estimated loss in the SNS SCL is reported as $\sim 0.05 - 0.17 \text{ W/m}$ [58], which is more than the value we obtained. Perhaps, it is because the result presented in Fig. 6.25 only indicates the loss due to IBS, whereas, the reported result in Ref. [58] incorporate all possible losses. ISNS linac is designed for a micropulse average beam current (I_{av}) of $\approx 14.5 \text{ mA}$, whereas, the current in the SNS linac is $\approx 35 \text{ mA}$ [16]. As we know, the intrabeam stripping loss varies with the square of the total charge of a beam bunch, therefore, nearly double the value of beam current (*i.e.* in the case of SNS,) indicates a loss 4 times more than the loss we have calculated.

6.4 Discussion and conclusion

To summarize, we have discussed an optimization procedure for the beam optics design

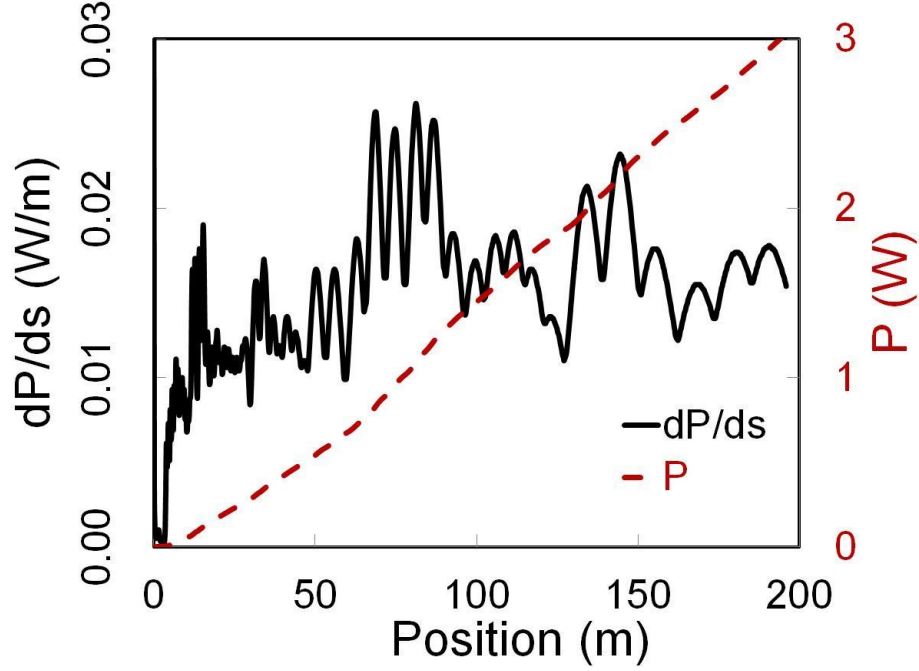


Figure 6.25: Calculated power loss per unit length (solid black line) as well as integrated power loss (broken red line) due to the occurrence of intrabeam stripping along the length of the linac.

of a 1 GeV, 1 MW superconducting injector linac for the proposed ISNS. The linac will consist of a number of independently phased cavities and focusing magnets, grouped into several sections. Different important issues related to longitudinal as well as transverse beam dynamics of such a long linac has been elaborated in this chapter. The aim has been to keep the linac compact, while also ensuring a robust lattice design and a beam loss strictly under the permissible limit of 1 W/m. This goal has been achieved by a careful design procedure that was discussed in this chapter.

In this chapter, we have mentioned that the ISNS project is seen as the precursor of the Indian ADS project, and justified our inclination towards designing the entire ISNS injector linac using SRF cavities. However, in the low energy realm of a pulsed hadron linac, below the energy about 180 MeV, the use of superconducting cavities might not be cost efficient, especially keeping in mind that the technology for room temperatures structures is well developed. On the other hand, being an emerging technology for the frontier accelerators, standardization and global acceptancy of the spoke resonators may

still require significant R&D work. Therefore, for the ISNS project, we have also worked out an alternative lattice design, where the low energy part of the linac will comprise of a normal conducting Drift Tube Linac (DTL) structure.

To make the design compact, acceleration gradient in the cavities should be pushed towards their maximum permissible values, and if possible, absolute value of cavity synchronous phase ϕ_s should be close to zero. However, the choice of ϕ_s is limited by the fact that longitudinal phase acceptance of a cavity is around $|3\phi_s|$. On the other hand, there are two constraints in setting the maximum permissible value of the acceleration gradient: (i) peak field at the cavity surface should be less than the field corresponding to breakdown, and (ii) the longitudinal phase advance per period should be less than 90 degree. It may be noted here that the first constraint is in terms of peak electric field E_0 whereas the second constraint is in terms of E_{acc} , i.e., E_0T . In case of the second one, the limiting gradient and the RF power requirement ($\sim I_B E_0 T \cos(-\phi_s)$) turns out to be independent of transit time factor. For a given acceleration gradient (E_0T), the power dissipation P_c on cavity surface, being dependent on E_0 , is higher if T is lower. P_c is proportional to $1/T^2$. Therefore, we have tried to keep the normalized transit time factor greater than 70% to ensure that the cryogenic power requirement does not exceed by a factor of two due to this effect. Next, when we are limited by the first constraint, the maximum attainable value of E_{acc} is proportional to T . Hence, here we will aim for high value of T , for example ~ 0.9 . From Figs. 6.8 and 6.9, we notice that nearly 93% of the cavities in this design confirm this requirement. It is quite relevant to mention here that the choice of appropriate geometric beta (β_g) values of the SRF cavities, along with optimum value of transition energies, have also played a crucial role in minimizing the number of cavities. For example, a switch in the β_g value from 0.9 to 0.81 simply resulted in a change in the requirement of total number of elliptic cavities 82 to 72 in the medium and high energy section.

We would like to mention that one main aim of this design was to make the linac as

compact as possible. In order to achieve this, we have ensured the use of maximum acceleration gradient in most of the cavities. Towards the same aim, we tried to set the absolute value of synchronous phase to be as small as possible; ensuring that bunch length is well within the acceptance. However, we have noticed that in the majority of the operational high power linacs, the absolute value of the synchronous phase is $\geq 25^\circ$, to increase the area of the RF bucket and accommodate halo formation due to phase and amplitude errors. The beam dynamics studies presented in the thesis do not include the analysis of the dynamic and static errors of the accelerating and focusing elements, and the acceptability of this lattice will be confirmed after we complete our beam dynamics studies extensively including the effect of static and dynamic errors of the accelerating and focusing elements, along with its correction scheme, which is now ongoing. Based on the feedback, we will revisit the lattice design, if required. As it is shown in Fig. 6.12, there are particles close to the boundary of the stable area in this design, especially in the low energy section. Although, our multiparticle simulation shows that near the phase space boundary the density of the particle is very small, yet after completing the study of static and dynamic errors of the lattice elements on the beam dynamics, we will revisit this issue, and we will verify whether it is necessary to improve the longitudinal phase space area resetting the synchronous phase values.

In a high power hadron linac, proper matching of the beam parameters at the entrance of each section is very important, and this is ensured by the design of suitable matching sections in between two lattice section of the linac. An unmatched beam may result in significant emittance growth, and sharp changes in k_l and k_t . These matching sections are also important since we need to fine tune the lattice parameters in each section, so that the lattice footprint lies in the desired zone on Hofmann diagram. In our work, we have aimed to concentrate all (or most of) the lattice footprints in a resonance free zone of the Hofmann diagram. The footprints have been localized in the zone between the third and fourth order even resonance peak, since we chose $k_{l0} > k_{t0}$, to make the linac compact. Besides, to ensure the use of maximum acceleration gradient and adequate transverse

focusing, we have fixed the footprint area very near to the outside of the the fourth order resonance peak in the Hofmann diagram. However, we would like to add an important point here. Hofmann diagram provides a ingenious insight about the emittance exchange due to core-core resonance, as well as the chances of emittance growth, yet, for a periodic lattice, it may not be the ultimate performance indicator. The reason is that the diagram is generated considering *smooth approximation*. Hence, in order to estimate and control the growth in the beam size and emittance in a precise manner along the length of the linac, a careful and robust multiparticle simulation is truly inevitable.

Since we chose a lattice based on the conventional criterion of limiting values of phase advances per period, we thought it may be appropriate to ensured that the design is free from the envelope instability, by performing an analysis of the same for the *actual* lattice. It may also be interesting to further explore, if for a particular lattice, higher value of phase advances per period is possible, as has been seen in some cases [164], particularly in the longitudinal plane. We have performed these analyses, taking a bunched beam for the actual optimized lattice. Similarly, we have performed the analysis of beam halo using PCM for the actual periodic lattice, *i.e.*, without invoking smooth-approximation in the calculation. This ensures no undesired effects related to beam halo even when the periodic variations are considered in a matched envelope, for our design. Our analysis on the formation of the beam halo is an extension of the work in Ref. [55]. We verified that the formula for the maximum transverse extent of the halo particle (x_{max}) as a function of mismatch parameters (μ) for our optimized lattice is similar in nature to the formula given in Ref. [55]. The two constants in the formula however differ slightly.

While designing a high-energy, high-current H⁻ linac for a large value of micropulse current, the issue of intra beam stripping is of extreme importance. From Eq. 11 (of the Appendix A), it can be shown that the fractional beam loss is inversely proportional to the beam size, as well as it is proportional to the square of the average beam current. Such loss for a low emittance beam may thus be higher due to reduced beam size. Therefore,

the beam size as well as the micropulse averaged beam current should be appropriately chosen, to satisfy the stringent beam loss criteria due to intra beam stripping.

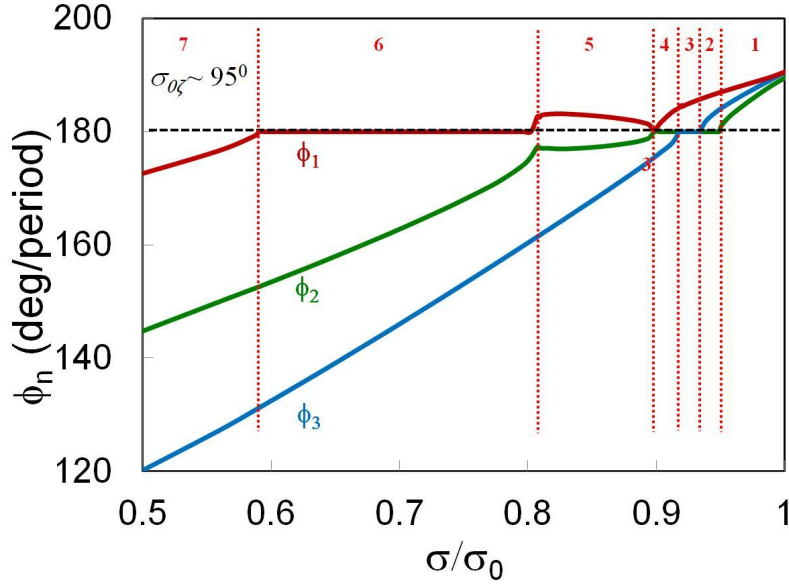


Figure 6.26: Phase advance per period ϕ_n of mismatched envelope oscillation as a function of the tune depression considering $\sigma_{z0} = 95^\circ$.

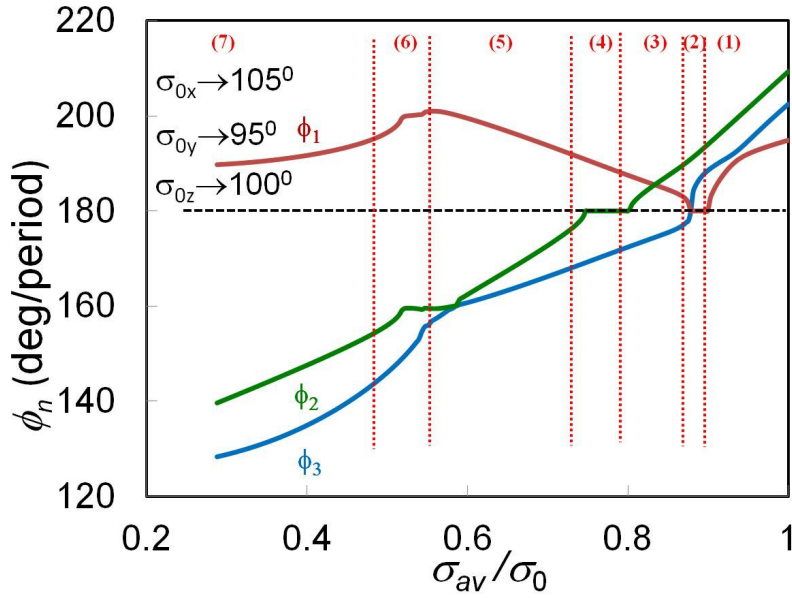


Figure 6.27: Phase advance per period ϕ_n of mismatched envelope oscillation as a function of the tune depression considering $\sigma_{x0} = 95^\circ$, $\sigma_{y0} = 105^\circ$ and $\sigma_{z0} = 100^\circ$.

For a three-dimensional bunched beam in a periodic lattice, out of the six possible cases of envelope oscillations as shown in Fig. 6.25, only ‘Case1’, ‘Case 2’ and ‘Case 6’ have

been seen depending on the chosen parameters. However, we have explicitly verified that the remaining cases are also possible by choosing different values of σ_0 . For SR0 lattice, Fig. 6.26 shows that ‘Case 3’ is possible in Region 3, assuming $\sigma_0 = 95^0$. Similarly for $\beta_g = 0.61$ lattice, Fig. 6.27 proves that ‘Case 5’ is possible in Region 4 where $\sigma_{x0} = 95^0$, $\sigma_{y0} = 105^0$ and $\sigma_{z0} = 100^0$.

Chapter 7

Conclusions and future work

Accelerator based spallation neutrons have proven themselves as an excellent probe for exploring the properties and dynamics of almost all materials. To shape the modern day neutron based science in our country, a proposal is there to build one Indian Spallation Neutron Source (ISNS). An important part of this complex accelerator will be a *megawatt* class Superconducting Radio-Frequency (SRF) linac, which will boost the energy of H^- beam up to the full energy of 1 GeV.

In this linac, H^- beam will gain a major part of its energy in the superconducting elliptic cavity sections. Electromagnetic (EM) design of such state of the art SRF cavities involves a rigorous optimization for their best electromagnetic performances. After the EM design of these cavities, beam optics design of the linac using these cavities is also challenging because of their stringent beam dynamics requirements. Therefore, motivation of this research was two fold:

1. to design such multicell elliptic SRF cavities for their optimized electromagnetic performance, as well as
2. to evolve a technique for the lattice design of a megawatt class H^- linac.

Accordingly, we developed a generalized methodology for the electromagnetic design

optimization of these multicell elliptic SRF cavities, and finally designed three families of 5-cell, 650 MHz elliptic SRF cavities, using this methodology. Based on thorough beam optics studies, a 1 GeV, 1 MW H^- injector linac lattice has been designed for the ISNS, satisfying stringent beam dynamics requirements.

Electromagnetic design of the elliptic SRF cavity was optimized for the maximum achievable acceleration gradient, considering two main constraints - first one arising from the tolerable limits of the peak surface electric field (limited by the field emission), and the second one arising from the tolerable peak surface magnetic field (limited by the breakdown of superconductivity of the material). Instead of the conventional technique of multivariable optimization, we have developed a step-by-step, one-dimensional optimization procedure for the optimization of the electromagnetic design of a TESLA type SRF cavity, aiming for maximum achievable acceleration gradient (E_{acc}). We have described the geometry of an elliptic cavity in terms of seven independent parameters. Following the developed sequence, one can calculate the optimum value of these parameters, one at a time, with appropriate scientific reasoning, for achieving the targeted E_{acc} . In the case of a multi-cell cavity geometry, end cells require further optimization. For this, we have evolved a simple technique, where end half-cell length is optimized to tune the cavity to its design frequency for the fundamental mode. Such tuning also maximizes field flatness in the multicell geometry. Although the primary aim of our optimization technique has been to maximize the achievable E_{acc} , it also ensures a reasonably high value of the shunt impedance in the final cavity geometry. While designing a multicell cavity, another important issue is to optimally choose the number of cells in a cavity. We have optimized the number of cells, mainly considering the range of β for which the cavity will be used, and also based on the limitation of input RF power that can be fed using a single input power coupler. Our methodology was finally benchmarked with the help of the reported optimized electromagnetic parameters of the 1.3 GHz TESLA cavity, as obtained by using the standard multi-variable optimization technique. Our methodology is generalized in the sense that following this sequential

one-dimensional technique, TESLA type SRF cavity geometry of any frequency can be optimized for the maximum achievable E_{acc} . A future study may be to explore the design optimization of re-entrant type cavity geometries, following this optimization procedure.

The above mentioned sequential methodology will ensure the optimized electromagnetic design of a multicell SRF cavity for the fundamental mode. However, such optimization will not take care of the unwanted effect of Higher Order Modes (HOMs) and wakefields induced in the cavity, in presence of beam. As an example, the problem of trapped mode requires us to redesign the cavity end cell. Our methodology is however effective only for a limited number of trapped HOMs as the geometry optimization options are limited in the case of cavity end-cells. In future, a thorough optimization analysis can be evolved, which can take care of the design with multiple trapped modes. If we increase the beam current in a linac, a threshold will be reached, beyond which beam gets unstable, because of regenerative Beam Break-Up (BBU) instabilities. On this topic, several studies have been reported earlier, which give the formula for the calculation of threshold current for onset of this instability. We have worked out the details of intermediate steps, to understand the detailed derivation of the formula, and based on this we have evolved a detailed procedure the estimation of the threshold beam current in a multi-cell cavity geometry. Calculation for the dispersion diagram for dipole pass bands for a multicell cavity, was an essential part of this calculation. We have performed the study of BBU instability, to ensure that the design current in the superconducting injector linac will not be limited by this threshold value. As a future work, the BBU instability can be performed in the case of a single or double cell cavity. In the SRF cavities, another crucial aspect is to minimize the chances of heat load due to the resonant excitation of HOMs induced by the beam. This analysis was performed for the medium and high beta elliptical cavities optimized for the ISNS linac. An estimate was obtained for the Q_{ext} of HOM coupler, to ensure that the strength of HOMs in the cavity is not significant.

A simple procedure was developed for the calculation of the longitudinal wake-loss factor for the beam, which is not ultra-relativistic. Calculation based on conventional approach is time consuming as well as resource consuming. Therefore, a procedure was developed to calculate the same in an axisymmetric cavity structure, using the freely available two-dimensional code SUPERFISH. Such an analysis gives us the rigorous estimation of the unwanted effect of HOMs and wakefields on the electromagnetic performance of the cavity, as well as on beam. Loss factor calculation technique can also be extended for non-axisymmetric cavity structures.

Next, an analysis was presented on the dynamic Lorentz Force Detuning (LFD) for a $\beta_g = 0.9$, 650 MHz elliptic cavity, which will be used in the high energy section of our pulsed injector linac. Compensation of detuning due to Lorentz force is essential during the operation of an SRF cavity, especially from the point of view of RF power feeding. A methodology has been reported for the LFD analysis, as well as its compensation. In particular, the dynamic LFD is an important concern, particularly for a pulsed machine like ISNS. Our methodology starts from the analysis of static LFD. Based on the static analysis, we have optimized the shape and the thickness of the helium vessel. Also, we have explained how the static analysis gives an approximate range of radial locations of the stiffener rings, for the reduction of LFD, which can be then compensated using a tuner. In the dynamic LFD analysis, we have calculated the structural mode frequencies, and have performed the transient analysis of the structural deformation, which is explained as an integrated effect of the vibrations of the normal structural modes dominantly present in the cavity - helium - vessel assembly. Fourier series of the periodic Lorentz pressure pulse was calculated, and we have explained the mechanism of structural resonance with the frequency components available in the pressure pulse. Based on a theoretical analysis and simulation, we have concluded that for the multicell elliptic SRF cavities helium vessel assembly, the dynamic LFD will reduce to a level, which is well within the compensatory range of piezo tuner, if we can ensure that all the structural modes are vibrating with a frequency more than 250 Hz. We have also

explained with a few examples, that the dangerous resonances in the case of dynamic LFD can be evaded by avoiding those structural mode frequencies which are the multiple of the repetition rate (PRR) of the input RF power pulse. We have calculated the radius of the stiffener rings and the required compensation range of the cavity tuning mechanism based on the study. Our procedure is applicable for the LFD analysis of any RF cavity. It will be interesting to extent the Lorentz force detuning analysis work to low β cavities.

So far, we have presented the optimization of the cavity geometry to push the achievable acceleration gradient. Interestingly, the achievable acceleration gradient can also be pushed by proper choice of material parameter that decide the maximum permissible value of peak magnetic field for the material. Particularly, considering the purity of the material as a parameter, we have performed a rigorous magnetothermal analysis, where the threshold value of the magnetic field (beyond which the superconducting breakdown of niobium will occur) was calculated for range of niobium purity values.

In order to perform the magneto-thermal analysis, we have incorporated an elaborate discussion on the dependence of superconducting surface resistance R_s and thermal conductivity κ of the material on the purity level of the material, temperature and the applied magnetic field. To make it more realistic, in the calculation, we have included the nonlinear behavior of R_s in presence of the applied magnetic field. A subroutine was also developed, considering nonlocal response of the superconductor to the RF electromagnetic field. We have discussed the Kapitza resistance, which is an important part of our analysis. Also, based on a thorough literature review, realistic contributions from the phonon peak was incorporated in the calculation of the thermal conductivity. Our calculations have been benchmarked with the results reported for the 1.3 GHz TESLA cavity. This analysis shows that in the place of a highly pure, RRR 300 grade niobium material, one can devise SRF cavities with relatively less pure RRR 100 grade

niobium. Particularly, for the cavities used in the SNS or ADSS accelerator, RRR 100 graded niobium will not only provide the required gradient of 20 MV m^{-1} , but also offer around 10 % higher value of the cavity quality factor. Other advantage of using RRR 100 graded niobium material is that it gives rise to considerable reduction in the cost, and also it leads to improvement in the mechanical properties of the material in the low temperature realm. Based on ASTM B393 standard, RRR 100 graded niobium will offer 30 % higher mechanical strength. Therefore, we can think of the reduction in the cavity wall thickness, which will improve the design in two ways: (i) reduced material requirement will reduce the cost further, as well as (ii) reduced wall thickness will reduce the thermal resistance and this will further improve the scope for high gradient operation. Therefore, in future we will thoroughly analyze the mechanical aspects like buckling, considering this thickness reduction. As another extension of this magnetothermal analysis, one can study the effect of nitrogen or titanium doping in SRF cavity material niobium. Further, for relatively moderate gradient ($\sim 20 \text{ MV m}^{-1}$) application, one can think of a feasibility analysis on the alternative material like niobium titanium alloy as an SRF cavity material.

It is challenging to design the beam optics of a megawatt class H^- linac, because of the stringent beam dynamics criteria that need to be fulfilled. A procedure was developed, based on which we have designed an optimized lattice for the 1 GeV 1 MW H^- injector linac for ISNS. In this H^- linac, beam loss above a stringent limit of 1 W/m is detrimental, as because it can produce the hazard of long-lived radioactivity in the accelerator. Hence, different loss mechanisms were reviewed in detail. Also, an elaborate derivation and discussion was described for the Intra Beam Stripping (IBS). We have evolved the dynamics of a single particle as well as beam bunch, and finally the mismatched beam envelope. After reviewing conventional beam dynamics recipes, a procedure was established for the selection of an optimum lattice for the medium and high energy section, aiming at the minimization of the total number of elliptical cavities. Most of the RF cavities will be operated at their designed accelerating gradient in this

compact design. Therefore, we have developed the philosophy of dedicated matching sections in respective lattice transitions, for a better beam matching. We have followed the non-equipartitioned design approach to make the design compact based on the techniques conceptualized by Hofmann. We have qualified our procedure for the design of a MW class hadron linac on the basis of analytic and simulated results obtained by performing beam dynamics with the optimized linac lattice. Along with insignificant growth in emittance and beam size, we have also reported the stability of the beam, showing that the lattice footprints are in the resonance free zone of the Hofmann diagram. To the best of our knowledge, our analysis on the instabilities of a three-dimensional beam bunch is reported for the first time. We have extended the stability analysis of the beam envelope, including the influence of RF field of the cavity. In this analysis, new set of resonances were found, especially, we have observed confluence resonance in the lattices, where solenoids are used as focusing elements. We have observed a maximum of around six times extent of the halo particle in the radial direction through an extended calculation of the beam halo on the periodic lattices. Also, for the optimized lattice, we have reported the results and the calculation procedure of the beam loss due to IBS. We have developed a general recipe for the design of a megawatt class hadron linac, satisfying all the essential beam dynamics criteria. However, in this analysis, beam halo was studied for a two-dimensional coasting beam, which can be extended in future for a three dimensional beam bunch.

To conclude, the work reported in this thesis includes a general methodology describing the electromagnetic design optimization of a multicell elliptic SRF cavity, aiming at the maximization of the achievable accelerating gradient; and also a generalized methodology for design of low loss, high power, compact linac using these cavities. On the optimized cavity geometry, an in-depth analysis of HOM and wakefield analysis is also presented, and further optimization is done to ensure that the cavity performance is not limited by unwanted effects of HOMs. A methodology was discussed for performing LFD analysis for the elliptic SRF cavity, based on which, the

cavity-helium vessel design can be optimized. In order to optimize the cavity performance with respect to the material purity, we have reviewed the correlation between the threshold magnetic field and purity level of the SRF cavity material, i.e., niobium, and this analysis suggests that the moderately pure RRR 100 graded niobium may be a suitable alternative of the conventional RRR 300 graded niobium as an SRF cavity material. Also, we have reported the generalized beam optics studies and lattice design studies, paying special attention to issue, like beam instability in case of beam mismatch for a three-dimensional beam bunch, formation of beam halo and beam loss due to intra-beam stripping, considering the realistic scenario. The procedure discussed in the thesis may be useful for the design of a MW class hadron linac satisfying all the stringent beam dynamics requirements.

Finally, we present some of the possible extension of our present work, described in the thesis, as well as some new studies that can be carried out in future.

1. In the geometry optimization of the elliptical cavities, our research was confined mainly to maximize the achievable acceleration gradient by varying the geometrical parameters of the cavity. Although, there we found that the final optimized geometry shows a reasonable high value of the shunt impedance, yet, one can extend this optimization work including the shunt impedance or the parameter $G(R/Q_0)$ also as another parameter to maximize. Such a multi-objective optimization of cavity geometry, using modern techniques will ensure an optimized cavity design, where maximization of the acceleration gradient will be ensured, and simultaneously the Ohmic loss will be minimized.
2. Detailed estimation of heat load due to HOMs, in case of geometrical errors in cavity, will be an interesting future work, and will be useful to decide the capacity of the cryomodule.
3. One can think of an interesting future work in the form of a study on the feed forward correction required for the compensation of dynamic LFD. Also, a feasibility

study of the suitability of double stiffener rings in the cavity assembly can be performed to analyze the reduction LFD. Such an analysis will be useful to decide the requirement of the cavity tuning armament in the linac.

4. One natural extension of our beam dynamics work will be to study the effect of RF cavities and focusing magnets failure on the beam dynamics of the ISNS linac, as well as to chalk out schemes for their mitigation / compensation through tuning the strength and phase of neighboring lattice elements, *i.e.*, cavities and magnets.
5. In this analysis, we have considered fixed values of the parameter R_{res} in the calculation of the superconducting surface resistance. However, advance analysis can be performed exploring the dependence of R_{res} on material parameters.
6. Similarly, a thorough study of the effect of misalignment or tilting errors of the lattice elements like RF cavities, magnets and beam position monitors on the beam dynamics of the optimized lattice may be another extension of our present research to fulfil the demand of a complete physics design of ISNS linac.
7. Another interesting future work may be to explore new resonances that we have discovered and described in here, in multi-particle simulations, by setting suitable initial conditions for the onset of this resonance. A thorough study on this will help us to decide proper phase advance values in the case of a particular beam current in a more accurate manner.

Summary

There is a proposal to build an Indian Spallation Neutron Source (ISNS), which will be a linear accelerator based high flux pulsed neutron source for experimental studies of condensed matter physics and various engineering applications. In the medium and high energy section of the superconducting injector linac of a typical spallation neutron source, multicell elliptic superconducting radio-frequency (SRF) cavities have become an indispensable choice for efficient acceleration of a high power beam. For such a hadron linac, lattice design is challenging because of the stringent requirement of low beam loss limit. The physics design of the injector linac for the proposed ISNS will be discussed in this dissertation, where we present a study of the electromagnetic design optimization of the 650 MHz elliptic SRF cavities, as well as the lattice design and beam dynamics studies for the 1 GeV injector linac, satisfying all the stringent beam dynamics requirements.

In Chapter 1, we will start our discussion, describing the spallation process and the other proven methods of neutron generation, followed by a brief review of the worldwide activities on the linac based spallation neutron sources and their applications. In this introductory chapter, we will also discuss the advantages of the use of SRF technology, and then about the loss mechanisms, along with the allowable loss limits followed worldwide for such a high power machine. When we began our optimization work on the two sets of elliptic SRF cavities for the ISNS linac, to the best of our knowledge, we did not find a complete optimization procedure reported anywhere in literature. This was the motivation behind the development of a step by step one-dimensional optimization methodology described in Chapter 2. Following our procedure, one can perform the design optimization of an elliptic SRF cavity for the maximum achievable acceleration gradient (E_{acc}) by varying the geometrical parameters of the cavity. Besides, the final optimized geometry also shows a reasonable high value of the shunt

impedance. An RF cavity can support higher order modes (HOMs) having frequency higher than the fundamental mode. Those can affect the beam and produce instabilities. An analysis on HOM and wakefield generated in the optimized elliptic cavities will be described in Chapter 3. There, we will emphasize the procedure for the calculation of the threshold value of the beam current for the excitation of beam break-up (BBU) instability. In addition, we will also present a methodology for the calculation of heat load due to resonantly excited HOM. In Chapter 4, we will describe how the Lorentz pressure of an electromagnetic mode deforms the cavity geometry, resulting in a detuning of the resonant frequency from the designed value. Such a detuning is called the Lorentz Force Detuning (LFD), which may cause significant reflection of the input RF power. In this chapter, we will discuss how the unwanted coupling, possible between structural frequencies of cavity assembly and pulse repetition rate (PRR) of input RF power in the pulsed mode of operation, may result in resonant amplification of the detuning in the cavity resonant frequency, which is known as dynamic LFD. To attain an optimum desired performance from an SRF cavity, the choice of material parameters also plays an important role. In Chapter 5, we will present a rigorous magnetothermal analysis, describing the influence of material parameters on the electromagnetic performance of niobium based SRF cavities. There, we will show that for the ISNS cavities, relatively low purity, and therefore low cost niobium can ensure an $E_{acc} = 20$ MV/m. In the sixth chapter, we will elaborate a procedure to choose the field strength of the focusing magnets, and accelerating gradient of the cavities in a compact linac, restricting the beam loss below the allowable limit of 1 W/m. This will be followed by an analysis on the intra beam stripping (IBS) and beam halo performed on our designed lattices in case of a mismatch in input beam parameters, for a three dimensional beam bunch. In this chapter, we will also discuss our study on the envelope instability with a three-dimensional beam bunch, which is reported for the first time for a linac lattice. In Chapter 7, we will conclude by describing the interesting findings of our research, along with a discussion on the possible future work.

References

- [1] A. Brown, *The neutron and the bomb: a biography of Sir James Chadwick*. Plunkett Lake Press, 2019.
- [2] J. Chadwick, “The existence of a neutron,” *Proceedings of the Royal Society of London. Series A, Containing Papers of a Mathematical and Physical Character*, vol. 136, no. 830, pp. 692–708, 1932.
- [3] R. Rhodes, *The making of the atomic bomb*. Simon and Schuster, 2012.
- [4] H. L. Stimson and H. S. Truman, “The decision to use the atomic bomb,” *Bulletin of the Atomic Scientists*, vol. 3, no. 2, pp. 37–67, 1947.
- [5] N. Morishima and D. Mizobuchi, “Cross section models for cold neutron scattering from liquid hydrogen and liquid deuterium,” *Nuclear Instruments and Methods in Physics Research Section A: Accelerators, Spectrometers, Detectors and Associated Equipment*, vol. 350, no. 1-2, pp. 275–285, 1994.
- [6] J. C. Chen, B. L. Hanson, S. Z. Fisher, P. Langan, and A. Y. Kovalevsky, “Direct observation of hydrogen atom dynamics and interactions by ultrahigh resolution neutron protein crystallography,” *Proceedings of the National Academy of Sciences*, vol. 109, no. 38, pp. 15301–15306, 2012.
- [7] W. S. Churchill, *The Gathering Storm: The Second World War*, vol. 1. Rosetta-Books, 2010.

- [8] B. L. Hart, *A history of the Second World War*. Pan Macmillan, 2015.
- [9] B. C. Shull and B. Brockhouse, “Nobel prize lecture,” *Nobel Prize Lecture*, 1994.
- [10] C. G. Shull, “Early development of neutron scattering,” *Reviews of Modern Physics*, vol. 67, no. 4, p. 753, 1995.
- [11] B. N. Brockhouse, “Slow neutron spectroscopy and the grand atlas of the physical world,” *Reviews of modern Physics*, vol. 67, no. 4, p. 735, 1995.
- [12] J. A. Hughes, *The Manhattan project: big science and the atom bomb*. Columbia University Press, 2003.
- [13] L. Liang, R. Rinaldi, and H. Schober, *Neutron applications in earth, energy and environmental sciences*. Springer Science & Business Media, 2008.
- [14] G. I. Bell and S. Glasstone, “Nuclear reactor theory,” tech. rep., US Atomic Energy Commission, Washington, DC (United States), 1970.
- [15] W. M. Stacey, *Nuclear reactor physics*. John Wiley & Sons, 2018.
- [16] R. L. Kustom, “An overview of the spallation neutron source project,” *arXiv preprint physics/0008212*, 2000.
- [17] W. Chou, “Spallation neutron source and other high intensity proton sources,” in *Accelerator Physics, Technology And Applications: Selected Lectures of OCPA International Accelerator School 2002*, pp. 231–255, World Scientific, 2004.
- [18] P. Strugar, “Maximum neutron flux in thermal research reactors,” *Journal of Optimization Theory and Applications*, vol. 5, no. 4, pp. 301–312, 1970.
- [19] A. V. Belushkin, “Ibr-2—the fast pulsed reactor at dubna,” *Neutron News*, vol. 2, no. 2, pp. 14–18, 1991.

- [20] A. Taylor, M. Dunne, S. Bennington, S. Ansell, I. Gardner, P. Norreys, T. Broome, D. Findlay, and R. Nelves, “A route to the brightest possible neutron source?,” *Science*, vol. 315, no. 5815, pp. 1092–1095, 2007.
- [21] N. Bohr and J. A. Wheeler, “The mechanism of nuclear fission,” *Physical Review*, vol. 56, no. 5, p. 426, 1939.
- [22] W. R. Shea, *Otto Hahn and the rise of nuclear physics*, vol. 22. Springer Science & Business Media, 2012.
- [23] J. B. Gough, “Glenn t. seaborg. with, eric seaborg. adventures in the atomic age: From watts to washington. 312 pp., illus., index. new york: Farrar, straus & giroux, 2001. \$25 (cloth),” *Isis*, vol. 94, no. 3, pp. 554–555, 2003.
- [24] J. M. Carpenter, R. K. Crawford, S. W. Peterson, M. H. Mueller, J. D. Jorgensen, and A. H. Reis, Jr, “Argonne pulsed neutron source program,” 1 1978.
- [25] R. L. Kustom, “Intense pulsed neutron sources,” *IEEE Transactions on Nuclear Science*, vol. 28, pp. 3115–3119, June 1981.
- [26] J. M. Carpenter, “Pulsed spallation neutron sources,” *ANL/IPNS/CP-89589, APR 17*, vol. 1, 1996.
- [27] J. M. Carpenter, “Pulsed spallation neutron sources for slow neutron scattering,” *Nuclear Instruments and Methods*, vol. 145, no. 1, pp. 91 – 113, 1977.
- [28] B. Schwarzschild, “Storage ring intensifies los alamos neutron source,” *Physics Today*, vol. 38, no. 6, p. 21, 1985.
- [29] R. McGreevy, “Isis neutron and muon source: Annual review 2016,” *RAL-TR-2016-008, RAL Library, STFC Rutherford Appleton Laboratory*, 2016.
- [30] W. E. Fischer, “Dynamics of structures, (revised),” *Physica B* 234-236 (1997) 1202-1208, 1997.

- [31] T. Mason, D. Abernathy, I. Anderson, J. Ankner, T. Egami, G. Ehlers, A. Ekkebus, G. Granroth, M. Hagen, K. Herwig, J. Hodges, C. Hoffmann, C. Horak, L. Horton, F. Klose, J. Larese, A. Mesecar, D. Myles, J. Neuefeind, M. Ohl, C. Tulk, X.-L. Wang, and J. Zhao, “The spallation neutron source in oak ridge: A powerful tool for materials research,” *Physica B: Condensed Matter*, vol. 385-386, pp. 955 – 960, 2006.
- [32] Y. Ikeda, “J-parc status update,” *Nuclear Instruments and Methods in Physics Research Section A: Accelerators, Spectrometers, Detectors and Associated Equipment*, vol. 600, no. 1, pp. 1–4, 2009.
- [33] J. Wei, H. Chen, Y. Chen, Y. Chen, Y. Chi, C. Deng, H. Dong, L. Dong, S. Fang, J. Feng, S. Fu, L. He, W. He, Y. Heng, K. Huang, X. Jia, W. Kang, X. Kong, J. Li, T. Liang, G. Lin, Z. Liu, H. Ouyang, Q. Qin, H. Qu, C. Shi, H. Sun, J. Tang, J. Tao, C. Wang, F. Wang, D. Wang, Q. Wang, S. Wang, T. Wei, J. Xi, T. Xu, Z. Xu, W. Yin, X. Yin, J. Zhang, Z. Zhang, Z. Zhang, M. Zhou, and T. Zhu, “China Spallation Neutron Source: Design, R&D, and outlook,” *Nuclear Instruments and Methods in Physics Research Section A: Accelerators, Spectrometers, Detectors and Associated Equipment*, vol. 600, no. 1, pp. 10 – 13, 2009.
- [34] M. Lindroos, S. Bousson, R. Calaga, H. Danared, G. Devanz, R. Duperrier, J. Eguia, M. Eshraqi, S. Gammino, H. Hahn, A. Jansson, C. Oyon, S. Pape-Møller, S. Peggs, A. Ponton, K. Rathsman, R. Ruber, T. Satogata, and G. Trahern, “The european spallation source,” *Nuclear Instruments and Methods in Physics Research Section B: Beam Interactions with Materials and Atoms*, vol. 269, no. 24, pp. 3258 – 3260, 2011. Proceedings of the 10th European Conference on Accelerators in Applied Research and Technology (ECAART10).
- [35] P. Jung, “Radiation effects in structural materials of spallation targets,” *Journal of nuclear materials*, vol. 301, no. 1, pp. 15–22, 2002.

- [36] A. R. Jana, V. Kumar, A. Kumar, and R. Gaur, “Electromagnetic design of a $\beta_g = 0.9$ 650-mhz superconducting-radio-frequency cavity,” *IEEE Transactions on Applied Superconductivity*, vol. 23, no. 4, pp. 3500816–3500816, 2013.
- [37] A. R. Jana and V. Kumar, “On the electromagnetic design of a $\beta_g = 0.61$ 650-mhz superconducting radio frequency cavity,” *IEEE Transactions on Applied Superconductivity*, vol. 24, no. 6, pp. 1–16, 2014.
- [38] C. Rubbia, “Energy amplifier for nuclear energy production driven by a particle beam accelerator,” jun 1998. US Patent 5,774,514.
- [39] S. Kapoor, “Accelerator-driven sub-critical reactor system (ads) for nuclear energy generation,” *Pramana*, vol. 59, no. 6, pp. 941–950, 2002.
- [40] S. Degweker, S. Lawande, and S. Kapoor, “Accelerator driven sub-critical systems with enhanced neutron multiplication,” *Annals of nuclear energy*, vol. 26, no. 2, pp. 123–140, 1999.
- [41] A. R. Jana and V. Kumar, “Beam optics studies and lattice design of the 1 GeV H^- injector linac for isns,” *Nuclear Instruments and Methods in Physics Research Section A: Accelerators, Spectrometers, Detectors and Associated Equipment*, vol. 942, p. 162299, 2019.
- [42] A. Sharma, A. Jana, C. B. Patidar, M. K. Pal, N. Kulkarni, P. K. Goyal, P. K. Jana, R. Gaur, R. Prakash, and R. Dhingra, “Reference physics design for 1 gev injector linac and accumulator ring for indian spallation neutron source,” *arXiv preprint arXiv:1609.04518*, 2016.
- [43] R. Gaur and V. Kumar, “Beam dynamics and electromagnetic studies of a 3 MeV, 325 MHz radio frequency quadrupole accelerator,” *EPJ Nuclear Sciences & Technologies*, vol. 4, p. 9, 2018.

- [44] R. Dhingra, N. S. Kulkarni, and V. Kumar, “Lattice design of medium energy beam transport line for a spallation neutron source,” in *Proceedings of the seventh DAE-BRNS Indian particle accelerator conference: book of abstracts*, 2015.
- [45] H. A. Bethe and E. E. Salpeter, *Quantum mechanics of one-and two-electron atoms*. Springer Science & Business Media, 2012.
- [46] V. Senecha, R. Kumar, R. Khare, R. Vadjekar, D. Ghodke, S. Jain, A. Kasliwal, V. Gauttam, and S. Joshi, “Extraction of H^- ion beam from filament based multicusp H^- ion source,” in *Indian Particle Accelerator Conference (InPAC-2013)*, VECC, Kolkata, 2013.
- [47] C. B. Patidar and A. Sharma, “Beam optics design studies of the isns high energy beam transport line,” in *Proceedings of the eighth DAE-BRNS Indian particle accelerator conference*, 2018.
- [48] P. K. Goyal, A. Sharma, A. Ghodke, and V. Kumar, “Studies on linear lattice for a 1 gev proton accumulator ring,” in *Proceedings of the Indian particle accelerator conference*, 2013.
- [49] U. Singh and A. Sharma, “Preliminary optics design of ring to target beam transport line for a 1gev spallation neutron source,” in *Proceedings of the eighth DAE-BRNS Indian particle accelerator conference*, 2018.
- [50] S. Chandrasekhar, “Some remarks on the negative hydrogen ion and its absorption coefficient.,” *The Astrophysical Journal*, vol. 100, p. 176, 1944.
- [51] G. I. Budker and G. I. Dimov, “On The Charge Exchange Injection Of Protons Into Ring Accelerators,” in *Proceedings, 4th International Conference on High-Energy Accelerators, HEACC 1963, v.1-3: Dubna, USSR, August 21 - August 27 1963*, pp. 1372–1377, 1963.

- [52] S. Kapoor, “Accelerator-driven sub-critical reactor system (ads) for nuclear energy generation,” *Pramana*, vol. 59, no. 6, pp. 941–950, 2002.
- [53] A. Krása, “Spallation reaction physics,” *Manuscript for the Lecture “Neutron Sources for ADS” for Students of the Faculty of Nuclear Sciences and Physical Engineering at Czech Technical University, Prague*, pp. 1–61, 2010.
- [54] N. V. Mohkov and W. Chou, eds., *Beam halo and scraping. Proceedings, 7th ICFA Mini-Workshop on High Intensity High Brightness Hadron Beams, Lake Como, Wisconsin, September 13-15, 1999*.
- [55] T. Wangler, K. Crandall, R. Ryne, and T. Wang, “Particle-core model for transverse dynamics of beam halo,” *Physical review special topics-accelerators and beams*, vol. 1, no. 8, p. 084201, 1998.
- [56] J. Carneiro, B. Mustapha, and P. Ostroumov, “Numerical simulations of stripping effects in high-intensity hydrogen ion linacs,” *Physical Review Special Topics-Accelerators and Beams*, vol. 12, no. 4, p. 040102, 2009.
- [57] P. Ostroumov, “Physics design of the 8 GeV H^- minus linac,” *New Journal of Physics*, vol. 8, no. 11, p. 281, 2006.
- [58] A. Shishlo, J. Galambos, A. Aleksandrov, V. Lebedev, and M. Plum, “First observation of intrabeam stripping of negative hydrogen in a superconducting linear accelerator,” *Physical review letters*, vol. 108, no. 11, p. 114801, 2012.
- [59] P. N. Ostroumov, B. Mustapha, and J.-P. Carneiro, “Beam dynamics studies of the 8 GeV linac at fnal,” tech. rep., Fermi National Accelerator Lab.(FNAL), Batavia, IL (United States), 2008.
- [60] M. Reiser and P. O’Shea, *Theory and design of charged particle beams*, vol. 312. Wiley Online Library, 1994.

- [61] B. Aune, R. Bandelmann, D. Bloess, B. Bonin, A. Bosotti, M. Champion, C. Crawford, G. Deppe, B. Dwersteg, D. A. Edwards, H. T. Edwards, M. Ferrario, M. Fouaidy, P.-D. Gall, A. Gamp, A. Gössel, J. Graber, D. Hubert, M. Hüning, M. Juillard, T. Junquera, H. Kaiser, G. Kreps, M. Kuchnir, R. Lange, M. Leenen, M. Liepe, L. Lilje, A. Matheisen, W.-D. Möller, A. Mosnier, H. Padamsee, C. Pagani, M. Pekeler, H.-B. Peters, O. Peters, D. Proch, K. Rehlich, D. Reschke, H. Safa, T. Schilcher, P. Schmüser, J. Sekutowicz, S. Simrock, W. Singer, M. Tigner, D. Trines, K. Twarowski, G. Weichert, J. Weisend, J. Wojtkiewicz, S. Wolff, and K. Zapfe, “Superconducting tesla cavities,” *Phys. Rev. ST Accel. Beams*, vol. 3, p. 092001, Sep 2000.
- [62] D. Proch, “Superconducting cavities for accelerators,” *Reports on Progress in Physics*, vol. 61, no. 5, p. 431, 1998.
- [63] D. Reschke, L. Lilje, and H. Weise, “Analysis of rf results of recent nine-cell cavities at desy,” in *TTC-Report 2009-01, Oct. 2009*, 2009.
- [64] G. Ciovati, “Review of high field q slope, cavity measurements,” tech. rep., Thomas Jefferson National Accelerator Facility, Newport News, VA, 2008.
- [65] T. P. Wangler, *RF Linear accelerators*. John Wiley & Sons, 2008.
- [66] H. Padamsee and J. Knobloch, *RF superconductivity for accelerators*, vol. 2011. Wiley Online Library, 2008.
- [67] A. Saini, K. Ranjan, A. Lunin, S. C. Mishra, N. Perunov, N. Solyak, and V. P. Yakovlev, “Superconducting RF cavity design study for the squeezed ILC section of the high intensity H^- linac for the Project-X facility,” *Superconductor Science and Technology*, vol. 25, p. 025024, jan 2012.
- [68] A. Rowe, S. K. Chandrasekaran, A. Grassellino, O. Melnychuk, M. Merio, T. Reid, and D. Sergatskov, “Cavity Processing and Preparation of 650 MHz Elliptical

- Cell Cavities for PIP-II,” in *28th International Linear Accelerator Conference*, p. MOPLR043, 2017.
- [69] K. McGee, B. Barker, K. Elliott, A. Ganshyn, W. Hartung, S. H. Kim, P. N. Ostroumov, J. T. Popielarski, A. Taylor, C. Zhan, M. P. Kelly, and T. Rei, “First Cold Test Results of a Medium- β 644 MHz Superconducting 5-Cell Elliptical Cavity for the FRIB Energy Upgrade,” in *Proceedings of NAPAC2019, Lansing, MI, USA*.
- [70] V. Shemelin, “Optimal choice of cell geometry for a multicell superconducting cavity,” *Physical Review Special Topics-Accelerators and Beams*, vol. 12, no. 11, p. 114701, 2009.
- [71] K. Halbach, “SUPERFISH: A computer program for evaluation of rf cavities with cylindrical symmetry,” 1976.
- [72] N. Juntong and R. Jones, “High-gradient srf cavity with minimized surface em fields and superior bandwidth for the ilc,” *arXiv preprint arXiv:0910.1305*, 2009.
- [73] S. Belomestnykh and V. Shemelin, “High-beta cavity design-a tutorial,” in *SRF International Workshop, Ithaca, New York*, 2005.
- [74] S. Belomestnykh, M. Liepe, H. Padamsee, V. Shemelin, and V. Veshcherevich, “High average power fundamental input couplers for the cornell university erl requirements, design challenges and first ideas,” *Cornell LEPP Report ERL*, pp. 02–8, 2002.
- [75] G. Ciovati, P. Kneisel, J. Brawley, R. Bundy, I. Campisi, K. Davis, K. Macha, D. Machie, J. Mammoser, S. Morgan, R. Sundelin, L. Turlington, K. Wilson, M. Doleans, S. H. Kim, D. Mangra, D. Barni, C. Pagani, P. Pierini, K. Matsumoto, R. Mitchell, D. Schrage, R. Parodi, J. Sekutowicz, and P. Ylae-Oijala, “Superconducting prototype cavities for the spallation neutron source (sns) project,”

- in *PACS2001. Proceedings of the 2001 Particle Accelerator Conference (Cat. No.01CH37268)*, vol. 1, pp. 484–486 vol.1, 2001.
- [76] D. Nagle, E. Knapp, and B. Knapp, “Coupled resonator model for standing wave accelerator tanks,” *Review of Scientific Instruments*, vol. 38, no. 11, pp. 1583–1587, 1967.
 - [77] M. Dohlus and V. Kaljuzhny, “Relative non uniformity in the amplitude of the accelerating field along the $m \times n$ cell tesla super cavities, tesla collab., tesla 98-26, desy, germany, 1998.”
 - [78] D. Myakishev and V. Yakovlev, “The new possibilities of superlans code for evaluation of axisymmetric cavities,” in *Proceedings Particle Accelerator Conference*, vol. 4, pp. 2348–2350, IEEE, 1995.
 - [79] S. Vaganian and H. Henke, “The panofsky-wenzel theorem and general relations for the wake potential,” *Part. Accel.*, vol. 48, pp. 239–242, 1995.
 - [80] W. K. H. Panofsky and W. Wenzel, “Some considerations concerning the transverse deflection of charged particles in radiofrequency fields,” *Rev. Sci. Instrum.*, vol. 27, p. 967, 1956.
 - [81] P. B. Wilson and J. Griffin., “Physics of high energy particle accelerators,” in *AIP conference proceedings*, 1982.
 - [82] J. J. Bisognano, “Superconducting rf and beam cavity interactions,” in *Proc. 3rd Workshop RF Supercond*, 1987.
 - [83] M. G. Kelliher and R. Beadle, “Pulse-shortening in electron linear accelerators.,” *Nature*, vol. 187, 1960.
 - [84] M. C. Crowley-Milling and T. R. Jarvis, “Pulse-shortening in electron linear accelerators.,” *Nature*, vol. 463, 1961.

- [85] P. B. Wilson, “Physics of high energy particle accelerators,” in *Internal Memorandum HEPL-297, High Energy Physics Laboratory, Stanford University*, 1963.
- [86] P. M. Lapostolle and A. L. Septier, *Linear Accelerators*. North-Holland, Amsterdam, 1970.
- [87] R. L. Gluckstern and H. S. Butler, “Pulse-shortening in Electron Linear Accelerators,” *IEEE Trans. Nucl. Sci. NS-12*, vol. 607, 1965.
- [88] V. Kumar, A. R. Jana, N. Kulkarni, and R. Dingra, “Analysis of regenerative beam break up instability in linear accelerators,” in *Indian Particle Accelerator Conference(InPAC)*, 2013.
- [89] D. Jeon, L. Merminga, G. Krafft, B. Yunn, R. Sundelin, J. Delayen, S. Kim, and M. Doleans, “Cumulative beam break-up study of the spallation neutron source superconducting linac,” *Nuclear Instruments and Methods in Physics Research Section A: Accelerators, Spectrometers, Detectors and Associated Equipment*, vol. 495, no. 2, pp. 85 – 94, 2002.
- [90] A. Farricker, R. Jones, and S. Molloy, “Beam dynamics in the ess linac under the influence of monopole and dipole homs,” *Physics Procedia*, vol. 79, pp. 21 – 29, 2015. ICFA mini Workshop on High Order Modes in Superconducting Cavities, HOMSC14.
- [91] R. M. Jones and C. Glasman, “Higher order mode wakefield simulations and beam dynamics simulations in the ilc main linacs,” in *Proc. of the 2006 LINAC*, 2006.
- [92] Y. H. Chin, “ABCI USER’S GUIDE (AZIMUTHAL BEAM CAVITY INTERACTION),” 1988.
- [93] S. S. Kurennoy, “Dependence of bunch energy loss in cavities on beam velocity,” *Phys. Rev. ST Accel. Beams*, vol. 2, p. 032001, Mar 1999.
- [94] CST Team, *Computer Simulation Technology| CST STUDIO SUITE Manual*. 2016.

- [95] S. K. Lunin, A. and V. Yakovlev, “Cavity loss factors of non-relativistic beams for project x,” in *Proceedings of Particle accelerator conference (PAC-2011-TUP075)*, 2011.
- [96] Z. H. O. U. Feng, “Wakefield induced correlated energy spread and emittance growth at ttf fel,” in *TESLA Collab., Hamburg, Germany, DESY-TESLA FEL-Rep* 5, 1999.
- [97] S. ho Kim, M. Doleans, D. o Jeon, and R. Sundelin, “Higher-order-mode (hom) power in elliptical superconducting cavities for intense pulsed proton accelerators,” *Nuclear Instruments and Methods in Physics Research Section A: Accelerators, Spectrometers, Detectors and Associated Equipment*, vol. 492, no. 1, pp. 1 – 10, 2002.
- [98] R. Prakash, A. R. Jana, and V. Kumar, “Analysis of generation and effect of higher order modes (homs) in superconducting cavities,” in *Indian Particle Accelerator Conference(InPAC)*, 2018.
- [99] D. J. Griffiths, *Introduction to Electrodynamics.*, vol. 576. Prentice Hall, Upper Saddle River, NJ, 1999.
- [100] A. Kumar, A. R. Jana, and V. Kumar, “A study of dynamic Lorentz force detuning of 650 MHz $\beta_g = 0.9$ superconducting radiofrequency cavity,” *Nuclear Instruments and Methods in Physics Research Section A: Accelerators, Spectrometers, Detectors and Associated Equipment*, vol. 750, pp. 69–77, 2014.
- [101] R. R. Mitchell, K. Y. Matsumoto, G. Ciovati, K. Davis, K. Macha, and R. M. Sundelin, “Lorentz force detuning analysis of the Spallation Neutron Source (SNS) accelerating cavities.,” tech. rep., Los Alamos National Laboratory, 2001.
- [102] S. N. Simrock, “Lorentz force compensation of pulsed SRF cavities,” in *Proceedings of LINAC*, pp. 554–558, 2002.

- [103] J. Grimm, T. T. Arkan, M. H. Foley, T. N. Khabiboulline, and D. J. Watkins, “1.3 GHz RF Nb cavity to Ti helium vessel TIG welding process at Fermilab,” 2009.
- [104] R. Losito and S. Marque, “Coupled analysis of electromagnetic, thermo-mechanical effects on RF accelerating structures,” tech. rep., 2002.
- [105] A. Bandyopadhyay, O. Kamigaito, S. K. Nayak, H. K. Pandey, M. Mondal, and A. Chakrabarti, “Design of linac post-accelerator for vecc rib facility using realistic field,” *Nuclear Instruments and Methods in Physics Research Section A: Accelerators, Spectrometers, Detectors and Associated Equipment*, vol. 560, no. 2, pp. 182 – 190, 2006.
- [106] ANSYS Team, *Mechanical applications Theory reference AM APDL, ANSYS Release*. 2016.
- [107] S. Posen and M. Liepe, “Mechanical optimization of superconducting cavities in continuous wave operation,” *Phys. Rev. ST Accel. Beams*, vol. 15, p. 022002, Feb 2012.
- [108] W. Thomson, *Theory of vibration with applications*. CrC Press, 2018.
- [109] K. M. Wilson, G. Ciovati, E. F. Daly, J. Henry, R. Hicks, J. Hogan, D. Machie, P. Kneisel, C. Reece, and J. Sekutowicz, “Mechanical cavity design for 100 mv upgrade cryomodule,” tech. rep., Thomas Jefferson National Accelerator Facility, Newport News, VA (US), 2003.
- [110] I. Gonin, M. Awida, E. Borissov, M. Foley, C. Grimm, T. Khabiboulline, and Y. Pischalnikov, “Update of the mechanical design of the 650 MHz $\beta = 0.9$ cavities for Project-X,” 2013.
- [111] D. Edited by Hitchings, *Introduction to superconductivity*. NAFEMS Ltd., 1992.
- [112] R. W. Clough and J. Penzien, “Dynamics of structures, (revised),” *Computers and Structures, Inc., Berkeley, Calif*, 2003.

- [113] M. Kim, S. H. Doleans and Y. K., “Efficient design scheme of superconducting cavity,” in *Proceedings of 20th International Linac Conference, Monterey, USA*, 2000.
- [114] A. Sun, H. Wang, and G. Wu, “Effect of the tuner on the field flatness of sns superconducting rf cavities,” in *Proceedings of LINAC*, vol. 815, 2004.
- [115] R. Paparella, *Fast Frequency Tuner for High Gradient SC Cavities for ILC and XFEL*. PhD thesis, UNIVERSITA’ DEGLI STUDI DI MILANO, <https://cds.cern.ch/record/1118577/files/care-thesis-08-001.pdf>, 2007.
- [116] Y. Pischalnikov, “Resonance Control of LB 650 MHz and HB 650 MHz SRF Cavities,” tech. rep., Fermi National Accelerator Lab.(FNL), Batavia, IL (United States).
- [117] P. Bosland, S. Chel, G. Devanz, Y. Gasser, P. Hardy, J. Plouin, J. P. Poupeau, D. Roudier, and B. Visentin, “Stiffened Medium β 704 MHz Elliptical Cavity for a Pulsed Proton Linac,” in *Proceedings of SRF 2007, Peking University, Beijing, China*, 2007.
- [118] P. Ostroumov, C. Contreras, A. Plastun, J. Rathke, T. Schultheiss, A. Taylor, J. Wei, M. Xu, T. Xu, Q. Zhao, I. Gonin, T. Khabiboulline, Y. Pischalnikov, and V. Yakovlev, “Elliptical superconducting RF cavities for FRIB energy upgrade,” *Nuclear Instruments and Methods in Physics Research Section A: Accelerators, Spectrometers, Detectors and Associated Equipment*, vol. 888, pp. 53 – 63, 2018.
- [119] C. Pagani, A. Bosotti, P. Michelato, N. Panzeri, R. Paparella, and P. Pierini, “The fast piezo-blade tuner for scrf resonators,” in *Proceedings of the 12th International Workshop on RF Superconductivity, Cornell University, Ithaca, New York, USA (TUP29)*, vol. 1, pp. 303–307, 2005.
- [120] S. Roy and G. Myneni, “Qualification of niobium materials for superconducting

- radio frequency cavity applications: View of a condensed matter physicist,” in *AIP Conference Proceedings*, vol. 1687, p. 020006, AIP Publishing, 2015.
- [121] M. Tinkham, *Introduction to superconductivity*. Courier Corporation, 2004.
- [122] G. Ciovati, “Review of the frontier workshop and Q-slope results,” *Physica C: Superconductivity*, vol. 441, no. 1-2, pp. 44–50, 2006.
- [123] G. Ciovati, G. Myneni, F. Stevie, P. Maheshwari, and D. Griffis, “High field Q slope and the baking effect: Review of recent experimental results and new data on Nb heat treatments,” *Physical Review Special Topics-Accelerators and Beams*, vol. 13, no. 2, p. 022002, 2010.
- [124] B. Seeber, *Handbook of applied superconductivity*, vol. 2. CRC press, 1998.
- [125] B. Goodman and G. Kuhn, “Influence of extended defects on superconducting properties of niobium,” tech. rep., Centre de Recherches sur les Tres Basses Temperatures, Grenoble, France, 1968.
- [126] L. S. Brooks, “Determination of common impurities in niobium metal by the fusion d.c. arc technique,” *Spectrochimica Acta*, vol. 21, no. 5, pp. 1029 – 1031, 1965.
- [127] W. Weingarten, “Field-dependent surface resistance for superconducting niobium accelerating cavities,” *Physical Review Special Topics-Accelerators and Beams*, vol. 14, no. 10, p. 101002, 2011.
- [128] G. Ciovati, P. Dhakal, P. Kneisel, and G. R. Myneni, “Summary of performance of superconducting radio-frequency cavities built from cbmm niobium ingots,” in *AIP Conference Proceedings*, vol. 1687, p. 030001, AIP Publishing, 2015.
- [129] N. W. Ashcroft and N. D. Mermin, “Solid state physics (saunders college, philadelphia, 1976),” *Appendix N*, 2010.

- [130] J. Turneure, J. Halbritter, and H. Schwettman, “The surface impedance of superconductors and normal conductors: The mattis-bardeen theory,” *Journal of Superconductivity*, vol. 4, no. 5, pp. 341–355, 1991.
- [131] J. Halbritter, “Comparison between measured and calculated rf losses in the superconducting state,” *Zeitschrift für Physik*, vol. 238, no. 5, pp. 466–476, 1970.
- [132] D. Mattis and J. Bardeen, “Theory of the anomalous skin effect in normal and superconducting metals,” *Phys. Rev.; (United States)*.
- [133] G. E. Reuter, E. H. Sondheimer, and A. H. Wilson, “The theory of the anomalous skin effect in metals,” in *Proc. R. Soc. Lond. A*, vol. 195, 1948.
- [134] J. R. Hook, “A method for calculating the microwave surface impedance of superconducting films,” *Journal of Low Temperature Physics*, vol. 23, pp. 645–661, Jun 1976.
- [135] C. Underwood, *The MATLAB Handbook*. USA: CreateSpace Independent Publishing Platform, 2016.
- [136] H. Swan, *SRIMP Code an online calculator*.
- [137] A. Gurevich, “Reduction of dissipative nonlinear conductivity of superconductors by static and microwave magnetic fields,” *Physical review letters*, vol. 113, no. 8, p. 087001, 2014.
- [138] A. Gurevich, “Multiscale mechanisms of srf breakdown,” *Physica C: Superconductivity*, vol. 441, no. 1-2, pp. 38–43, 2006.
- [139] L. S. Chandra, M. Chattopadhyay, S. Roy, V. Sahni, and G. Myneni, “Magneto thermal conductivity of superconducting Nb with intermediate level of impurity,” *Superconductor Science and Technology*, vol. 25, no. 3, p. 035010, 2012.

- [140] F. Koechlin and B. Bonin, “Parametrization of the niobium thermal conductivity in the superconducting state,” *Superconductor Science and Technology*, vol. 9, no. 6, p. 453, 1996.
- [141] J. Bardeen, G. Rickayzen, and L. Tewordt, “Theory of the thermal conductivity of superconductors,” *Physical Review*, vol. 113, no. 4, p. 982, 1959.
- [142] H. Padamsee, *RF Superconductivity: Science, Technology and Applications*. New York: Wiley-VCH, 2009.
- [143] P. Bauer, N. Solyak, G. Ciovati, G. Eremeev, A. Gurevich, L. Lilje, and B. Visentin, “Evidence for non-linear bcs resistance in srf cavities,” *Physica C: Superconductivity*, vol. 441, no. 1-2, pp. 51–56, 2006.
- [144] K. Mittag, “Kapitza conductance and thermal conductivity of copper niobium and aluminium in the range from 1.3 to 2.1 k,” *Cryogenics*, vol. 13, no. 2, pp. 94–99, 1973.
- [145] H. Safa, “An analytical approach for calculating the quench field in superconducting cavities,” tech. rep., 1996.
- [146] S.-h. Kim and I. E. Campisi, “Thermal stabilities and optimal operating parameters for the oak ridge spallation neutron source superconducting linear accelerator,” *Physical Review Special Topics-Accelerators and Beams*, vol. 10, no. 3, p. 032001, 2007.
- [147] J. Vines, Y. Xie, and H. Padamsee, “Systematic trends for the medium field Q-slope,” in *Proceedings of the 13th International Workshop on RF Superconductivity, TuP27*, 2007.
- [148] D. Reschke, “Thermal model calculations for 1.3 GHz TTF accelerator cavities,” *Palmieri [37]*, p. 385, 1997.

- [149] H. Leupold and H. Boorse, “Superconducting and normal specific heats of a single crystal of niobium,” *Physical Review*, vol. 134, no. 5A, p. A1322, 1964.
- [150] F. Gerigk, “Beam halo in high-intensity hadron linacs,” 2006.
- [151] I. Hofmann, “Stability of anisotropic beams with space charge,” *Physical Review E*, vol. 57, no. 4, p. 4713, 1998.
- [152] C. K. Allen and N. Pattengale, “Theory and technique of beam envelope simulation,” *Los Alamos National Laboratory Internal Report LA-UR-02-4979*, 2002.
- [153] S. M. Lund and B. Bukh, “Stability properties of the transverse envelope equations describing intense ion beam transport,” *Physical Review Special Topics-Accelerators and Beams*, vol. 7, no. 2, p. 024801, 2004.
- [154] P. M. Lapostolle and M. Weiss, “Formulae and procedures useful for the design of linear accelerators,” tech. rep., 2000.
- [155] M. Ball, A. Burov, B. Chase, A. Chakravarty, A. Chen, S. Dixon, J. Edelen, A. Grassellino, D. Johnson, and S. Holmes, “The PIP-II conceptual design report,” tech. rep., Argonne National Lab.(ANL), Argonne, IL (United States); Fermi National Accelerator Laboratory, 2017.
- [156] Z. Li, P. Cheng, H. Geng, Z. Guo, and Y. He, “Physics design of an accelerator for an accelerator-driven subcritical system,” *Phys. Rev. ST Accel. Beams*, vol. 16, p. 080101, Aug 2013.
- [157] H. Klein, “Spallation neutron sources,” in *Proc. 1994 Linac Conf., Tsukuba*, p322, 1994.
- [158] M. Eshraqi, “Design and Optimization of the ESS LINAC,” *proceedings of IPAC11, San Sebastian*, 2011.
- [159] R. Duperrier, N. Pichoff, and D. Uriot, “CEA Saclay codes review,” in *ICCS conference, Amsterdam*, 2002.

- [160] R. Duperrier, N. Pichoff, and D. Uriot, “Frequency jump in an ion linac,” *Phys. Rev. ST Accel. Beams*, vol. 10, p. 084201, Aug 2007.
- [161] D. Uriot and N. Pichoff, “Tracewin documentation,” *CEA internap report CEA/DSM/DAPNIA/SEA/2000/45*, 2011.
- [162] G. Parzen, “Electric fields of a uniformly charged elliptical beam,” *arXiv preprint physics/0108040*, 2001.
- [163] V. Lebedev, N. Solyak, J.-F. Ostigy, A. Alexandrov, and A. Shishlo, “Intrabeam stripping in H^- linacs,” *arXiv preprint arXiv:1207.5492*, 2012.
- [164] I. Hofmann and O. Boine-Frankenheim, “Revisiting the longitudinal 90^0 limit in high intensity linear accelerators,” *Physical review letters*, vol. 118, no. 11, p. 114803, 2017.
- [165] M. Chanel, R. Giannini, P. Lefevre, R. Ley, D. Manglunki, and D. Möhl, “Measurements of H^- intra-beam stripping cross section by observing a stored beam in lear,” *Physics Letters B*, vol. 192, no. 3-4, pp. 475–477, 1987.

Appendix A. Intrabeam stripping (IBS) - a brief review

Intrabeam stripping (IBS) was observed for the first time only in the previous decade during the commissioning of LEAR [58] [165]. Most of the multiparticle tracking codes presently used in the accelerator community do not include the calculation of beam loss due to IBS [163]. We have evolved a semi-numerical treatment in order to calculate the fractional beam loss due to IBS. A brief review of the procedure for this calculation will be done in this appendix. Within the beam bunch, all the particles (ions) mostly performs continuous oscillations around the synchronous one, which develops the chances of binary collisions between those particles. Such inelastic impacts between negative hydrogen ions in an H^- accelerator may result in separation of the loosely bound electrons from the ions, which is known as intra-beam stripping. Among various possibilities of binary collisions, $H^- + H^- = H^0 + H^- + e$ is the dominant one in this stripping process. Along with H^- and electron, the third outcome is a neutral hydrogen atom produced in this process, which finally gets lost from the beam bunch.

Intrabeam stripping is a probabilistic process, where the stripping probability of an H^- ions per collision can be estimated from the stripping cross section σ_H and we can calculate the likelihood of stripping from the following empirical equation [163]:

$$\sigma_H(\beta_r) = 240 \frac{\alpha_F^2 r_0^2}{(\beta_r + \alpha_F)^2} \frac{(\beta_r - \beta_c)^6}{(\beta_r - \beta_c)^6 + \beta_c^6} \ln \left(1.79 \frac{\beta_r + \alpha_F}{\alpha_F} \right), \quad (1)$$

where, \vec{v}_r ($|\vec{v}_r| = \beta_r c$) is the relative velocity between the colliding ions, $\alpha_F \simeq 1/137$ is the fine structure constant and $r_0 \simeq 5.29177 \times 10^{-13}$ m is the Bohr radius. This cross-section approaches zero once $\beta_r \rightarrow \beta_c \approx 7.5 \times 10^{-5}$ [163]. The typical variation of σ_H with the relative velocity is shown in Fig. (A1).

Let us calculate the number of binary collisions taking place within an H^- beam bunch. We will assume N is the number of ions within the bunch following Gaussian distributions in position (η) and in velocity (v_η) space, where η is the generalized

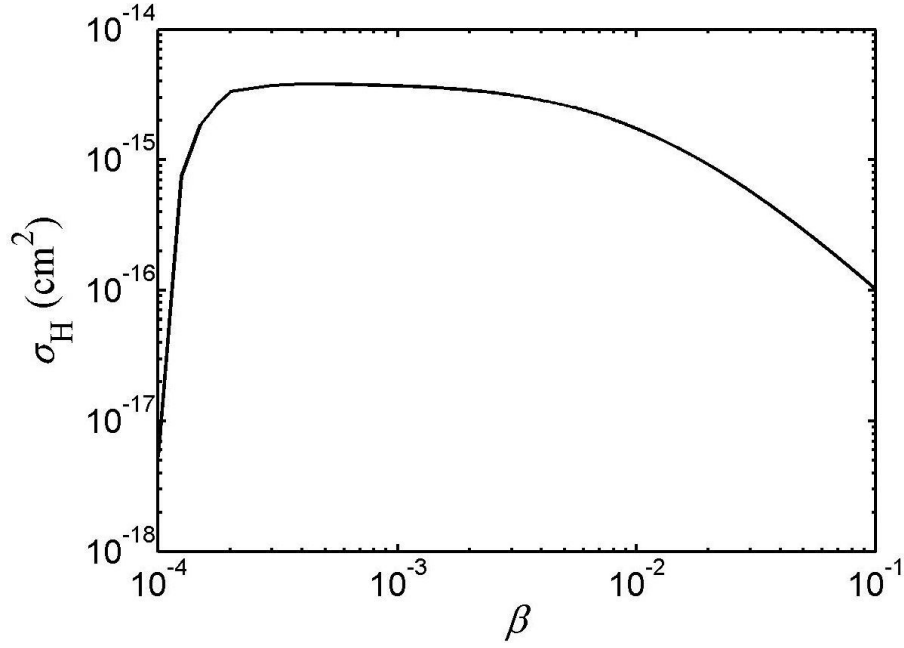


Figure 1: Variation of σ_{H^-} is plotted as a function of the relative velocity β_r .

representation of the three cartesian coordinates x , y and z of the particle in the beam frame w.r.t. the synchronous particle propagating along s . Hence, following standard representation, normalized distribution of a beam bunch in the 6D hyperspace of space and velocity coordinates can be written as

$$\begin{aligned}
 f(x, y, z, v_x, v_y, v_z) &= f_p(x, y, z) \times f_v(v_x, v_y, v_z) = \prod_{\eta}^{x,y,z} f_{\eta}(\eta) \times f_{v_{\eta}}(v_{\eta}) \\
 &= \prod_{\eta}^{x,y,z} \left[\frac{1}{\sqrt{2\pi}\sigma_{\eta}} e^{-(\eta^2/2\sigma_{\eta}^2)} \right] \times \left[\frac{1}{\sqrt{2\pi}\sigma_{v_{\eta}}} e^{-(v_{\eta}^2/2\sigma_{v_{\eta}}^2)} \right].
 \end{aligned} \tag{2}$$

In this distribution function σ_{η} is the rms bunch size and $\sigma_{v_{\eta}}$ represents the rms velocity spread. For the 6D hyperspace, we define an explicit normalization criteria for the beam bunch as $\int_{-\infty}^{\infty} f_{\varrho}(\varrho) d\varrho = 1$, where, ϱ represents any coordinate of the distribution.

Let us assume a particle at the position $\vec{r}_1(x_1, y_1, z_1)$ and velocity $\vec{v}_1(v_{x1}, v_{y1}, v_{z1})$ within beam bunch in this 6D hyperspace. We calculate the stripping probability for this particle because of the likelihood of binary collisions with other particles in the beam

bunch having velocities between $\vec{v}_2(v_{x2}, v_{y2}, v_{z2})$ and $\vec{v}_2 + d\vec{v}_2$ as $Nf_p(x_1, y_1, z_1)\{\sigma_H(|\vec{v}_r|)\}\{|\vec{v}_r|\Delta t\}f_v(v_{x2}, v_{y2}, v_{z2})$ in a time interval of Δt . Hence, we need to perform the following integration to evaluate the total stripping probability P_1 because of the other of H^- ions in the beam bunch:

$$P_1 = Nf_p(x_1, y_1, z_1) \int_{\vartheta_2} \{\sigma_H(|\vec{v}_r|)\}\{|\vec{v}_r|\Delta t\}f_v(v_{x2}, v_{y2}, v_{z2})d\vartheta_2. \quad (3)$$

In the above equation, $\vec{v}_r = \vec{v}_2 - \vec{v}_1$ represents the relative velocity between two colliding particles and $d\vartheta_2$ represents an elementary volume $dv_{x2}dv_{y2}dv_{z2}$ in the velocity space.

Extending the above calculation for all particles in the entire bunch, finally we can calculate the total number of stripped particles in the time interval Δt as

$$\Delta N_{all} = \frac{N}{2} \int_{\Gamma_1} \int_{\vartheta_1} f(x_1, y_1, z_1, v_{x1}, v_{y1}, v_{z1})(P_1)d\vartheta_1 d\Gamma_1, \quad (4)$$

where, $d\vartheta_1 = dv_{x1}dv_{y1}dv_{z1}$ and $d\Gamma_1 = dx_1dy_1dz_1$. Two particles will participate in a binary collision. Therefore the term $1/2$ is included in the above equation to avoid the double counting of the stripped particles.

In the next, let us calculate the number of particles stripped per unit time from the following explicit equation

$$\begin{aligned} \frac{\Delta N_{all}}{\Delta t} &= \frac{N^2}{2} \int_{\Gamma_1} [f_p(x_1, y_1, z_1)]^2 d\Gamma_1 \times \\ &..... \int_{\vartheta_1} \int_{\vartheta_2} |\vec{v}_r|\{\sigma_H(|\vec{v}_r|)\}f_v(v_{x1}, v_{y1}, v_{z1})f_v(v_{x2}, v_{y2}, v_{z2})d\vartheta_2 d\vartheta_1. \end{aligned} \quad (5)$$

Inserting the distribution functions explicitly within the above equation (Eq. 5), we

obtain the following equation, which requires integration over the entire hyperspace:

$$\frac{\Delta N_{all}}{\Delta t} = \frac{N^2}{2} \frac{\int_{-\infty}^{\infty} \int_{-\infty}^{\infty} \int_{-\infty}^{\infty} \int_{-\infty}^{\infty} \int_{-\infty}^{\infty} \int_{-\infty}^{\infty} \prod_{v_\eta}^{x,y,z} |\vec{v}_r| \{\sigma_H(|\vec{v}_r|)\} e^{-\frac{(v_{\eta 1}^2 + v_{\eta 2}^2)}{2\sigma_{v_\eta}^2}} dv_{\eta 1} dv_{\eta 2}}{8\pi^3 \sigma_x \sigma_y \sigma_z (\sigma_{vx} \sigma_{vy} \sigma_{vz})^2}. \quad (6)$$

The above equation can be simplified further by introducing the variable $v_{s\eta} = (v_{\eta 1} + v_{\eta 2})$ and $v_{r\eta} = (v_{\eta 2} - v_{\eta 1})$, where, $v_{\eta 1} = \frac{1}{2}(v_{s\eta} + v_{r\eta})$ and $v_{\eta 2} = \frac{1}{2}(v_{s\eta} - v_{r\eta})$. For this transformation, we obtain the Jacobian $dv_{\eta 1} dv_{\eta 2} = \left| \frac{\delta(v_{\eta 1}, v_{\eta 2})}{\delta(v_{s\eta}, v_{r\eta})} \right| dv_{s\eta} dv_{r\eta} = \frac{1}{2} dv_{s\eta} dv_{r\eta}$, which maps the elementary volume from old coordinate to this transformed coordinate. In the transformed frame of $v_{r\eta}$ and $v_{s\eta}$, Eq. 6 can be integrated over $v_{s\eta}$ to obtain the final expression for the fractional loss rate as

$$\frac{1}{N} \frac{\Delta N_{all}}{\Delta t} = \frac{N}{2} \frac{\int_{-\infty}^{\infty} \int_{-\infty}^{\infty} \int_{-\infty}^{\infty} \prod_{v_\eta}^{x,y,z} |\vec{v}_r| \{\sigma_H(|\vec{v}_r|)\} e^{-\frac{v_{r\eta}^2}{4\sigma_{v_\eta}^2}} dv_{r\eta}}{(4\pi)^3 \sigma_x \sigma_y \sigma_z \sigma_{vx} \sigma_{vy} \sigma_{vz}}. \quad (7)$$

The quantity β_r will remain around 2×10^{-3} in the entire ISNS linac. The corresponding $\sigma_H(|\vec{v}_r|)$ values can therefore be taken more or less as constant with a little approximation and we can assume $\sigma_H(|\vec{v}_r|) \approx \sigma_{max}$. This assumption further simplifies Eq. 7 as the following expression for the fractional beam loss

$$\frac{1}{N} \frac{\Delta N_{all}}{\Delta t} = \frac{N \sigma_{max} \sqrt{(\sigma_{vx})^2 + (\sigma_{vy})^2 + (\sigma_{vz})^2}}{8\pi^2 \sigma_x \sigma_y \sigma_z} \chi(\sigma_{vx}, \sigma_{vy}, \sigma_{vz}). \quad (8)$$

The function $\chi(\sigma_{vx}, \sigma_{vy}, \sigma_{vz})$ denoted in the above equation explicitly represented as

$$\chi(\sigma_{vx}, \sigma_{vy}, \sigma_{vz}) = \frac{1}{16\pi} \int_{-\infty}^{\infty} \int_{-\infty}^{\infty} \int_{-\infty}^{\infty} \sqrt{\frac{\sum_{\eta}^{x,y,z} v_{r\eta}^2}{\sum_{\eta}^{x,y,z} \sigma_{v_\eta}^2}} \prod_{\eta}^{x,y,z} \left\{ e^{-\frac{v_{r\eta}^2}{4\sigma_{v_\eta}^2}} \frac{dv_{r\eta}}{\sigma_{v_\eta}} \right\}. \quad (9)$$

These derivations are performed so far in the beam frame. Following the special

theory of relativity, we need to transform the time from moving frame to the lab frame $\Delta t' \rightarrow \gamma \Delta t$ and the rms sizes $\sigma_{vx} \rightarrow \gamma \sigma_{vx}$, $\sigma_{vy} \rightarrow \gamma \sigma_{vy}$ in the laboratory frame. Inserting these transformed quantities in Eq. 7, we obtain the following formula for the fractional stripping loss rate of H^+ ions in the laboratory frame:

$$\begin{aligned} \frac{1}{N} \frac{\Delta N_{all}}{\gamma \Delta t} &= \frac{1}{N} \frac{\Delta N_{all}}{ds} \frac{ds}{\Delta t'} = \left(\frac{1}{N} \frac{\Delta N_{all}}{ds} \right) \left(\beta_z c \right) \\ &= \frac{1}{\gamma} \frac{N \sigma_{max} \sqrt{(\gamma \sigma_{vx})^2 + (\gamma \sigma_{vy})^2 + (\sigma_{vz})^2}}{8\pi^2 \sigma_x \sigma_y \sigma_z \gamma} \chi(\gamma \sigma_{vx}, \gamma \sigma_{vy}, \sigma_{vz}). \end{aligned} \quad (10)$$

and in terms of per unit length, this can be written in the lab frame as [163]

$$L = \frac{1}{N} \frac{\Delta N_{all}}{ds} = \frac{N \sigma_{max} \sqrt{(\gamma \theta_x)^2 + (\gamma \theta_y)^2 + (\theta_z)^2}}{8\pi^2 \sigma_x \sigma_y \sigma_z \gamma^2} \chi(\gamma \theta_x, \gamma \theta_y, \theta_z). \quad (11)$$

In this formula θ_x , θ_y and the θ_z denote the relative rms angular spread in x , y and z directions.

A1: Algorithm followed for the semi numerical calculation

In this sub-section, we will sketch the brief methodology followed for our calculation for the estimation of the beam loss due to intra-beam stripping in the ISNS injector linac. For this calculation, the required beam dynamics simulations were performed extensively, using the beam dynamics code TRACEWIN.

Following algorithm was developed for the estimation of IBS in the ISNS linac:

- From TRACEWIN simulation, we have extracted β and γ values as a function of the length of the linac for the synchronous particle.
- From the simulation, we also have extracted the three rms beam sizes σ_x , σ_y and σ_z which are plotted in Fig. 6.11.
- Another required information in this formulation is the evolution of the transverse

and longitudinal emittance values along the length of the linac, which is shown in Fig. 6.14 .

From these data, values of the angular spread were calculated using $\theta_\eta = \frac{\epsilon_{\eta}}{\beta\gamma\sigma_\eta}$, where η corresponds to the three directions x , y or z . These values are shown in Fig. 2 in this appendix. In this calculation, corresponding collision cross sectional values were obtained from Fig. 1 in this appendix.

ISNS injector linac is designed for an average micropulse beam current of $I_{av} \approx 14.5$ mA. Here the bunch frequency is $f_{bunch} = 325$ MHz. Hence, in this linac the number of H^- ions within the beam bunch can be calculated as $N_{H^-} = \frac{I_{beam}}{q \cdot f_{bunch}} \approx 2.88 \times 10^8$.

With these input values, we have estimated beam loss due to IBS from Eq. 11 for our ISNS linac, whcih is shown in Figure 6.25.

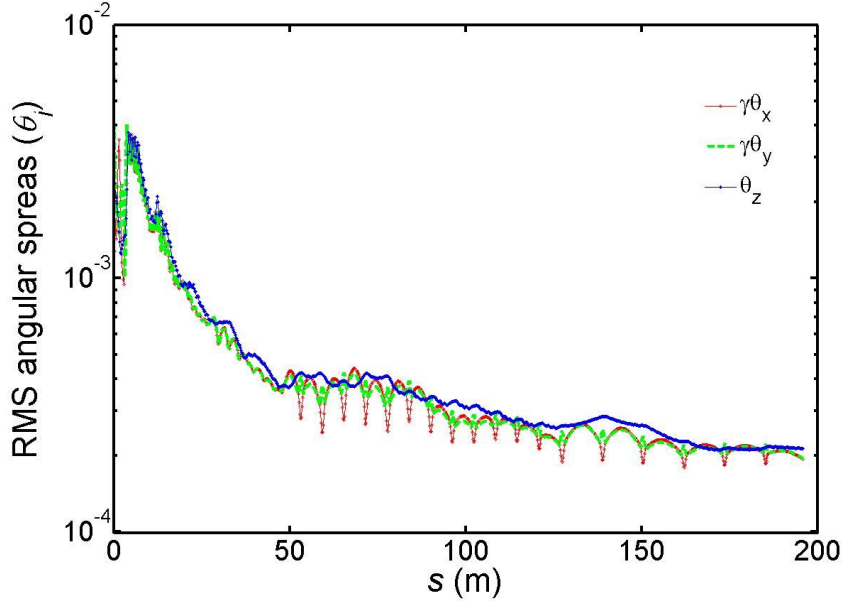


Figure 2: Evolutions of the transverse and longitudinal rms angular momentum spread obtained from TRACEWIN simulation, along the length of the ISNS injector linac.

Thesis Highlight

Name of the Student: Arup Ratan Jana

Enrollment No.: PHYS03201304004

Name of the CI/OCC: Raja Ramanna Centre for Advanced Technology, Indore

Thesis Title: Electromagnetic Design and Beam Dynamics Studies in Elliptic Superconducting Radiofrequency (SRF) Cavities

Discipline: Physical science

Sub-Area of Discipline: Accelerator Physics

Date of viva voce: 29/12/2020

The proposed Indian Spallation Neutron Source (ISNS) will be a linear accelerator based high peak flux pulsed neutron source for experimental studies of condensed matter physics and various engineering applications. The injector linac for the proposed ISNS is designed, using five sets of superconducting radio-frequency (SRF) cavities, where the two sets corresponding to medium and high energy, are of elliptic cavities. In the first part of this research work, we have established a step by step one-dimensional optimization methodology, and

following this one can perform the design optimization of an elliptic SRF cavity for maximum achievable acceleration gradient. A rigorous methodology has also been evolved to perform the calculation of the threshold beam current responsible for the excitation of beam break-up instability in the elliptical cavities. Effect of dynamic deformation of the cavity wall due to Lorentz pressure has been studied for the pulsed mode of operation. Cavity stiffening

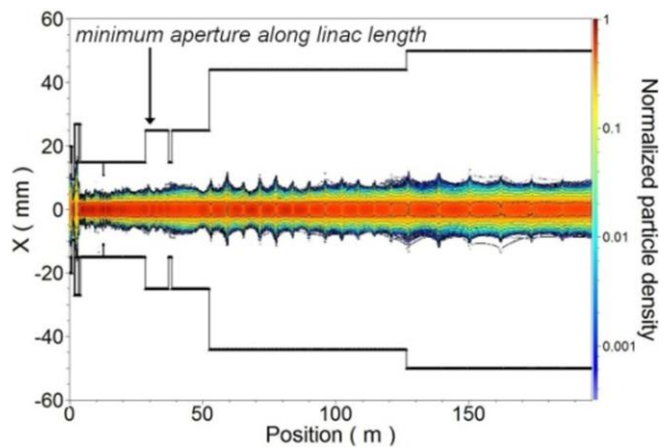


Figure 1: Color map shows radial distribution of normalized particle density along with the available aperture (black), along the linac.

has been done to minimize the associated dynamic detuning of the cavity during its operation, under the constraints of tunability of the cavity and maintaining the field flatness. The optimization of the electromagnetic performance of the SRF cavities was concluded with an interesting magnetothermal analysis, showing the possibility of the low purity, low cost niobium as an alternative SRF cavity material. The next part of this research was the development of a general methodology to perform a compact design of this 1 GeV, 1 MW H^- ion linac superconducting injector linac, by following the *non-equipartitioned* design approach, where the emittance growth of the beam is controlled through appropriate adjustment of the strength of lattice elements, and an acceptable evolution of beam profile inside the available aperture in the linac, as shown in Fig. 1, is obtained. Analytical studies of the stability of mismatched envelope oscillations have been performed for a three dimensional beam bunch. A rigorous beam halo analysis based on Particle Core Model (PCM) was also pursued, considering the actual periodicity of the ISNS lattice, in order to estimate the maximum radial extent of the halo particle in case of a mismatch in the input beam parameter.